Characterization and decoupling of high-quality graphene grown by fullerene decomposition on Cu foils

Memoria presentada para optar al grado de Doctor en Ciencias Físicas

Jon Azpeitia Urkia

Directoras: **Carmen Munuera López and**

Mª Francisca López Fagúndez

Instituto de Ciencia de Materiales de Madrid

Tutor: **Hermann Suderow**

Universidad Autónoma de Madrid

Junio, 2018

Perdida la esperanza, perdida la ilusión,

los problemas continúan

sin hallarse solución.

"*Cerebros destruidos*"**. Eskorbuto, 1985.**

Resumen

El objetivo de la presente tesis se basa en la optimización del crecimiento de grafeno por métodos novedosos con precursores en estado sólido (C60) y en una exhaustiva caracterización de dicho grafeno tanto morfológica como estructural y química por métodos tales como la microscopía de fuerzas atómicas (AFM), espectroscopía Raman, fotoemisión de electrones por rayos X (XPS) o difracción de electrones de baja energía (LEED). Este estudio se ha complementado con el seguimiento por medio de otras técnicas experimentales tales como: espectroscopía de fotoemisión en ángulo resuelto (ARPES), difracción de electrones retrodispersados o microscopía electrónica de barrido (SEM). Esta caracterización exhaustiva nos ha permitido obtener resultados que concluyen que el método de crecimiento alternativo planteado ofrece muestras de grafeno en cobre policristalino de alta pureza (debido al entorno controlado que ofrece el ultra alto vacío) con una fracción nula de bicapas o multicapas de grafeno. Se ha observado que el método es autolimitante. Esto se debe en gran parte a que la ruta que hemos explorado ofrece la capacidad de formación de grafeno a más baja temperatura en comparación con la empleada convencionalmente en métodos de deposición química en fase vapor (CVD). El control de la limpieza de la superficie realizada para promover la formación de grafeno consigue que la acción catalítica del sustrato sea más efectiva, debido a que la completa ausencia de contaminantes que puedan dificultar dicha interacción sustrato-precursor.

Para buscar aplicaciones tecnológicas del grafeno en cobre, se han llevado a cabo experimentos para la optimización del proceso de transferencia del grafeno a sustratos aislantes, tales como el SiO_2, por métodos químicos. Para dicha optimización se han considerado dos aproximaciones: por un lado, la intercalación en la interfase grafeno/cobre de moléculas por métodos electroquímicos. Por otro lado, se han empleado técnicas de ultra alto vacío para la intercalación de elementos como el oxígeno en dicha interfase también con el propósito de debilitar interacciones que afectan directamente a su transferencia. A su vez, estos dos procedimientos han sido mejorados apoyándose en continuas caracterizaciones tanto estructurales como químicas y electrónicas con las técnicas arriba mencionadas. Se han llevado a cabo la evaluación de las propiedades eléctricas de las muestras transferidas a sustratos aislantes por medio de medidas de efecto Hall a baja temperatura (2K), medidas de magnetotransporte y determinación local del potencial superficial (KPFS).

Finalmente, se ha equipado el laboratorio con un imán vectorial superconductor con capacidad de aplicar campo magnético en todas las direcciones del espacio, ensamblado a un equipo criogénico y a un microscopio de fuerzas magnéticas (MFM) con capacidad de medir de manera local las propiedades magnéticas superficiales. Se ha caracterizado el perfil del campo magnético en el área donde reside la muestra, para certificar la homogeneidad del campo en toda la zona donde se llevan a cabo las medidas. Para la observación de las capacidades del sistema construido se han estudiado dos sistemas físicos. Por un lado se ha

evaluado un disco duro donde la inclinación del campo magnético se refleja en la respuesta magnética de los bits. Por otro, en aras de determinar la capacidad del equipo experimental, se ha medido un material heterostructural, basado en un material superconductor donde se ha depositado grafeno crecido por el método que hemos planteado. Los resultados, aunque preliminares, validan este método de caracterización local de sistemas complejos para su uso en sistemas como pueden ser los altamente correlacionados, ya que este equipo experimental permite relacionar respuestas físicas con variaciones tanto en la intensidad como dirección del campo magnético, así como de temperatura que puede variar en un rango entre 1.5 y 300K.

Index

Chapter 1. Introduction

Since it was firstly isolated, in 2004, graphene has become one of the most known material not only for the scientific community, but also for the society. Everybody, no matter their background, has heard about this material, and although a Nobel prize (A. K. Geim and K. Novoselov were awarded in 2010 for being the main authors of the pioneering work that consisted on the isolation, detection and characterization of some of electronic properties of graphene in 2004) can help in the popularization process of any scientific milestone, the fact of being a one atom thick material, attracted in the subsequent years the interest of the general media. Nevertheless, it is just graphite, so common material (composed of C atoms, not an exotic element), taken to its minimum expression: one single atom thick of graphite. And the emerging physical properties marked the route of material science up to these days, 14 years gone by, and counting.

The first use of the ease exfoliation property of graphite has been known to be in the 4th millennium B. C., during the Neolithic Age. It is known that the Boian culture (a Neolithic archaeological culture of southeast of Europe where now are Romania and Bulgaria) used graphite in a ceramic paint for decorating pottery [1]. The way Novoselov et. al. isolated a one atom thick carbon layer is based in the same property that made graphite useful for the ancient Neolithic settlers[1]. The groundbreaking point was not the isolation of graphene (we all have done it since a pencil arrived to our hands) but its identification (to realize that it could be distinguished by an optical microscope) and the design of the experiments that determined some of its amazing electronic properties [2].

1.1 Graphene

Graphene is a one atom thick carbon layer, ordered in a honeycomb-like crystallographic lattice arrangement (***figure 1.1***). This arrangement is due to the sp^2 hybridization of the s and p_x and p_y electronic orbitals, that form a trigonal geometry, with a 120° rotational symmetry, with one electron in each lobe that produces a covalent bond with the next carbon atom. Due to this symmetry, the atoms are arranged in this mentioned honeycomb-like lattice. The p_z orbital points out of plane with another electron. The lateral coupling of these orbitals forms a huge delocalized molecular orbital, known as π cloud. While the covalent bonding of the sp^2 orbitals is the main responsible of the strength and rigidity of this material, the π cloud is the responsible of the high electronic mobility that graphene presents.

[1] This fact shows the importance that the comprehension of the employed systems has.

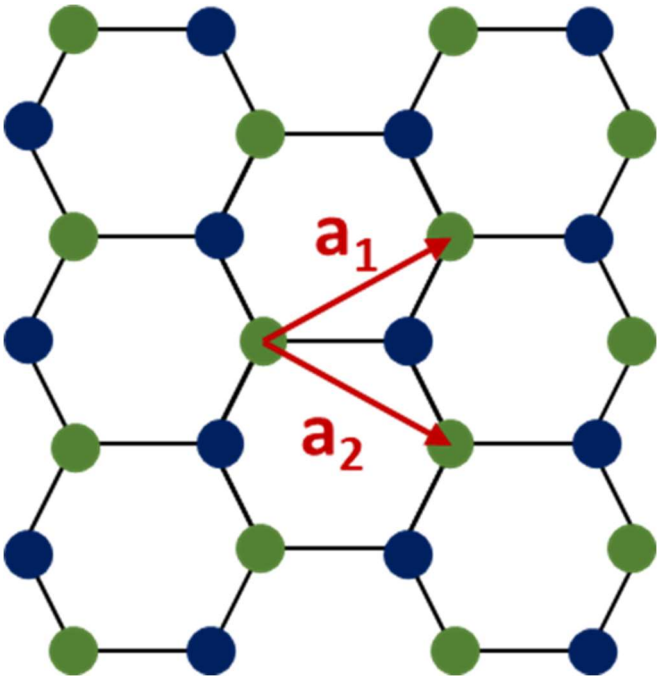

***Figure 1.1**. Sketch of the carbon atoms forming graphene. The different colors distinguish the two sublattices. The two red vectors form the base that describes the green sublattice (the second sublattice, in blue, is equivalent but independent).*

The distance between the nearest two carbon atoms is 1.42 Å. The lattice is formed by two sublattices (see ***figure 1.1***), as it was presented by Wallace to calculate the band structure of a single graphite layer by using the tight-binding approximation in 1947 [3]. The lattice parameter of these sublattices is 2.46 Å.

1.2 Electronic structure and properties

Graphene is a zero-gap semiconductor, or semimetal. The term semimetal refers to the fact that although there is no gap, the density of states at the Fermi level is zero, thus it is not a traditional semiconductor nor a traditional metal. The conduction and valence bands meet at the so-called Dirac points, which are locations in momentum space (***figure 1.2***). There are two sets of three Dirac points at the corners of the first Brillouin zone, derived from the two equivalent but independent sublattices. The two sets are labeled as K and K´. This fact, gives to graphene a degeneracy (electrons in K and K´ are in two different states with same energy) and generates some of the interesting electronic properties of graphene, as can be the chirality of electrons [4].

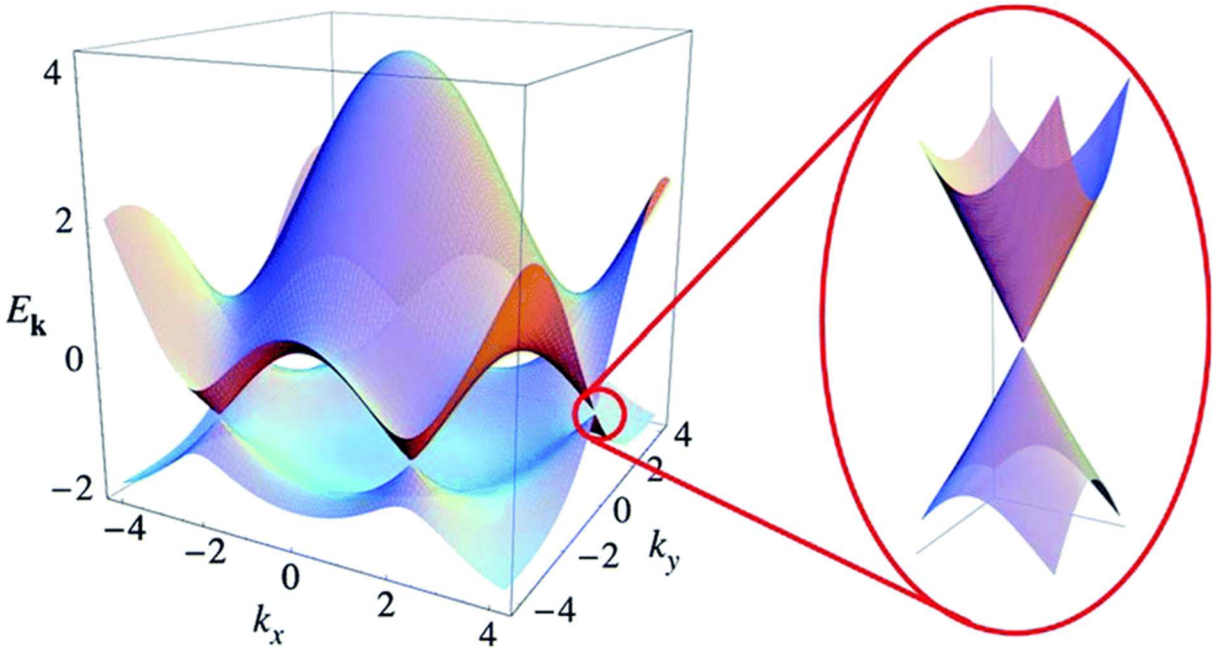

***Figure 1.2**. Electronic structure of graphene. The zoom at K (or K´) point shows the Dirac cone. Figure obtained from [4].*

Within an energy of ± 1eV, the dispersion relation at the Dirac point (K or K´) is linear, and electrons behave as low-energy massless Dirac fermions, with a velocity of $v_F = 1.10^6$ m/s. This is one of the main reasons way graphene became so popular. In addition to these property, the valley degeneration (the fact that K and K´ points are equivalents but independent) generates the chirality of electrons. It can be understood in the sense that each Dirac point contributes with one of the branches of the dispersion. One branch of dispersion cannot be transformed by into the other. This chirality indicates the existence of a pseudospin, a new degree-of-freedom together with orbital and spin, due to the basic lattice structure that comprises two independent sublattices [5]. In addition, derived from the Dirac equation (relativistic Schrödinger equation), an exotic property appears for the charge carriers. When an electron of a typical semiconductor finds a potential barrier higher than the kinetic energy of the carrier, the electron wave function will decay exponentially within the barrier. The higher and wider the barrier is, the less the probability of quantum tunneling of the electron. In the case of graphene (actually, for all particles governed by the Dirac equation), an electron that finds a potential barrier will turn into a hole, cross the barrier and turn back into an electron. This phenomenon is known as Klein tunneling. This effect, that implies the absence of backscattering, was discovered by Ando et. al for carbon nanotubes [6] and found to be the

responsible of the high conductivity exhibited in the presence of disorder. Experimental evidences of the Klein tunneling in graphene have been reported [7,8].

Graphene presents really exotic electronic properties, therefore, when comparing this material with traditional semiconductors the following differences have to be remarked:

- While semiconductors are defined because of the band-gap they have, in the case of graphene the band-gap is zero. In graphene, the nature of the carrier changes from electron to hole and vice-versa at the Dirac point.
- In graphene the dispersion relation of charge carriers near the Dirac point is linear while in typical semiconductors is quadratic. There are many impressive physical phenomena derived from this fact, as can be the ballistic velocity of the carriers at low energies.
- In graphene the carriers, near the Dirac point, are massless relativistic particles, deriving in exotic phenomena like the Klein tunneling.
- Graphene has a finite minimum conductivity even in absence of charge carriers, i.e. although there are no available states at the Dirac point, the band-gap is zero. This leads to an issue for its application as field-effect transistor, since it would have low on/off ratios with the consequence of high energy consumption [9,10].

1.3 Vibrational structure and properties

The vibrational properties of a material are determined by its phonon dispersion relation. A theoretical calculation of the branches of the phonons in graphene is shown in ***figure 1.3***. The two sublattices have to be taken into account with three spatial degrees-of-freedom that leads to six vibrational normal modes or phonons. Two of them are out-of-plane phonons: the acoustic mode (ZA) and the optic mode (ZO). The remaining four phonons correspond to in-plane vibrations: TA (transversal acoustic), TO (transversal optic), LA (longitudinal acoustic) and LO (longitudinal optic).

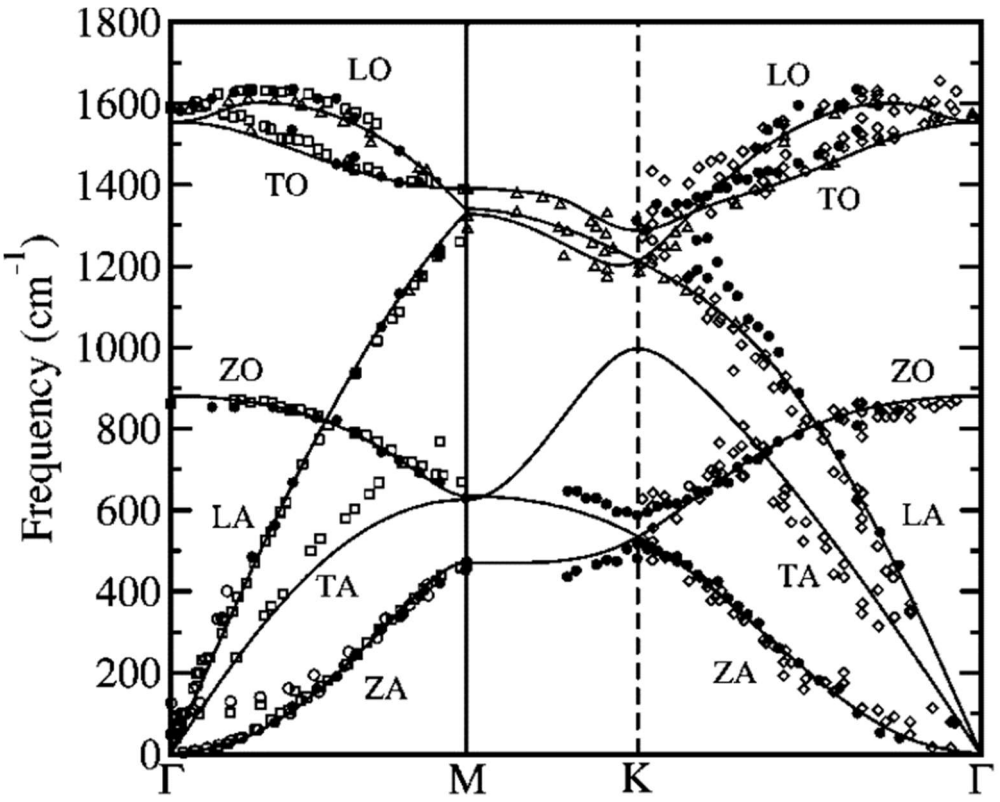

***Figure 1.3**. Calculated phonon relation dispersion of graphene (continuous lines). Experimental data for graphite are overlapped (dots). Figure taken from* [11].

The light atoms graphene is formed of, together with a strong covalent in-plane bonding of those atoms lead to the phonon dispersion shown in figure 3. An important consequence of this relation is a high in-plane sound velocity. Thus, graphene exhibits a very high thermal conductivity.

From the kinetic theory of gases, phonon-driven thermal conductivity depends on the sound velocity, specific heat per unit volume (temperature dependent) and the mean free path of the phonons. Extremely high thermal conductivities have been reported for graphene ($\kappa \approx 3080 - 5150$ W/mK) [12,13]. It is important to note that for supported graphene on SiO_2 the values found were smaller, although still larger than metals like copper [14].

1.4 Synthesis methods

There has been an important development of different graphene synthesis methods since it was firstly isolated in 2004 by the scotch tape technique [2]. The most interesting goal of a synthesis process would be the one that could gather the capacity to form high-quality, defect-

free, high-yield, cost-efficient and scalable graphene. Nowadays there is no such a method. There are several techniques, and each one has advantages and drawbacks.

The scotch tape technique is a mechanical exfoliation method. The advantages of this technique involve the high quality of the resulting graphene flakes. As a drawback, the lack of scalability and the limitation of the size of the flakes as well as the yield.

The method consists on placing a scotch tape on top of a HOPG (highly oriented pyrolytic graphite) and through several adhering-releasing operation exfoliate it repeatedly. The scotch tape is full of different thicknesses of graphite flakes, that are deposited onto a substrate. The use of thermally oxidized Si (~280-300 nm of SiO_2), as substrate for graphene flakes, was motivated to be able to rapidly identify the flakes onto the substrate [2]. The oxide thickness of Si (the thickness is decisive) permits to identify one-atom-thick flakes by optical microscopy [15] (***figure 1.3***). Photons reflected on top of the SiO_2 interfere constructively with the ones reflected on the surface of the Si along a wavelength. The atom-thick layer moves this wavelength slightly, obtaining a different color where the flakes have been deposited.

The flakes obtained by this method present the highest mobility reported for charge carriers ($\sim 200000\ \frac{cm^2}{S\,V}$) [16]. The industrial application is not possible but it is very useful for prototyping and research purposes.

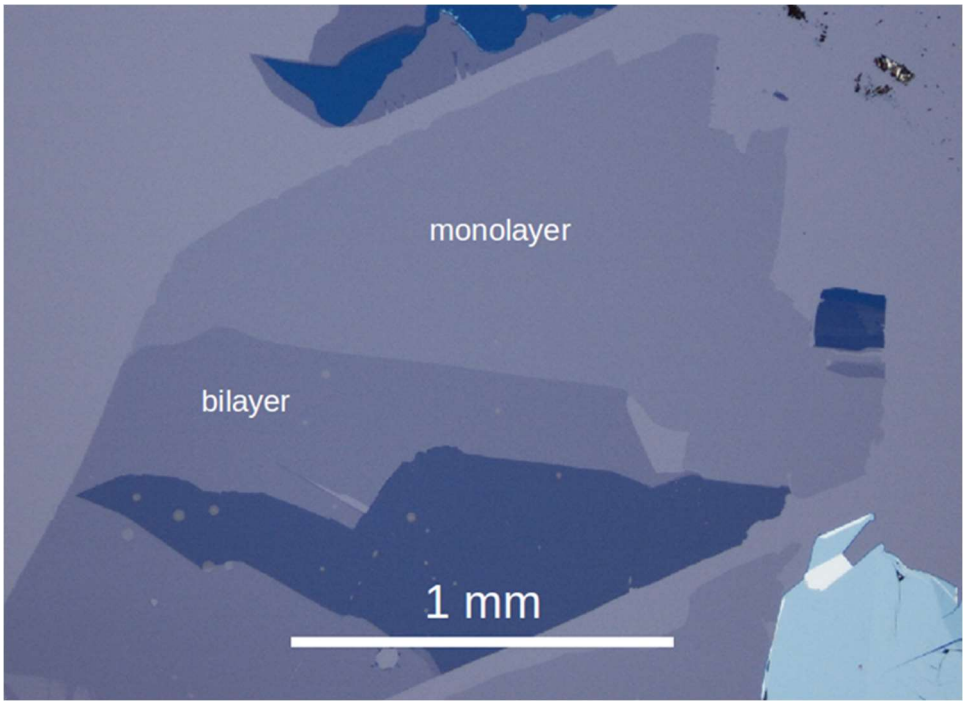

Figure 1.4*. Optical image of a graphene flake together with a bilayer and a multilayer flake. Figure extracted from [4].*

This method was improved in the incoming years by using a viscoelastic polymer (PDMS) with an experimental set-up that permitted a deterministic transfer [17].

The graphitization of SiC is another technique for the synthesis of graphene and consists on the sublimation of the Si atoms of the silicon terminated face of SiC. The carbon atoms that are left on the surface rearrange to form graphene [18]. This method provides scalability up to several cm, produces high quality extended graphene layers and, since the substrate is a semiconductor, could have an applicability in the semiconductor industry. The main drawbacks are the high temperature needed for the sublimation of the silicon atoms (temperatures ranging from 1000 to 1500°C) and the high cost of the substrates.

In the case of the two methods shown until now, the quality prevails to the scalability and yield. On the other hand, methods like liquid-phase exfoliation or exfoliation of graphite oxide provide low-cost graphene production, whereas the quality of graphene is lower comparing to the above described methods. The applications of the product obtained by these techniques could be others, less demanding, like conductive inks or graphene-based composites that could lead to specific applications such as transparent-conductive electrodes or thin film transistors.

Liquid-phase exfoliation consists on the exfoliation of graphite in an aqueous solution by employing an adequate solvent, like the N-methyl-pyrrolidone with a sonication process [19] where a yield of up to 12% of non-oxidized single-layer graphene could be obtained. One of the problems, in addition to the difficult removal of the solvent, is that the size of the obtained flakes is not larger than 1 μm. On the other hands lies the versatility of the technique, because with the adequate interaction of the liquid with the crystal, almost any layered material could be exfoliated [20].

Looking for a compromise between the quality, yield and cost-efficiency, the CVD (chemical vapor deposition) method is considered the most efficient. This method is based on the catalytic action of the employed substrate. For this purpose, the chosen substrates are transition metals with dissimilar reactivity (nickel [21], copper [22], ruthenium [23], rhodium [24] iridium [25] or platinum [26,27] among others) that catalyze, via surface, the decomposition reaction of the employed precursors (carbon-rich molecules in gas phase such as methane, acetylene or ethylene [28]) (***figure 1.5***). A compromise is needed between the reactivity and the diffusion capacity of the metal surfaces, in order to on one hand, be able to decompose the molecule at a reasonable temperature (around 1000°C in CVD on copper processes) and

on the other hand to provide the carbon atoms with the needed mobility to meet each other and rearrange into the sought honeycomb-like lattice.

Among all these substrates, copper has been considered the most promising candidate for a high-production low-cost high-quality graphene synthesis [28]. In order to decrease costs, the employ of single crystals is completely discarded, and few micron copper foils have been the most extended substrates for this purpose, although polycrystalline nickel and platinum foils have been also employed [27]. Together with the mentioned low cost of polycrystalline copper foils, the self-limiting character of the process (low solubility of C into the bulk [29], avoiding posterior segregation on the surface that would lead to the formation of more than one layer of graphene) and great performance in the decomposition of the precursor molecules has promoted its utilization.

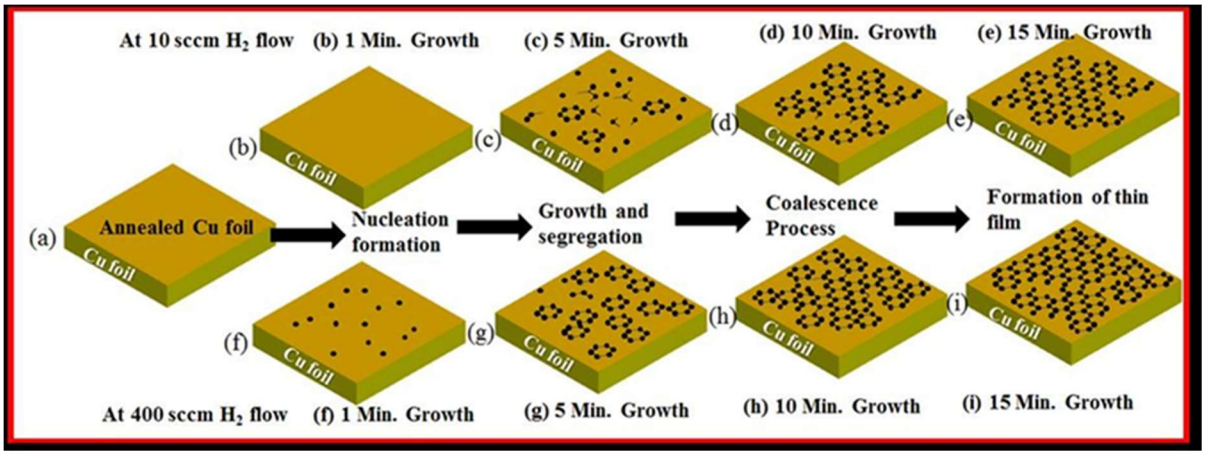

Figure 1.5*. Illustration of the growth process of CVD graphene on Cu. At 950°C for 1, 5, 10, 15 min at constant 10 and 400 sccm H2 flow (a-i). Illustrative growth schematics: (i) incubation, (ii) nucleation formation, (iii) growth and segregation, (iv) coalescence process, and (v) formation of films. Figure obtained from ref.* [30].

Graphene grows polycrystalline on copper by CVD methods because of the different nucleation points present in the growth procedure, where graphene starts to grow following different orientations (***figure 1.6***). Nonetheless, a great improvement has been observed in this direction, with reported 1 mm single crystal graphene grains, by employed the pocket-method [31] where the pressure of the precursor gas is drastically decreased, leading to less nucleation points. The drawback of this technique is the long duration, that can last more than 6 hours [31].

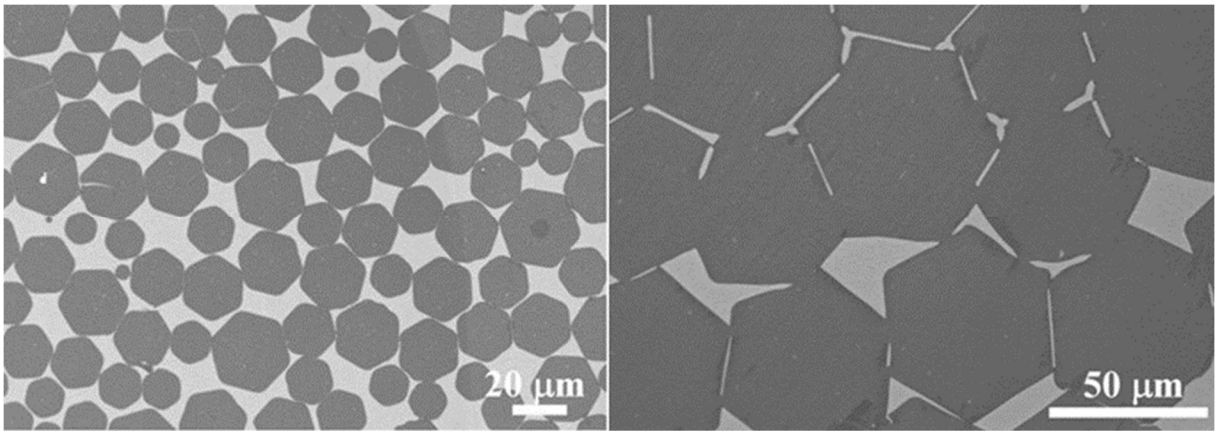

***Figure 1.6**. Scanning electron microscopy (SEM) images of graphene patches on molten Cu. Left panel: a partially covered and well-dispersed hexagonal graphene patches using 6 sccm CH4/300 sccm H2 at 1,120 °C for 30 min. Right panel: large-sized HGFs showing that the average sizes are approximately 50 μm. Figure adapted from* [32].

In the presented thesis, an alternative route is proposed, based on copper substrates, but by employing a solid phase precursor that is directly sublimated onto the target surface. Due to the physical process of the precursor sublimation, it is a physical vapor deposition (PVD) method. Moreover, and in order to precisely control the growth environment, ultra high vacuum (UHV) technology has been employed for a complete cleanness not only of the precursor arriving to the surface but also of the metallic surface that will catalyze the synthesis reaction. The solid phase precursor employed has been the C_{60} molecule.

The growth on metals demands a posterior transfer methodology in order to study the electrical parameters of the layer that otherwise would be short-circuited by the underlying metal. The alternative methods are described in the 1.7 section of this introduction.

1.5 Graphene/metal interaction

As already mentioned, the use of metals for the growth of graphene has carried many advantages, but since the aim is to transfer those grown layers onto arbitrary substrates, the interaction between graphene and the metal needs to be taken into account. Although the most common metallic substrate for CVD graphene growth, is copper, several metals have been proven to have the catalytic-like activity that promotes the reaction.

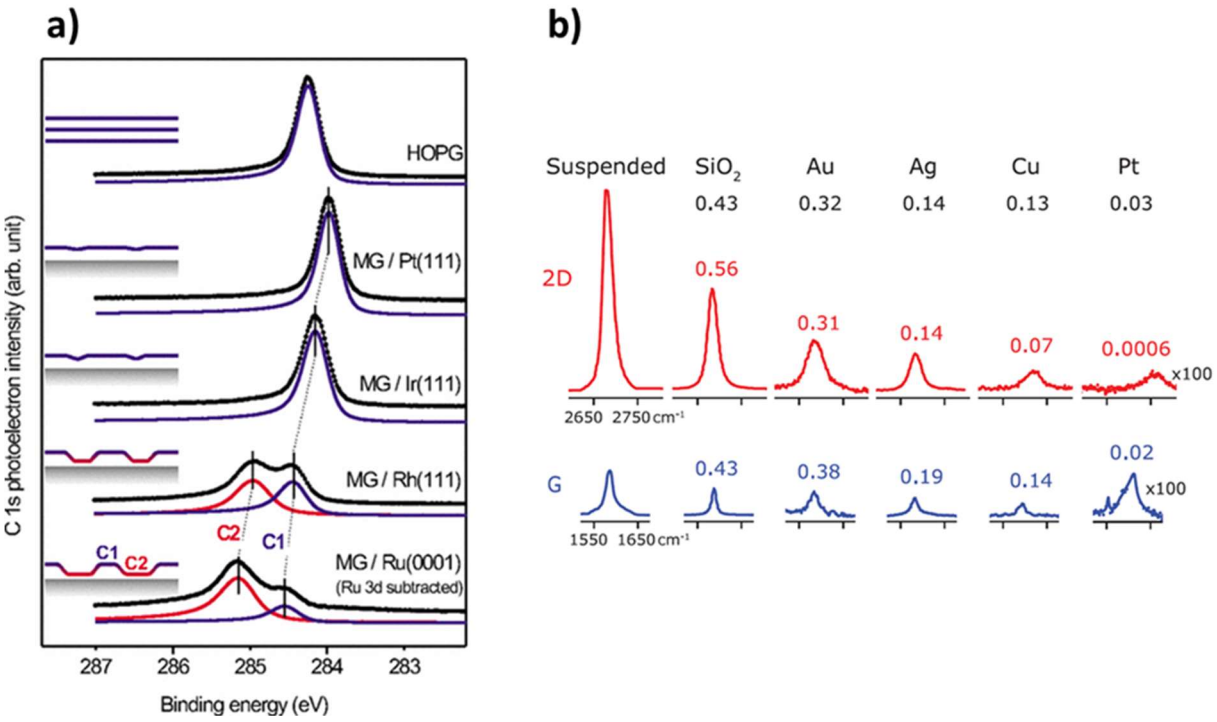

Figure 1.7*. Examples of the effect of the graphene/substrate interaction. a) XPS spectra centered on the C 1s core level for graphene on different metallic substrates where a displacement is observed with respect the peak of HOPG. A shift in energy is observed for low interacting metals while there is a splitting of the C 1s peak for high interacting metals* [33]*. b) 2D and G peaks of Raman spectroscopy where the effect of the substrate with respect to suspended graphene is evidenced* [34]*.*

Figure 1.7a shows the effect of the substrate on the graphene evidenced in XPS (X-Ray Photoemission Spectroscopy). Observing the peak position corresponding to the C 1s core level emission of a HOPG sample, a shift in energy is observed for graphene on platinum and iridium, meaning that there is a charge transfer between the graphene layer and the metal that moves the Fermi level of the graphene and thus, the binding energy of the core level C 1s electrons. This effect will be deeply discussed in chapter 4. The case of rhodium and ruthenium is more aggressive, where there are two non-equivalent graphene positions due to chemical interaction generated by the substrates. These type of "chemisorbed" graphene is out of the scope of the present thesis. From the Raman spectroscopy perspective, ***figure 1.7b*** shows the effect of different substrates on the graphene layer, traduced on the attenuation of the characteristic graphene Raman peaks (G and 2D peaks) with respect to the free-standing graphene Raman peaks. This effect will be discussed in chapter 3 and 4 for the case of copper substrates.

1.6 Intercalation of chemical species in the graphene/metal interface

Graphene has been described in the first section. Later on, we have mentioned some methods to synthesize graphene on metals. But does that graphene (carbon) layer grown on different type of metals fulfill the graphene characteristics? The answer is "no". The properties of the graphene layer on different type of metallic substrates are altered. The aim of retrieving the free-standing graphene properties (relaxation of strain and recovery of the electronic structure among others) has generated an interest in the decoupling of graphene from the interaction it can have with the metal. In this direction, intercalation of chemical species in graphene on metallic substrates such as iridium, ruthenium or rhodium among others have been reported [35–38]. In addition, the interest in modifying the chemistry under graphene has led also to intercalation processes [39,40]. For all these purposes, many investigations on the intercalation of different chemical species (hydrogen, oxygen, gold, cesium, europium…) have been performed [40–44].

A proposal of the oxygen intercalation mechanisms on Gr/Ru(0001) was reported in [23] and more extensively on the Gr/Rh(111) system [45], where oxygen first intercalates through grain boundaries and defects of graphene, then dissociates on top of the metallic substrate and finally diffuses to inner parts of the sample.

In chapter 4 of the present manuscript results on the intercalation of oxygen in UHV-grown graphene on copper substrates will be described, where the graphene layer, with non-negligible interaction with the copper underneath, decouples from substrate and the transfer of the layer to SiO_2 substrates is improved.

1.7 Transfer of graphene grown on metals

Mainly two routes have had success on transferring graphene to arbitrary substrates. The first one is based on the chemical etching of the metal layer in a solution, that leaves the graphene layer floating on the etching solution and it is fished with the target substrate. This was the most important reason to use cheap substrate (the use of polycrystalline copper foils). Each metallic substrate was disposable and, for this reason, other more expensive materials were avoided as it was, of course, the case of single crystals.

Later, the electrochemical delamination method was developed [46] that allowed to reuse the substrate. This lead to the use of for example platinum foils, where the platinum foil was repeatedly used [27].

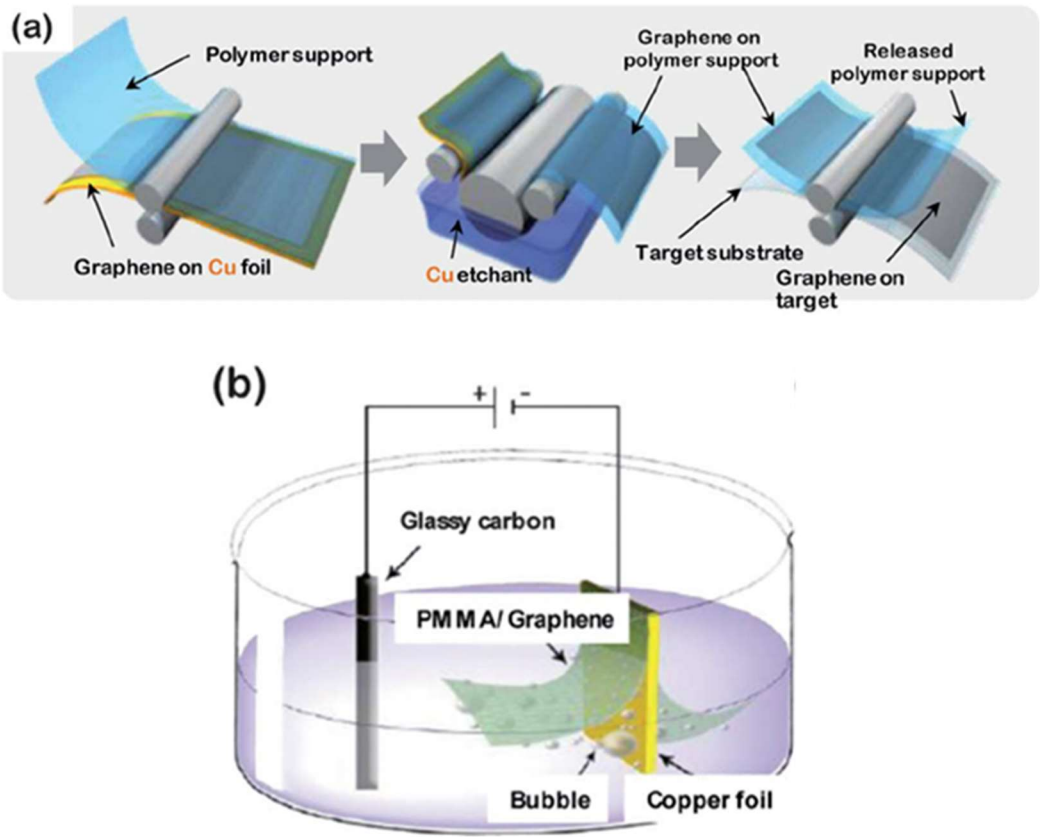

***Figure 1.8**. (a) Roll-to-roll transfer of graphene grown on a Cu foil, using thermal release tape. (b) Schematic diagram of the electrochemical transfer of graphene from a metal substrate using an electrochemical cell. Figure adapted from* [47].

In ***figure 1.8a*** is shown the etching process of a roll-to-roll transfer process by the copper etching process, while ***figure 1.8b*** represents the electrochemical delamination method. The transfer method employed in chapter 3 is based on this second technique.

1.8 Thesis outline

The present thesis is composed of two scientific works. The first one deals with the research of an alternative method of growth of graphene on polycrystalline copper foils and the characterization of the graphene obtained by this new procedure. The second one consists in the implementation of an experimental set-up consisting on a He cryostat with a home-made three-axis vector magnet for the local characterization of magnetic properties within RT and 2K under tilted magnetic fields, that allows the study of some properties of graphene on particular substrates.

After the description of the most relevant experimental techniques employed for the consecution of the current thesis, that will be detailed in chapter 2, the results of the two previously mentioned sections will be presented.

On one hand in chapter 3, an alternative route for the growth of graphene on polycrystalline copper foils is proposed. The characterization of the obtained layers is made through different techniques to determine the structure and morphology of the layers as well as the chemical and electronic structure characterizations. The employed techniques encompass electron diffraction and scanning electron and force microscopy techniques and Raman spectroscopy methods for structural and morphological characterization. Employed polycrystalline copper substrate surface and bulk crystallographic structure have been studied by means of X-ray and electron backscattering diffraction methodologies. Photoemission spectroscopies have been employed for the chemical and electronic structure characterization, and a high quality of the obtained layer has been observed. Moreover, suppression of resonant effects in Raman spectroscopies have been noticed due to substrate interaction, that has led to the intercalation of oxygen in the graphene/copper interface described in chapter 4. Two different strategies have been followed for the intercalation of chemical species in the graphene/copper interface to favor the transfer procedure of the layer to insulating substrates. Thus, in chapter 4, the transfer process is described and the characterization of the resulting layers has been made.

On the other hand, the description of the construction of an experimental set-up will be shown in the last part, chapter 5. The set-up relies on a superconducting three-axis vector magnet to produce tilted magnetic fields, immersed in a ^{4}Helium cryostat able to scan in temperatures ranging between 300-2 K. A commercial MFM has been placed for the acquisition of local magnetic correlated with the surface topography by means of simultaneous image acquisition. Finally, some preliminary results on graphene transferred after growing by the proposed alternative route to the superconducting β-Bi_2Pd substrate is detailed in this section.

The most relevant conclusions obtained within this work are summarized in the final chapter.

The realization of the presented work would be impossible to accomplish without the grant of the FPI program from Spanish MINECO, BES-2012-058600. Therefore, I would like to acknowledge all the Spanish citizens that with their taxes have made it possible.

Chapter 2. Experimental methods

This chapter describes the most relevant experimental techniques as well as the substrates (copper single crystals and polycrystalline foils) and the carbon precursor that have been used over this thesis. Besides, the UHV chamber employed for the preparation of the samples will be also described. Thus, some details on the techniques based on the diffraction of low energy electrons (LEED), the atomic force microscopy (AFM) together with the Kelvin force probe spectroscopy (KPFS), Raman spectroscopy and the X-Ray photoemission spectroscopy (XPS) will be addressed below. This chapter tries to describe the methodology of the used procedures, in order to understand how have been obtained the results that will be detailed in the following chapters.

The explanation of these techniques does not intend to be exhaustive, considering that all the employed techniques are well established in the scientific community and there are many works that can explain in a very detailed way all the experimental set-ups utilized here [48]. However, attending to the multidisciplinary trend that science has acquired in general and material science in particular, it is worth to gather the different techniques that have been employed to give as a result a more comprehensive understanding of the growth, intercalation, transfer process and functional properties of the studied graphene systems.

Several techniques have been occasionally used in addition to the ones listed above, together with some theoretical calculations that have shed light on the systems that have been studied. Nonetheless, the use of those techniques has not been so extended or have been within the framework of scientific collaborations. Within those techniques, X-ray diffraction (XRD) have been performed at the ICMM, scanning electron microscopy (SEM) measurements were done also at the ICMM microscopy service, μ-LEED patterns were acquired at CIRCE in Alba synchrotron. Electron backscattering diffraction (EBSD) measurements were done by V. Vales from the group of M. Kalbac and angle-resolved photoemission spectroscopy (ARPES) were carried out at Cassiopé line in Soleil synchrotron. In addition, the theoretical calculations shown in chapter 3 and 4 were performed by J. I. Martínez. A brief description of these techniques will be presented in the chapters where the corresponding methods were applied.

2.1 PVD Growth Chamber

The graphene growth was accomplished in an ultra-high vacuum chamber with a base pressure of 3 x 10^{-10} mbar (***figure 2.1a***). This base pressure is essential to perform surface

science studies. According to the kinetic theory of gases, with a pressure of 1 x 10^{-6} mbar, and considering a sticking factor of 1, the sample is covered with 1 monolayer of contamination within 1 second (1 Langmuir) [49]. In the case of the graphene growth, where the complete process lasts about typically 1 hour, a pressure of 3 x 10^{-10} mbar ensures a clean copper interface for several hours, preventing undesirable contamination of the surface. This is one of the differences of our growth method compared to conventional CVD processes, where the pressure is in the order of the mbar.

Working in UHV environment implies that the deposition and the heating of the samples need to be done by using methods that are different from those employed in conventional CVD. We described now the different components used in the growth system:

- An electron bombardment heater stage. This system yields a very localized heating. Current passes through a cathode (thoriated tungsten in the present case), and generates a Joule heating effect, providing energy to the electrons, until they overcome the work function energy, intrinsic of the material, and escape from the filament (represented in red in ***figure 2.1c***). Once free, they feel the electric field between the cathode (grounded) and the sample (at high voltage). The electrons impact the sample (depicted in orange in ***figure 2.1c***) and dissipate their energy provoking the heating of the sample (***figure 2.1b***). There are two parameters to control the heating temperature: the current measured on the sample (number of electrons arriving the sample) and the energy of each electron. This energy depends exclusively on the voltage difference (1kV → 1KeV). Additionally, the part below the filament (see ***figure 2.1c***) is negatively charged for the electrons to be repulsed towards the sample and avoid the unnecessary heating of the rest of the heater.

- A molecular evaporator. It consists of a home-made tantalum crucible to be introduced in the UHV chamber, attached to a feedthrough. The electrical current flows within the crucible and due to the Joule effect the molecules are heated up until they reach their evaporation temperature. This desired temperature is monitored with a K-type thermocouple that is spot-welded to the back of the crucible (see ***figure 2.1d***).

- Low energy electron diffraction (LEED). This is the only in-situ diagnosis tool, together with the mass spectrometer. It consists of an electron gun and a screen. It shows the superficial crystallographic structure of the samples by the electron diffraction phenomenon (this technique is explained in more detail in the next section).

- Mass spectrometer. This system determines the chemical species of the residual gas of the vacuum chamber including those desorbed from the samples. In this thesis it has been used for contamination determination and leak test procedures.

- Ion gun. It is used for cleaning the samples by ion bombardment. It consists of a cathode emitting electrons that ionize the argon gas (an inert gas that will not chemically interact with the target, in this case the copper surface). Then, a plate acting as repeller (where a suitable potential is applied) accelerates the Ar^+ ions towards the sample. This Ar^+ bombardment pulls out everything it finds (at atomic level), including contaminants.

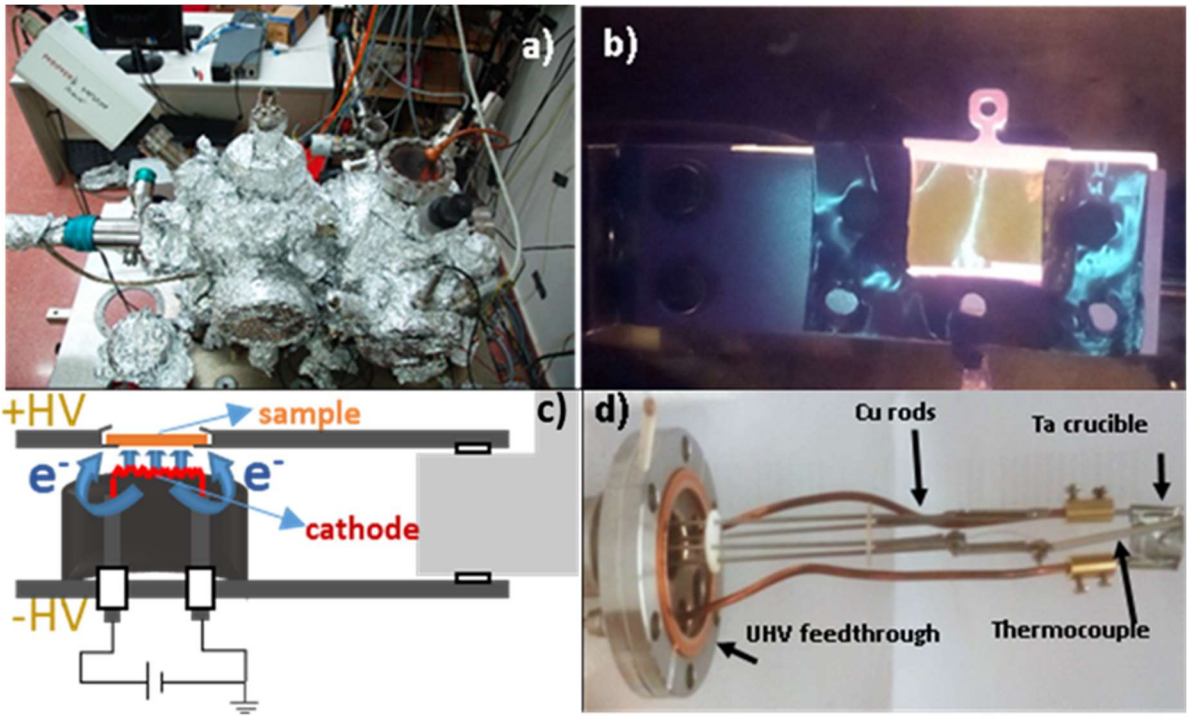

***Figure 2.1**. Images of a) the UHV growth chamber, b) a copper foil, on the sample holder, being annealed in the heater, c) a schematic view of the electron bombardment heater and d) the molecular evaporator.*

2.2 Low Energy Electron Diffraction (LEED)

The wave nature of electrons was firstly predicted by L. de Broglie in 1924 [50] and, three years later, experimentally confirmed by the observation of the electron diffraction patterns of a solid, as it was demonstrated in 1927 [51]. Years went by until this phenomenon was applied in the characterization of crystalline surfaces under UHV conditions.

Nowadays, LEED is a basic technique in surface science, able to extract qualitative and quantitative information of the crystallographic structure of conductive crystalline surfaces. An electron beam, with energies in the range of 20-300 eV is used to interact with the sample (***figure 2.2***). The wave length of the electrons in this range of energies is similar to the interatomic distances, and fulfills the diffraction conditions. After this interaction, some of the electrons are backscattered. The inelastically scattered electrons are stopped by the negatively charged grids, while the elastically scattered ones are accelerated towards the screen (***figure 2.2***). When reaching the surface, the ordered atomic network that forms the surface of a crystal acts as a diffraction grid, where the interference of the electrons is constructive at some points and destructive at others. These elastically backscattered electrons are collected in a fluorescent screen that is set at a high voltage, with respect to the sample, to accelerate the electrons towards it [49]. The pattern observed on that screen is a representation of the reciprocal lattice surface structure.

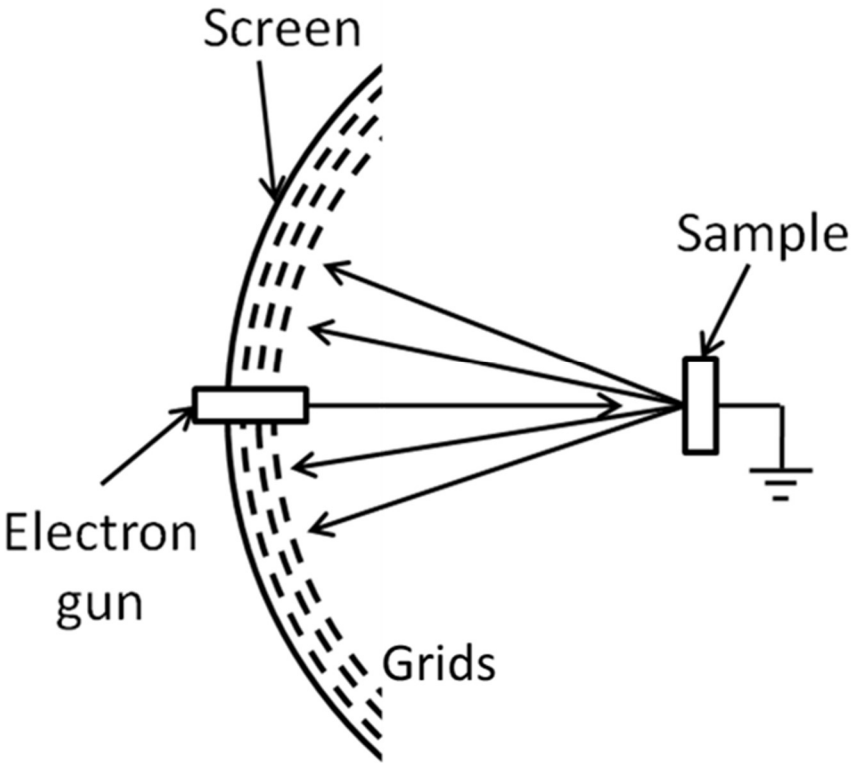

Figure 2.2. *Schematic view of the LEED technique. The electron gun throws low energy electrons towards the sample. The elastically scattered electrons will impact the fluorescent screen and show a diffraction pattern that is correlated with the crystallographic symmetry of the surface of the sample.*

Figure 2.2 shows a sketch of the LEED system where the sample appears grounded. In this technique, the sample needs to have an ordered surface (a long range arrangement of the atoms is necessary to have a collective diffraction signal that can be measured) and it needs to be conductive and to be grounded, to avoid to get charged by the electrons that arrive to the surface. With respect to the electron gun, it is a filament (cathode) where a current is applied and electrons gain energy until they leave the filament. Once out, they feel an electric field that accelerates them towards the sample. Then, tuning this electric field is how electron energy is tuned. Since the distance of the cathode and anode is constant, the electric field is varied by varying the voltage of the anode.

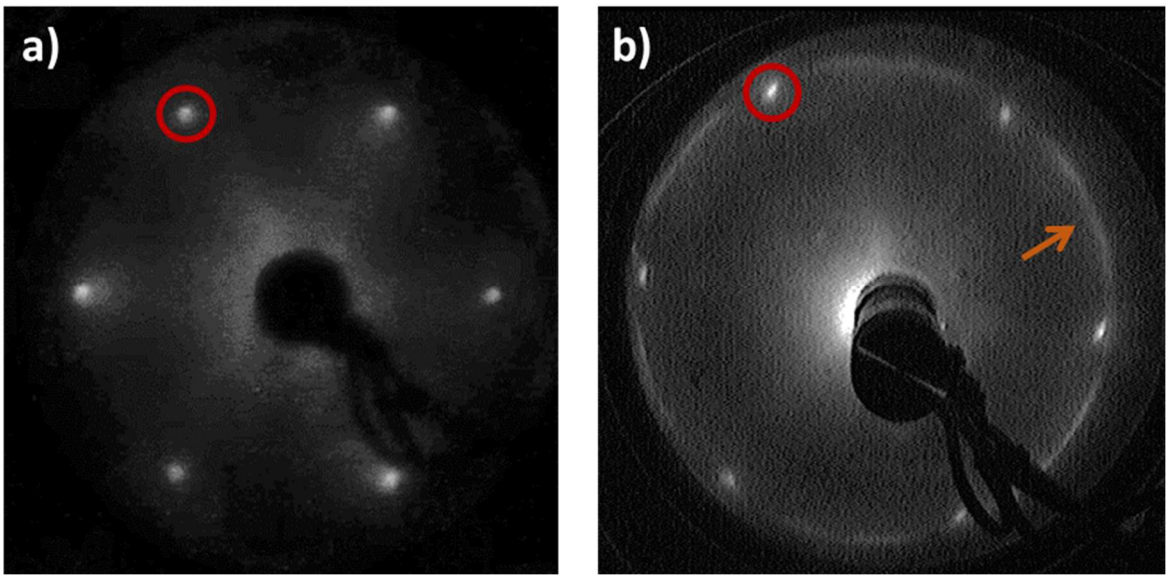

***Figure 2.3**. Examples of the diffraction pattern obtained for a) bare Cu (111) surface and b) Cu (111) surface with polycrystalline graphene layer on top. Individual spots like one marked in red correspond to the Cu (111) single crystal. The ring observed in b (orange arrow) is the contribution of the polycrystalline graphene*.

In ***figure 2.3***, two LEED patterns are shown, which correspond to a Cu (111) single crystal surface (***figure 2.3a***) and to a graphene layer on top of a Cu(111) surface (***figure 2.3b***). The well-discernable spots of ***figure 2.3a*** exhibit the hexagonal symmetry that characterizes the surface of a face centered cubic (FCC) solid when the normal vector of the plane is the (111). Therefore, the observed hexagon corresponds to the reciprocal space lattice of the surface. In ***figure 2.4a*** is represented the hexagonal lattice of the Cu atoms in the surface of its (111) face. On the other hand, ***figure 2.4b*** shows the surface reciprocal lattice for a hexagonal lattice. The green hexagon highlights the Brillouin zone in the reciprocal space (it is also a hexagon rotated by 30º) that corresponds to the spots detected in ***figure 2.3a*** [52].

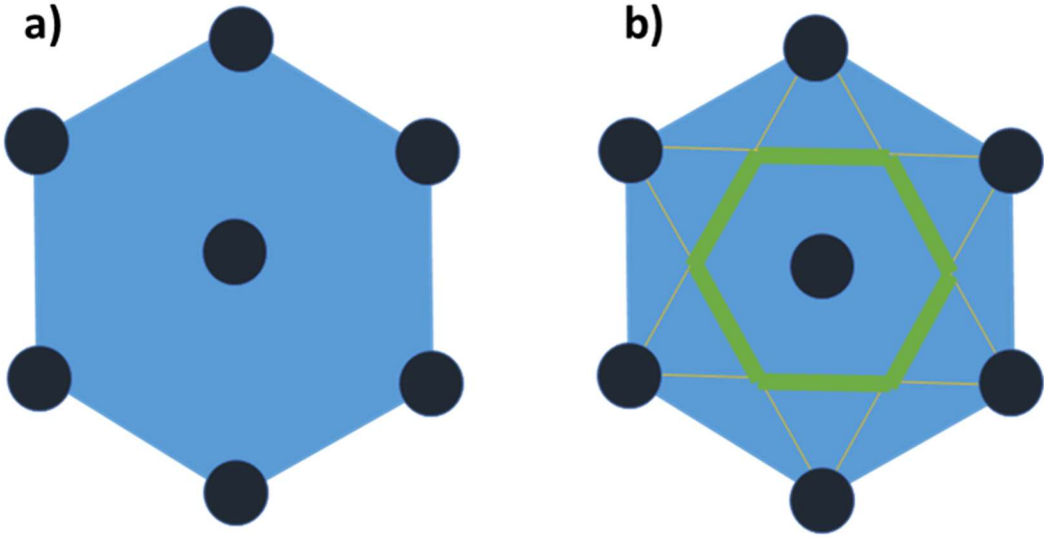

***Figure 2.4**. Schematic view of the relation between the a) real arrangement of the atoms and b) the diffraction pattern obtained due to that symmetry. The yellow lines are the lines connecting the point to all others in the lattice, bisecting each line with another line (in 3D it would be a plane), and taking the smallest polygon (polyhedron in 3D) containing the point bounded by these lines (planes in 3D)* [52].

In the case of a polycrystalline sample, the situation is different. In ***figure 2.3b*** a ring can be observed in addition to the spots that correspond to the Cu (111) single crystal. The reason why a ring is detected instead of a lot of spots is illustrated in ***figure 2.5***. The ring signal is the result of the presence of many graphene crystallites randomly oriented and, therefore, exhibiting a rotational misalignment.

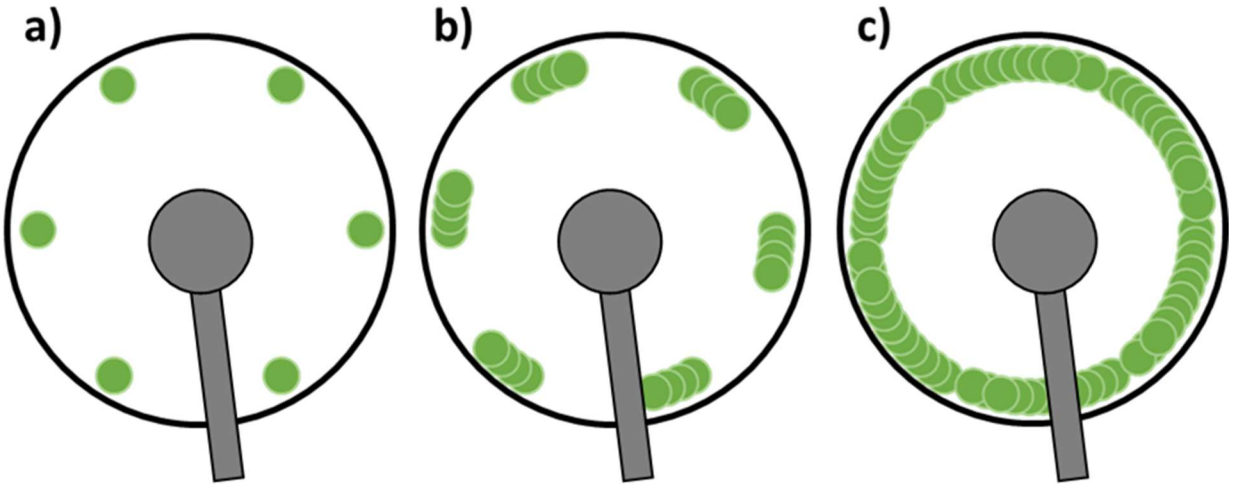

***Figure 2.5**. Schematic view of a rotational disorder that contributes with a ring in the LEED signal (reciprocal space). a) Single domain contribution with clear spots, b) modulated ring with some preferential orientations and c) rotational disorder where a ring is observed (still a small modulation is present).*

2.3 Atomic Force Microscopy (AFM)

The atomic force microscopy is one of the scanning microscopy techniques that compose the scanning probe microscopy (SPM) discipline. This family of microscopes tackles the study of short range interactions between the surface and a nanometric probe. The first scanning microscope was the scanning tunneling microscopy (STM) invented in 1982 by Heinrich Roher and Gerd Binnig [53]. In the case of the STM, the interaction is the tunneling current while the probe is a metallic tip. The technique is based in the quantum tunneling effect of electrons between two electrodes separated by a thin insulator. After this new technique appeared, the development of many different techniques with local properties sensitivity became a field of interest.

The AFM was an extension of the STM [54], where the probe consists of a force sensor called cantilever, where the force between probe and sample can be measured. The range of the measured forces ranges from pN to μN and the typical lateral resolution is around 10 nm while the vertical one is of the order of Ångstroms. The nature of the tip-sample interactions is very diverse (Van der Waals forces, chemical forces, elastic, electrostatic, magnetic…) and so is the information that can be obtained with this technique, beyond a morphological characterization, with nanometer (and even atomic) spatial resolution [55,56].

The main advantage of this technique compared to the STM is the possibility to image surfaces independently of their conducting properties, a severe limitation of the STM technique.

AFM measurements (***figure 2.6***) can be carried out in contact mode (the feedback parameter is the force between the tip and the surface of the sample) or in dynamic mode [57]. This latter mode consists in oscillating the cantilever close to its resonant frequency (depends on the elastic constant, k, and the dimensions of the cantilever). At this point, the feedback parameter can be the amplitude of the oscillation or the phase of the oscillation. All the results obtained by using this technique presented in this manuscript have been measured in amplitude-modulated dynamic mode. Two types of measurements have been carried out, topography and surface potential characterization. Besides, magnetic imaging has been performed but the corresponding description is not included here although in chapter 5.

For the AFM measurements a commercial AFM system and a software (WSxM) from Nanotec [58] operating in ambient conditions were employed. The tips used for topographic characterization were acquired from Next-Tip [59] and excited to its resonance frequency (~75

kHz). In the case of the KPFS measurements, commercial Cr-Au-coated tips from Mikromasch were employed, with a resonance frequency of also ~75 kHz.

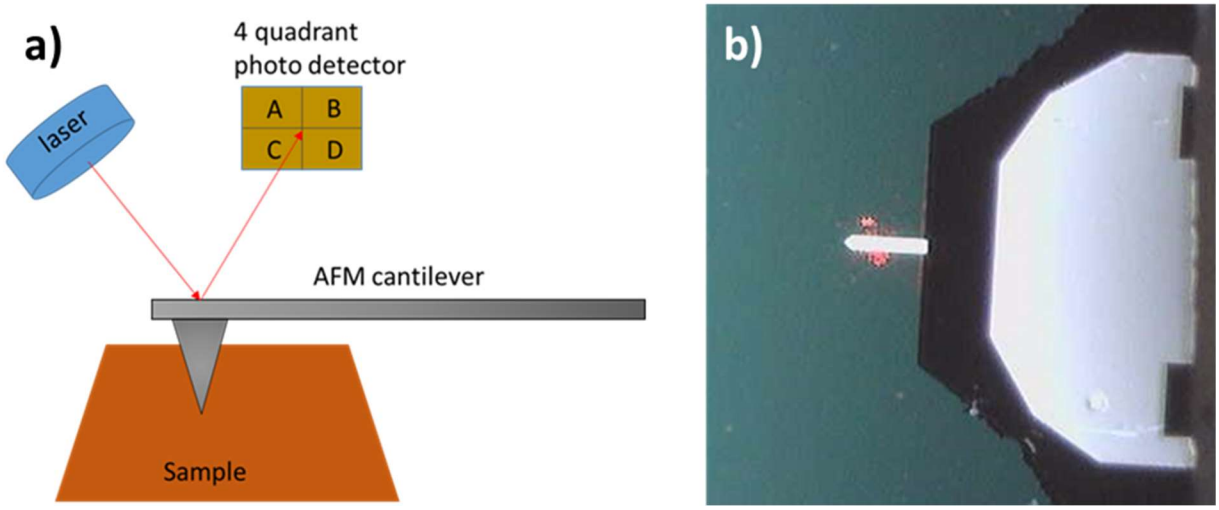

***Figure 2.6**. a) Schematic view of the working principle of the AFM. A laser spot is reflected on the back side of the cantilever, and registered at the four-quadrant photodiode. The response of the cantilever to the interaction (lateral or normal deflection, depending on the force type, deviates the laser spot to a given position of the photodiode) with the sample is registered in the photodiode. A voltage is generated due to the reflected laser impact at a known position. Depending on the generated voltage value and the position (that is why the photodiode is divided in four quadrants) the quantity of the force and the type of force (lateral, attractive or repulsive) can be discerned. b) Picture of a cantilever where the laser reflects.*

The description of the different parts that contribute to the image acquisition (the force sensor, the deflection sensor, the scanning system, etc.) can be found elsewhere [56]. The next section is focused on the working principles of the Kelvin probe force spectroscopy (KPFS) mode.

Kelvin Probe Force Spectroscopy (KPFS)

The KPFS technique owes its name to Lord Kelvin, who introduced the grounds of this technique to explain the formation of surface potentials (V_{SP}) in metals, 1898 [60]. The local scanning method was introduced in 1991 by Nonnenmacher et. al. [61].

The $\boldsymbol{V_{SP}}$ between two conducting materials, like a conducting AFM tip and a conducting sample is represented by the next equation:

$$eV_{SP} = \Phi_{sample} - \Phi_{tip} \qquad (1)$$

Where $\boldsymbol{\Phi_{sample}}$ and $\boldsymbol{\Phi_{tip}}$ are the work functions of the sample and the tip, respectively, while $\boldsymbol{e}$ is the elementary charge. Therefore, changes in the surface potential are directly related with changes in the work function of the sample under study (assuming that the $\boldsymbol{\Phi_{tip}}$ remains constant). That is the critical point, to ensure that the tip conditions do not change, particularly the work function. To monitor this, a reference sample of known work function is measured between samples (in the measurements shown in chapter 4, HOPG was used as a reference sample).

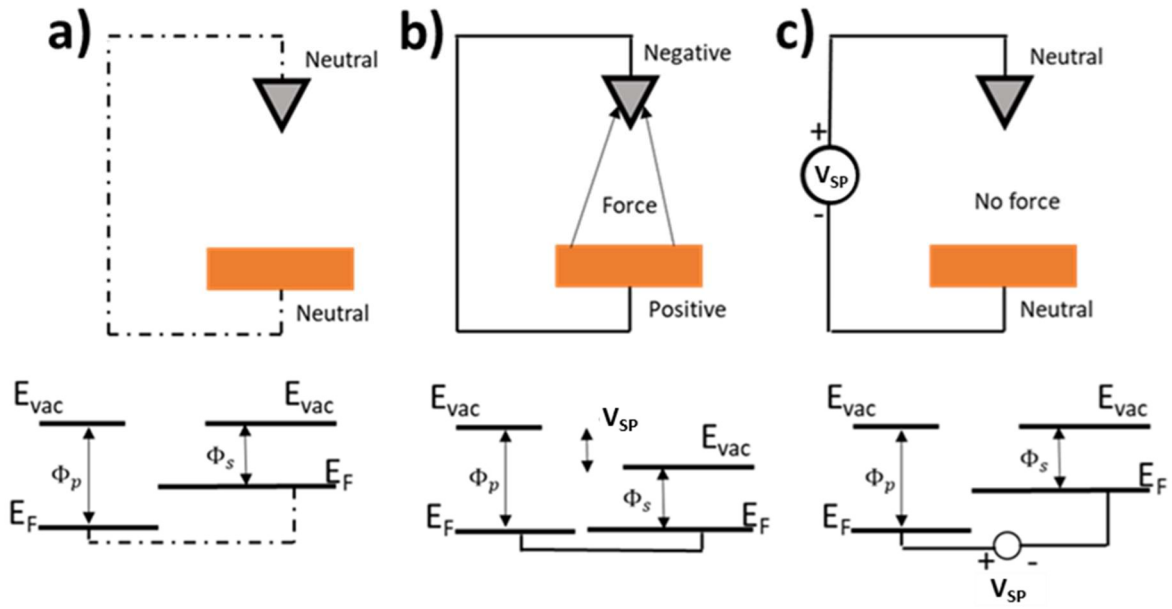

***Figure 2.7**. Definition and basic measurement setup of surface potential (VSP). Sketch of two metals with different work functions. In a) the Fermi levels of the two metals are different, as it is a characteristic feature of each material. If they are connected as shown in b), the Fermi levels are aligned and a potential difference appears in the vacuum level (VSP). c) With an external bias voltage, the vacuum levels are aligned. Figure adapted from* [62].

Figure 2.7 shows the functioning of the KPFS. When the two electrodes are not connected, a difference in the Fermi level is observed, as two independent metals have their own intrinsic electronic structure (***figure 2.7a***). When the two electrodes are electrically connected, the Fermi levels are equaled, with a charge transfer from the most energetic level to the lower level. A difference in the vacuum levels of both electrodes is observed, since the work functions of both metals remain unaltered (the work function is a constant parameter of a material) and a force appears between both metals due to the surface potential difference (V_{SP}). This surface potential can be nullified with an external bias voltage. The magnitude of the surface potential between both electrodes is the same that the applied bias voltage. Differences in the applied

bias voltages for different samples are directly related with the difference between the work functions of the measured samples.

The obtained force-voltage or frequency-voltage (depending on the detection mode used [63]) curves have parabolic voltage dependence (see ***figure 2.8***), and the position of the minimum of the fitted parabola yields the V_{SP} value. Two representative curves are shown in ***figure 2.8***, for a graphene on polycrystalline copper foil with intercalated oxygen and a HOPG sample employed as reference sample. The difference in the minimum position of the curves corresponds to the difference in the Fermi level [64]. For sample comparison, several curves are acquired on different locations, and measurements are repeated altering the sample order, to ensure reproducibility of the measured differences of the surface potential.

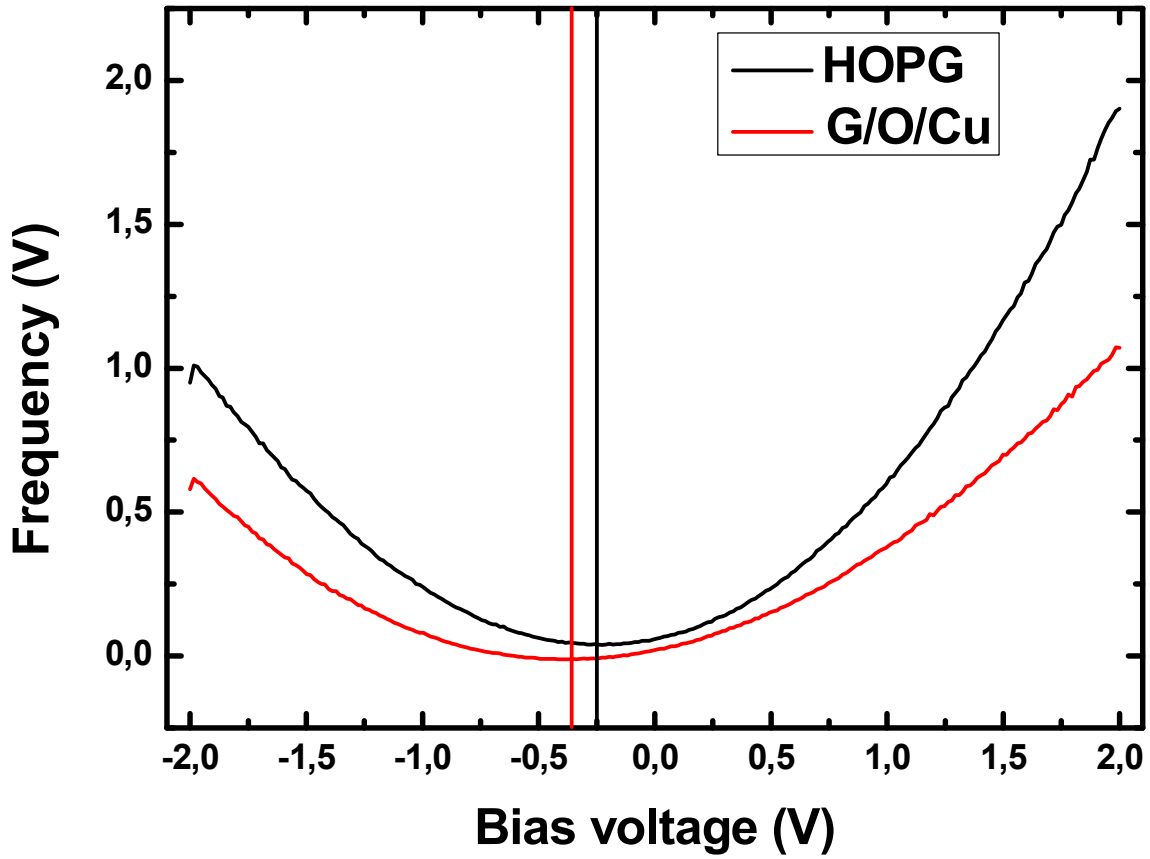

Figure 2.8. *Frequency versus voltage curves acquired on a HOPG sample used as a reference and a graphene sample grown on polycrystalline copper foil where oxygen has been intercalated. The difference in V_{SP} between the sample and the reference sample (HOPG)corresponds to the distance between the minimum of the sample parabola, marked with the vertical red line, with HOPG parabola (vertical black line).*

2.4 Raman spectroscopy

Although the Raman effect was discovered in 1928 [65], and it was widely implemented in the 1960s with the invention of the laser and its assembly in Raman spectrometers as illumination source, the discovery of new carbon allotropes in the 1980-90s (fullerenes and nanotubes) and more recently the isolation of graphene from graphite brought a renovated interest in this technique. This is due to the non-destructive character of Raman spectroscopy together with its high sensitivity due to enhancement of the Raman signal generated by the electronic resonances that these carbon allotropes present when using excitation lasers in the visible region of the electromagnetic spectrum [66,67].

When a specimen is illuminated by monochromatic electromagnetic radiation, this can be dispersed either elastically or inelastically. In the first case, the energy of the incident and scattered photon remains unaltered, giving rise to the so-called Rayleigh scattering. In the second case, i.e., when the scattering is inelastic, the incident and scattered photon differ in energy. Within the several processes that can produce inelastic scattering (e.g., rotons, magnons), in the Raman effect the optical phonons are the scattering entities due to the interaction with the incident photons [68]. In this way, the incident photon excites the vibrational state of a molecule to a virtual vibrational state, followed by a relaxation from this virtual state to a final vibrational state different from the initial one. In this process a photon is emitted with a shift in energy equal to the difference in energy between the initial and final states. If the energy of the final state is higher than the initial state, the process is referred to Stokes while, on the contrary, when the energy of the final state is lower than the initial one the process is known as Anti-Stokes (see ***figure 2.9***). Moreover, the Stokes part of the Raman scattering is more intense than the anti-Stokes part [68]. Even being around six orders of magnitude weaker than the Rayleigh scattering, it is possible to further enhance the Raman signal by tuning the incident laser wavelength so as to produce resonant Raman effect.

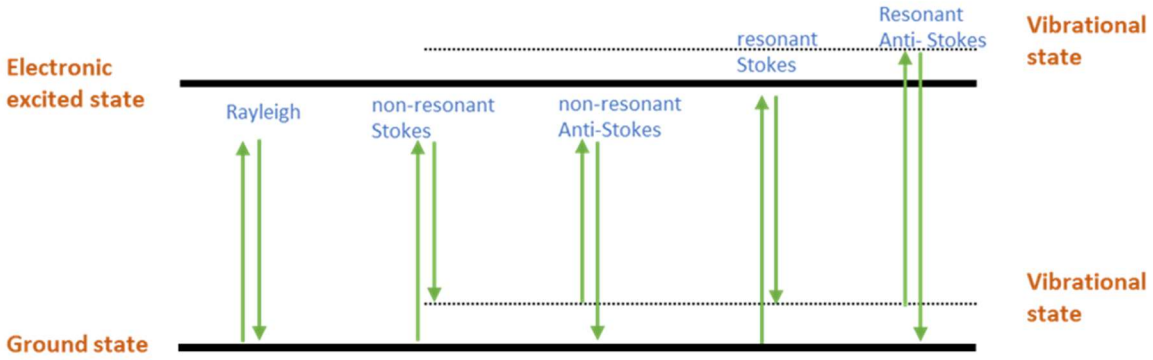

***Figure 2.9**. Sketch of the Rayleigh scattering, and Raman scattering in resonant and non-resonant processes. Figure adapted from* [69].

In the case of resonant Raman scattering, the incident photon energy is resonant with a permitted electronic transition of the system. Thus, the abovementioned virtual state is no longer virtual but a real electronic excited state of the system which produces an enhancement of the signal of around 3 orders of magnitude. Due to this resonance, considering that graphene is a single atom thick layer material, it has a measurable signal, and has converted this technique (non-invasive, fast and powerful in the sense that strain, doping, defects, number of layers etc. can be determined) essential for the characterization of this material [69].

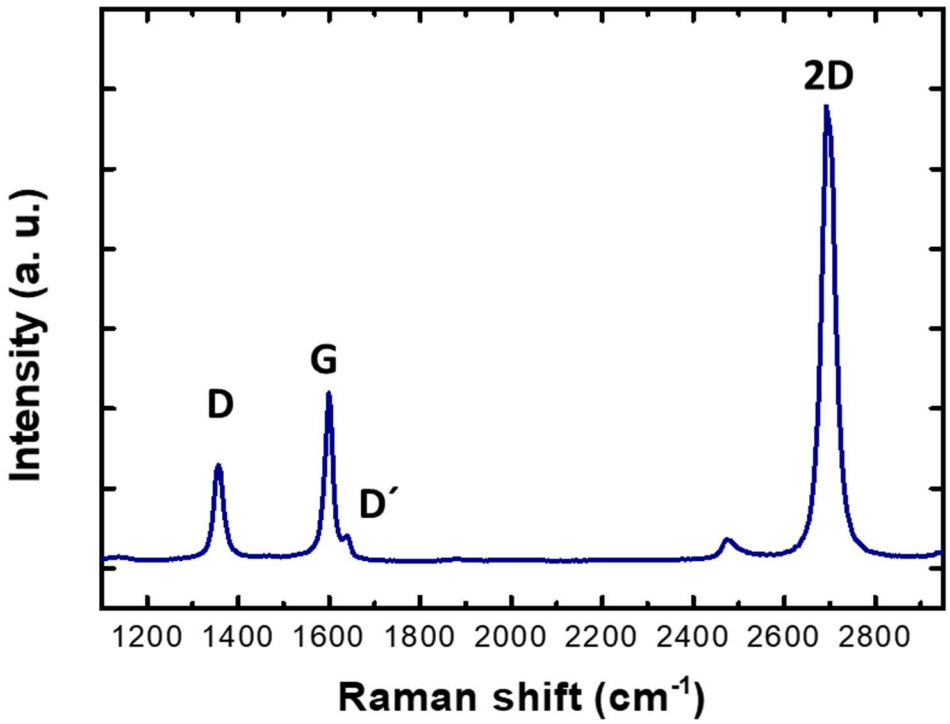

***Figure 2.10**. Typical spectrum of a graphene layer. This corresponds to a graphene sample grown by PVD and by using fullerenes as carbon precursor and transferred onto SiO2 by employing the method described in chapter 4.*

The most intense Raman peaks for graphene are the G and the 2D peak (see ***figure 2.10***). The G peak, around 1580 cm^{-1}, appears by exciting the E_{2g} vibrational mode at the Γ point, while the 2D band, around 2700 cm^{-1}, is due to the second order excitation of the phonons at the K point [69]. The 2D band is the overtone of the D band, i. e. it is a second order transition or a two-phonon process. The D band, observed around 1350 cm^{-1} is a double resonance process and is active when symmetry of graphene unit cell is broken, i. e. with defects, strong interactions with substrate that corrugates graphene etc. In addition to these typical peaks corresponding to graphene, there are others less intense, that are commonly present. The D´ band (around 1620 cm^{-1}) is related to defects, but there is still a discussion opened with respect to the origin of those peaks [69].

The relation between the D and D´ peaks has been empirically demonstrated to give information about the nature of the defects (vacancies in the lattice, grain boundaries…) [70].

Two different Raman microscopes have been used for the characterization presented in this work: a confocal Raman microscope (Witec alpha-300R) equipped with a 532 nm laser and a 100x objective lens (NA=0.9), and a Renishaw inVia-Reflex Raman equipped also with a 100x objective lens (NA=0.85) and a laser wavelength of 514 nm. The incident laser power, in the case of the Witec equipment, was 1 mW, while in the Renishaw equipment it was the 10% of the total power, around 5 mW.

2.5 X-Ray Photoemission Spectroscopy (XPS)

XPS, a technique developed by K. Siegbahn in the 50s-60s of the last century [48], provides a qualitative and quantitative analysis of the chemical elements of a surface. Based on the photoelectric effect [71], when a monochromatic X-Ray beam arrives to the sample, a photon is absorbed and a core-level electron is emitted (see ***figure 2.11a***) with a kinetic energy determined by the relation:

$$E_k = h\nu - E_B - \phi \qquad (2)$$

Where $h\nu$ is the energy of the incident photon, E_B the binding energy of the core-level emitted electron (the unknown variable of the equation), ϕ the work function of the sample and analyzer and E_k is the kinetic energy of the emitted electron that is determined by the energy analyzer. This technique is surface sensitive and permits the detection of not only chemical elements, but also their oxidation state.

A typical XPS experiment runs as follows: the sample is illuminated with an X-ray beam. With the energy gained by the photons, electrons exit the sample and arrive to the energy analyzer (a semispherical detector that discriminates electrons as a function of their kinetic energy, see ***figure 2.11b***). This kinetic energy is related to the binding energy (equation 2) of the core electrons of different chemical species. Depending on the oxidation state, these binding energies shift in energy with respect to the zero oxidation state, enabling the discernment between different type of molecular species by knowing how they are bonded. The main drawback of this technique is the lack of information in the case of hydrogen and helium atoms.

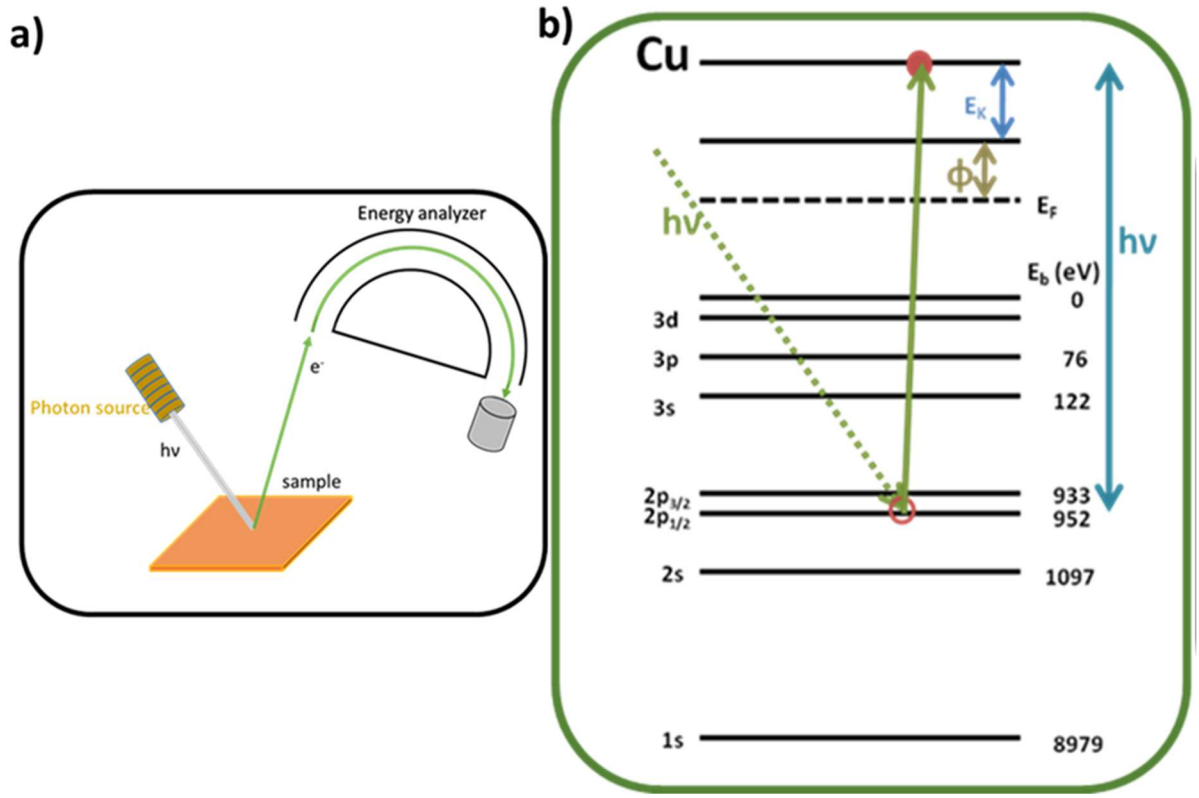

Figure 2.11. *a) Schematic image of the collection of electrons expelled from the sample surface after being illuminated with a with an X-Ray beam. b) The energies of the electronic levels for the case of copper. Illustratively, when a core level electron absorbs a photon with a known energy, the kinetic energy that will have that electron at the detector´s location will be directly proportional to the binding energy that has overcome.*

In the case of graphene, XPS is an adequate tool to observe its quality as well as the presence or lack of contaminants. In ***figure 2.11*** an XPS spectrum centered on the C 1-s position shows a sharp peak that is deconvoluted in two components. The most intense corresponds to the sp^2-hybridized carbon component and a smaller one that corresponds to the sp^3contribution. Thus, the spectrum shows a well-formed graphene layer with a small sp^3 component that may arise from different contributions as it is the case of the C atoms of the graphene layer interacting with the copper substrate, or the C atoms located at the graphene grain boundaries or even some carbon oxidized species. There is more information that can be obtained from the XPS spectra, for example relating the signal coming from one component with the signal coming from another component like it is the case of studying the evolution of different chemical species (oxides formations, bury of an element into the bulk, …) [72].

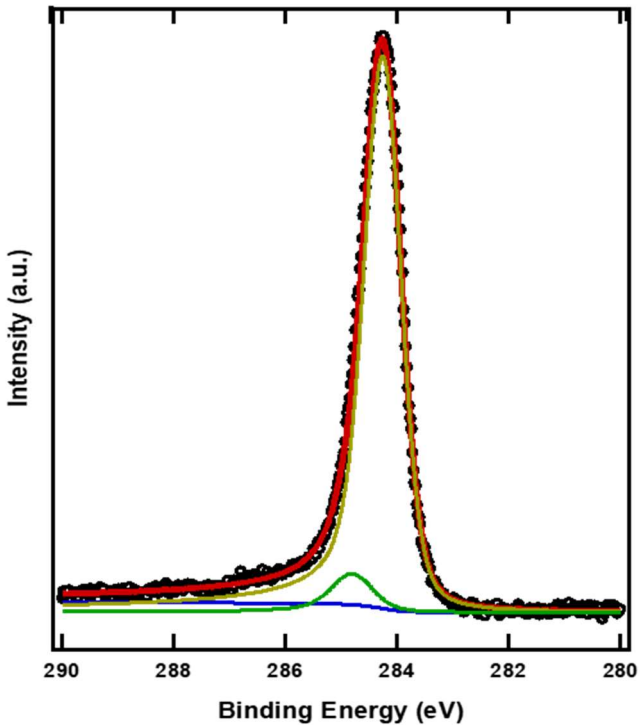

***Figure 2.12**. XPS spectrum corresponding to the C 1-s electronic core level of carbon. The spectrum was acquired from a graphene sample grown on polycrystalline copper by using fullerenes as precursors in UHV.*

Two different XPS instruments have been used in this work. On one hand an equipment with a hemispherical analyzer SPECS Phoibos 100 MCD-5 was utilized. In that case, Al K_α radiation (1486.7 eV) was employed as X-ray source in a system with a base pressure of 10^{-10} mbar. On the other hand, a system with a VG-CLAM hemispherical analyzer was used, where the incoming X-xay photons correspond to a Mg K_α anode (1253.6 eV).

2.6 The substrates

The growth of graphene was made mainly in polycrystalline copper foils, due to its low carbon solubility, catalytic-like action and low price and its relevance from a technological point of view. Nevertheless, single crystals were employed as model systems for a better comprehension of the growth mechanism and its dependence with the surface orientation. The chosen single crystal orientations were the (111) and the (100). Intuitively, and expecting an epitaxial growth, one would choose the (111) substrate as a more favorable substrate due to

its hexagonally packed surface. However, we also grew graphene on the (100) surface to observe differences in the growth parameters. The procedure of conditioning of the substrate was the same for all thicknesses of the foils and also for the single crystals, consisting on Ar^+ sputtering and annealing cycles. The energy of the argon ions started at 1.5 keV for the first treatments, while the last sputtering process was done with a softer energy of 0.8 keV. The employed argon pressure also was decreased for the last treatments. First argon pressures were 1.10^{-5} mbar, obtaining an ion current of around 5-6 μA, while the current obtained in the final sputtering cycle was procured to be of 2 μA or lower (obtained with pressures around 2.10^{-6} mbar) to avoid excessive roughness.

Figure 2.12 shows the unit cell of copper (FCC) and the different surface symmetries a FCC structured material presents depending on the chosen face.

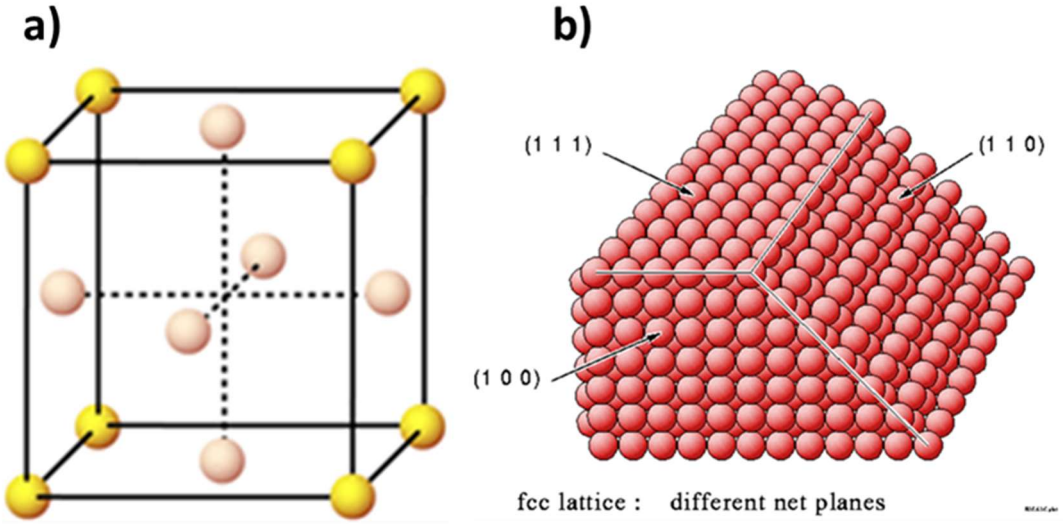

Figure 2.13*. a) Scheme of a FCC (Face Centered Cubic) unit cell. It is not a primitive cell since each cell contains 4 atoms. b) Schematic view of different copper surfaces, taking into account that it is a FCC solid. The represented surfaces are the (100), (110) and the (111). Image from ref. [BALSAC picture gallery of Prof. K. Hermann, Fritz-Haber-Institut, Berlin].*

2.6.1 Cu(111)

The lattice parameters of copper, being a cubic unit cell are:

a=b=c= 3.61 Å

with the lattice angles:

α=β=γ= 90°C

Taking these parameters into account in addition to the fact that it has some atoms also in the faces, the surface lattice parameter of the Cu (111) single crystal is:

a.√2/2=2.55 Å

This value is close to the cell parameter of graphene (2.46 Å).

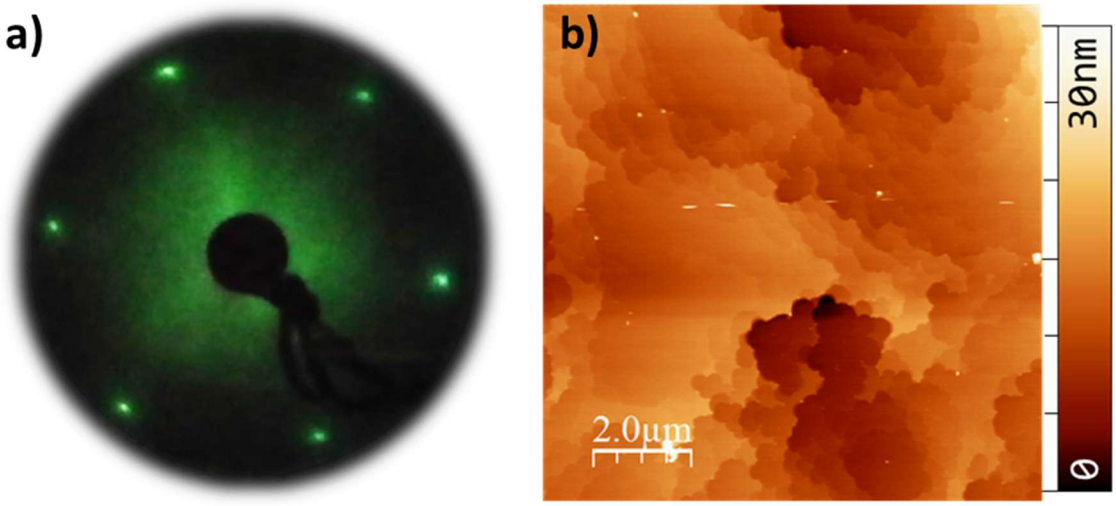

***Figure 2.14**. a) LEED pattern of the previously cleaned the Cu(111) single crystal acquired with an electron energy of 70 eV. b) AFM topographic image of the Cu(111) surface.*

The LEED pattern of Cu(111) is shown in ***figure 2.14a***, evidencing its hexagonal structure. The local topography of the surface, obtained by means of AFM is exhibited in ***Figure 2.14b***. The AFM image shows a clean copper surface with terraces of the order of microns while the height of the terraces is in the range of few nm.

2.6.2 Cu(100)

In the case of the (100) face, the lattice parameter of the surface corresponds to the one of the unit cell. In this case, the lattice parameter of the copper considerably differs from the lattice parameter of graphene.

Lattice parameter:

Cu(100)=3.61 Å

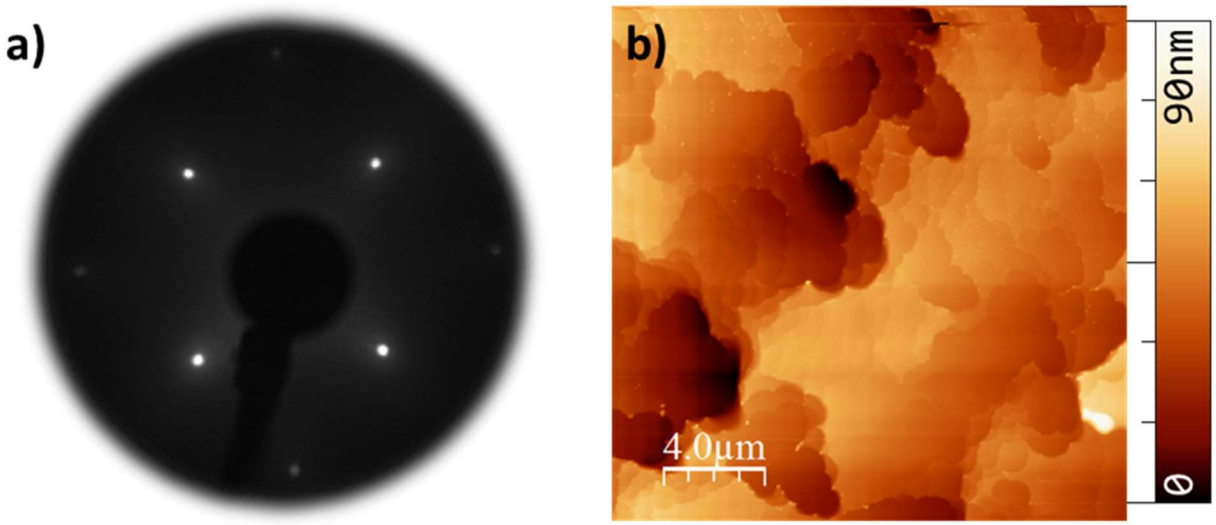

***Figure 2.15**. a) LEED pattern of the previously cleaned Cu(100) single crystal acquired with an electron energy of 147 eV. b) AFM topographic image of the Cu(111) surface.*

LEED pattern (***figure 2.14a***) of Cu(100) that shows a square symmetry corresponding to the (100) surface structure. In ***figure 2.14b*** the topography of the surface of Cu(100) determined by AFM is shown. The size of the terraces is of the order of few microns while its height is of the order of few nanometers.

2.6.3 Polycrystalline copper foil

The employed polycrystalline copper foils (Alfa Aesar) had different thicknesses. The industrial manufacturing/production of these foils demands extrusion methods to achieve the thickness that the market offers (25, 35 and 50 µm and 1.27mm in our case). According to metallurgical studies [73], these extrusion methods tend to produce textures in the material. This means that even though the material is polycrystalline, there might be some preferential orientations on the surface of the metal, depending on the extrusion directions utilized.

The way to avoid any kind of memory from the production process, is the recrystallization process of the copper. Over 250°C the copper grains start to recrystallize, and the higher the temperature the faster the recrystallization process. The annealing temperature determines the final dominant texture of the copper substrate. As will be shown along this chapter, we have found differences between our treated copper foil (annealed at 800°C) and the one used for CVD growth procedures (typically annealed at temperatures not below 1000°C).

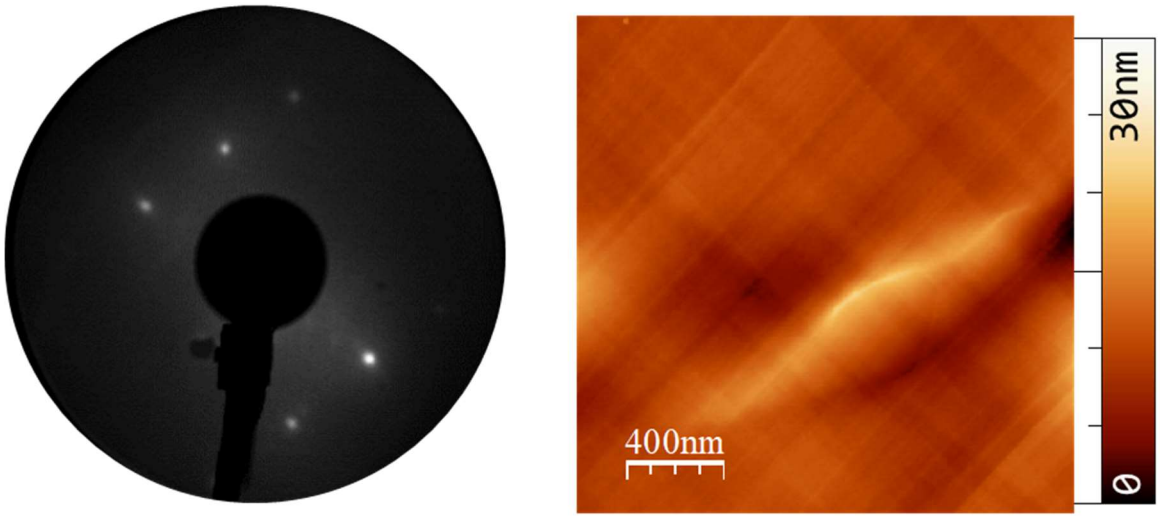

***Figure 2.16**. a) LEED pattern of a previously cleaned polycrystalline copper foil, acquired with an electron energy of 57.6 eV. b) AFM Topographic image of a previously cleaned polycrystalline copper foil.*

The LEED pattern shown in ***figure 2.16*** exhibits the rectangular arranged spots corresponding to a thermally treated Cu foil (up to 800°C), suggesting a (110) texture of our copper foils, after being treated in UHV. In terms of AFM topography, the surface is flat and the grain sizes are in the order of tens of microns as will be show later in the chapter 3.

2.7 The carbon precursor for graphene growth: C_{60} molecules

As carbon source, C_{60} molecules were used [74]. The main motivations are that they could represent an optimal choice, since they only contain the desired chemical element for graphene growth, together with their relative low cost and highest abundance among the fullerene family.

Fullerenes are an allotropic form of carbon discovered in 1985 by Kroto et. al. [74]. In their work, they assigned the name “Buckminsterfullerene” to these molecules due to the resemblance of the molecules with the geodesic domes R. Buckminster Fuller designed. From a topological point of view, graphite is a 3D material, graphene a 2D material, carbon nanotubes a 1D material and fullerenes are a 0D material, all of them are carbon structures.

The most common molecule within the family of fullerenes is the C_{60}. The carbon atoms are bonded in 20 hexagons and 12 pentagons forming a curved and closed structure (***figure 2.17***). It resembles a nanometric football. The molecular hybridization of the orbitals forms an sp^2 structure, providing stability to the molecule, but the curvature of the molecules induces a certain strain in the bonds [75]. The thermal decomposition temperature for these molecules is beyond 700°C [76]. For this reason, it is expected that not extremely high temperatures will be needed to favor the chemical reaction for growing graphene from C_{60} molecules, making this new route advantageous.

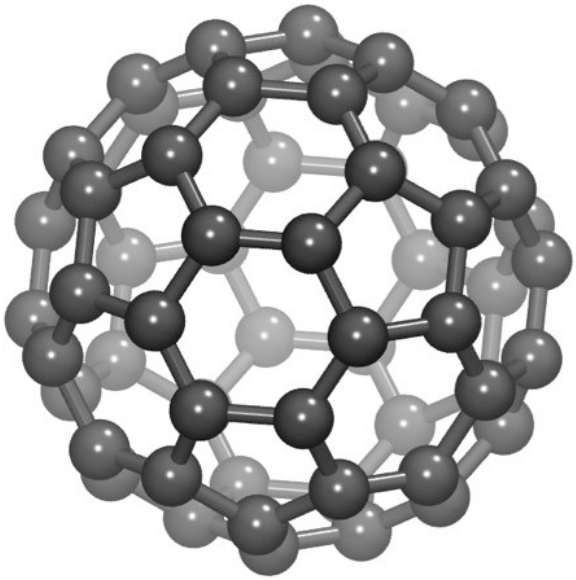

Figure 2.17*. Pictoric view of a C60 molecule. The carbon atoms are arranged in such a way that 20 hexagons and 12 pentagons form the molecule.*

The deposition of fullerenes on different type of substrates have been already studied [77–82]. To optimize the experimental conditions for our work, the adsorption of C_{60} molecules on Cu foils was performed.

Figure 2.18 shows the STM images of fullerenes on the polycrystalline Cu surface after its evaporation, which was performed keeping the temperature of the substrate at 700°C, i. e., near the C_{60} thermal decomposition threshold.

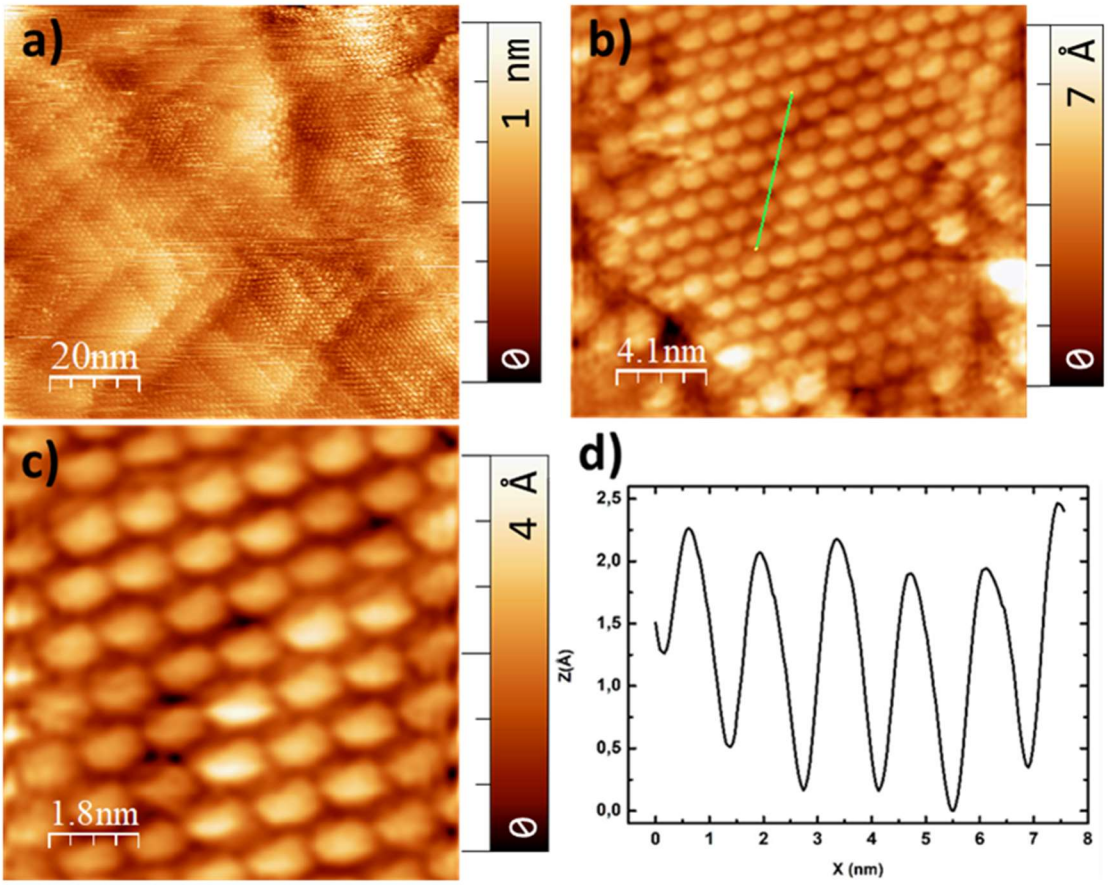

Figure 2.18*. STM images of fullerenes deposited on a copper foil. The images were acquired with a voltage bias of 1 V and a tunnel current of 28 pA of tunnel current. a) Large area image where fullerenes form ordered structures. b) STM image centered on one island of fullerenes. As can be observed, they are forming a hexagonal arrangement. c) High resolution image corresponding to a zone of the island of figure b. d) Profile of the highlighted zone of image in b.*

Figure 2.18a exhibit a large area STM image with the fullerenes on the Cu foil surface forming ordered structures. That ordered distribution of the C_{60} molecules on the surface is hexagonal, as it is evidenced in ***figures 2.18b and c***. Finally, a height profile along the green line of ***figure 2.18b*** is represented in ***figure 2.18d.***

From the information extracted from those STM images, and taking into account that the substrate was kept at 700°C while depositing C_{60} molecules, it can be deduced that the

interaction of the molecules with the substrate is strong enough not to desorb the molecules but weak enough to allow the molecules interact between them and form ordered structures. Thus, the molecule/substrate interaction allows the molecules to diffuse over the copper substrate yielding to the formation of a hexagonal arrangement.

This exploratory step, previous to the graphene growth, was very promising because the STM images of fullerenes on top of the copper substrate indicates that at 700 °C (far away from the Cu melting point, 1085 °C) the substrate allows diffusion of the C_{60} molecules but no desorption occurs. Therefore, it could be suitable for a graphene growth process to keep the substrate at slightly higher temperatures than 700 ºC during C_{60} evaporation.

Chapter 3. PVD graphene growth by C_{60} decomposition on Cu foils

3.1 Introduction

The major impact that graphene produced at first on the scientific community because of its diverse and exceptional properties (high carrier mobility, high elasticity, chemical inertness, high thermal conductivity, tunable band gap, half-integer quantum Hall effect, etc.) [83] gave way eventually to the focus on its promising technological applications. Since then, many different experimental protocols have been established to achieve a controlled, scalable and low-cost production of this carbon allotrope, though still a single formula combining all the aforementioned aspects is lacking [84].

Exfoliation of graphene from graphite, the pioneering method used by Novoselov et. al. [2] led to numerous exciting discoveries of graphene electronic and mechanical properties [4,85]. The lack of scalability of this protocol has motivated the exploration of other preparation methods involving different types of precursors and substrates [19,86–88]. Undoubtedly, the most extended method has been the graphene growth on metal substrates by chemical vapor deposition (CVD) using hydrocarbon gaseous reactants such as methane, acetylene or ethylene [28]. However, the current CVD processes usually require elevated temperatures (around 1000°) to decompose the gaseous reactant and to succeed in the graphene formation. In order to overcome the high temperature drawback of this method, many efforts have been made to lower these values in the search of a cost efficient and environmentally friendly route.

In this chapter a different graphene synthesis methodology, requiring lower temperatures in a controlled ultra-clean environment, is proposed. As it was already mentioned in chapter 2, the selected substrate was copper in the form of foil and the carbon source was C_{60} molecules.

Indeed, the transformation of C_{60} into graphene was previously reported on Ni thin films, Pt(111), Ru(0001) and Ir(111) surfaces, in which the metal-catalyzed cage-opening of C_{60} was achieved in the 700-1000°C temperature range [89–92]. All the above mentioned systems fall into the category of strongly interacting interfaces, in which C_{60} adsorption is dominated by molecule-substrate interaction rather than intermolecular interactions. In fact, for these systems several studies report that the C_{60} surface interaction induces the formation of surface vacancies, increasing the substrate-carbon bonding strength [26,91,93]. This would explain why annealing at elevated temperatures does not cause desorption of the molecule (as observed for other metal surfaces) but rather C_{60} fragmentation and subsequent graphene formation.

Less explored is the conversion of C_{60} to graphene on not so strongly interacting interfaces. It is particularly striking that, being one of the most employed substrates in the widely used CVD growth method, to our knowledge only two works have reported the attempt to grow graphene using C_{60} on copper, with dissimilar results. Yamada and collaborators did not succeed in inducing C_{60} cage unzipping on Cu (111) upon annealing to 580°C, reporting the formation of disordered clusters on the surface due to molecular polymerization [90]. The other work corresponds to Tatti and co-workers [94]. They reported the synthesis of graphene on copper by C_{60} supersonic molecular beam epitaxy (suMBE). The quality of the resulting graphene, however, is far from the aforementioned C_{60} derived counterparts, with the presence of pentagons and vacancies and a small coherence length that even hinders the formation of a low energy electron diffraction (LEED) pattern [94].

In this chapter we describe the successful growth of high quality graphene by directly evaporating C_{60} molecules on thin polycrystalline copper substrates at 800°C in ultra-high vacuum (UHV) conditions.

3.2 Description of the growth procedure

In order to study the most suitable substrate for the graphene growth, polycrystalline Cu surfaces with different thicknesses were tried: 25 μm, 35 μm, 50 μm, 1.27 mm. In addition, Cu gaskets with 1.2 mm, used routinely for UHV flanges were also employed as substrates for the graphene growth. Among all these different thicknesses, the 25 and 50 μm thick substrates were the most employed ones. Nevertheless, a potential drawback of the 25 μm foil was the occasional bending of the surface by the effect of the temperature. Since in UHV heat transmission is just given by contact or radiation (there are no heat exchange gases), a temperature gradient could be formed between the corners (where the foil was attached to the heater) and the center of the foil. Except for those infrequent cases, the results were similar for all substrates.

The surface of the Cu substrate was prepared by following a standard cleaning procedure in an UHV chamber (base pressure 3.10^{-10} mbar) consisting of consecutive cycles of argon sputtering and thermal annealing at 800°C. The substrate temperature was monitored with an optical pyrometer. Commercial C_{60} molecules (Sigma Aldrich 99.8%) were used as precursor species for growing graphene on the substrate. These fullerenes were evaporated directly in the UHV system using a home-made evaporator based on a tantalum crucible with a K-type (chromel-alumel) thermocouple spot-welded to the crucible. Prior to the experiments, C_{60}

molecules were evaporated in UHV at a sublimation temperature of 450°C for several hours to degas the crucible and the molecules. As a preparation step of the procedure, the clean Cu foil was heated up to 800°C and kept at this temperature. Then, the fullerene molecules were sublimated with the substrate held at 800°C during typically 1 h.

In ***figure 3.1a*** an image of the chamber is shown. In the center appears the sample in the heater stage. At the bottom right side, the evaporator is visible. For the growth, the sample, in the manipulator, is placed facing the envelope to maximize the fullerene rate arriving to the copper surface (***figure 3.1b***).

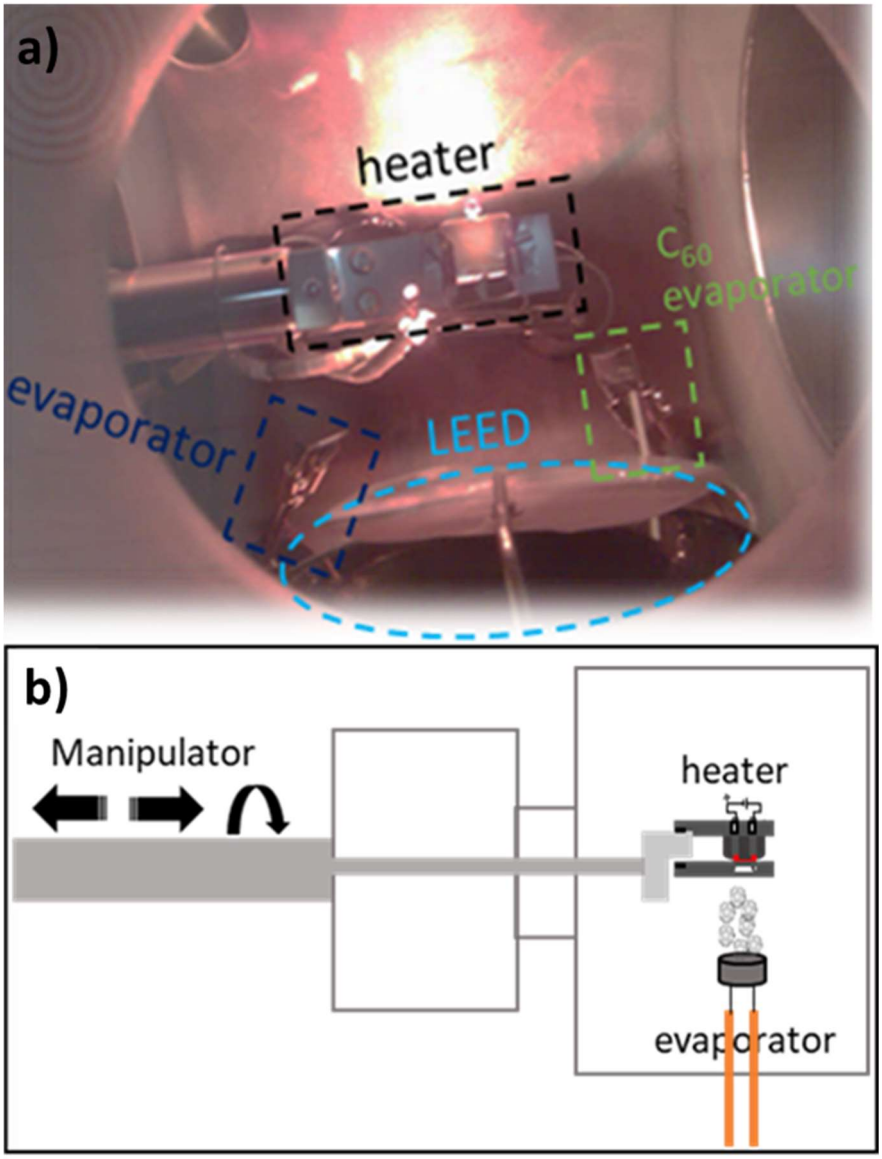

Figure 3.1*. a) Image of the inside of the UHV growth chamber with the different labeled components used for the growth procedure. b) Schematic view of the chamber where the growth process is represented.*

CVD graphene was grown on copper for comparative purposes. 25 μm thick copper foil was exposed to a hydrogen atmosphere and heated up to 1000°C. At this temperature, the hydrogen flow of 50 sccm (standard cubic centimeters per minute) was switched on for 20 min to passivate the reactive sites of the copper foil (grain boundaries, defects etc.). Afterwards, the methane (the carbon precursor in this procedure) was introduced. The CVD process with the mixture of H_2 (50 sccm) and CH_4 (1 sccm) gases was carried out for 30 minutes and an additional 5 minutes of pure hydrogen flow allowed etching of the top of the layers [95]. Then the sample was cooled to 90°C and removed from the reactor. The pressure of the precursors (either the H_2-CH_4 mixture or only hydrogen) was kept constant at a value of 350 mTorr during the whole process.

3.3 Characterization

The novel growth method exposed in this chapter, as any new experimental procedure, demands a characterization of the results obtained in each and every one of the different stages. For this reason, a multitechnique characterization was performed, beginning with the characterization of the substrate after the conditioning treatments made in UHV and continues with a complete study of the final graphene layer. Thus, diffraction techniques (LEED, μ-LEED, XRD and EBSD), microscopy techniques (AFM and SEM) and spectroscopic techniques (XPS, Raman spectroscopy and ARPES) were combined for an exhaustive characterization of different aspects of the graphene layer.

3.3.1 LEED, μ-LEED, XRD and EBSD: comparison of PVD graphene with CVD graphene

LEED patterns were used to determine the crystallinity and cleanliness of the substrate. In the case of the as-received Cu foil, no LEED spots are observed, as expected for an oxidized surface. However, after successive sputtering-annealing (800°C) cycles of the substrate in UHV a recrystallization process is thermally promoted, leading to a notorious increase of the grain sizes and the appearance of bright and sharp spots at the LEED pattern (see ***figure 3.2***).

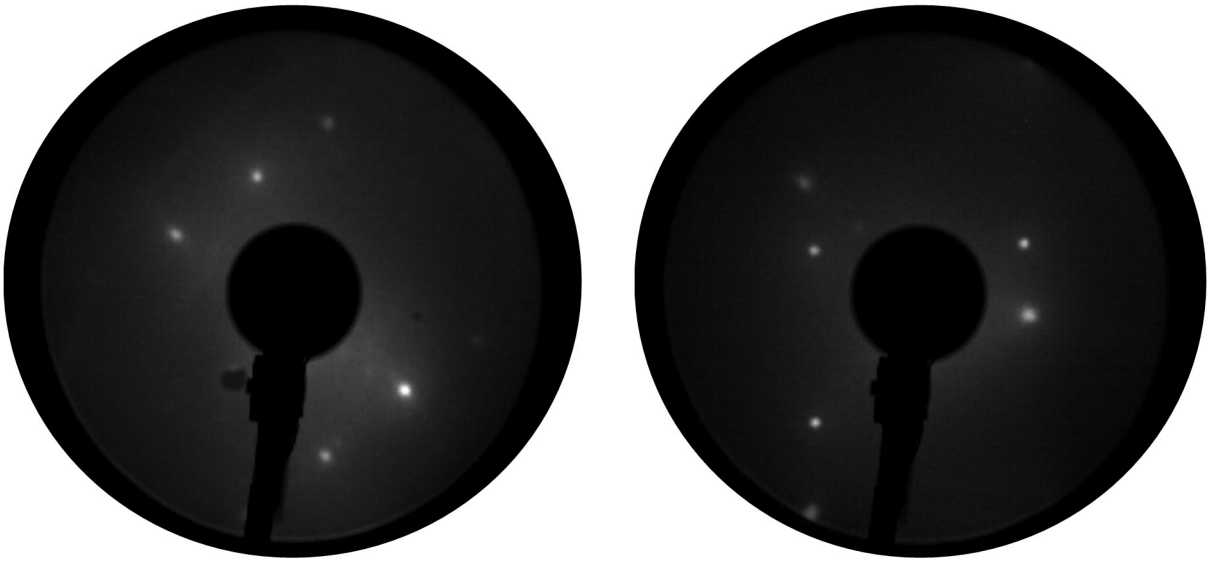

***Figure 3.2**. Representative LEED patterns of thermally treated copper foil prior to growth, acquired in-situ at different electron beam energies (57.6 eV left panel and 107.2 eV right panel). The heat treatment (800°C) promotes the recrystallization of the substrate, yielding bright and well defined diffracted spots corresponding to different crystallographic orientations of the polycrystalline copper foil.*

The crystallographic configuration was different for different Cu foil samples or from one region to another, indicating both a grain-size smaller than the electron beam spot and that there is not a common geometrical orientation. In our case the electron beam size of our LEED equipment is within the sub-millimeter range, and considering that just few spots can be seen, this indicates that just a few crystallites are sampled by the electron gun, and therefore should have an approximate size of tens of microns.

Different optimization processes were carried out. First of all, the optimal temperature for the substrate during the fullerene evaporation was determined as 800°C, after a trial and error process starting from the 700ºC as established threshold in chapter 2 (section 2.7). Besides, it was determined that the optimal surface exposure time to fullerenes was one hour. After the determination of these parameters and some preliminary tests in the laboratory, μ-LEED experiments were performed at the ALBA synchrotron. ***Figure 3.3*** represent a typical μ-LEED pattern obtained after graphene growth on the Cu foil surface. As can be observed, the μ-LEED pattern acquired at 40 eV shows a ring of modulated intensity and multiple bright spots mainly in square or rectangular geometries. The ring is the fingerprint of a polycrystalline

graphene layer (as described in chapter 2) and arises from the superposition of hexagonal patterns coming from differently rotated graphene domains, as its radius with respect to the (00) spot corresponds to the graphene lattice parameter (2.46 Å). Moreover, the modulation of the graphene ring indicates that some of the graphene orientations appear more frequently than others, which is related to the larger stability of some particular graphene orientations with respect to the surface (known as Moiré superstructure in single crystal surfaces) [96]. This pattern is observed along the whole sample surface evidencing the formation of a continuous graphene layer. On the other hand, the multiple bright spots, which are observed in addition to the ring, exhibit mainly rectangular crystallographic order, that would correspond to Cu(110) grains. This result contrasts with the LEED pattern reported for graphene grown by CVD on Cu foils. In that case, the main crystallographic orientation of the Cu grains is hexagonal [97], corresponding to Cu(111) grains.

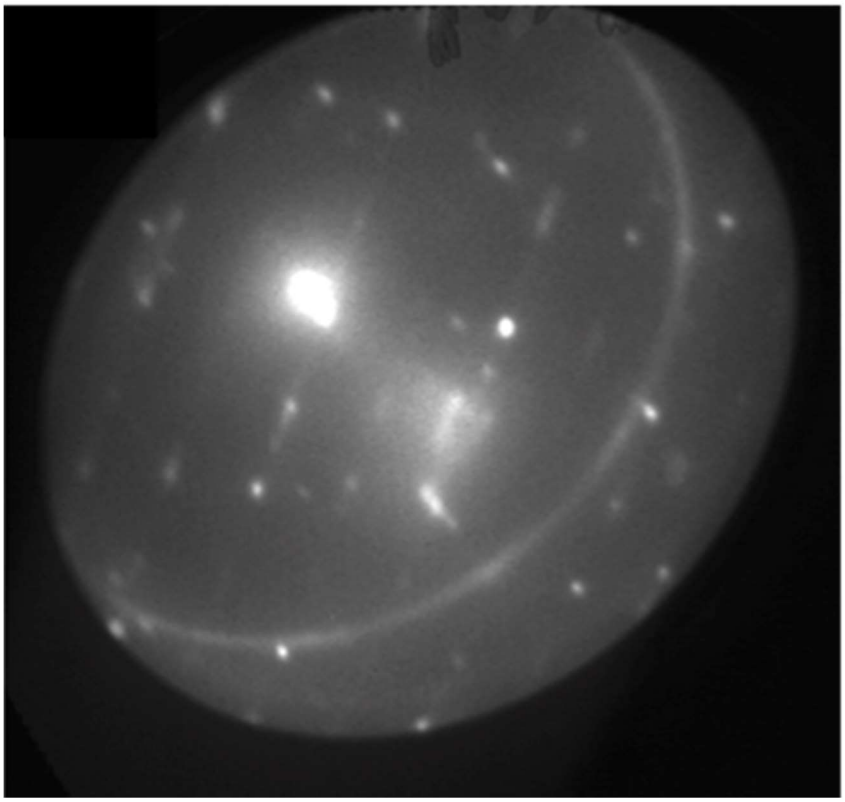

Figure 3.3*. μ-LEED pattern obtained after graphene growth on the Cu foil surface, taken at 40 eV. The pattern evidences that the surface crystal structure of the graphene and the Cu is very similar in different parts of the sample*.

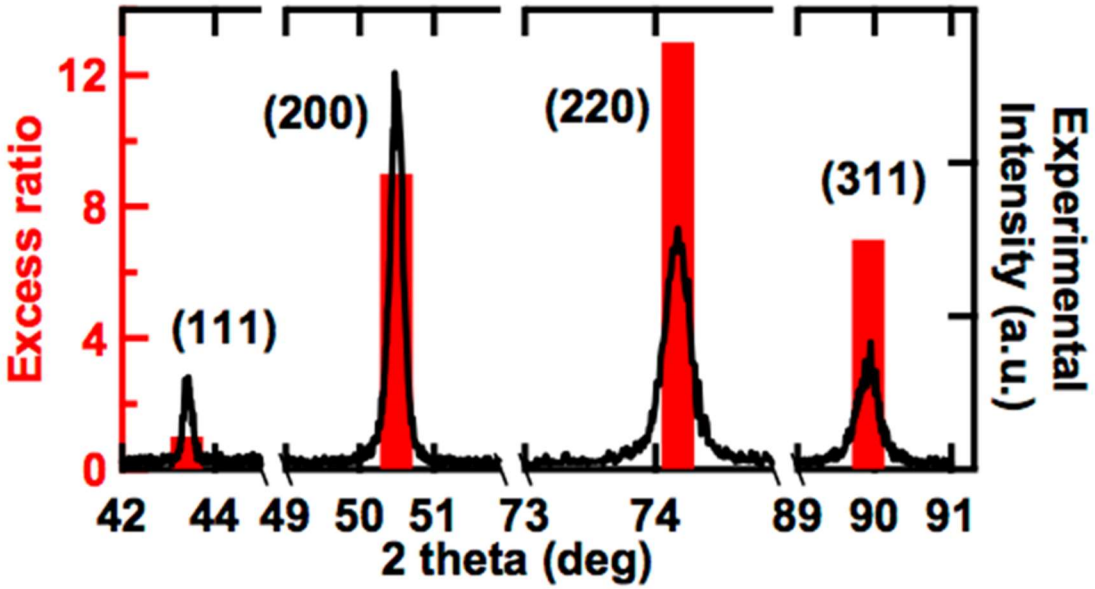

***Figure 3.4**. XRD diffraction pattern shows a raw and normalized intensities (black curves and red bars, respectively) indicating a predominance of the (110) orientation.*

In order to gain insight into the crystal orientation prevalence of the substrate used for PVD growth, XRD patterns were obtained from Cu foils which have been taken out of the vacuum chamber just before the graphene growth (see ***figure 3.4***). The black peaks on this figure represent the experimental diffraction data and the red bars the excess ratios with respect to normalized ideal powder intensities. Those excess ratios are obtained by dividing the experimental intensity by the ideal powder intensity for each reflection and the resulting value is then normalized to the (111)-reflection intensity. Thus, ***figure 3.4*** evidences an abnormal pattern in the observed diffraction peak intensities by comparison with the powder average and after normalization to the intensity of the (111) reflection: there is an increase by factors 7, 9 and 13 of the observed intensities for the (311), (200) and (220) reflections, respectively. The latter we interpret as an increase in the number of (110) oriented grains. In that case, the temperature used for the cleaning process was 800°C, i. e. the same as that used for the graphene growth method and much lower than the typical temperature used in CVD processes. This is a remarkable finding, due to the important role of the substrate lattice orientation in the growth process, as reported by Kalbac et. al. [98].

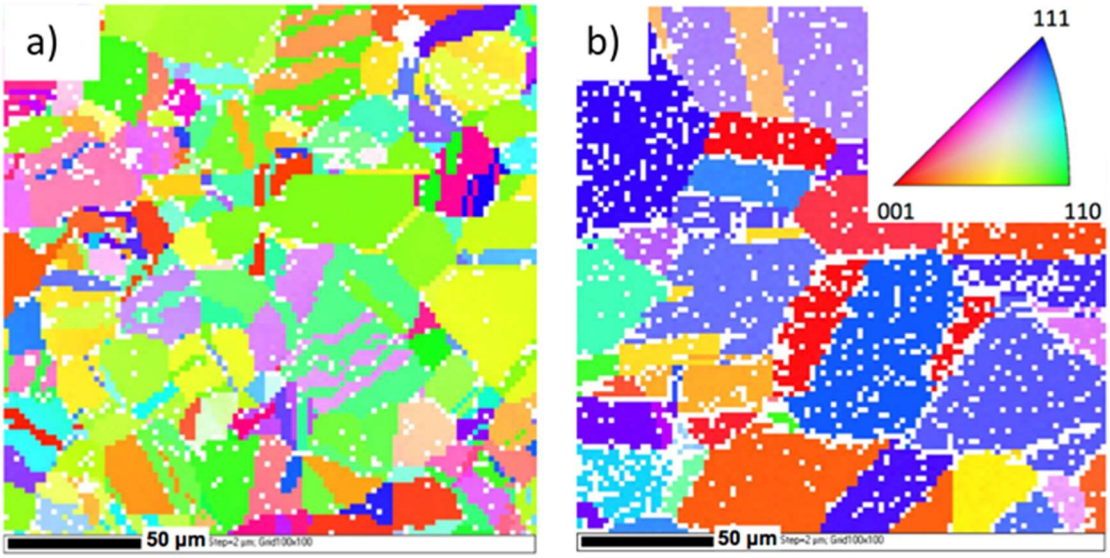

Figure 3.5*. a) EBSD orientation map for a Cu foil after growing one monolayer of graphene by using C60 molecules. b) EBSD for a Cu foil with CVD graphene. The inset shows the color code for the different lattice orientation. CVD sample and EBSD measurements were performed by the group of M. Kalbac.*

EBSD measurements also corroborate this difference in preferred crystallographic orientation of the copper grains, depending on the growth method. ***Figure 3.5*** shows representative EBSD orientation maps of graphene grown on Cu by different methodologies, and the inset in ***figure 3.5b*** exhibits the color code assignment for the different Cu lattice orientations. ***Figure 3.5a*** corresponds to a Cu foil where graphene has been grown using our protocol based on low-temperature decomposition of C_{60}. The image exhibits multiple grains with different crystal orientations. However, the (110) orientation seems to dominate. On the other hand, ***figure 3.5b*** represents the EBSD orientation map for the case of the CVD graphene grown sample by using methane as precursor. In this case, the most prevailing orientation for the multiple grains is (111). Though the particular grain crystallographic distribution differs from sample to sample, the average orientation is representative of all samples grown with the two different methodologies. The different behavior of the Cu foil itself obtained for the two graphene formation methods is remarkable. In fact, this result is in agreement with the LEED observation. These results suggest the influence of the temperature used in each process on the final favored crystallographic orientation of the substrate. The higher temperatures used for CVD growth could be responsible for the formation of (111) grains [99] while the lower temperatures used in the C_{60} based procedure may lead to the formation of mainly (110)-type Cu grains with grain sizes of the order of 50 microns.

3.3.2. SEM and AFM

After in-situ characterization, ex-situ measurements were carried out. For this purpose, the sample was extracted from the UHV chamber to perform the structural and morphological characterization of the graphene layer.

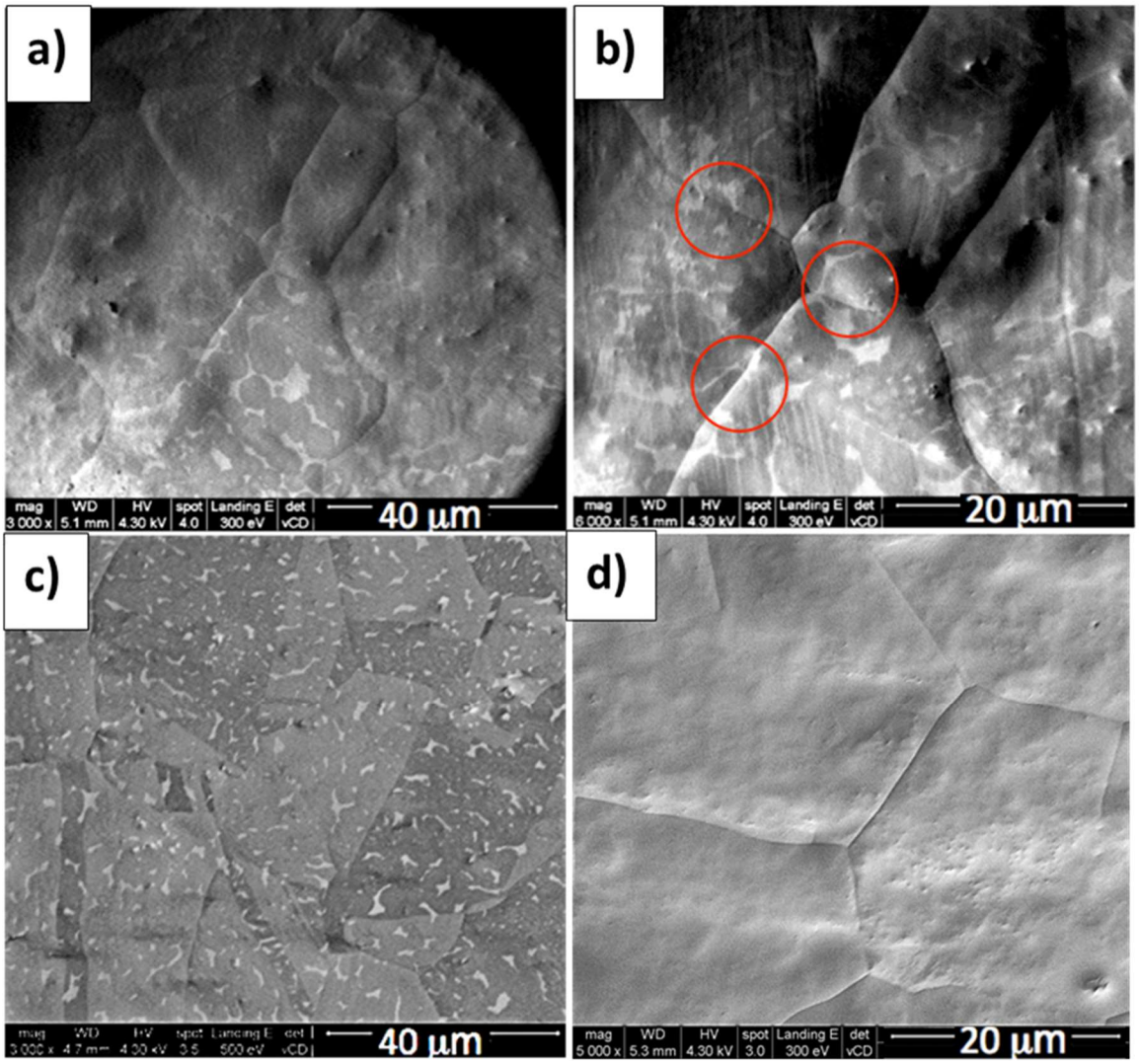

***Figure 3.6**. a) and b): SEM images for an incomplete graphene layer showing the large Cu grains, the small graphene grains (dark rounded features) and the substrate (lighter region). The red circles highlight regions where graphene nucleation occurs through adjacent Cu grains. c) SEM image where, an uncompleted layer of graphene can be observed, exhibiting tonal contrast, as well as different copper crystallographic domains (uncovered Cu regions are lighter than those covered by graphene, that crosses along them. b) SEM image of a completed graphene layer where different copper grains are observed without any contrast associated with graphene.*

Images a) to c) in ***figure 3.9*** show SEM micrographs for the particular case of a Cu foil substrate partially covered by graphene, where the presence of several Cu grains with a typical width of tens of microns can be observed. The growth of this incomplete graphene layer was performed with the aim of studying the graphene morphology before the formation of the complete monolayer (about 0.8 ML in ***figures 3.9a, b and c***). In this particular case, we checked that uncovered Cu areas appear lighter than those from graphene in SEM image. The boundaries between Cu grains are clearly observed. Interestingly, in some cases the graphene layer crosses the boundaries between neighboring Cu crystallographic domains, extending over different Cu grains, as it is shown in the encircled regions in ***figure 3.9b***. These areas show that graphene growth is not confined to the crystallographic grain were nucleation start, but extend to neighboring grains. In the case of completed graphene layers (***figure 3.9d***), such a contrast associated with graphene was not observed by SEM and only the morphology of the Cu grains could be distinguished.

The top images of ***figure 3.7*** show AFM images of the bare copper surface in an as-received state (***figure 3.7a***) and after sputtering-annealing cycles in UHV (***figure 3.7b***). The height scale is one order in magnitude smaller in the treated copper foil image (200 nm for a, 20 for b). The bottom images of ***figure 3.7*** (c and d) show the morphology of the graphene covered surface. The images are recorded on a single Cu grain, and the presence of different atomic steps delimiting terraces confirms the surface cleanness prior to the growth process. In the images the presence of a graphene layer is detected by the formation of the characteristic wrinkles that appear in the surface [29]. These wrinkles are observed to cross the substrate terraces, indicating that structurally coherent regions of graphene extend beyond the steps. The length of these wrinkles is no longer than one micron, which is shorter than the values reported in the literature [59], and probably related to the lower growth temperature. From a close inspection of the AFM images, one can realize that in our case wrinkles do not define a closed area, but leave open paths all over the surface, indicating that the extension of graphene is larger than the Cu grain size as it was shown in the SEM images, where the graphene patches were shown to extend from one copper grain to another (red circles in ***figure 3.6b***). In the inset image a height profile corresponding to one of the wrinkles can be observed (with a measured height of 6 Å). The typical width of the substrate terraces is in the order of hundred nanometers. In some of the wrinkles or grain boundaries the graphene could change the relative orientation with respect to the substrate, increasing the number of different rotational domains and also contributing to the diffraction ring seen in the μ-LEED pattern (see ***figure 3.3***).

To determine the influence of the cleaning and growth procedures on the substrate morphology, a roughness analysis was performed on the as-received Cu foil, the treated Cu foil and the foil with graphene grown on top. The root mean square (RMS) roughness value, calculated for a 500 x 500 nm^2 area, is 1.2 nm for the as-received foil, decreases to 0.4 nm after the UHV cleaning procedure and remains constant after graphene growth (see insets ***figure 3.10***). Excluding wrinkles, the AFM images show a uniform graphene layer covering the copper terraces, with no evidence of the presence of bilayer or multilayer patches. Most previous works reported that the advantage of using copper as substrate for graphene formation, beyond its low cost, is related to the low solubility of carbon into the bulk, conferring a quasi-self-limiting character to the growth. Attending to the binary phase diagram of Cu-C [100], the carbon solubility in Cu decreases with decreasing temperature, being around 0.002% at 800°C, in contrast to typical CVD temperatures around 1050°C, where the solubility is four times larger. As it will be detailed below, in addition to AFM measurements, different experimental techniques used in the present study confirm the formation of a single graphene monolayer, suggesting a self-limiting mechanism in the catalytic-like action of Cu.

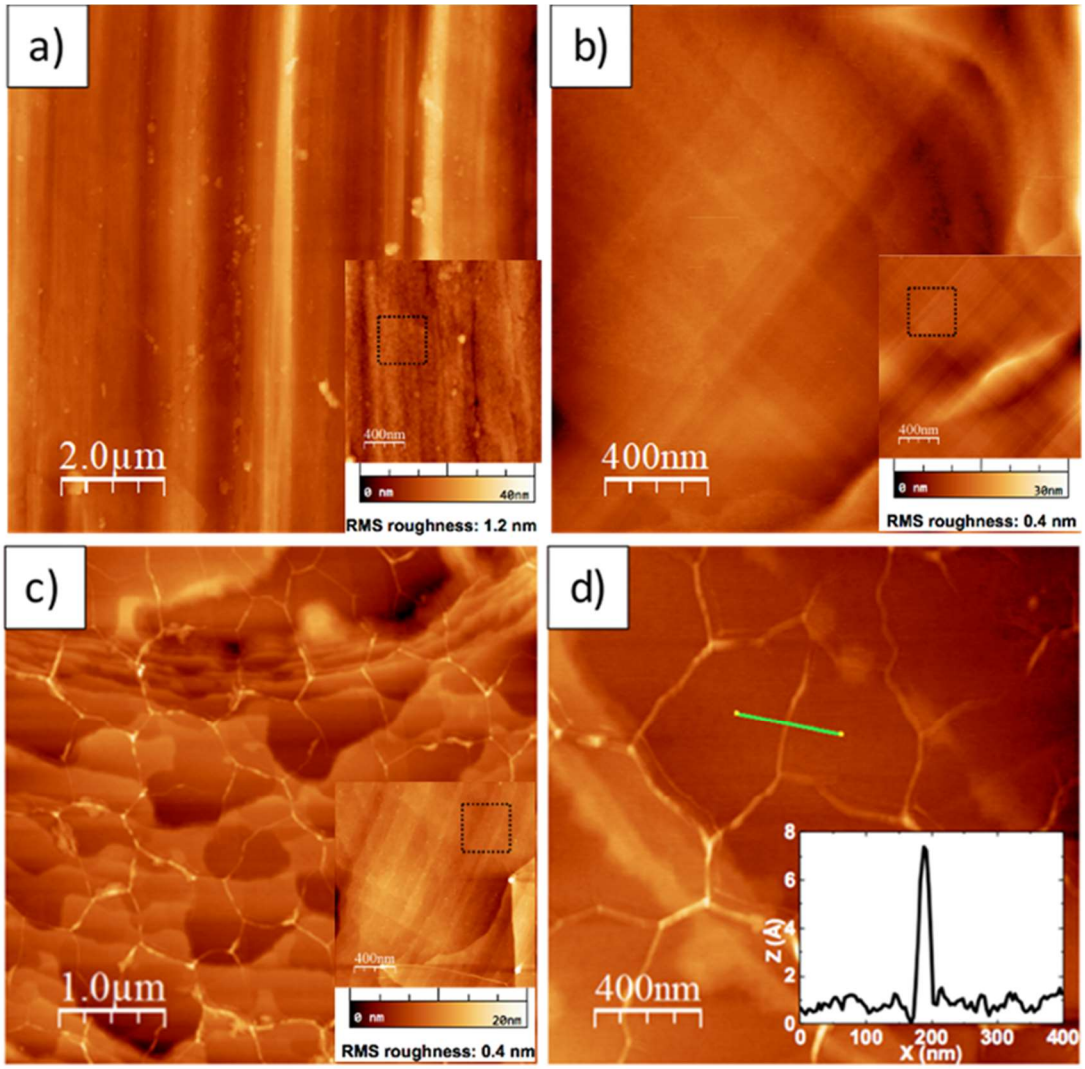

***Figure 3.7**. AFM topographic images of a) the as-received copper foil and b) the treated copper foil. c) and d): topographic images of the graphene layer grown on the Cu foil by the decomposition of C60 molecules. The characteristic wrinkles of graphene are observed crossing along the Cu grains. The inset in a), b) and c) show the area where roughness was measured and the value obtained. The inset in d) shows a height profile corresponding to one of the wrinkles. Height scale of the images: a) 0 to 200 nm, b) 0 to 20 nm, c) o to 10 nm and d) 0 to 5 nm.*

Most previous works reported that the advantage of using copper as substrate for graphene formation, beyond its low cost, is related to the low solubility of carbon into the bulk, conferring a quasi-self-limiting character to the growth. Attending to the binary phase diagram of Cu-C [100], the carbon solubility in Cu decreases with decreasing temperature, being around 0.002% at 800°C, in contrast to typical CVD temperatures around 1050°C, where the solubility is four times larger. As it will be detailed below, in addition to AFM measurements, different experimental techniques used in the present study confirm the formation of a single graphene monolayer, suggesting a self-limiting mechanism in the catalytic-like action of Cu.

3.3.3 XPS

XPS measurements were carried out to identify the chemical species on the sample surface. XPS experiments were performed ex-situ: after growing the graphene layer on the Cu foil substrate under UHV conditions, the sample was exposed to air in order to transfer it to the XPS equipment. ***Figure 3.8*** shows an XPS C-1s spectrum of a graphene layer grown on the Cu foil using C_{60} as precursor. It is important to mention that the sample was measured without any cleaning treatment before the XPS data acquisition.

To determine the different components of the C-1s emission, the XPS spectrum was fitted using standard Gaussian-Lorentzian lines and the corresponding integral background. In order to accommodate the typical asymmetric line shape of sp^2 carbon, this component was fitted using a Doniach and Sunjic line shape with an asymmetry parameter of 0.068 [101]. The solid black line through the data points represents the result of the least-squares fit. Five components were used to simulate the emissions corresponding to the different chemical environment of the carbon atoms. Thus, the subspectra located at 284, 285, 286.3, 288.1 and 290.1 eV, are assigned to C-sp^2, C-OH, C-O, C=O, C-C=O together with O-C=O species, respectively. The strong intensity of the C-sp^2 component with respect to the oxide components evidences, even after air exposure, the high quality of the graphene. In most cases of graphene layers grown by CVD, the XPS intensities corresponding to the oxygen-rich species are larger than those observed here, which indicates a higher presence of oxygen-containing groups in those CVD samples [101].

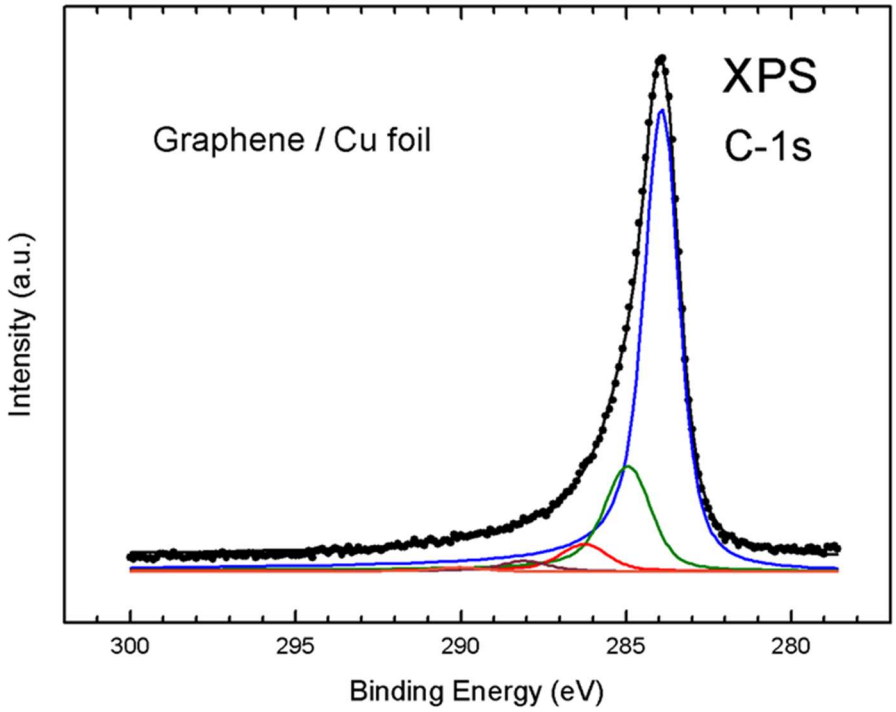

***Figure 3.8**. XPS C-1s core level spectrum (black dots) of the graphene layer on the Cu foil. The main subspectrum (blue line) corresponds to the sp2 carbon emission.*

In our case, the combination of UHV conditions and low temperatures involved in the growth process, which prevents segregation of many of the contaminants contained in the copper bulk ensures a controlled and cleaner procedure. The oxide components in the XPS spectrum are probably coming from the exposure of the sample to air. It is worth mentioning that the XPS technique does not allow distinguishing whether some unbroken C_{60} molecules are present on the surface, because the C-sp^2 C_{60} emission from such species undergoes a very small shift, around 0.06 eV [26] with respect to the C-sp^2 graphene signal, which is below the resolution of the equipment.

3.3.4 Raman Spectroscopy

The ultimate evidence for single-layer synthesis is generally given by Raman Spectroscopy. Before the Raman data acquisition, images of the graphene/Cu sample were taken with 100x optical confocal microscope, showing copper grains, with sizes of the order of tens of microns,

as can be seen in a representative image shown in the inset of ***figure 3.9***. This again, confirms the increase of the mean Cu grain size due to the recrystallization process induced by the annealing treatment, and agrees with the observation of multiple spots in the μ-LEED patterns shown in ***figure 3.3***. Raman measurements were performed on different regions of the samples to check the uniformity of the graphene layer. A representative spectrum of a freshly prepared sample is shown at the lower curve of ***figure 3.9***, in red color. It exhibits the G, 2D and D peaks that are distinctive of graphene although with very reduced intensity. Similar low intensity Raman spectra have been observed for epitaxially grown graphene on single crystals [34] and has been interpreted as a quenching of the vibrational spectral features. The upper black curve presents the Raman spectrum of the same sample, taken two months after growth. During this time the sample was exposed to air under ambient laboratory conditions (at temperatures varying between 18°C and 30°C and relative humidity values between 20% and 60%). Surprisingly the peaks have now a much larger intensity, though no visible changes are observed in the morphology of the sample measured with AFM indicating that the measured intensity enhancement is most likely related to the evolution of the graphene-copper interface. A similar enhancement has been observed in graphene on copper foils exposed to air, and has been related to the formation of copper oxide and to the intercalation of molecules from the atmosphere through defects in the graphene lattice [102,103]. Additional experiments, that will be detailed in the next chapter, were carried out to study this effect, that certainly points out to a decoupling of the graphene layer from the copper substrate due to ambient molecular intercalation, resulting in an enhanced Raman signal due to the reduction of electromagnetic screening from the copper substrate [104].

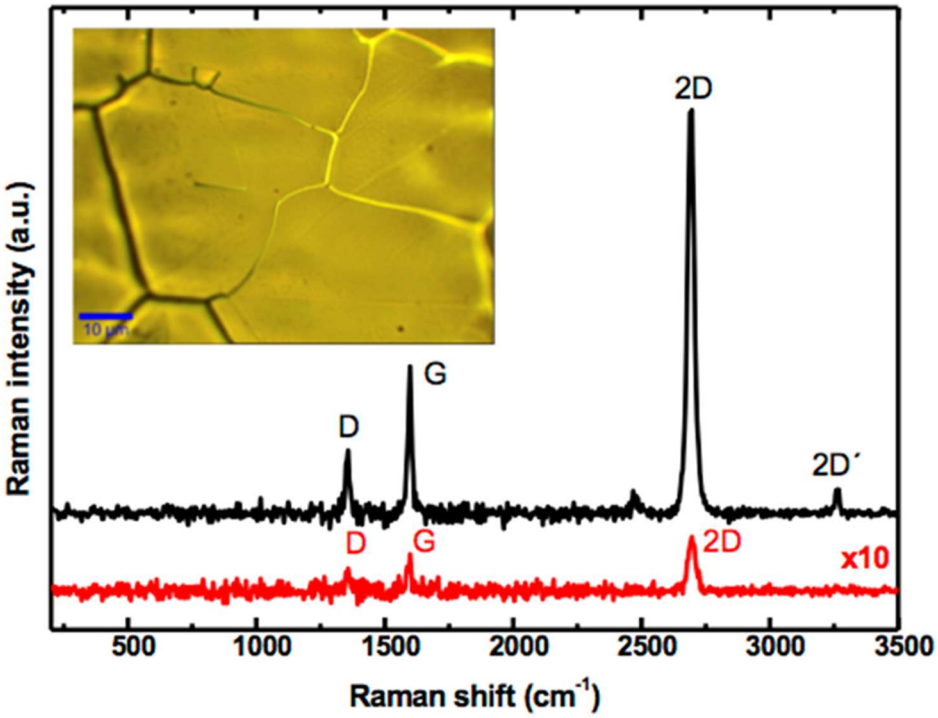

***Figure 3.9**. Representative Raman spectra, taken with a laser wavelength of 532 nm. Red spectrum at the bottom was obtained just after the graphene growth (note that the spectrum is x10 in order to make it visible in the figure) while black spectrum at the top corresponds to aged graphene. A sharp 2D emission is observed together with less intense D and G bands. The inset shows a 100x optical image taken on the graphene grown surface, where the copper substrate grains are visible.*

The intensity and position of the 2D peak are generally used to gather information on the number of graphene layers. For a monolayer graphene, a single peak with full-width-half-maximum (FWHM) ~30 cm^{-1} and normalized intensity (I_{2D}/I_G) > 1 (<1 for multilayers) is expected [40]. From the black curve in ***figure 3.9***, an intense 2D peak is observed at 2689 cm^{-1}. The spectral shape of the 2D peak is quite narrow, with a FWHM of 26.6 cm^{-1} (as adjusted with a Lorentz profile), and highly symmetric, i. e. it is fitted of a single component, as is the case for monolayer graphene. The calculated integrated I_{2D}/I_G ratio gives a value of 5.2, corroborating the previous observation of the presence of a monolayer graphene. On the other hand, the G peak, located at 1594 cm^{-1}, exhibits a FWHM of 15.6 cm^{-1}. All these values fall within the typical range of values established for a graphene monolayer not significantly subjected to strain [67].

Additionally, a small D peak, associated typically to the presence of defects, was also detected at 1351 cm^{-1} with a FWHM of 15.6 cm^{-1}. Although the D peak intensity is low, the factor that could influence that emission will be discussed below. In fact, the D peak is less intense than the one found in a previous work on C_{60} decomposition on nickel where, due to the strong D signal, the possibility of improving the quality of the graphene layer by using another metallic

substrate or another precursor was suggested [89]. Raman spectra collected at different points of the fresh sample showed that the monolayer of graphene uniformly covers the copper foil surface (see ***figure 3.10***).

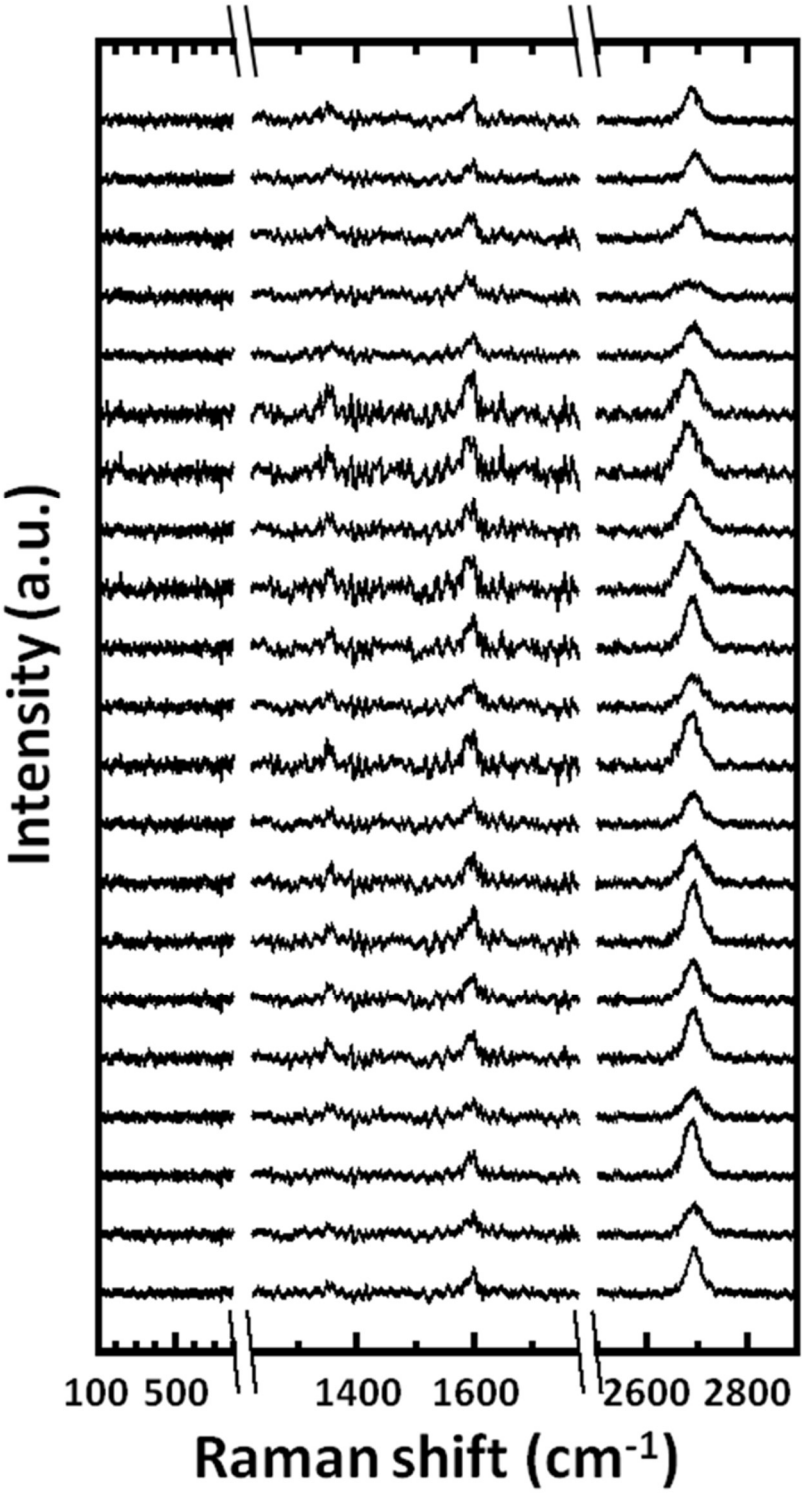

Figure 3.10*. Raman spectra taken with a laser wavelength of 532 nm at different points of the sample separated of about 0.3 nm. The plot is divided in three parts: at low energies for a better observation of the absence of copper oxide species, at intermediate values to detect the D and G peaks and a third region exhibiting the 2D peak.*

To gain some insight into the interactions at the interface and be able to understand the Raman spectra, theoretical calculations of the vibrational modes of free-standing graphene and of graphene on Cu single crystals were performed, as a crude approximation to the Raman spectrum, excluding the well-known Raman resonant processes in graphene as well as two-phonon phenomena.

In our experimental protocol, graphene grows on a previously vacuum-treated Cu polycrystalline substrate with a certain (110) texture. Under these conditions a coupling between the metal surface and graphene can be expected. In this direction, the perturbation of the substrate in the vibrational modes of the free-standing graphene were studied, that, as will be shown, vary from one copper surface to another. Hence, Cu (100), Cu (110) and the Cu (111) surfaces were used as model systems in the calculations to have a better understanding of the process.

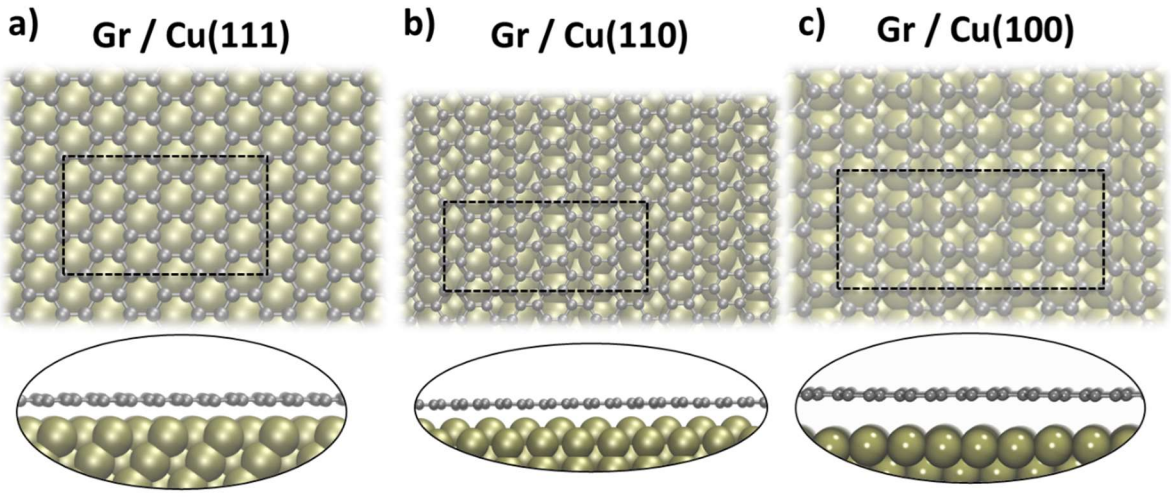

d)

	Gr/Cu(111)	Gr/Cu(110)	Gr/Cu(100)
d_{Gr-Cu}	3.09 Å	3.14 Å	3.16 Å
C^{Gr}	0.17 Å	0.22 Å	0.11 Å
E_{ads}/C	0.14 eV	0.11 eV	0.12 eV
Lattice size	(7.5 x 13.5) Å^2	(7.5 x18.0) Å^2	(7.5 x18.0) Å^2
Θ^{rot}	0°	0°	0°

***Figure 3.11**. Top view (upper panel) and side view (lower panel) of the optimized a) Gr/Cu(111), b) Gr/Cu(110) and c) Gr/Cu(100) interfaces, showing the employed lattice size. d) Table ascribing the average perpendicular distance between Gr and Cu, d_{Gr-Cu} the corrugation induced in the SLG, C^{Gr} and the adsorption energy per C atom, E_{ads}/C for Gr/Cu(111), Gr/Cu(110) and Gr/Cu(100). Chosen lattice size and rotational angle, θ^{ot}, between graphene and Cu are also listed.*

The results of the DFT structural optimization reveal that the interaction of the graphene with the metal substrate strongly depends on the surface configuration. The optimization of the simulation cell leads to a buckled graphene surface due to the interaction of some distinct C atoms with the Cu atoms underneath, inducing a corrugation on the graphene layer of about 0.22 Å for G/Cu (110), 0.11 Å G/Cu (100) and 0.17 Å G/Cu (111) (***figure 3.11)***. At these particular points the C atom is displaced towards the Cu surface, interacting more strongly with the Cu, thus acquiring a sp^3 character. ***Figure 3.15*** shows that the calculation of the vibrational modes for free-standing graphene presents, as expected when excluding anharmonic effects, a unique feature at 1599 cm^{-1}, characteristic of sp^2 carbon, that can be assigned to the well-known G band. When the graphene layer is simulated on the Cu(110) surface G/Cu (100) and G/Cu (111) (***figure 3.11***), a new feature appears around 1365 cm^{-1} due to the interaction with the susbstrate. Our calculations show that the graphene-substrate interaction may induce the rupture of the sp^2 hybridization producing the appearance of local regions with sp^3 character [105] and a diamond-like sp^3 vibrational band, whose frequency lies in the same spectral region as the graphene D band characteristic of structural defects (***figure 3.12***). Therefore, in our case, in addition to a D band accounting for structural defects at grain boundaries or graphene wrinkles, the aforementioned sp^3 carbon hybridization due to the interaction with the Cu surface could also contribute to this spectral feature. Nevertheless, even though we may have an extra contribution to the D band in the Raman spectra, our D intensity (***figure 3.9***) is comparable to that already published [106].

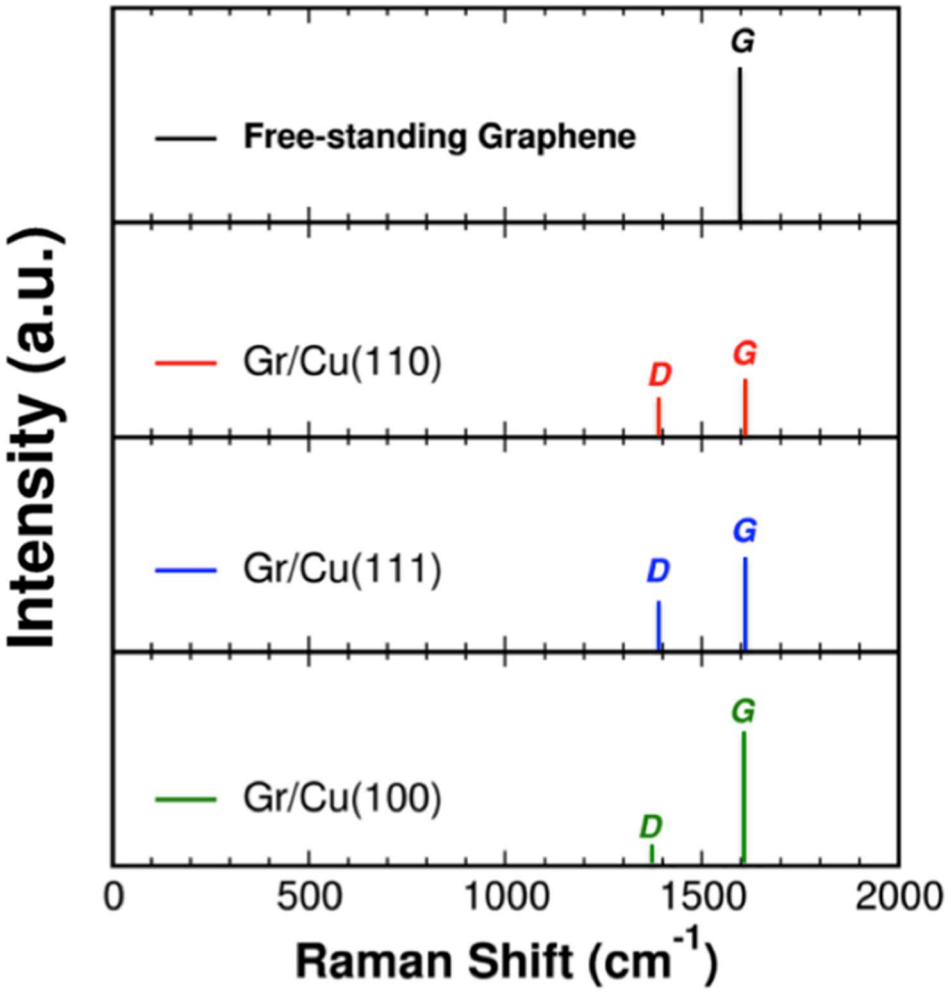

***Figure 3.12**. First approximation of the theoretical calculation of the Raman scattering for free standing graphene, Gr/Cu(110), Gr/Cu(111) and Gr/Cu(100). The G band is visible in all cases while the D band is visible only for the Gr/Cu interfaces*

3.3.5 ARPES

As we have already mentioned, the experimental conditions for the typical CVD growth of graphene do not exclude the presence of oxide species below the graphene layer, favoring a decupling with the substrate. Following our PVD methodology, the presence of oxide species in the surface is almost negligible, as determined by XPS. In this conditions, the clean Cu atoms in the terraces are prone to react with C atoms from the graphene, favoring coupling at specific locations, as concluded from the calculations. This can lead to a charge transfer effect between the layer and the substrate, deriving in a doping effect of the graphene layer. In this section we will explore how this behavior influence on the mentioned graphene layer doping.

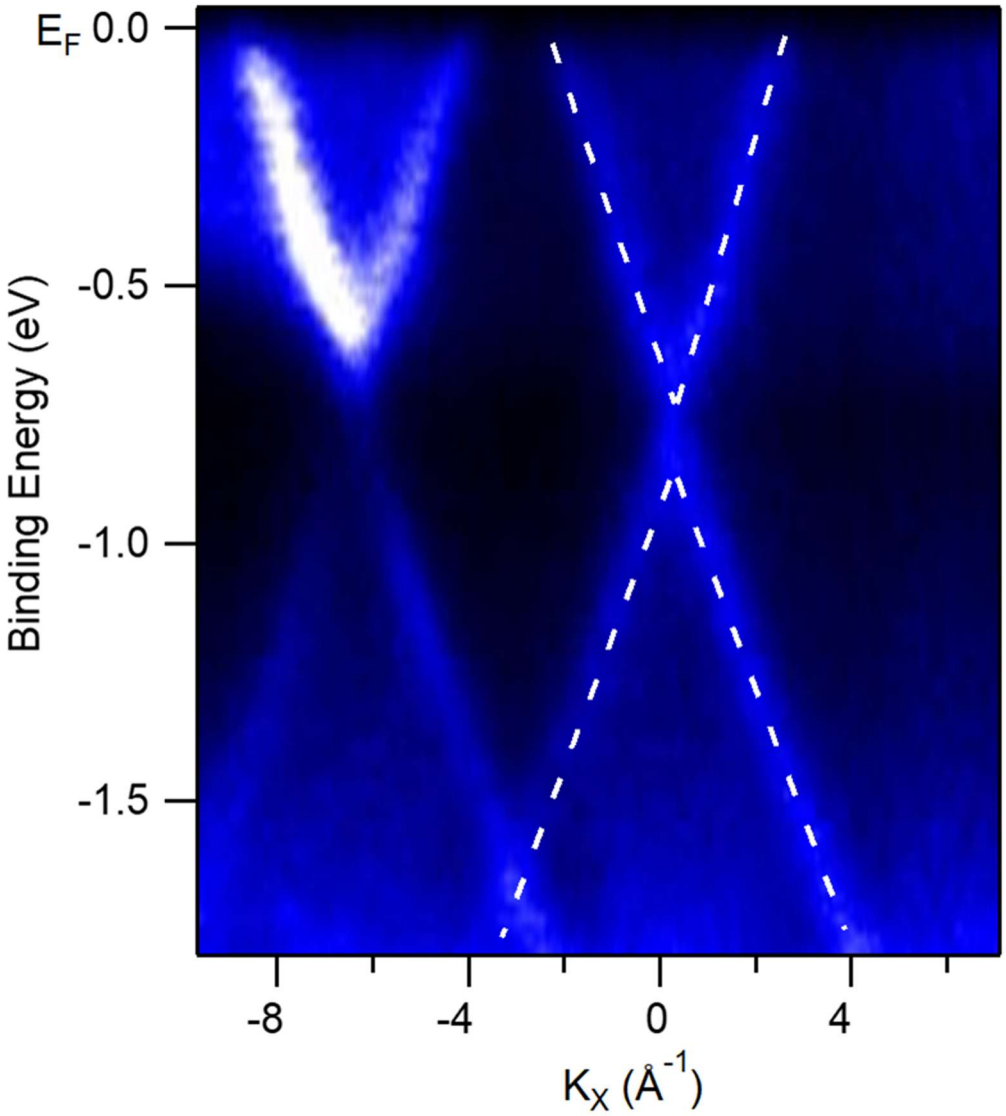

***Figure 3.13**. Energy-momentum dispersion of a multi-grain graphene layer on a Cu foil measured with circularly polarized light of 36 eV near K point along Kx direction. Due to the contribution of different graphene grains more than one Dirac cone dispersion band is observed.*

With the aim of investigating the electronic structure of our single layer graphene, ARPES measurements were performed. ***Figure 3.13*** shows a multigrain photoemission momentum map along K_x direction of the sample using circularly polarized light of 36 eV. In this case and due to the polycrystalline nature of our sample, the photoemission data taken along any ΓK direction will show not only one Dirac cone but multiple π bands. That is the case in ***figure 3.13***, where the two Dirac cones are observed in the image, corresponding to two adjacent graphene grains. The right one (labeled as K_x=0 $Å^{-1}$) is exactly at one K point whereas the one near K_x= -6 $Å^{-1}$ is slightly misaligned, and therefore it should not be considered to study the doping and the gap of this sample. It can be clearly observed that the electronic bands are

completely linear, as corresponds to a massless Dirac fermion behavior. A deeper study of the data shows an n-type doping of 0.77 eV, probably due to the coupling of the graphene π bands and the copper d-band [107]. This result differs from previous observations of graphene grown by CVD on Cu foil, where a lighter doping, around 0.4 eV [97,108], or even an undoped [109] behavior was found. This difference can be ascribed to the present growth procedure, involving UHV conditions, clean surface, C_{60} molecules and a complete single layer graphene, leading to a larger coupling between graphene and the substrate, as the theoretical calculations suggest. This coupling would also be responsible for the charge transfer from the Cu foil to the graphene layer. In this sense, gaps of 0.36 eV have been reported for graphene on Cu in UHV [107]. Moreover, our ARPES data also evidence the existence of a small bandgap of 0.12 eV, that is in the range of other gaps already reported for similar systems [97,107]. Finally, figure 3.16 does not show parabolic bands, typical of the presence of bilayer graphene or graphene oxide regions, indicating the growth of an extended single layer graphene in agreement to the Raman, AFM and SEM data, and the prevalence of the graphene electronic properties on this technologically relevant kind of samples.

3.3.6 Statistics on Raman spectroscopy data

Throughout this chapter, the most representative results of the characterization of the graphene layer grown by using C_{60} molecules as precursors have been described. In this section, a statistical study of the main parameters derived from the Raman spectroscopy data performed on different types of copper substrates is shown. The motivation of this study is the evidence from a previous work of Casiraghi, [70] of strong variations in the Raman spectra of different transferred graphene layers (deposited on a SiO_2 substrate). The changes in some of the parameters of the Raman data are related to some significant factors as structural disorder, doping or strain [70,110]. In that work [70], a correlation between the main Raman characteristics and the doping level of the graphene layer was inferred. Then, with the aim of extracting relevant information of the numerous Raman spectra acquired for the different samples under study in the present work, a statistical analysis was performed. The results were derived from the data of Raman spectra performed on graphene layers grown on polycrystalline copper foils with thicknesses of 25 μm, 35 μm, 50 μm and 1.27 mm, on top of 1.2 mm thick copper gaskets employed for UHV sealing, on Cu single crystals (Cu(111) and Cu(100) surfaces) and on graphene layers transferred to SiO_2 substrate after the PVD growth on Cu foils (detailed in next chapter). However, as it has been already commented, the optimal graphene samples were grown on top of 25 and 50 μm thick substrates. It has to be mentioned

that the previous studies on the Raman spectrum variations [70] were performed just on transferred graphene layers being the relevant information mainly related to the graphene layer, commonly decoupled from the substrate. In the present case, most of the Raman spectra were acquired on graphene layers just after growing on different Cu samples and only some spectra were obtained from transferred layers.

Figure 3.14a shows the relation between the FWHM and the position of the G peak for different types of copper substrates while ***figure 3.14b*** exhibits the position of the 2D peak as a function of the position of the G peak. Due to the evident dispersion of so much data, just global conclusions on the doping level of the graphene layers can be extracted from those graphics. From one side, it can be deduced, for example, that by employing the growth method detailed in this chapter, graphene is always doped by an effect of the substrate, i.e. copper, does not matter the crystallographic configuration. In addition, in ***figure 3.14*** the 25 and 50 μm thick copper substrates appear as the ones with the lowest dispersion in the position and width of the peaks. This confirms the evidence on the optimal graphene growth for this kind of samples. As it was already mentioned, there are also represented data of transferred graphene samples on the plots. The transferred graphene samples were previously grown on the 25, 35 and 50 μm thick substrates. Although is in the next chapter where the transfer of graphene to SiO_2 will be tackled, it illustrates very graphically that this group of samples exhibits the smallest dispersion amongst all of the substrates employed for the growth.

in summary, the result of these graphics unveils how strongly the copper substrate interacts with the graphene layer, leading to variations on the Raman spectrum parameters. The graphene/Cu interaction is diverse, depending on the type of copper but results in a relevant dispersion, which strongly diminishes when the graphene is transferred to a non-metallic substrate. Importantly, although the copper substrate influence is significant, it can be cut out since once the graphene layer is transferred, independently from the used substrate for the growth, all the Raman spectra become rather similar. Next chapter will support this assumption, since by intercalating oxygen we will observe that the graphene/Cu interaction decreases.

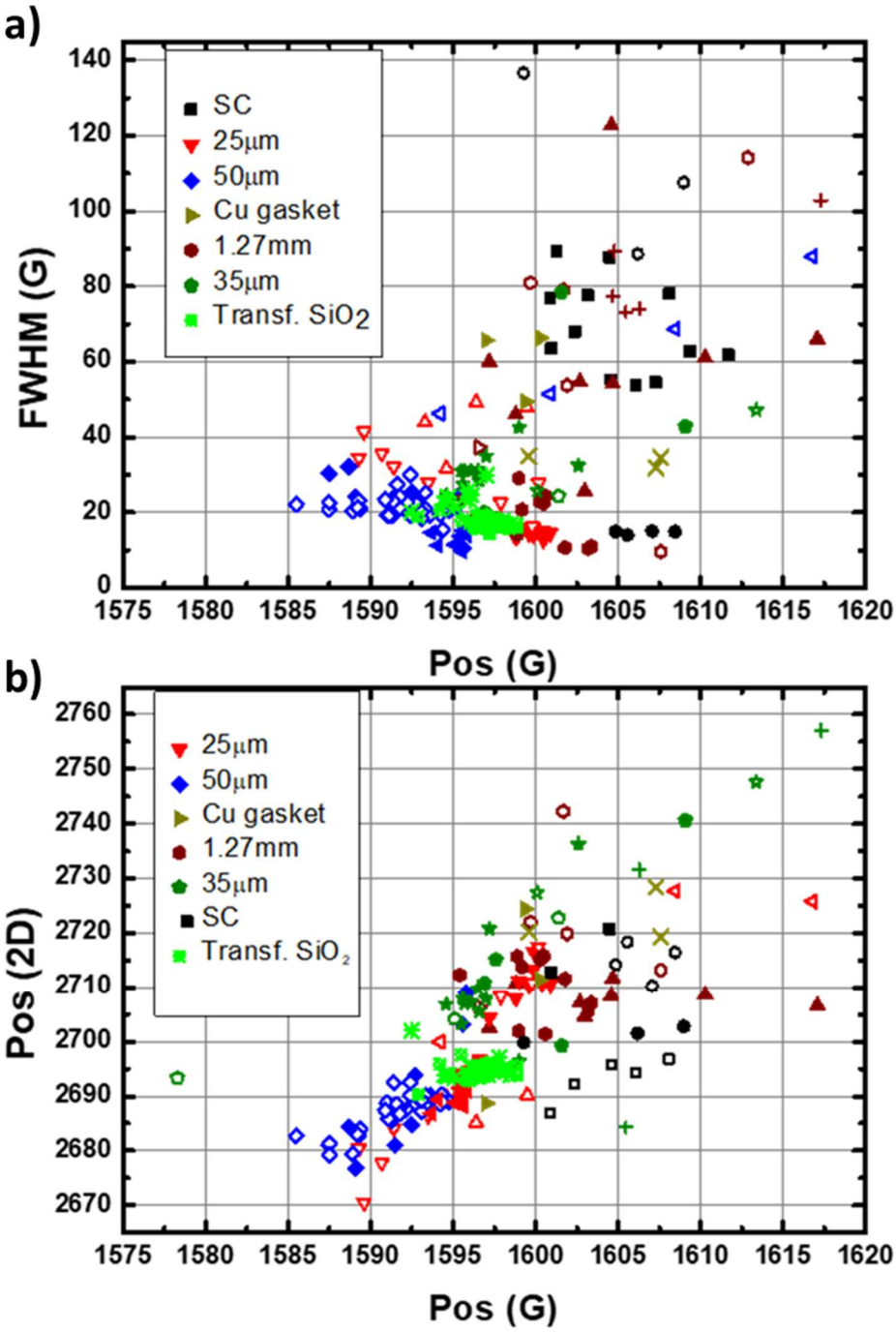

Figure 3.14. *a) Representation of the FWHM of the G peak versus the G peak position and b) representation of the 2D peak position as a function of the G peak position for different types of copper substrates as well as for the graphene layers transferred to SiO2.*

3.4 Conclusions

We have described the growth of large area graphene monolayer on Cu foils in UHV conditions using C_{60} as precursor molecules. The mechanism of graphene layer formation on the Cu surface is based on the decomposition of the C_{60} molecules, a thermally activated process promoted by the Cu surface. The above-mentioned process presents several advantages with respect to the use of hydrocarbons as carbon sources. First, the process is self-limiting and only single layers are obtained. Second, it requires lower substrate temperature than conventional CVD graphene growth methods. The decrease of the temperature results in two main advantages: on one hand, fewer impurities are segregated to the surface, promoting an ultra-pure graphene-copper interface, and on the other hand the solubility of carbon into the Cu bulk is reduced, avoiding the formation of bilayer or few layer domains in the graphene layer. Moreover, in our experimental protocol UHV conditions were used, and therefore, the surface was atomically clean before experiments, so no oxygen was involved or intercalated during the process.

With the aim of evaluating the quality and properties of the graphene layer, different characterization techniques were applied on the as-grown samples. The in-situ LEED pattern of the Cu foils after the surface cleaning process showed characteristic spots of different Cu facets, corresponding to a typical polycrystalline specimen. After graphene growth, a clear ring feature appears in the in-situ LEED pattern, evidencing the presence of a multidomain graphene film on the surface, although some graphene orientations prevail. The morphology of the graphene layer was studied by ex-situ AFM. The AFM images exhibited complete coverage of the areas measured and uniform graphene film on the Cu foil. The presence of graphene wrinkles, crossing the substrate terraces, was also observed. Raman spectra, similar along the sample surface, showed a narrow 2D band as well as G and D peaks. By investigating the surface chemical composition by XPS, sp^2 hybridized carbon emission is the main contribution and only low contents in functional groups were observed after exposing the sample to atmospheric conditions. ARPES measurements showed that the band structure of the graphene grown on the Cu foil is based on multiple linearly dispersing graphene bands, corresponding to different graphene grains. All results prove that the envisaged protocol to synthesize graphene from C_{60} molecules is a successful strategy to obtain large area uniform single layer graphene on technologically relevant substrates at lower temperature than the wide-spread CVD method.

Chapter 4. Transfer of graphene and decoupling strategies

4.1 Introduction

As mentioned in the previous chapter, many methods have been developed for the synthesis of graphene. Among them, the growth of this material on metals by PVD is one of the most appealing protocols [26,111] because it takes advantage of the catalytic properties of the metallic substrates lowering the temperature required for the graphene growth. Nevertheless, metal substrates are incompatible with the exploitation of the unusual electronic properties of graphene, making mandatory the consequent transfer protocols from the initial growth substrate to an insulating material.

Several techniques have been developed for the transferring of graphene to more suitable substrates such as SiO_2. Wet transfer techniques such as the electrochemical delamination method [27,112,113] have been demonstrated to be exceptional transfer methods. That case, it is a simple electrochemical process that allows recycling the substrate. The procedure, extensively explained in the next section, consists in the use of the graphene/metal system as one of the electrodes (cathode, negatively biased) of a typical electrolysis process. The hydrogen outgoing from the electrochemical reaction enters to the graphene/metal interface starting from the sides. This method has been widely used on graphene grown by CVD on copper foils.

4.2 Graphene transfer to SiO_2 substrates

The choice of SiO_2 as a suitable substrate for graphene films is not arbitrary. The silicon industry is huge and in a constant evolution since the electronic revolution launched by the emergence of silicon-based transistors. In other words, silicon wafers are cheap and, for the time being, easy to obtain. Moreover, almost any silicon-based technological demand has a commercial solution. The second reason is related to the thermally promoted 300 nm SiO_2 layer that the used Si wafer has. As it was already mentioned in chapter 1, the wavelength of the constructive interference formed between the reflected visible light at the SiO_2/Si interface and that reflected at the SiO_2/air interface suffers a small change when graphene layers are on top of the SiO_2(300 nm)/Si substrate (from now on, it will be named as SiO_2). This change is observable as a contrast and, moreover, this phenomenon allows also to discern between different graphene thicknesses (monolayer, bilayer…) [15].

4.2.1 Sample preparation

Both materials involved in the transfer procedure, target SiO_2 substrate and Gr/Cu sample, need to be conditioned prior to the transfer process itself. On one side, the cleaning of the target substrate is a first order demand. Then, with the aim of procuring a contamination-free surface, an optimized protocol has to be strictly followed. On the other side, concerning the Gr/Cu system, to preserve the continuity of the as-grown graphene when detaching it from the Cu substrate, a polymeric coating is used as a supporting layer for the transfer process. The most extended compound is polymethylmethacrylate (PMMA). For both, an optimal coating and the most effective posterior removal of this polymer, the coating must be carefully performed to obtain a homogeneous and a relative thin (300 nm) coverage.

4.2.1.1 SiO_2 substrate cleaning procedure

Prior to the graphene transfer, the cleaning procedure of the ultimate substrate needs to be carefully followed. The protocol we employed, described below, was learned from the group of Prof. Strupinski at the Instytut Technologii Materiałów Elektronicznych (ITME) in Warsaw (Poland), where it is routinely applied.

In a first step, SiO_2 samples are immersed in a hot acetone bath (56°C, boiling temperature of acetone) for two minutes. Then, that bath with the SiO_2 sample is introduced into an ultrasonic cleaner for three minutes. Once the ultrasound process finishes, the sample is extracted from the glass, laid on a dust-free tissue and, right after, held with clean tweezers while the surface is rubbed with a cotton bud wetted with acetone. It is important to rub the surface kindly just in one direction. If the rubbing produces some noise, the pressure against the surface must be released. At this point, the sample is dipped once again into the hot acetone bath for thirty seconds. Once this procedure is completed, the cleanness of the SiO_2 substrate should be checked with an optical microscope. If the sample still shows traces of dirt, the rubbing process must be repeated until a clean surface is achieved as determined by means of the microscope. At this stage, the sample is immersed in a hot acetone bath for two minutes, followed by immersion in a hot isopropanol bath (82° C boiling temperature) for another two minutes. Lastly, the SiO_2 target will be immersed in a deionized water (18.2 MΩ) bath at RT for another two minutes.

4.2.1.2 PMMA coating of graphene/copper samples

In parallel to the cleaning process of the SiO_2 substrates, the graphene-on-copper samples were covered with PMMA. As mentioned, this coating acts as a supporting layer in order to preserve intact the graphene layer. For this purpose, PMMA was used with a molecular mass of 495 KiloDalton in anisol solution (4% concentration). Contrary to methods where samples are grown using gases as precursors (such as CVD), in our PVD grown samples only one side was covered with the graphene layer. Therefore, cleaning of the back side of the sample was not necessary.

For a homogeneous distribution of the supporting polymer, the graphene samples were spin-coated using the next procedure, also developed at ITME. A micropipette was employed to distribute some drops of PMMA on the samples surface, until the surface was completely covered with the polymer solution, and then, the samples were spun at 400 RPM for fifty seconds and at 1000 RPM for ten seconds. Finally, the spin-coated samples were left overnight at RT to get rid of the solvent. It is important not to cure the PMMA at high temperature.

4.2.2 Transfer process

With this method, the dimensions of the transferred layer were smaller than the original sample since, the part attached to the alligator clamp (***figure 4.1***) has to be discarded. Moreover, the other three borders of the square sample were cut using a scalpel to obtain smooth edges, reducing more the dimensions of the resulting samples.

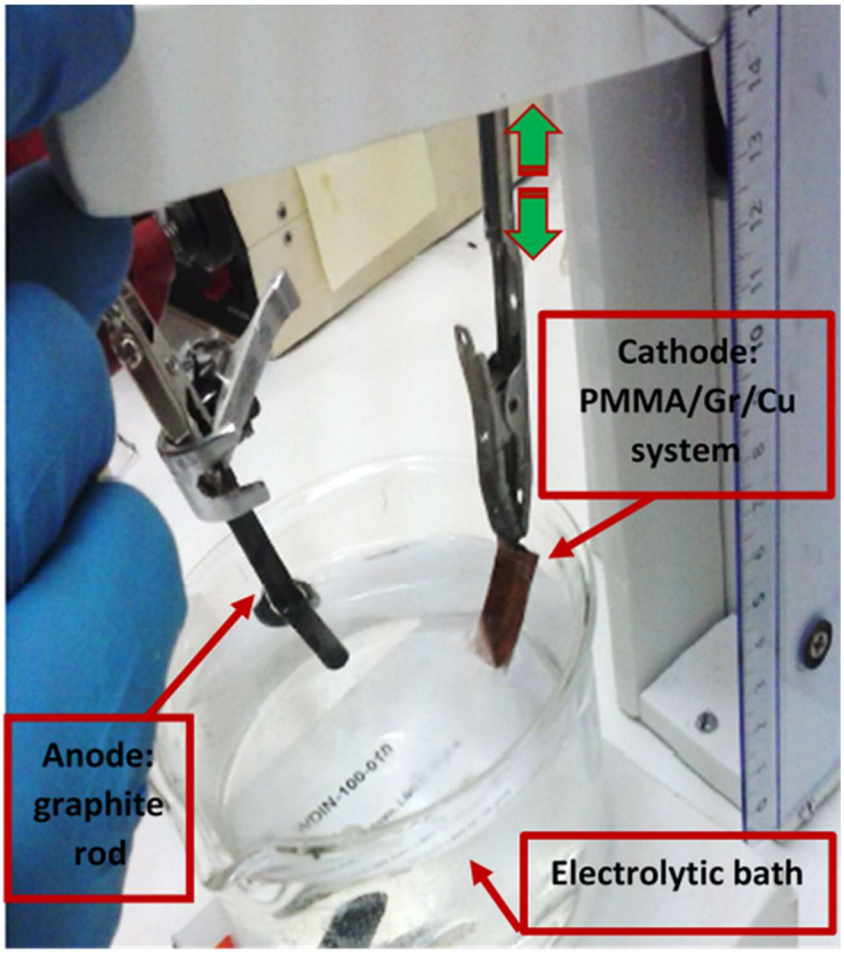

***Figure 4.1**. Experimental set-up for the electrochemical delamination process. The cathode (PMMA/Gr/Cu system) is held from a mechanical arm that allows to move the sample, attached to an alligator clamp, up and down with adjustable velocity. The anode is a graphite rod immersed in the electrolytic bath. KCl was used as electrolyte in a concentration of 1M. The set-up was designed and mounted by C. Sebastián-Checa.*

The set-up for the electrochemical process consists of a two-electrode cell (***figure 4.1***). The Gr/Cu sample is the cathode while a graphite rod (10 cm long, 5 mm in diameter) is used as the anode (positively biased with 5 V). KCl was chosen as the electrolyte for two main reasons: on one hand, it has been proven that produces less contaminants that other chemical compounds like NaOH or KOH [113] and on the other hand, since it is a salt (pH ~7) is not aggressive from the chemical point of view. We used 1M KCl solution, employing 250 mL of ultra-pure water (18.2 MΩ). In principle, there is not a limiting number of samples that can be delaminated using the same bath. The only precaution to be taken is to control the pH level that could vary due to contamination accumulation. In the case of using the same materials as electrodes, the reaction rate depends on three parameters: the applied voltage, the size of the electrodes and the distance between them. The electrodes, Gr/Cu sample and graphite rod, are separated by ~3-4 cm. In our set-up, successful delamination processes were performed at an applied voltage 5V.

Once the graphite was biased and immersed in the bath, the sample was gradually dipped into the bath at a rate of 0.5 mm/s. Routinely, samples grown by CVD used an immersion rate of ~1 mm/s and the PMMA/Gr became progressively and smoothly detached [114]. Unfortunately, for the graphene samples grown by our procedure, using C_{60} in UHV conditions, the process was not so smooth. The difficulties to detach completely the layer from the substrate were present almost in every sample. The process, that for CVD graphene samples usually lasts less than 1 minute, took 10 times more with the PVD grown samples. Moreover, the rate of success was around 20%, mainly because the graphene layer released at some points while in other parts of the sample remained completely attached. Unfortunately, in these cases, the final transferred sample was useless. A picture of two successful graphene transfer can be seen in ***figure 4.2***, where the visible layer on top of the SiO_2 is the PMMA.

The chemical reaction that governs this process consists in the water reduction, producing hydrogen bubbles that intercalate in between the graphene and the copper:

$$2H_2O(l) + 2e^- \rightarrow H_2(g) + 2OH^-(aq) \quad (1)$$

The hydrogen bubbles start from the edges of the sample and extend along the sample surface while the sample goes deeper in the bath, until finally the layer is detached and lies suspended on the surface of the liquid. At this point, we used a petri dish to gather the graphene layer, always suspended in liquid, and placed it in a crystallizer, which was filled with two liters of ultra-pure water.

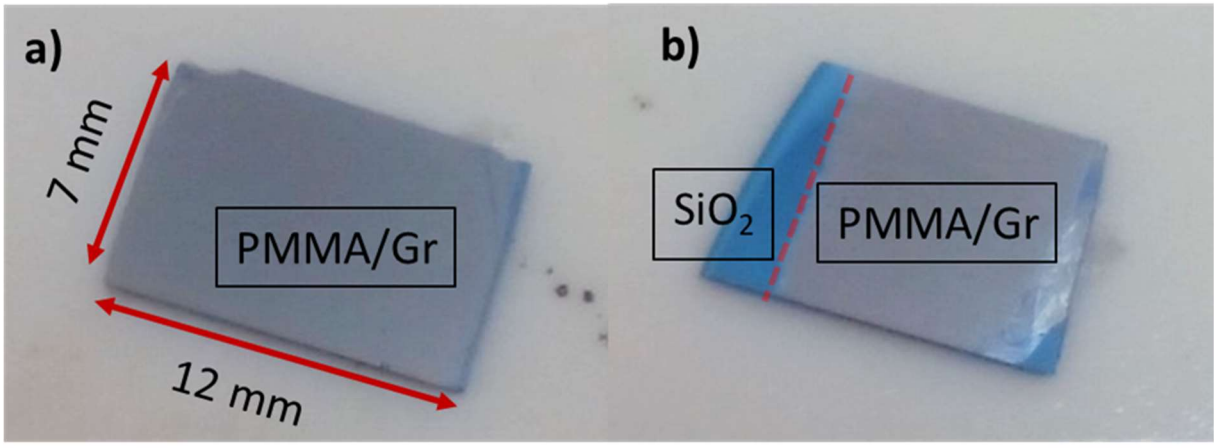

Figure 4.2. *Two PMMA/graphene samples transferred to SiO_2 substrates. a) The sample is completely covered with PMMA/graphene. b) The PMMA/graphene layer is smaller than the silicon substrate. A red line has been drawn to highlight the boundary of the PMMA/graphene layer.*

Then, to minimize the residues of KCl, a constant water flow was applied to the crystallizer procuring always to maintain the same level of water with the aim of avoiding the sticking of the graphene layer to the walls. A total volume of ten liters of water was used. The PMMA/graphene layer was picked up again using a clean petri dish, and placed in a different beaker with one liter of ultra-pure water. At this stage, an ultra-pure water jet was carefully applied with a syringe to remove some air bubbles trapped under the PMMA/Gr layer. At this point, when the PMMA/Gr appeared as a smooth surface, the previously cleaned SiO_2, held with clean tweezers, was immersed in the water to carefully deposit the PMMA/Gr layer onto the SiO_2 surface (***figure 4.2***).

The water trapped between the PMMA/Gr layer and the SiO_2 substrate was removed via capillarity by smoothly touching a border of the sample with a regular paper tissue. After that, the sample was left for half an hour at RT to remove the excess of water. Finally, it was deposited on a hot plate at 50°C for one hour until reaching a final temperature of 120°C (by gradually increasing 10°C every ten minutes) and then it was left there overnight.

The final step was the removal of the PMMA layer. The procedure consisted in a set of four hot baths: one in ultra-pure water at 80°C, two consecutive baths in hot acetone without reaching the boiling point to avoid bubbles that could damage the graphene layer, and the last one in ethanol, with the same conditions. The method, step by step, was the following:

- First, samples were immersed in the ultra-pure water and maintained there for two minutes.
- After that, they were transferred to the acetone bath for another two minutes, stirring the samples very gently to help the removal of the polymer.
- The next step was to immerse them into the other acetone bath, without stirring, to remove residues that samples could have grabbed when taking it out from the previous bath.
- Finally, samples were immersed in the ethanol bath.
- Once finished, the sample was picked up making sure that the sample dripped all the residual ethanol and it was gently deposited on a hot plate at 50°C.
- After thirty minutes, when the major part of the remaining liquid was evaporated, the temperature was gradually increased to 120°C and kept at this value for another thirty minutes.

4.2.3 Transferred graphene layer characterization

Prior to macroscopic and local measurements of the electronic properties of the transferred graphene samples, a morphological and structural study was performed to check the quality of the samples. For this purpose, the transferred samples were mapped with an optical microscope with a 100x objective. AFM topographic measurements were carried out to check the continuity of the graphene layer and to determine the quantity of chemical contamination (solvents, polymer residues…). In addition to these structural characterization techniques, μ-Raman spectroscopy maps were acquired in order to check the graphene layer continuity all over the surface. Thus, not only some structural information was extracted for the graphene layer but also some insights of the chemical nature of the contamination as well as on the uncontrolled electrical doping.

- **Optical microscopy**

As was explained before, although graphene has the thickness of one carbon atom, after transferring to SiO_2 it can be detected employing visible light as a probe by means of the contrast [15]. For this reason, optical microscopy has been a widely employed characterization technique in the study of graphene based prototype devices, mainly for the detection of monolayer graphene among flakes with different number of layers [15].

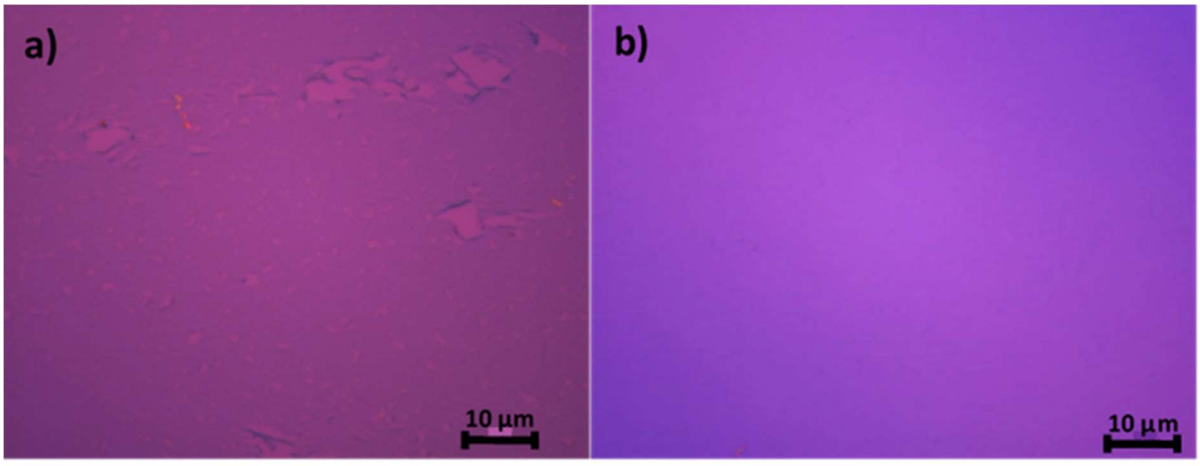

***Figure 4.3**. Representative optical microscope image (100x objective lens) of a) PVD graphene on a SiO_2 surface as transferred with the electrochemical delamination method. The layer extends over the whole image, although many holes are observed. b) CVD graphene shown for comparative purposes. The graphene layer extends homogeneously all over the surface.*

Figure 4.3a shows an optical image of a graphene layer grown on copper foil in UHV using C_{60} molecules as carbon source and transferred to a SiO_2 substrate by using the electrochemical delamination method. As it was already discussed in the chapter 3, the growth has generated a continuous layer on the metallic surface, however, during the transfer process to the SiO_2 substrate, this layer has been severely damaged. In ***figure 4.3b***, a graphene sample grown in a commercial CVD chamber transferred to a substrate piece of the same wafer is shown for comparative purposes [26]. Both delamination processes have been carried out with the same experimental set-up (the CVD sample was grown and transferred by A. Krajewska, ITME) with a time lapse of minutes. Although both are graphene on polycrystalline copper samples, grown by different methods, the transfer protocol produces dissimilar results.

- **AFM**

The optical microscope can explore the continuity of the graphene layer, detects macroscopic contamination like traces of solvents and distinguishes between covered and uncovered regions. AFM measurements instead, although providing similar information it probes locally, in a nanometric scale, observing what is undetectable for optical microscopy. ***Figure 4.4*** shows AFM images of PVD grown graphene transferred to the SiO_2 substrate, where visible holes are observed. However, it was determined by AFM in chapter 2 that the growth process formed a complete monolayer on the Cu substrates. Therefore, a plausible conclusion is that these holes are produced during the transfer process. Additionally, as detected by AFM the strain generated during the transfer process produces more wrinkles, which are undesirable since they can act as scattering zones for charge carriers. Finally, the AFM images also suggest that the contamination of the transfer process was not completely removed.

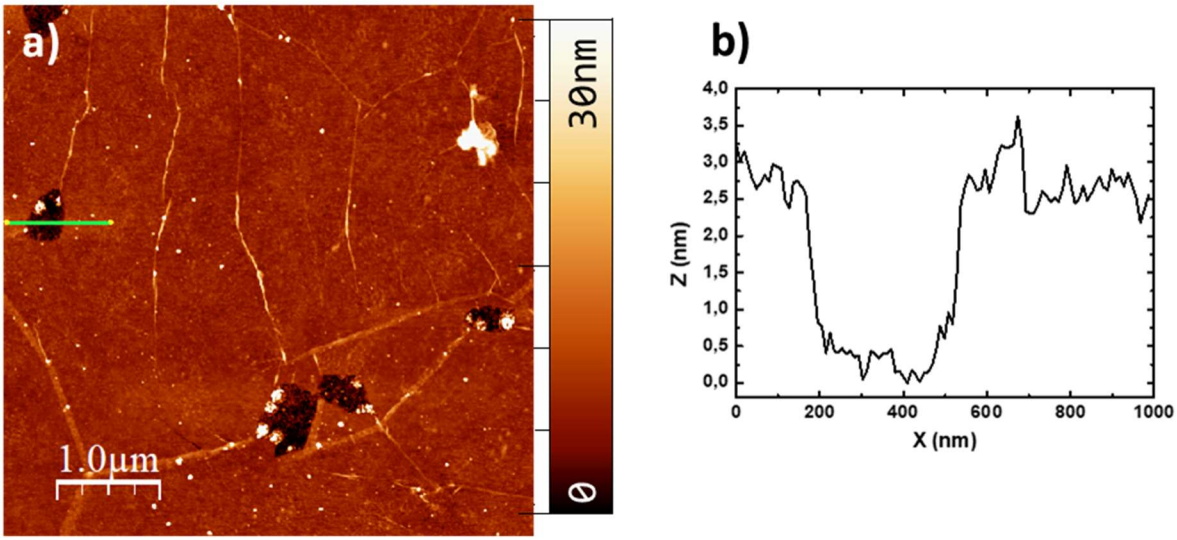

***Figure 4.4**. a) AFM topographic image of graphene transferred to SiO_2 substrate. The image was acquired in dynamic mode. Contamination is visible due to an inefficient removal of the transfer process residues. A height profile along the green line, which crosses one surface hole, is observed in (b).*

The depth of the hole, shown in the profile in ***figure 4.4b*** does not correspond with the height of the graphene layer. There might be for two reasons. On one hand, there are still some residues on top of the graphene layer that can give a higher height value. And on the other hand, it can be an effect of the measurement mode, that uses the amplitude of the oscillation of the cantilever as a feedback parameter, giving always a higher value of the z parameter. In the case of graphene, when measuring with this procedure the usual measured height value is 1 nm when a realistic data should not be more than 0.25-0.3 nm. The reason why has been measured by using this feedback parameter relies in the necessity of preserving the tip.

- **Raman spectroscopy mapping**

Raman spectroscopy mapping was performed in order to check the quality and the homogeneity of the transferred graphene layer. ***Figure 4.5*** shows three images corresponding to the same area but each image is the integrated signal within a defined band of wavenumbers. The results allow to compare the space distribution of the D, G and 2D peaks. For example, the ***figure 4.5a***, corresponding to the D peak, was obtained by integrating intensity values between 1330 and 1370 cm^{-1}. The same procedure was employed for the G and 2D peaks, shown in ***figures 4.5b and c*** respectively. From the Raman mapping can be seen that the sample has a considerable density of holes. ***Figure 4.5d*** shows the average spectrum of the whole region. The data exhibits a narrow and symmetric 2D peak located at

2695 cm^{-1}, being the most intense signal and 2 times more intense that the G peak. The areas were graphene is detected correspond to single layer graphene, as expected. The intensity of the defect peak D, located at 1353 cm^{-1}, indicates an important defect density that can be caused both by the structural defects generated in the layer due to the transfer process and by the rest of contaminants shown in the AFM image of ***figure 4.4***.

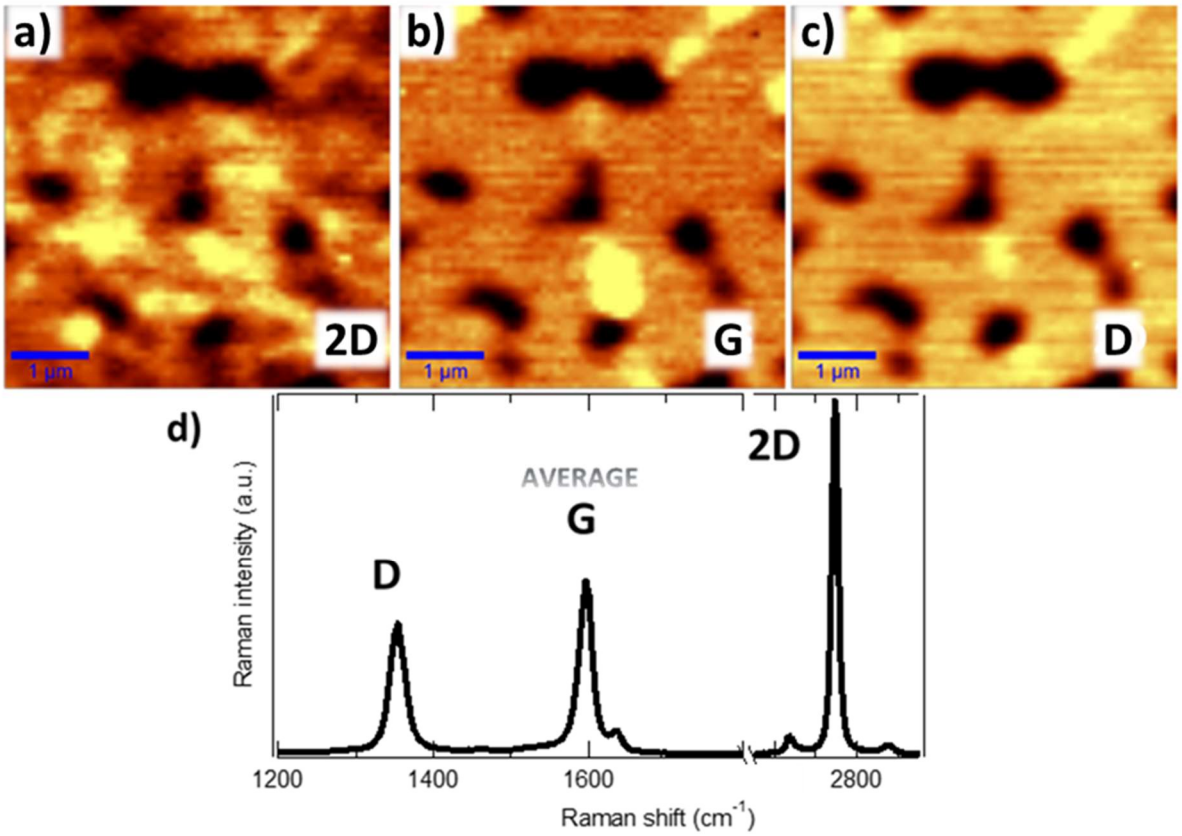

Figure 4.5*. Raman spectroscopy maps of the same region, 5 x 5 µm², centered in each characteristic peak of graphene: a) around the D peak, b) the G peak and c) the 2D peak. d) Average Raman spectrum of this 5 x 5 µm² scanned area.*

The Raman spectroscopy show some holes in the graphene layer that would affect the conductance of the layer due to the decrease of conducting area. This issue added to the contamination still present in the layer and the additional wrinkles formed in the transfer process compromises the electronic properties performance.

- **Room and low temperature magnetotransport measurements**

A preliminary determination of the transport properties of graphene on SiO_2 transferred samples was performed. Thus, to evaluate the efficiency of the transfer process, room and low temperature (2K) measurements were done employing the Van der Pauw configuration [115]. This geometry consists of four terminals at the edge of the sample, where resistivity and Hall effect measurements are easily measured by choosing adequately the channels for the excitation current and the measured voltage. These measurements were carried out in a commercial PPMS (Physical Properties Measurements System) from Quantum Design.

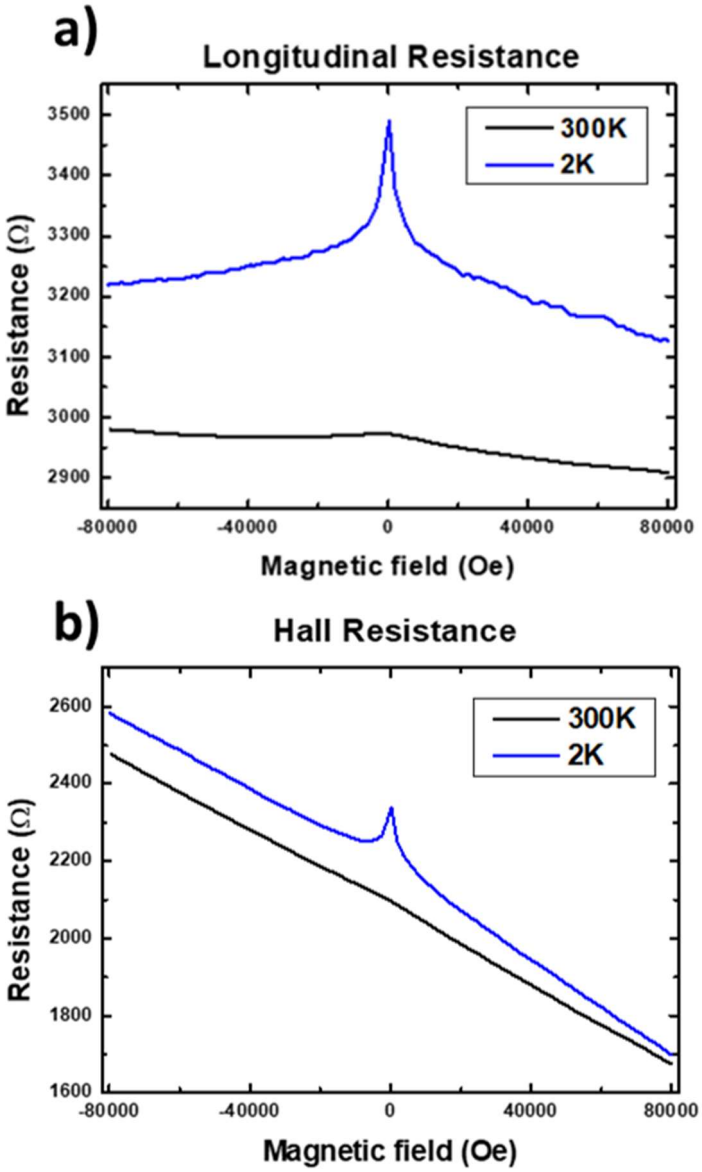

***Figure 4.6**. Electrical measurements at RT (blue curve) and 2K (black curve). a) Resistivity measurements in a Van der Pauw configuration. b) Hall resistance. The peaks observed at zero magnetic field at low temperature belong to the Anti-Localization scattering that increases the resistivity at zero fields*.

From the measurements of the resistance and the Hall resistance, an estimate to the values of the carrier concentration and mobility can be achieved. Taking into account the configuration employed for the measurements (terminal positions for the excitation currents and measured voltages) in the laboratory, and the asymmetry in the magnetoresistances (if the Dirac point is in the Fermi level, both magnetoresistances, the longitudinal and transversal or Hall would be symmetric with respect the ordinate axis), a hole type (positive charge carrier) conductance was observed. This is in disagreement with ARPES measurements as shown in the previous chapter for non-transferred samples. Therefore, it must be concluded that the transfer method altered the graphene layer with an uncontrolled doping, possibly provided by the polymer employed as supporting layer (PMMA) or due to charge impurities in the target substrate. Nevertheless, the calculated values for the carrier concentration and their mobility were acceptable. For this calculation, in absence of applied gate voltage, the following equations were applied [116]:

$$\boldsymbol{n_h = [e\left(\frac{dR_{Hall}}{dB}\right)]^{-1}} \qquad \textbf{(2)} \qquad\qquad \boldsymbol{\mu_h = \frac{L}{W}(en_hR_{xx})^{-1}} \qquad \textbf{(3)}$$

Where, in equation (2), e is the charge of the electron, R_{Hall} is the transversal resistance measured in the Hall configuration and B is the magnetic field. On the other hand, in equation (3), L is the length and W the width of the sample, e is again the charge of the electron, n_h is the hole concentration calculated in (2) and R_{xx} is the longitudinal resistance, related to the sheet resistance.

The values obtained from the resistance data shown in ***figure 4.6*** at 300 K, are:

$$\boldsymbol{n = 1.25.e^{13}cm^{-2}} \qquad\qquad \boldsymbol{\mu = 1441\ \frac{cm^2}{SV}}$$

Following the approach presented in [116], the values obtained for 2 K are:

$$\boldsymbol{n = 1.13.e^{13}cm^{-2}} \qquad\qquad \boldsymbol{\mu = 1333\ \frac{cm^2}{SV}}$$

From those data, it is evident that carrier concentration and mobility values at low temperatures, 2 K, are similar to the ones at RT. Besides, the mobility of the carriers obtained for the PVD transferred graphene is of the order of those established for silicon [117]. In view of the high quality of the graphene layer grown on copper by PVD, improved preliminary electrical results were expected. Presumably, the problems manifested during the transfer process might be the responsible for these moderate values. Moreover, the samples were measured in a Van der Pauw configuration [115]. One of the requirements to measure with this configuration relays on the absence of discontinuities of the sample under study. Due to

the presence of some holes, as determined by the optical microscope and the AFM measurements, these measurements are not conclusive, but only bring some insight on the potential electrical properties of the transferred samples. Nonetheless, the peak that appears at low temperatures (***figure 4.6***, black curve) at low magnetic fields is a manifestation of the quantum correction to the resistivity arising from weak localization. This reveals that the quality of graphene has not been completely degraded with the transfer process and that quantum interference effects are still present over regions with a characteristic coherence length of tens of nanometers, according to the relation [118]:

$$L = \frac{1}{2}\sqrt{\frac{B\hbar}{e}} \qquad (4)$$

Where L is the coherence length, B is the FWHM of the peak at low fields, $\hbar$ is the reduced Planck constant and e is the charge of the electron.

4.2.4 Conclusions on the transfer process of PVD graphene

The results of chapter 3 evidenced a noticeable contamination control achieved by the graphene growth method based on PVD using C_{60} in UHV as well as a lack of multilayer domains. These attributes should be used as an advantage to obtain excellent transport properties for the graphene layer. On the other hand, the transfer of the graphene layer has been proven to be not completely successful and the characterization of the resulting system supports this idea. In fact, the transport results of graphene/SiO_2, shown in the magnetotransport measurement section, indicate only acceptable charge carrier mobility. The outstanding transport values expected for graphene could not be reached due to the inefficient transfer process, which is probably due to the notable coupling of the graphene layer with the copper substrate underneath. Looking back briefly to the chapter 3 results, the reader shall remember the two spectra (red and black) shown in ***figure 3.12***, where the signal of the aged sample was much greater than the signal from the fresh one. At that stage, the concern of a graphene layer electronically coupled to the copper substrate, due to the ultra-pure interface obtained in the growth, was taken into account. As time went by, the Raman signal enhanced due to the intercalation of chemical compounds present in air. So, the need of a controlled intercalation of some chemical specie in between the graphene layer and the copper substrate, to decouple them for accomplishing a more effective transfer process, was contemplated. The next section of this chapter points in that direction, presenting two different ways of graphene layer decoupling under controlled processes.

4.3 Intercalation for the decoupling of graphene/copper interface

With the aim of achieving a favorable transfer process, we have revised the previously investigated decoupling methods of the Gr/substrate systems performed via intercalation of different elements underneath the graphene layer [119,120]. Although the methodologies are several, they can be divided in two groups: those following a chemical approach and those with a physical approach. Decoupling graphene by chemical methods consists in intercalating chemical species (atoms/molecules) by an electrolysis process while the physical approach consists in intercalating different type of light atoms in ultra high vacuum conditions. In this work we have explored two different strategies for graphene decoupling, each of them belonging to one of the approaches mentioned above: on one hand the electrolytic intercalation of a large molecule, tetraoctylammonium (TOA^+) based on the tetraoctylammonium bromide molecule (TOABr), and on the other hand, the intercalation of oxygen in ultra high vacuum conditions.

4.3.1 Approach I: TOA intercalation via electrochemical reaction

The TOA intercalation method was carried out in the laboratory of Prof. Osterwalder (Universität Zürich) applying a methodology previously reported [121]. This intercalation procedure follows a 3-electrode electrochemical procedure that requires the use of a potentiostat to ensure a precise control on the bias applied between working and reference electrodes.

- **TOA intercalation method**

The electrochemical cell was configured as schematically shown in ***figure 4.7a***. The sample (Gr/polycrystalline Cu) acts as the working electrode. A silver wire was used as a reference electrode, while the counter electrode was a platinum wire. The working and the reference electrodes should be facing each other and placed as close as possible. The counter electrode should be facing the working electrode, with the reference one in between. The electrodes should be immersed in such a way that the exposed area is as large as possible.

The electrochemical bath was prepared using a concentration of 0.1 M of TOABr in 20 ml of acetonitrile solution. The solution was homogenized with a stirring magnet and an argon flow

was put inside the solution for 15 minutes with a capillary tube in order to degas the solution (to take away the oxygen that could get trapped due to the stirring) (see ***figure 4.7b***).

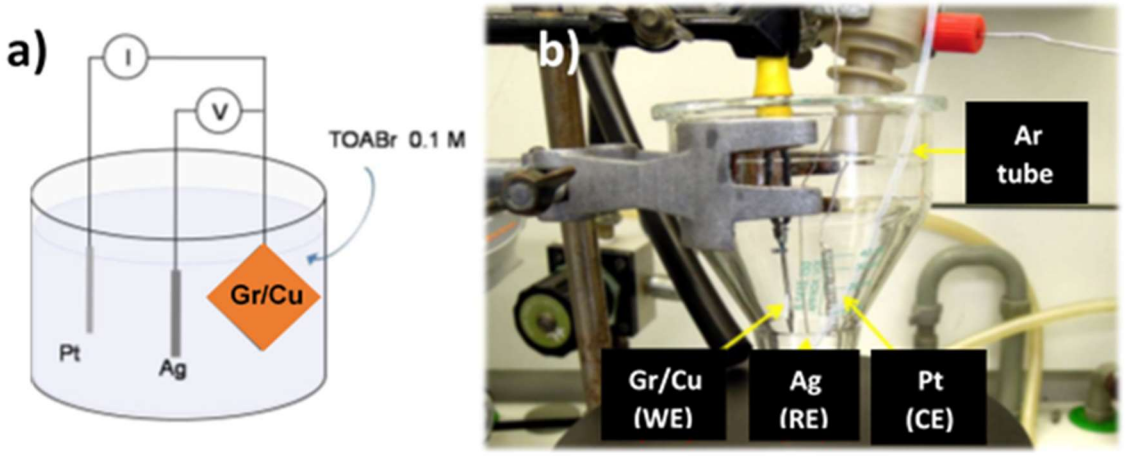

Figure 4.7. *a) Schematic view of the electrochemical cell. b) Image of the electrochemical cell, identifying the active subjects involved in the process. The argon tube is placed at the bottom in order to degas the solution. Scheme and picture courtesy of E. Miniussi (Universität Zürich).*

Once the solution was degassed with the electrodes in the corresponding position, the argon tube was maintained with a minimum flow right above the solution, to create a protective atmosphere over the solution that prevents air dissolution in the electrolytic bath.

The intercalation was carried out at a fixed voltage of -1.9 V versus Pt between the reference and the working electrodes yielding Gr/TOA/Cu. When the TOA intercalation procedure was over, the three electrodes were rinsed with acetonitrile and the sample (working electrode) was dried in a nitrogen atmosphere. Once the TOA intercalation was accomplished, the next step was the transfer process on a SiO_2 sample following the electrochemical delamination method described in section 4.2.2, which involved the spin-coating using PMMA as supporting layer (section 4.2.1).

- **Transferred graphene layer characterization**

After the TOA intercalated samples were transferred, they were characterized with an optical microscope and Raman spectroscopy for determining whether this methodology improves the transfer process.

For a comparison between the graphene transferred samples using the TOA intercalation method and the as-grown graphene transferred ones, optical microscopy images of both samples were acquired. It is important to remark that both graphene layers were transferred in the same electrochemical bath in a time lapse of minutes. The graphene growth for both samples was carried out in the same vacuum chamber under the same conditions. The time lapse between the graphen growth of both samples was two days.

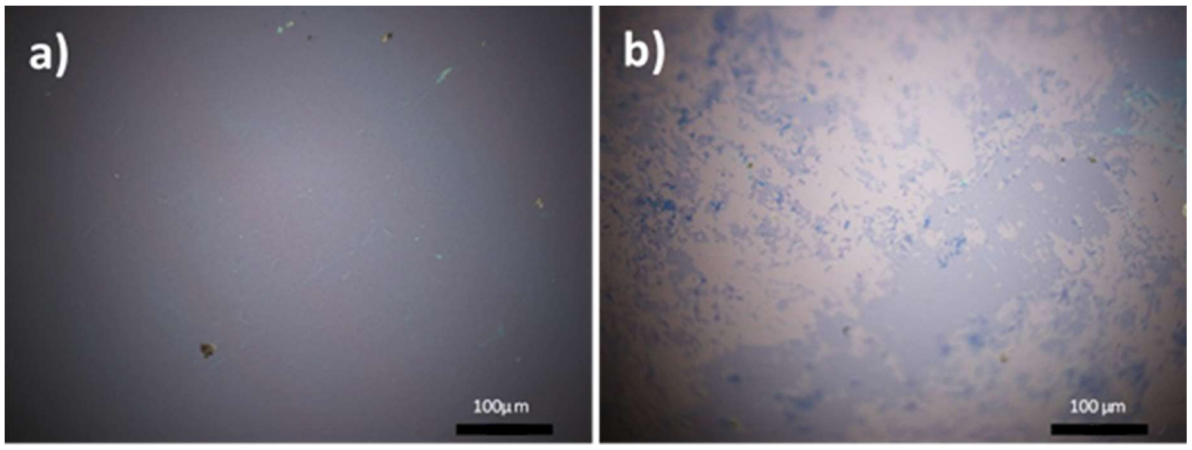

***Figure 4.8**. Optical microscopy images of two graphene/SiO_2 samples. The graphene layers were transferred from polycrystalline copper substrates, a) using a previously TOA-intercalated sample (Gr/TOA/Cu) and b) using an as-grown Gr/Cu sample. Both images were acquired with an 100x objective lens.*

At a first sight, there is an important difference between graphene transferred on SiO_2 samples from a previously TOA-intercalated sample (***figure 4.8a***) and from an as-grown sample (***figure 4.8b***). ***Figure 4.8*** shows cracks in the graphene layer for both cases, but the TOA-intercalated one shows a much higher continuity all over the surface. The improvement that the intercalation of this molecule provides is evident, at least in the continuity of the layer.

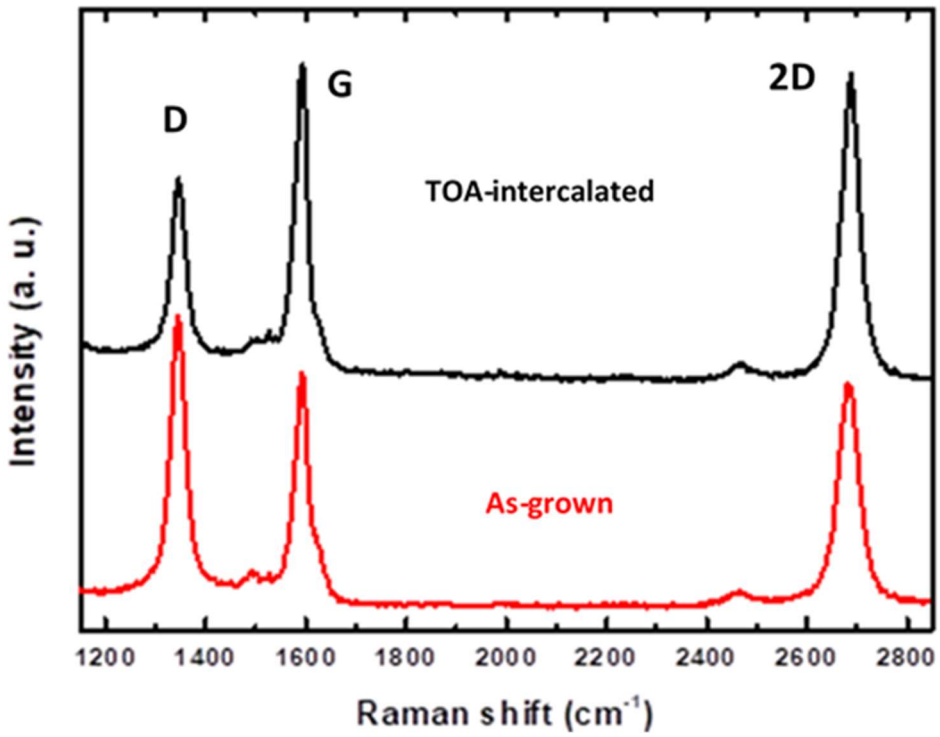

***Figure 4.9**. Raman spectra of two graphene/SiO_2 samples. The transferred graphene layers were previously grown on copper foil. The black spectrum corresponds to a sample where TOA+ ions were intercalated prior to transfer, while the red spectrum corresponds to a sample where the graphene layer was transferred with no previous treatment.*

The comparison between the Raman spectra after the transfer process to SiO_2 of a TOA-intercalated sample and of an as-grown sample is represented in ***figure 4.9***. Although both spectra present an intense defect peak (D), the corresponding to the transferred sample with a previous TOA-intercalation presents the smallest intensity for this signal. The 2D peak as well is more intense and sharper in the TOA-intercalated case than in the as-grown one. In ***table 4.1*** the most relevant values of the spectra are depicted, evidencing a better result for the graphene transferred after a previous TOA^+ ions intercalation process.

As-grown	Peak position (cm^{-1})	Integrated intensity	FWHM (cm^{-1})
D	1345	67234	31.4
G	1591	55146	32.7
2D	2683	76607	44.2
TOA-intercalated	**Peak position (cm^{-1})**	**Integrated intensity**	**FWHM (cm^{-1})**
D	1346	39557	29.3
G	1591	64908	28
2D	2687	90574	38.9

***Table 4.1**. Values of the different peaks for both spectra of **figure 4.9** (black and red). The integrated intensity of the defect peak is 1.7 times larger for the as-grown transferred sample than for the one previously treated with TOA, while the position of the peaks is the same. In addition, the 2D peak is 1.2 times more intense and sharper in the black spectrum (TOA-intercalated). The intensity relation between the 2D and the G peak remains the same for both samples, $I_{2D}/I_G = 1.4$.*

The parameters of ***table 4.1*** evidence an improvement of the transfer process by the TOA-intercalation, with a 2D peak sharper and more intense, and a defect peak smaller than in the direct transfer from an as-grown sample. Attending to the position of the peaks, there are no shifts in energy from one to the other samples suggesting that the strain and doping effects, are diminished when the graphene is transferred from the copper substrate, and thus, suggesting that the main effects were produced by the copper substrate used for the growth (this effect is shown in ***figure 3.17*** of the previous chapter).

4.3.2 Approach II: oxygen intercalation in UHV

The growth of graphene on different transition metals has brought many advantages (control of growth size and rates, scalability, …) but has also shown some drawbacks, being the most important one the impossibility to take advantage of the fancy electronic properties graphene exhibits, due to the short-circuit the underlying metal supposes. Thus, to overcome this drawback the scientific community is making a huge effort to work in this direction. The goal is

to isolate the graphene layer that has been grown on a metal with the aim of recovering the free-standing graphene electronic properties.

For this purpose, many works have been reported on the decoupling of graphene from strongly interacting substrates such as iridium, ruthenium or rhodium among others [35–38]. In those cases, the method used to decouple the graphene is the intercalation. However, there are different chemical elements that have been used with this purpose (hydrogen, oxygen, gold, cesium…) [40–43], using different substrates and by applying different techniques (intercalation in UHV, electrochemical intercalation…) [119,120]. In fact, the results obtained by intercalating different elements underneath the graphene layer suggests that the process can tune completely the electronic properties of the system, ranging from getting graphene with a strong n-type doping to a strong p-type doping [36].

On the other hand, there are also some previous studies on the effects of the oxidation and corrosion of copper underneath the CVD grown graphene layer for short and also long-term regimes [99,122,123] and under various environmental conditions [124], as well as studies on the role of oxygen on the growth mechanism of graphene on copper [125]. Moreover, oxygen intercalation has been widely studied in Gr/Ru(0001) [39,40,119,126–131] and it has been also investigated in the Gr/Ir(111) [37], Gr/Pt [132,133] and Gr/Rh [134] systems. Concerning Cu substrates, the oxygen intercalation for the Gr/Cu(100) interface was performed by exposing the sample to ambient conditions, while this process was not succeeded for the Cu(111) surface [135]. The reason was attributed to a stronger interaction of the graphene layer with this Cu surface in comparison with the Cu (100) and Cu (110) faces [136][124]. In the case of graphene on copper foils, the oxygen intercalation again was achieved by exposing the sample to ambient conditions [124,137].

4.3.2.1 Oxygen intercalation method

As it has been detailed in the previous chapter, graphene samples were grown in UHV environment on different type of polycrystalline copper substrates. For the oxygen intercalation process in addition to polycrystalline copper foils, graphene has been also grown on Cu (111) and Cu (100) oriented single crystals. The single crystals study was added to the polycrystalline substrates cases to help in the determination of the optimal conditions for the oxygen intercalation by means of LEED, as it will be shown below.

.

The oxygen intercalation was carried out in the same chamber used for the graphene growth. After checking with LEED patterns the graphene formation, samples were exposed to a controlled dose of molecular oxygen by means of a leak valve. The optimal temperature for the intercalation process was determined by testing different samples. In all cases the oxygen dose was the same, 20 KL (where 1 L is 10^{-6} Torr s). LEED patterns and XPS spectra were used to determine the optimal dose and intercalating temperature. Five different temperatures were explored: 280°C, 350°C, 400°C, 500°C and 550°C. Based on XPS data, the onset of graphene etching was observed at 550°C and the temperature for a most efficient intercalation was determined as 500°C. In this case, the temperature was monitored with a K-type thermocouple attached to the heater. In order to avoid the oxygen desorption from the samples, when finishing the intercalation procedure, the oxygen pressure was kept until the sample was cooled down to RT.

After oxygen intercalation, an exhaustive characterization was made in order to understand the mechanism of the process, which was studied by means of LEED patterns, XPS and Raman spectroscopy. In addition, AFM measurements were performed for both topographic and surface potential measurements.

4.3.2.2 Oxygen intercalation in Gr/Cu(100) and Gr/Cu(111)

A first study of the oxygen intercalation was performed in single crystals. The employed facets were the Cu(100) and the Cu(111). The main objective was to have a first approach of the conditions needed for the intercalation (temperature and dose) in order to be able to extrapolate them to the polycrystalline copper foils. To address this issue, a fast and reliable feedback based on the LEED patterns was needed. As on polycrystalline samples differently oriented grains contribute with different spots to the LEED pattern without possibility of accurate identification, the utilization of single crystals was mandatory. For the LEED characterization, Cu(100) was employed as it was the surface where the oxygen reconstruction was most clearly visible.

- **LEED**

As an example, ***figures 4.10a and d*** show the LEED pattern for the Cu (100) surface, where bright spots can be observed with a dark background confirming the cleanness of the

substrate. Once assured the substrate was in optimal conditions, graphene was grown on top by using C_{60} molecules following the procedure explained in the previous chapter. LEED measurements were used again to check this growth as shown in ***figures 4.10b and e***. The red arrows mark some of the spots corresponding to copper, while the orange arrows indicate the graphene ring. This ring corresponds to the polycrystalline growth of graphene where the observed modulation evidences again a not totally random orientation of the carbon layer, but the existence of preferred orientations [138]. The polycrystalline growth of graphene on the Cu (100) single crystal points to a smaller interaction compared to other substrates such as iridium or ruthenium where the graphene layer grows with one principal moiré, evidencing a strong interaction with the substrate, comparable to the one existing between layers of graphite [35], although the interaction of graphene in our system, based on the use of C_{60} as a precursor molecule, is not negligible as shown in chapter 3 [111]. A similar graphene ring was observed when using the Cu (111) single crystal as substrate or the Cu polycrystalline foil (shown in chapter 3).

The subsequent intercalation of the oxygen on the graphene/Cu (100) single crystal was also monitored by LEED. Thus, after the growth, the sample was annealed at 500°C while it was exposed to 20KL of oxygen. The resulting LEED patterns are shown in ***figures 4.10c and f***. In addition to the spots corresponding to the Cu (100) substrate (red arrows) and the graphene ring (marked with orange arrows) these two LEED patterns show the appearance of new spots (some of them marked with green arrows) not observed before exposing to oxygen. These new spots correspond to a surface reconstruction that intercalated oxygen forms on the surface of the copper and that is known to occur in absence of graphene [138]. The oxygen is dissociated and adsorbed forming a 4 x 4 reconstruction.

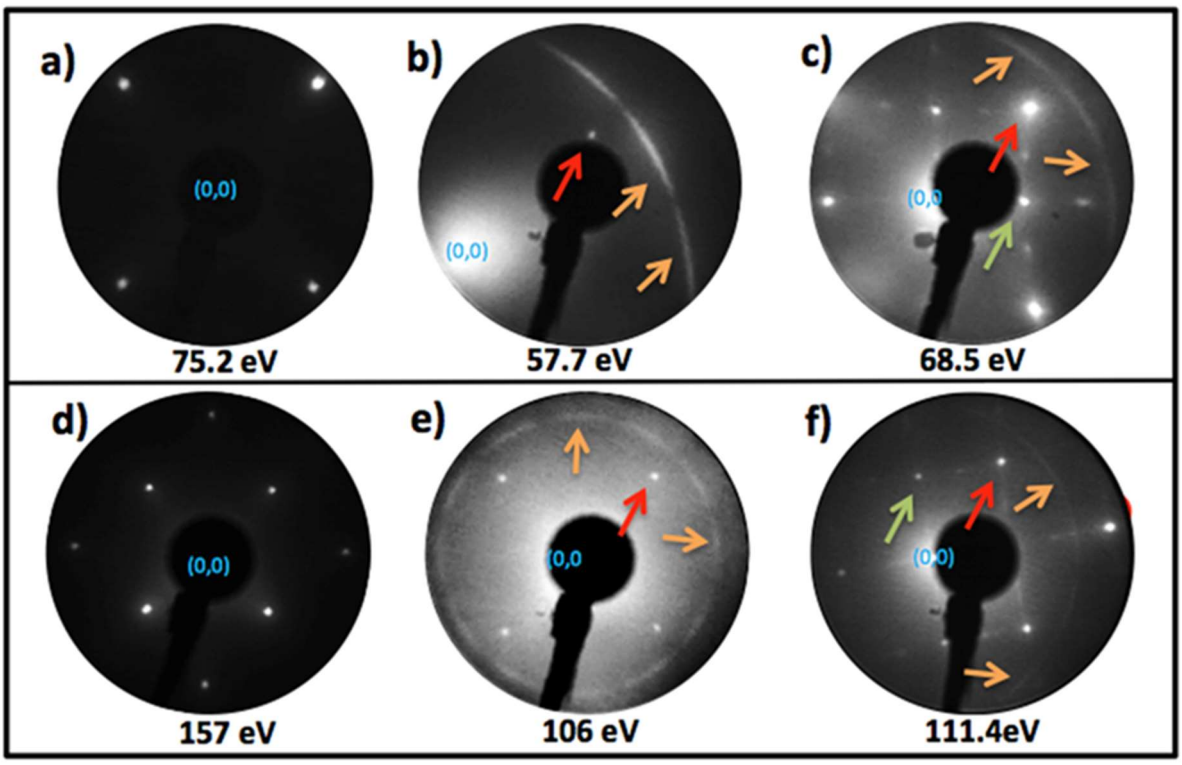

***Figure 4.10**. LEED patterns acquired at different energies and different stages of the intercalation process. The red arrow indicates the copper, the green the oxygen reconstruction and the orange arrows the graphene. The left panel (a and d) corresponds to bare Cu (100) surface, the middle panel (b and e) to the graphene on top of the copper and the right panel (d and f) to the oxygen intercalated between the graphene and the copper. In the last one, it can be observed the formation of a 4 x 4 superstructure due to the oxygen adsorption.*

- **AFM**

After the LEED experiments, the surface morphology of the graphene/Cu sample was characterized by AFM both, prior and after oxygen intercalation. ***Figure 4.11*** and ***figure 4.12*** show topographic images acquired prior to graphene growth, after growth and after the already mentioned oxygen intercalation process for Cu (100) and Cu (111), respectively. ***Figure 4.11a*** shows an AFM image of the surface of Cu (100) after cleaning under UHV conditions following the procedure explained in chapter 3. The surface appears flat, with terraces apparently of the order of microns. However, as atomic steps could not be resolved we cannot accurately establish the size of the atomically flat terraces. Presumably they are of the order of hundreds of nm, i.e., comparable to the sizes found in polycrystalline copper foils, shown in chapter 3. On the other hand, ***Figure 4.11b*** exhibits an AFM image of graphene on the Cu (100) substrate. The layer is not complete, some bare copper islands are still visible. It is interesting to observe that the shape of the copper surface changes after the graphene growth, presumably due to the interaction of the fullerenes with the copper atoms, at it has been

previously observed in the case of Pt [26]. ***Figure 4.11c*** shows an AFM image of graphene on copper with intercalated oxygen. Above the green line drawn in the image (right upper corner), the surface is very similar to the one belonging to the covered zones of **figure 4.11b**, suggesting that oxygen has not been intercalated in that zone. The area below the green line instead, appears with a different morphology, and there the terraces are smaller. In this region there are also visible wrinkles that maybe produced by the morphology change of the surface below. ***Figure 4.11d*** represents in more detail the area marked with the black square in ***figure 4.11c***. The blue circle highlights an uncovered zone, similar to those highlighted in ***figure 4.11b***.

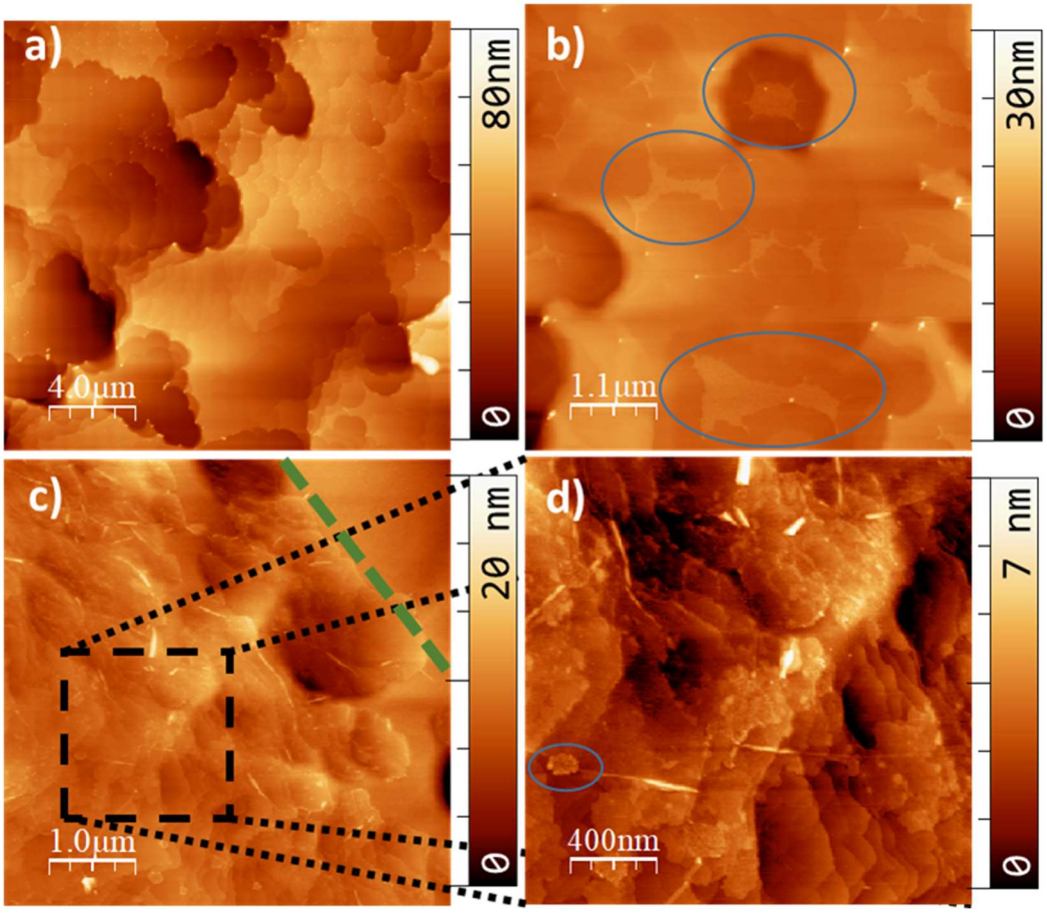

Figure 4.11 *AFM topographic images acquired in dynamic mode showing a) the Cu (100) surface prior to graphene growth and b) after the growth with a partial coverage. The blue circles indicate some of the not covered regions. c) Image of the sample surface after oxygen intercalation. There are two zones separated by a green line. While the zone below the green line has smaller terraces and the surface seems rougher, the zone above the green line is very similar to the covered zones of image b. Oxygen has intercalated not in the whole area, but just until the green line. d) AFM image of the region highlighted in c. The blue circle shows up an uncovered zone similar to those shown in b.*

For the case of Cu (111), an AFM image of that surface prior to growth is shown in ***figure 4.12a***. The global morphology of the surface is very similar to the one shown in ***figure 4.11a*** for the Cu (100) case, with large terraces with irregular borders. Again, some residual contamination is observed in this image as well as in the next one, ***figure 4.12b***, that exhibits an incomplete graphene layer grown on the Cu(111) sample. In fact, those contamination points seem to act as nucleation points for the graphene growth, as can be seen in ***figure 4.12b***. A change in the morphology of the copper surface after growth can be inferred by observing the region underneath the graphene islands. On the other hand, an AFM image of a complete monolayer of graphene on Cu (111) is observed in ***figure4. 12c***. The wrinkle density is higher than in the Cu (100) face. The surface of the oxygen intercalated G/Cu sample as measured by AFM is shown in ***figure 4.12d***. The copper terraces are not visible, suggesting an efficient oxygen intercalation, while the wrinkles are visible, indicating in a first approach that the graphene layer has not been altered.

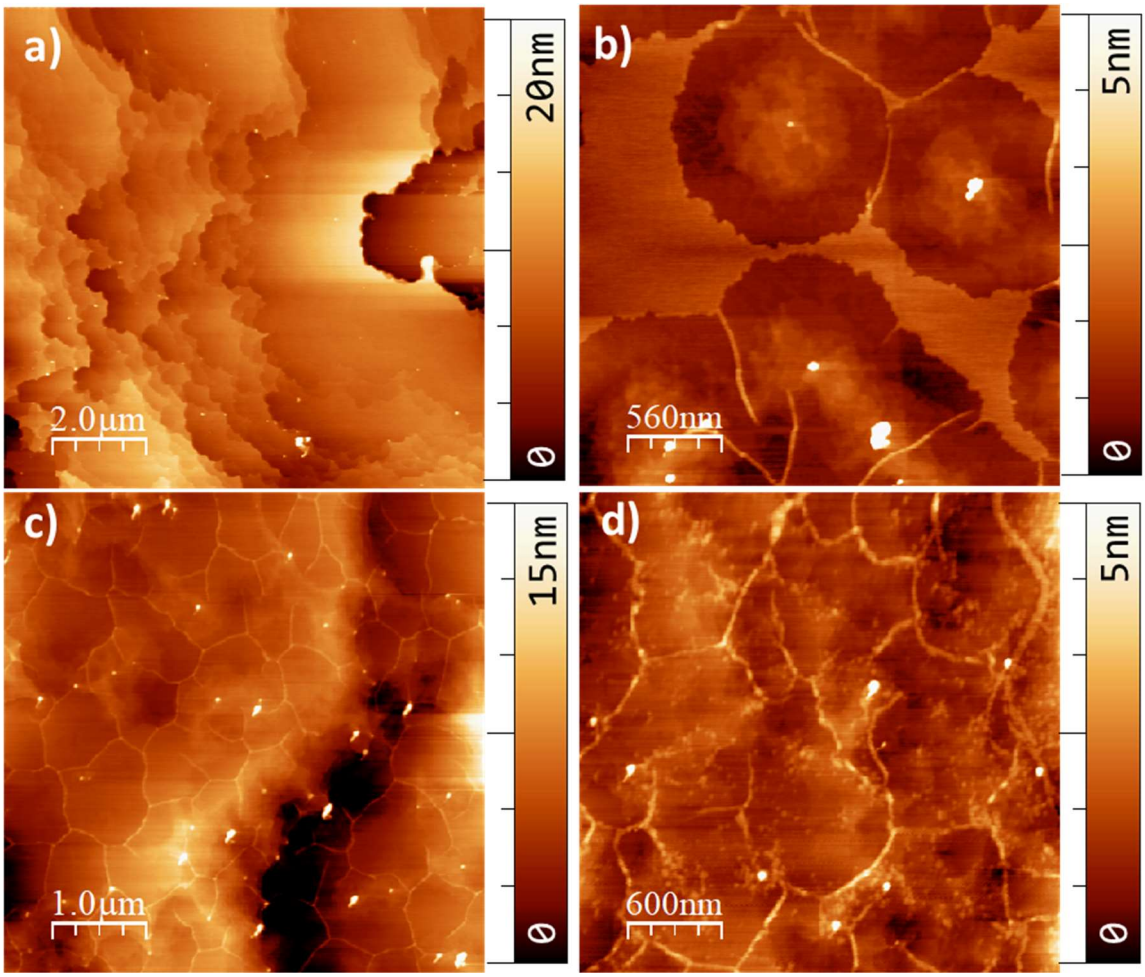

Figure 4.12*. AFM topographic images acquired in dynamic mode showing: a) the Cu (111) surface prior to growth, b) an intermediate stage of the graphene growth where not merged graphene islands can be seen, c) the complete graphene layer where the wrinkles cover the whole image and d) the Gr/Cu(111) system after the oxygen intercalation process.*

- **Raman spectroscopy mapping on Gr/Cu(100)**

With the aim of gaining some insights into the oxygen intercalation process, this method was applied to a partial graphene layer grown on the Cu(100) sample. Thus, figure 4.13 shows this partially grown graphene layer after the intercalation process as observed by optical microscopy. The oxygen intercalation was performed in a similar way as in the previous samples (20 KL, 300 ºC).

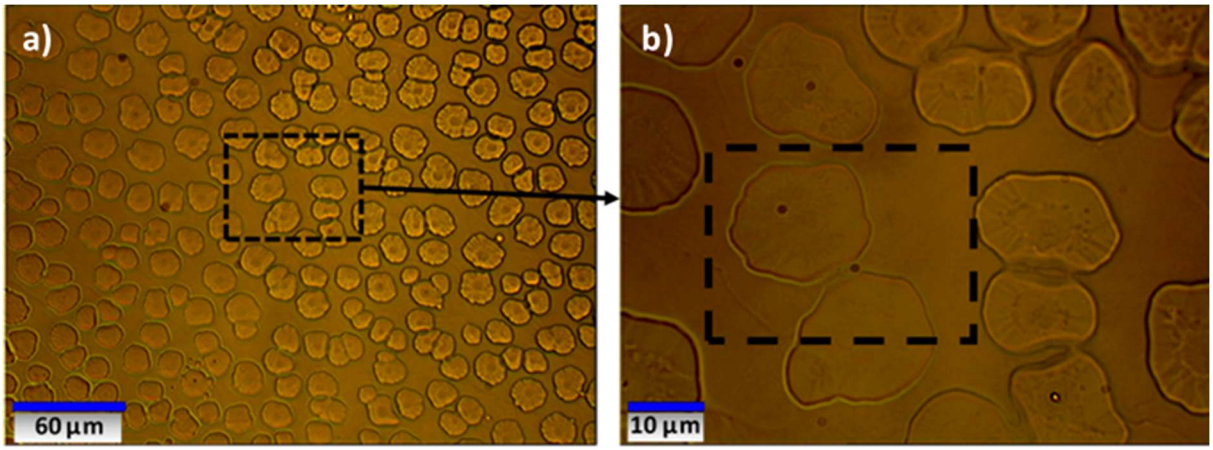

***Figure 4.13**. Optical images after oxygen intercalation of a) a half-covered graphene on Cu(100) surface where the differently oriented graphene grains are observed, with an estimated size larger than 10µm and b) zoom on the area marked in black in a).*

In the images, the nucleation points of graphene are observed, and the grain sizes are shown to be larger than 10 µm in diameter. After observing the AFM image of ***figure 4.12***, corresponding to the graphene on Cu(111) surface, the similarity in the shape of the grains is evident. However, for Cu(111) the sizes of the grains are around 1 µm while the graphene grown on Cu(100) has bigger single orientation domains. This fact was shown in the comparative work in ref. [139] where LEED studies of graphene on Cu(111) and on Cu(100) exhibited that the modulation of the graphene ring was higher for the Cu(100) sample. This result suggests more preferential orientations of the graphene layer on the Cu(100) surface, and thus, bigger single-orientation domains.

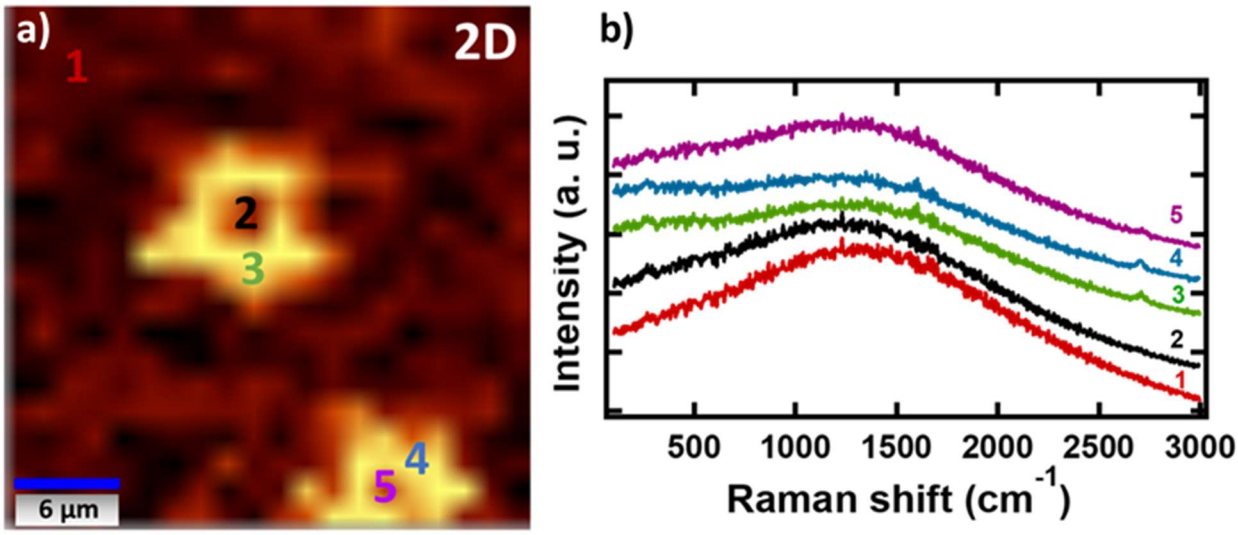

***Figure 4.14**. a) Raman spectroscopy mapping corresponding to the marked zone in figure 4.13b. b) Spectra acquired on different zones in a) where 1 is bare copper, 3 and 4 present a more intense 2D peak suggesting the oxygen intercalation while spectra 2 and 5, at the center of the patch, present an almost non-detectable signal, suggesting that the oxygen has not been intercalated in the central zone.*

The optical images shown in ***figure 4.13*** are correlated to the Raman spectroscopy mapping shown in ***figure 4.14***. The rectangle highlighted in ***figure 4.13b*** (the rectangle is a guide to the eye) represents the zone of the Raman map shown in ***figure 4.14a.*** The mapping is centered in the 2D band. The numbers in the image show the zone where the spectra shown in ***figure 4.14b*** were acquired. Thus, the spectra were taken in: a bare copper zone (spectrum 1), in the center of the graphene grain, where oxygen did not accede (spectrum 2), in the graphene grain where oxygen decoupled the graphene layer (spectra 3 and 4) and in the center of a graphene grain (spectrum 5). The spectra shown in ***figure 4.14b*** appear with the fluorescence of the copper due to the low signal-to-noise ratio, where a background subtraction would hide information. Spectra 3 and 4 show the most intense 2D band as it is also appreciated in the intensity of the map, while a very subtle 2D peak appears in spectra 5 and 2. Thus, the Raman mapping evidences that the oxygen starts the intercalation process at the boundaries of the graphene grains, penetrating towards the inner region. The 2D peak of the different zones reflects the decoupling process via the oxygen intercalation, in a similar way to that showed in chapter 3, where the 2D peak increased with ageing of the graphene grown sample. The Raman data also show an oxide peak at 360 cm^{-1} that appear in all spectra [140]. This peak, in 2 and 5 can be produced by the contribution of the area of the laser spot. For the spectra 3 and 4 is also observed a broad band at low intensities, from 0 to 600 cm^{-1} that could be related to air species located between graphene and substrate after oxygen has decoupled both of

them. Note that although the growth and intercalation process have taken place in UHV, Raman measurements were performed ex-situ at ambient conditions.

4.3.2.3 Oxygen intercalation in Gr/polycrystalline Cu foil

For the case of graphene on polycrystalline Cu foils, although LEED patterns were acquired as a first step prior and after the oxygen intercalation process, no useful information could be obtained, just due to the polycrystalline nature of the foils. As we already mentioned, the differently oriented grains of polycrystalline substrate make impossible the identification of new possible LEED spots due to the oxygen intercalation. Thus, for intercalating oxygen on Cu foils, the parameters that confirmed the oxygen intercalation process in the Cu single crystal cases will be also used (20 KL with the sample at 500°C).

- **AFM**

To study the influence of the oxygen intercalation on the graphene on Cu foils morpholophy, AFM images prior and after the process were acquired. Additionally, it is important to verify that there is not etching of the surface by exposing it to an oxygen atmosphere at these temperatures. ***Figure 4.15*** shows the graphene grown on polycrystalline copper foil, performed in the same way as explained in chapter 3 (***figure 4.15a***) and after the oxygen intercalation (20 KL with the sample at 500°C) (***figure 4.15b***). It is shown that the morphology of the graphene layer as well as that of the copper substrate remain unaltered.

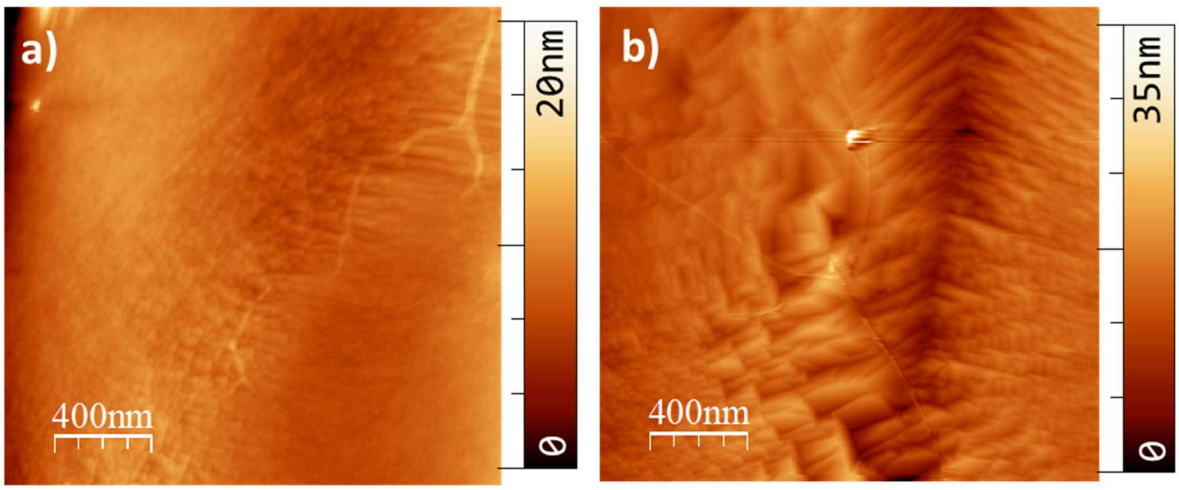

Figure 4.15*. AFM topographic image of (a) as-grown graphene on polycrystalline copper and (b) after oxygen intercalation (20 KL with the sample at 500°C). Graphene wrinkles are visible in both images, pointing to the preservation of the graphene layer.*

- **XPS**

Once observed by AFM that no etching was produced, and in order to understand the chemical processes involved in the intercalation process, a deep XPS study was carried out. The graphene grown on Cu foil was exposed to the same oxygen dose (20 KL) at different temperatures. The different stages were followed by XPS monitoring the C 1s, O 1s, and Cu 2p core levels. The spectra are labeled with the exposure temperature, starting at 280°C, and continuing upwards to 350°C, 400°C, 500°C and 550°C.

Figure 4.16 shows the XPS Cu 2p spectra at different temperatures. As it can be observed, no differences on the copper signal are detected by increasing the intercalation temperature. As it was already mentioned, the oxygen dose (20 KL) was the same for all temperatures. Since the spectral shapes as well as the peak positions present no changes upon annealing in the oxygen atmosphere, this would suggest that the intercalated oxygen is not forming any oxide species with the Cu atoms being in a physisorbed state.

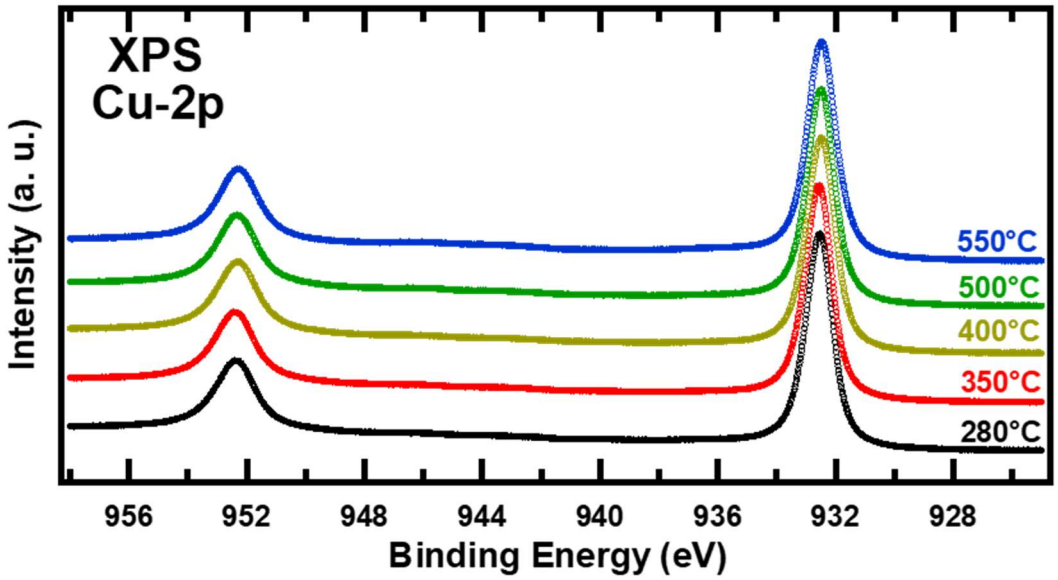

Figure 4.16*. Spectra centered in the Cu 2p core level where the corresponding doublet can be observed. The copper peaks remain unaltered while the intercalation temperature rises.*

Figure 4.17 shows the XPS C1s spectra as a function of the temperature upon oxygen exposure. The C1s subspectrum located at 284.21 eV, corresponding to the sp^2 emission was fitted using a Doniach and Sunjic function with asymmetry parameter of 0.068 [44]. A second subspectrum located at 284.81 eV was needed to get an optimal fitting of the experimental data and a Voigt curve was used in this case. This small peak is present from the beginning of the annealing process, suggesting a residual contribution of same CO species coming from the growth process. No new components appear by annealing at the different temperatures during the intercalation process pointing to a lack of chemical interaction between the graphene layer and the intercalated oxygen. The only change observed when increasing the temperature is related to the position of the sp^2 peak. There is a slight down shift in the binding energy (BE) for higher temperature, 0.08 eV for 400°C and 0.13 eV for 500°C. This shift in BE towards lower values would imply a hole-type doping tendency of the graphene layer with respect to the starting sample, as expounded by Michely et. al. [44]. Prior to the intercalation process, the graphene layer grown by the PVD method using C_{60} molecules as precursor shows a non-negligible interaction with the substrate that leads to a n-doping behavior, as it was previously reported [carbon]. The small shift in the BE observed after this intercalating process indicates that the oxygen atoms underneath the graphene layer decouple that layer, producing a change in the initial n-doping reducing slightly this n-doped behavior. On the other hand, the shift in energy observed in our system is much lower than the ones reported by Andersen et. al. [36] and the group of Michely [44]. However, it must be taken into account that the substrate in those cases, iridium, is different and its interaction with the graphene prior to intercalation is stronger than in the case of copper. For that reason, different BE values for the sp^2 emission would be expected. Upon further increasing the temperature, the onset for graphene etching was reached, at around 550°C. This temperature value for the graphene on copper etching is higher than in any other reported systems [141]. It has been already studied that the etching process of graphene with oxygen or hydrogen starts at the defects of the graphene layer [45]. Also, it has been demonstrated that the presence of a partial graphene layer diminishes the etching temperatures values [141]. In our case, the etching process occurs at a higher temperature (around 550°C) suggesting a low defect density and a uniformly covered single layer graphene. As it is shown in ***figure 4.17*** for 550°C, the carbon peak decreases considerably and shows a shift to a BE of 284.4 eV, suggesting the formation of volatile carbonaceous species that are desorbed under high vacuum conditions.

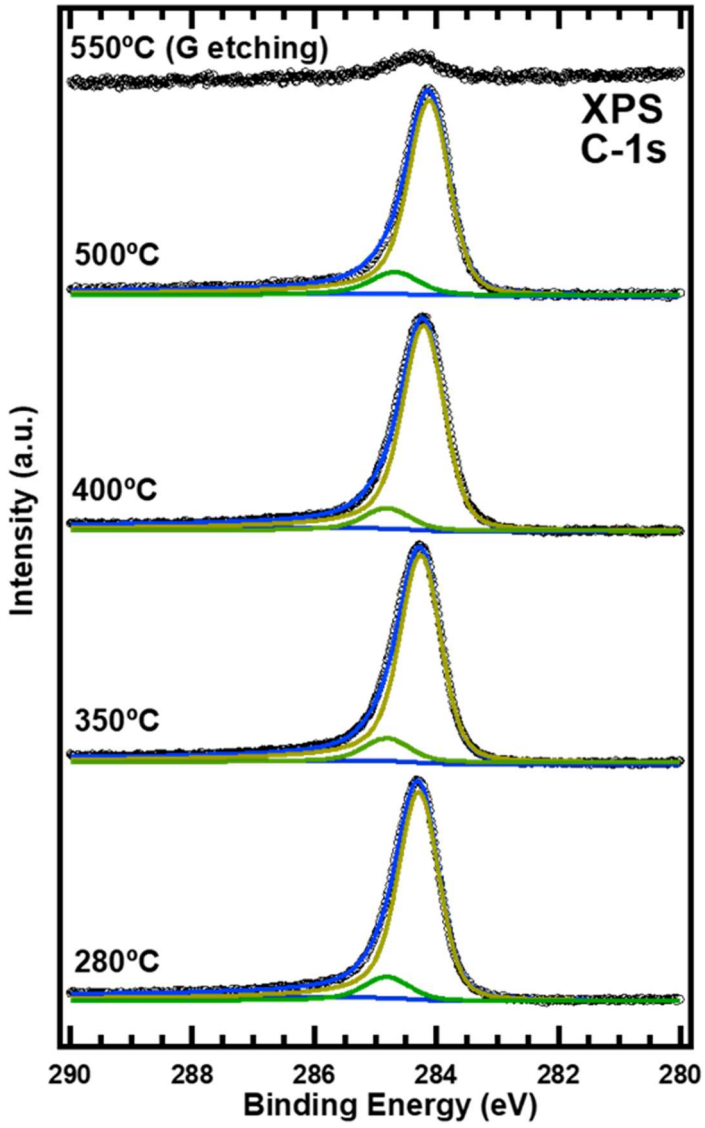

***Figure 4.17**. XPS spectra centered in the C 1s core level. Two subspectra are used for the fitting, which is represented by a dark blue line, with the peak corresponding to sp2 contribution appears in dark yellow, the component corresponding to sp3 contribution appears in green and the background in light blue. No additional components are observed while the intercalation becomes more effective, implying in a non-interacting oxygen intercalation. Black dots are the experimental data.*

Figure 4.18 shows the XPS O 1s spectra of the graphene/Cu foils system in oxygen atmosphere (20 KL) for the different temperatures. The fit of the curves was made by using Voigt profiles and two components contributing to the oxygen peak, located at 529.8 eV and 530.7 eV, were found. According to the literature, the subspectrum at higher binding energy would correspond to the presence of Cu_2O [142]. On the other hand, the peak at lower binding energy suggests the contribution of an atomic phase state, i. e. a low bound state [143], that would correspond to a physisorbed state. This latter increases strongly in intensity as the sample temperature increases. The lack of new peaks for the C 1s and Cu 2p signals for high

temperature values, confirm the presence of this atomic phase contribution. For the spectrum at 550°C, corresponding to the etching process, both components are shifted towards higher binding energies. This result is a consequence of the change in the chemical state of the oxygen at the surface during the attack process occurring around 550°C. The etching mechanism leads probably to the formation of some suboxides, which are different to the species that are present underneath the graphene layer for lower temperature values.

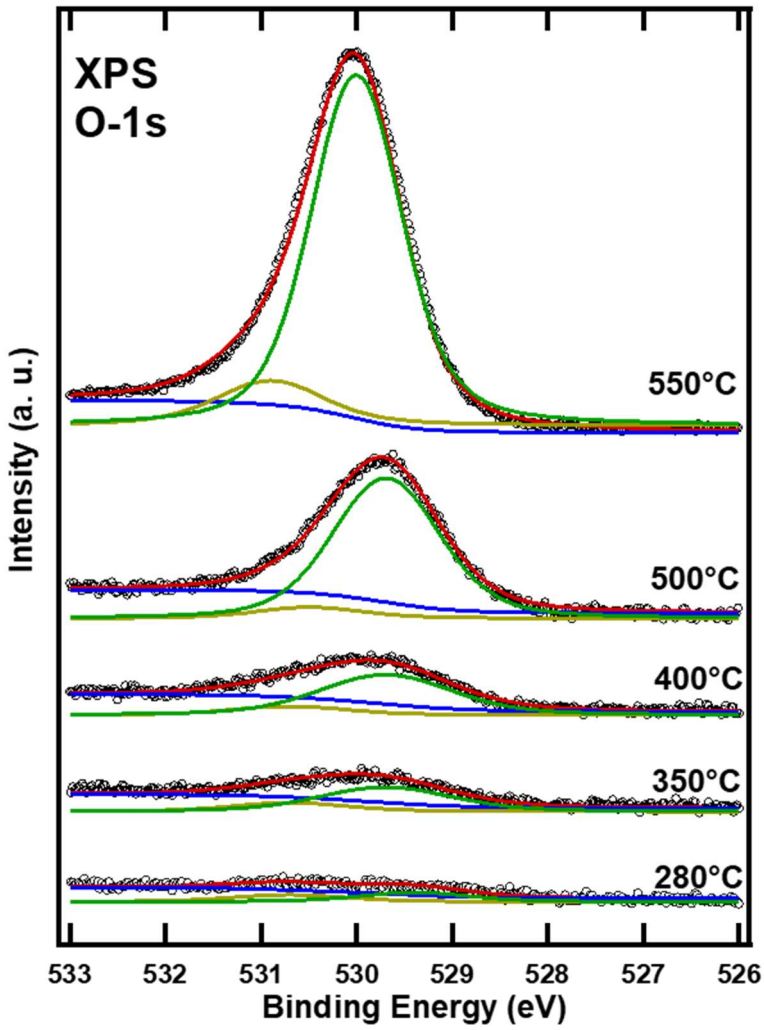

***Figure 4.18**. XPS O 1s spectra under controlled oxygen atmosphere for increasing sample temperatures. The last spectrum corresponds to the temperature at which the graphene has been etched. The experimental data are represented by open dots with two subspectra (green and dark yellow curves) resulting from the fit, which is denoted by the red curve. The blue curve corresponds to the background.*

On the other hand, the small component at high BE is visible during all the process, suggesting that it is not possible, even with the most controlled environment, to remove completely a minor contribution of copper oxide. However, the data suggests that it is the physisorbed oxygen contribution the responsible for the graphene/substrate decoupling.

- **Raman spectroscopy**

Raman spectroscopy measurements were carried out on this system with the aim of determining the oxygen intercalation influence on the graphene/substrate interaction. Thus, two Raman representative spectra are shown in ***figure 4.19***, corresponding to the as-grown graphene sample on Cu foil (black spectrum) and the graphene sample after oxygen intercalation (blue spectrum). It should be notice that both spectra belong to the same sample: half of the sample was put in UHV for the oxygen intercalation, while the other half was preserved as a reference. In the spectrum of the as-grown sample, the typical graphene peaks (D, G, 2D) are almost quenched due to the interaction of graphene with the substrate [34]. This phenomenon was already observed and discussed in chapter 3. ***Figure 4.19*** shows this effect, where the black spectrum exhibits a very low signal for D and G peaks, while the 2D peak is not observed. The spectrum after oxygen intercalation, however, shows the emergence of the 2D peak and a notorious enhancement of the G signal. ***Table 4.2*** collects some representative parameters extracted from the Raman data. These data indicate that the integrated intensity of the defect peak has slightly decreased, leading to the conclusion that the quality of graphene would not be affected by the intercalation. These Raman results confirm an effective intercalation, where it is observed an enhanced signal of the G and 2D graphene fingerprint peaks and a decrease of the graphene/copper interaction revealed by the sharpening of the D peak.

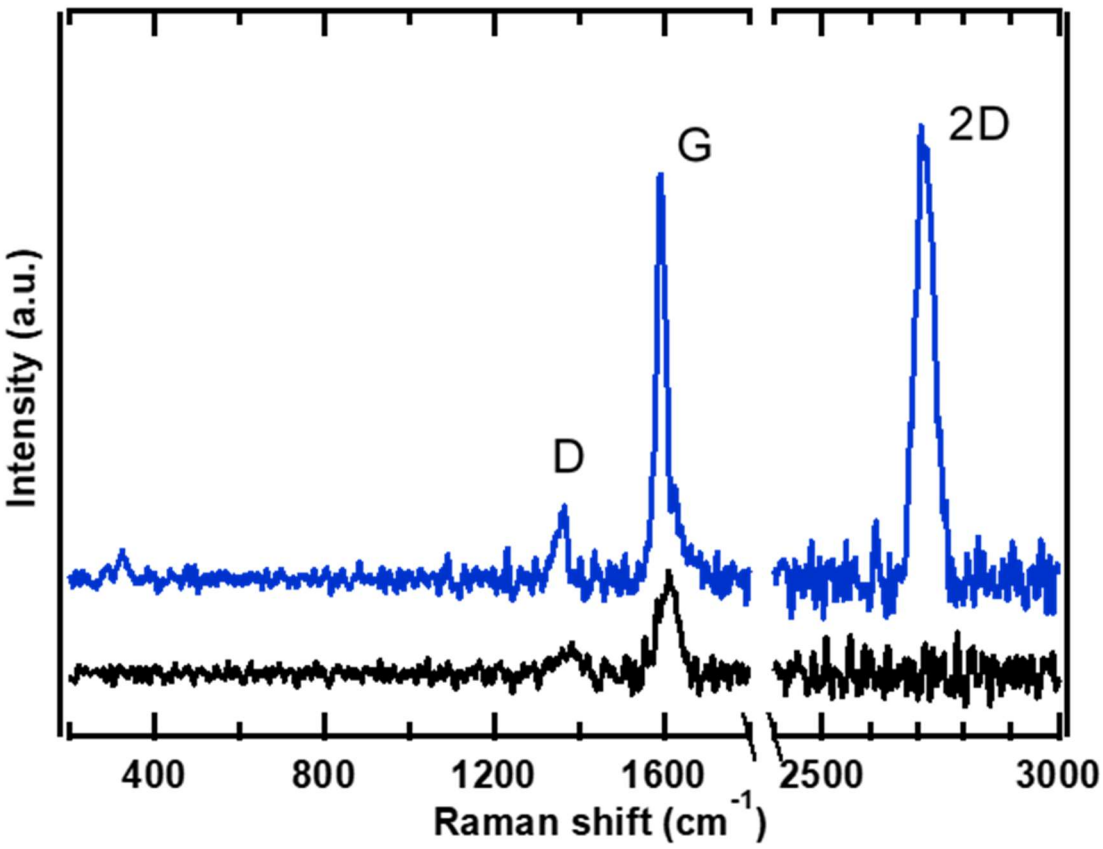

***Figure 4.19**. Raman spectra of as-grown (black) and oxygen-intercalated (blue) samples. Half of the sample was used as reference (black) while the other half was oxygen-intercalated (blue). Note the enhancement of the G and 2D peaks due to oxygen intercalation in the graphene/copper interface, as well as a small peak emergence related to Cu_2O at low energies (360 cm^{-1}).*

From ***table 4.2*** we can also see that the G and D peaks suffer an 18 cm^{-1} and 11 cm^{-1} shifts down in energy respectively. These displacements in energy can be ascribed to strain or to doping, or to a competition between both of them [69,70]. Previous works state that the decrease of the FWHM in G peak implies doping of graphene (n- or p-type) [144]. For hole-type doping, the position of the G peak decreases, increasing the position of the 2D peak. Attending to ***table 4.2***, a net hole-type doping of graphene after oxygen intercalation may occur. As we have already mentioned and determined previously in chapter 3, the graphene layer formed by using C_{60} as precursor in UHV conditions is n-doped [111]. Therefore, the oxygen intercalation would lead to a decoupling of the graphene layer from the substrate, decreasing the n-doping character of the layer. This result, concluded from the Raman experiments, is in nice agreement with the observed XPS shift towards lower values of the C-1s sp^2 component.

As-grown	Peak position (cm^{-1})	Integrated intensity	FWHM (cm^{-1})
D	1368.4	10930	66.3
G	1611.1	26867	46.5
2D	--	--	--
O-intercalated	**Peak position (cm^{-1})**	**Integrated intensity**	**FWHM (cm^{-1})**
D	1357.8	9149	26.4
G	1592.2	38804	20.1
2D	2716.8	97896	39.4

***Table 4.2**. Positions, integrated intensities and FWHM of the most relevant graphene peaks. Notorious shifts in peak positions are observed. The FWHM values narrow and the integrated intensity of the G peak increases sensitively with respect to the as-grown sample. The integrated intensity of the D peak is slightly smaller in the oxygen-intercalated sample.*

Finally, a small peak is observed at very low energies of the Raman spectrum after intercalating oxygen, around 360 cm^{-1}, corresponding to copper oxide species [140]. However, the small integrated intensity of this peak reveals a small contribution of oxygen. This result is in agreement with the observation in the XPS O 1s spectra of the small component at high BE and ascribed to copper oxide.

The Raman spectra of ***figure 4.19*** are two representative examples, but many others were acquired during these experiments. Thus, a statistical compendium of all of them, for graphene as-grown and oxygen intercalated samples, is shown in ***figure 4.20***. All as-grown graphene samples were split in two. One for measurements of as-grown samples and the other for oxyge measurements after the oxygen intercalation. In the same way as in chapter three, two plots are shown where in the first one (***figure 4.20a***) the positions of the 2D peak are related to the positions of the G peak, while the second one (***figure 4.20b)*** exhibits the full width of the G peak at its half maximum as a function of its position. Considering the study made by C. Casiraghi [145], the values show in both cases strained and slightly doped samples as compared to pristine graphene. Nevertheless, there is an evident relaxation in the case of oxygen-intercalated samples as can be inferred from the figure since the data for those samples appear in lower values for the ordinate and abzisa axes. In addition, it is important to note that there are more black dots than blue dots. This reflects the signal enhancement of the

Raman signal (specially for the 2D peak) as a direct consequence of the oxygen intercalation, confirming the decoupling effect that this procedure generates.

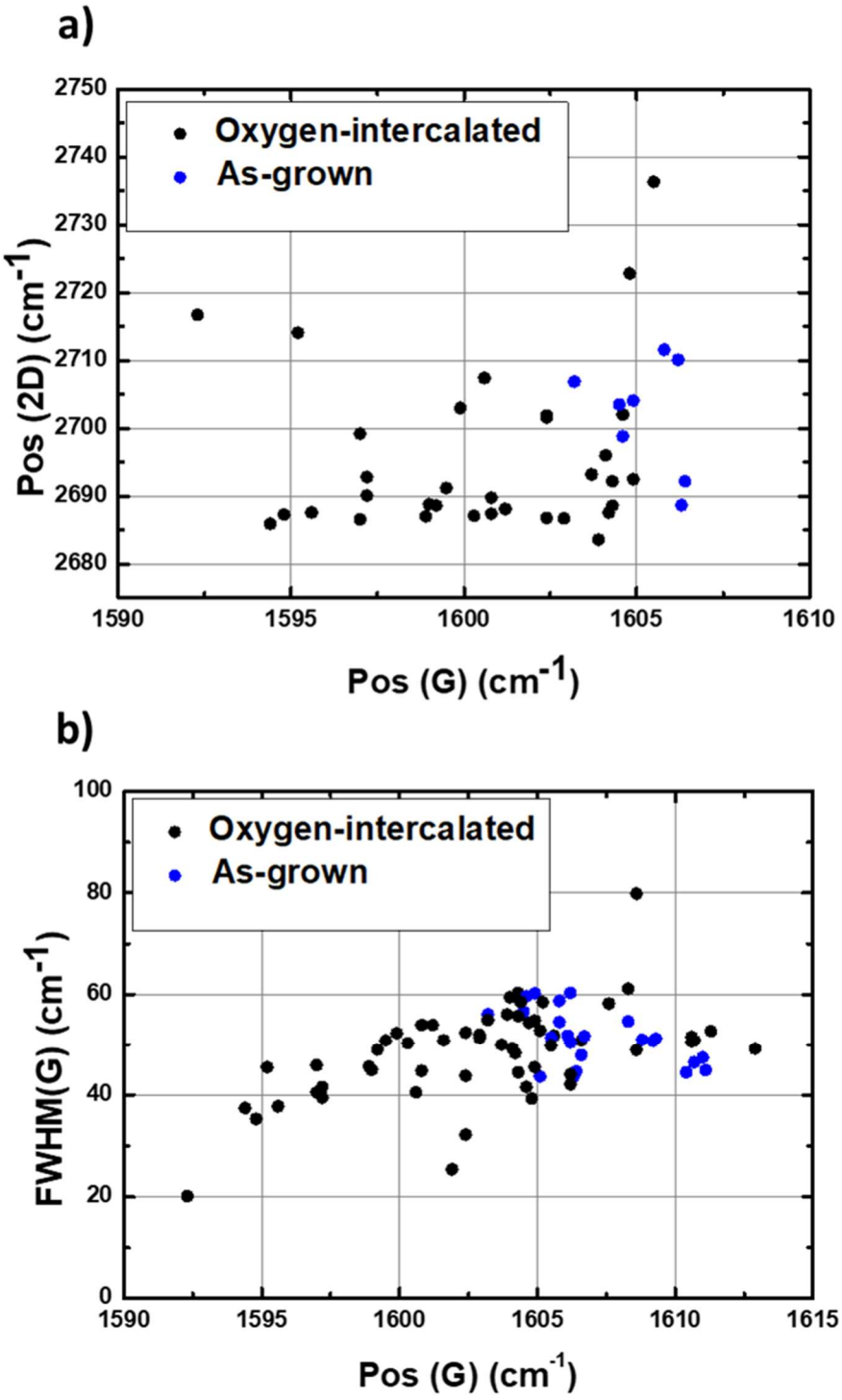

Figure 20. *a) Representation of the 2D peak position as a function of the G peak position and b) representation of the FWHM of the G peak versus the G peak position for as-grown (black dots) and oxygen-intercalated (blue dots) samples.*

- **KPFS**

Previous works have reported the n-doping character of graphene grown on copper foils grown by CVD [109]. In chapter 3 we have shown that the graphene layer obtained by PVD in UHV with C_{60} as precursor molecules exhibits also this n-doping behavior [111]. On the other hand, the XPS experiments shown in this chapter evidence that the oxygen intercalation modifies this type of doping since an observed small BE shift indicates a tendency to reduce this n-doping. This change in graphene doping upon oxygen intercalation is also corroborated by surface potential measurements with KPFM. Considering the relation between the surface potential (V_{SP}) and the work functions of the as-grown and oxygen-intercalated samples, can be expressed in the following equation [61]:

$$eV_{SP} = \Phi_{tip} - \Phi_{sample} \quad (4)$$

Where Φ_{tip} is the work function of the tip, while Φ_{sample} is the work function of the sample and e is the charge of the electron. The critical point in these studies was ensuring that the tip conditions (particularly, the work function) did not change. To monitor this, a reference sample of known work function (HOPG in our case, with a value of $\Phi = 4.6\ eV$) was measured between samples.

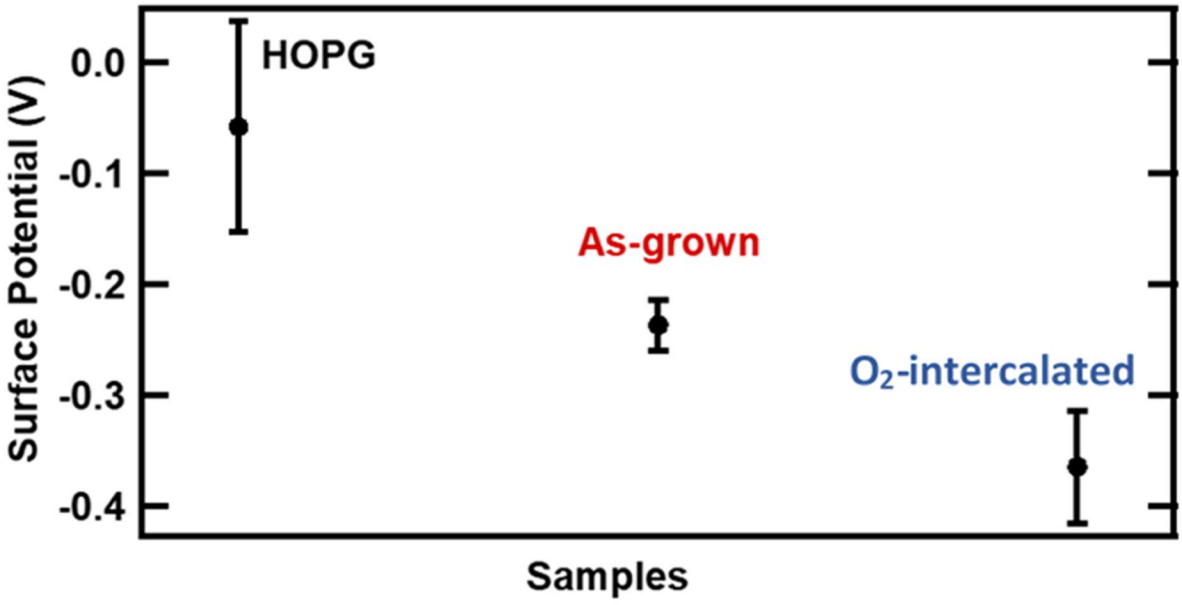

***Figure 4.21**. Surface potential measurements of the oxygen intercalated sample, compared to the as-grown sample. As a reference, HOPG has been used.*

Several curves were acquired on different locations, and measurements were repeated altering the sample order, to ensure reproducibility of the measured differences in surface potential. From each curve, a value of the surface potential was obtained. ***Figure 4.21*** shows the average value of the bias DC voltage of the minimum of the curves obtained, and the standard deviation was plotted as the error bar. The error bars of the two samples (as-grown and oxygen-intercalated) presented a smaller error bar than the HOPG and hence, the homogeneity of the samples was assumed.

Differences observed between the as-grown sample and the oxygen-intercalated one in the surface potential imply differences in the work functions (equation 4). There is a difference of -0.13 V between the as-grown and the oxygen-intercalated samples ($V_{As\text{-}grown}$-$V_{O\text{-}intercalated}$). For our experimental set-up (voltages applied to the tip and samples grounded) a lower surface potential indicates a higher work function value. Therefore, the results presented in ***figure 4.21*** indicate that the oxygen intercalated sample has a higher work function than the as-grown counterpart, verifying the hole-type doping trend observed in XPS and supported by the Raman data behaviour. Hence, as the as-grown samples have an intrinsic n-type doping, this results evidence that the intercalation process diminishes this n-doping character. For this reason, the results reinforce the idea that the oxygen layer acts as an electronically decoupling agent, what would suggest a better scenario for a transfer process to any desired substrate.

- Theoretical simulations

In order to understand the structural and electronic decoupling process of graphene from the copper substrate as the intercalated oxygen content increases in between the Gr/Cu interface, DFT based calculations for different intercalated oxygen coverages were performed. A detailed description of those simulations is exposed in the Appendix section. The main result concerning the oxygen intercalation process is represented in ***Figure 4.22***. This graphic shows the projected density of states (PDOS) onto the graphene layer for a free-standing single layer graphene (dashed black line), for Gr/Cu(111) in its most stable configuration (solid blue line) and for 0.75 ML of intercalated oxygen at the Gr/Cu(111) interface (solid orange line) as a function of the energy referred to the Fermi energy (in eV). The PDOS profile for the case of Gr/Cu(111) reproduces a well-formed Dirac cone. Nevertheless, the profile morphology is remarkably different from that obtained for free-standing graphene (black line). The smooth obtained for the free-standing layer is lost in this case due to several factors: the first one is the non-negligible graphene corrugation arising in this case (as shown in the Appendix), with

regions where the pristine sp^2 hybridization is slightly broken, second, the effect introduced in the electronic properties by the slight graphene strain of around a 3% and finally, by the non-negligible chemical interaction arising at some points of the interface. Importantly, the PDOS profile for the Gr/Cu(111) case is not perfectly symmetrical with respect to the Fermi energy, exhibiting a n-doping level developed in the graphene layer by effect of the electronic charge transferred from the substrate, in excellent agreement with our experimental evidence and previous literature [146]. From the calculations, the shift of the Fermi energy between the free-standing graphene and the Gr/Cu(111) n-doped case for the Gr/Cu(111) interface is around 0.5 eV. This value is similar to the 0.77 eV experimental experimental result, expounded in chapter 3. Finally, by inspecting the PDOS profile corresponding to the case of 0.75 ML, it is clearly appreciated that in this case the Dirac cone is again formed by a perfectly symmetrical distribution of the density of states around the Fermi level, indicating that the n-doping existing in graphene for the case of Gr/Cu(111) has completely vanished. This effect may be interpreted as the graphene, with an increasing O underlayer, decouples electronically, showing a very good agreement with the PDOS profile corresponding to a canonical free-standing graphene layer (dashed-black line).

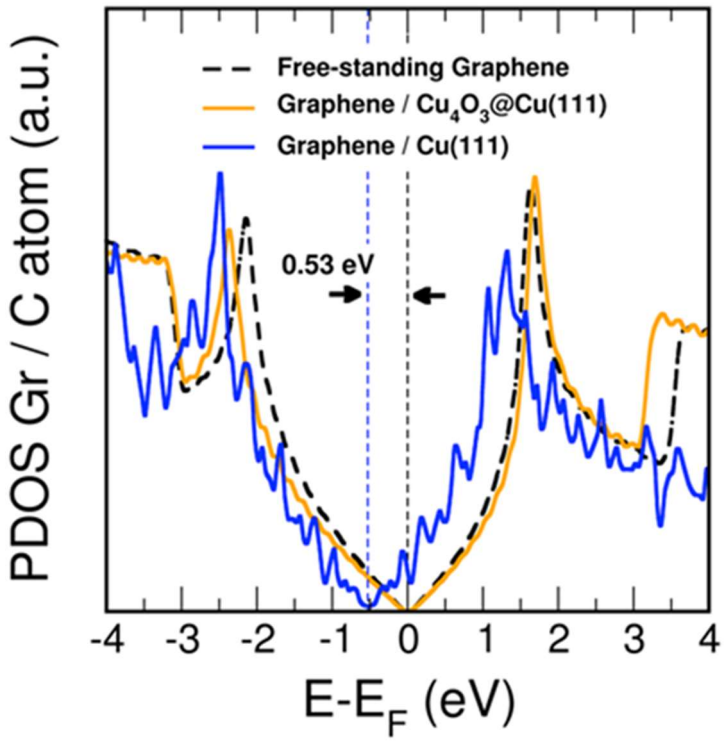

***Figure 4.22**. PDOS on the graphene layer for the cases of Gr/Cu(111) (solid-blue line) and Gr/Cu3O4@Cu(111) (solid-orange line) as a function of the energy referred to the Fermi energy (in eV). The canonical DOS of a freestanding single layer graphene is also shown (dashed-black) for a better comparison.*

4.3.2.4 Transferred graphene layer characterization

After the characterization to confirm the electronic decoupling as an effect of the intercalated oxygen process, samples were transferred on a SiO_2 sample following the method described in section 4.2 of this chapter. Prior to any kind of characterization, the transfer process was noted to be smoother. The transferred samples were characterized by optical microscopy and Raman spectroscopy.

- **Optical microscopy**

Although the intercalation process was observed to decouple the graphene layer from the metallic substrate, the decisive factor was to detect in the graphene transfer process differences between the O-intercalated and as-grown sample. As a first characterization, mainly to observe whether the holes produced by the initial transfer process (shown in the transfer section of this chapter) were reduced or eliminated, optical microscopy measurements were carried out. Although the transfer was not perfect in any of both cases, there was an evident difference in the preservation of the graphene layer between the O-intercalated sample and the as-grown one, as shown in ***figure 4.23***.

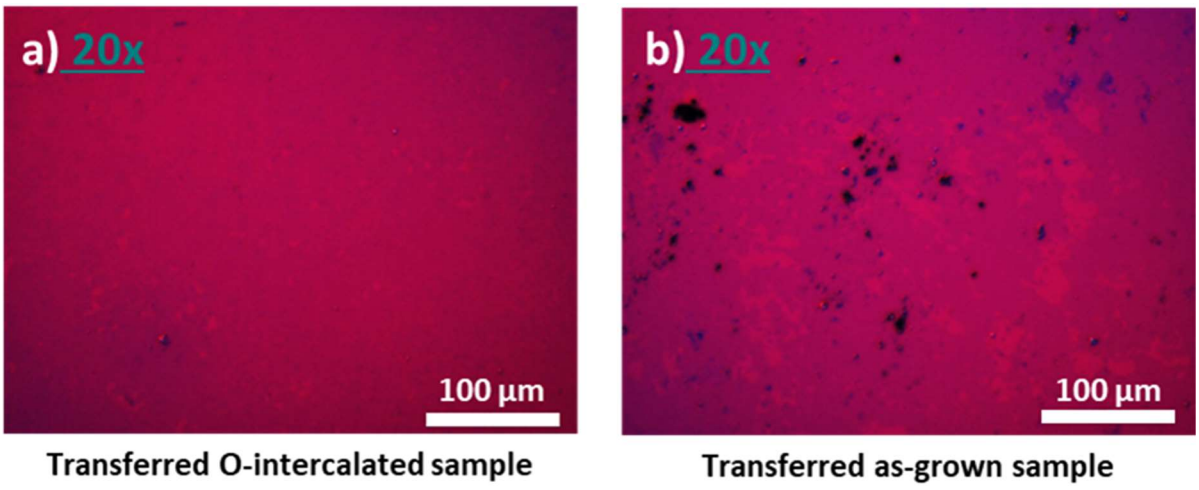

Figure 4.23*. Optical microscopy images of two Gr/SiO2 samples with an objective lens of 20x (a and c) and 100x (b and d): upper panel, a) and b), oxygen intercalated transferred sample and bottom panel, c and d), as-grown transferred sample.*

Figure 4.23 shows the difference on transferring O-intercalated and as-grown samples as observed by optical microscopy. The amount of imperfections and holes is less in the transferred sample after the intercalation process than in the transferred graphene of the as-grown sample. This fact is visible not only because of the contrast in continuity of the layer but also because of the contamination difference between both samples.

- **AFM**

The optical microscopy images shown in the previous subsection evidenced that the oxygen-intercalation process has improved the transfer of the graphene layer on SiO_2 samples. The AFM topographic image shown in ***figure 4.24a*** covers a 15x15 μm^2 area where it is observed that the layer is continuous along the sample. ***Figure 4.24b*** shows a profile, that corresponds to the green line drawn in the image, where a two nm difference in height is observed. It is important to mention that this value is not accurate due to the measurement mode employed (dynamic mode controlled in amplitude). Nevertheless, the observed excessive height could be due to the substrate, or to some residue of the supporting layer. The wrinkles, fingerprint of the graphene presence, discard holes in the graphene layer. Besides, the wrinkles cross those regions exhibiting height modulations, assuring the presence of graphene in those zones.

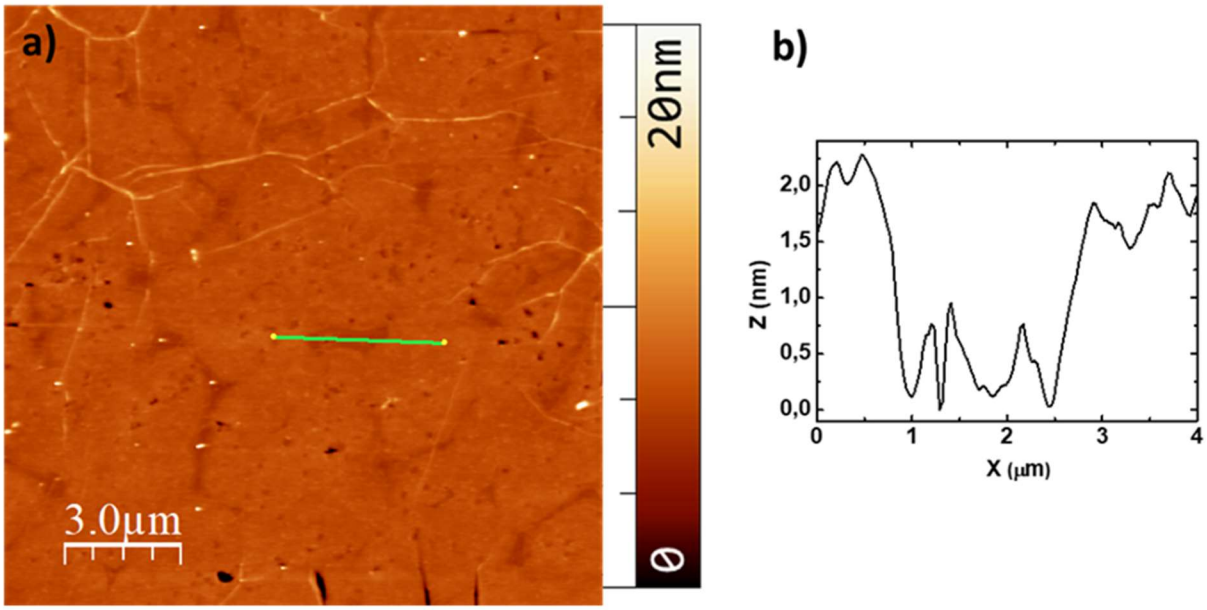

***Figure 4.24**. a) AFM topographic image of oxygen-intercalated graphene transferred to SiO2. b) Profile corresponding to the line drawn in a) where the difference in height of some zones of the sample is represented.*

- **Raman spectroscopy**

Beyond the insight optical microscopy and AFM can provide, Raman spectroscopy measurements contribute to give information of the transferred graphene layer.

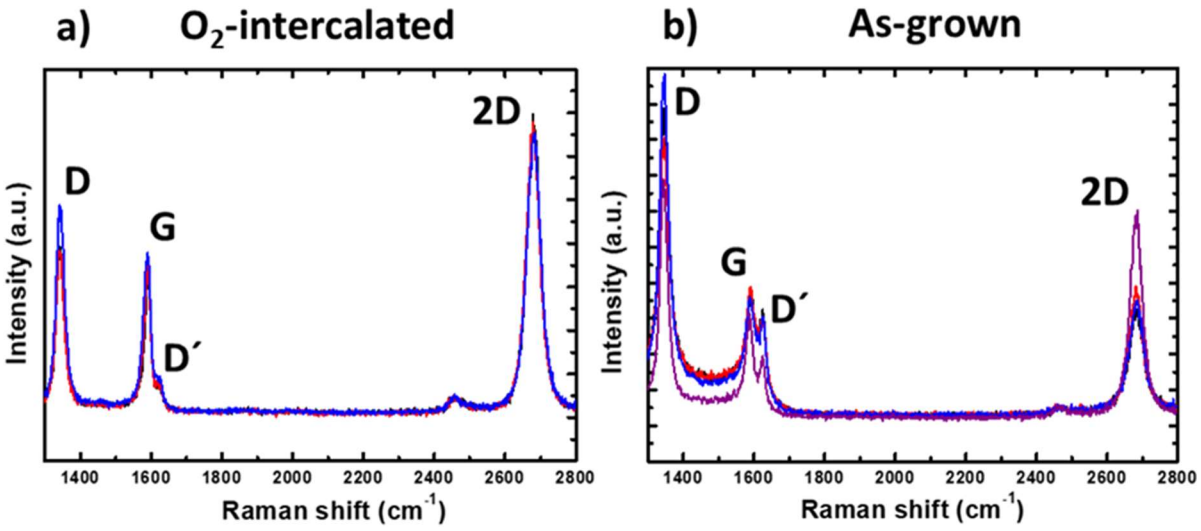

***Figure 4.25**. Raman spectroscopy measurements of graphene on SiO2 transferred samples from a) an O2-intercalated sample and b) an as-grown sample. The different spectra in each plot correspond to different zones of the sample.*

From the ***figure 4.25*** we can see that the defect peak is present in both samples. The difference lies in the intensity relation. In the oxygen-intercalated sample the most intense peak is the 2D whereas in the as-grown sample the most intense one is the D peak. Moreover, the relation between the intensities of the two defect-activated peaks (D and D´) is different. This implies that the nature of the defects of the graphene lattice for both samples is different, as it has been previously reported [147]. In this work, they conclude, empirically, that a relation of $\frac{I(D)}{I(D')} \sim 13$ is found in sp^3-type defects, while a factor of ~ 7 implies vacancy-type defects and a factor of 3 boundary-type defects. In our case, we have found a relation of ~ 7 for the oxygen-intercalated samples, while a relation of ~ 3 has been observed for the as-grown sample. This suggests that an improvement in the transfer process has been obtained: what is proposed here, is that the interaction between graphene and copper affects to the grain boundaries specially. Due to the disorder present in the boundary between two differently oriented grains, the detachment process produces an enhancement of the contribution of these grain boundaries to the Raman signal. In the case of oxygen-intercalated samples, it looks like this effect is attenuated, and the defects are identified as vacancy-like defects.

4.4 Conclusions

This chapter has been focused on the next step after the growth of graphene on transition metal substrates, in our case polycrystalline copper foils and copper single crystals. The first section shows the protocol employed for transferring the graphene layer to a SiO_2 substrate as well as the difficulties found to achieve optimal results due to non-negligible interaction between graphene and the substrate. Transport measurements at low temperature on the transferred graphene layer have shown acceptable results, but the high quality of the graphene layers obtained by the PVD method demands to improve those results. The main problem relies on the interaction between the graphene layer and the underlying substrate generated by using the PVD method with C_{60} molecules for growing graphene.

In this direction, two different approaches have been described to weaken this significant interaction: a chemical approach where a large molecule (TOA^+) is intercalated and a physical approach where oxygen has been intercalated in UHV environment. Both approaches have

shown to improve the transfer process and the results obtained on transferred samples. Moreover, we have demonstrated that the oxygen intercalation electronically decouples de graphene layer, as concluded by Raman spectroscopy, where the 2D graphene peak become detectable only after the intercalation. One could envisage that, with a proper optimization of the methodology, the intercalated oxygen could be tailored in order to have an insulating substrate without any transfer process. The main advantage would be that the whole process could be accomplished in UHV environment, avoiding contamination during the whole growth and intercalation process.

Chapter 5. Experimental set-up

As mentioned in the introduction, this chapter is dedicated to the description of an experimental set-up and of some preliminary results obtained with this equipment. The goal of this new set-up, that consists on a cryostat with a three-axis vector magnet for producing tilted magnetic fields in a wide range of temperature (300-2 K), is the local image acquisition, mainly focused in the magnetic characteristics of the sample. In the first sections of this chapter, the construction of the new system is described. After that, the last two sections will be devoted to describe the magnetic information obtained for two different systems making use of the installed equipment. From one side, a hard disk drive (HDD) will be explored to test the proper functioning of the instrument, and from the other, a graphene/superconductor system, will be used for determining its potential magnetic properties as a preliminary proof-of-concept.

5.1 Construction of the cryogenic system

In this section the construction of a cryogenic system is described. It consists of a helium cryostat where a three-axis vector magnet is placed. Looking towards the possibilities that graphene could open in terms of stacked heterostructural materials (graphene on superconductors, graphene on magnetic materials etc.), the implementation of a new experimental set-up for a surface magnetic characterization became of important concern. Indeed, considering that the origin of the macroscopic physics of such promising landscapes emerges from local quantum effects, to build a cryogenic system with a variable temperature and magnetic field (in strength and orientation) for low temperature local magnetic imaging was highly interesting. In this section, this experimental set-up construction will be detailed.

Low temperature physics (superconductivity and magnetism mainly) has been a field of interest for more than one century (in the case of magnetism, thousands of years) and still a complete understanding of those phenomena is lacking. In addition to the fundamental interest it has, low temperature physics is a topic of interest from a technological point of view. Although, as mentioned, there is not a complete comprehension of the phenomena that occur at low temperature, it has not been an impediment for the technological development of plenty of everyday-life devices based on magnetic materials (credit card, compass, recording media, electrical engine…) and in the case of superconductivity, many applications are being used in hospitals (magneto-nuclear resonance) and R&D centers (low temperature physics) for the achievement of high magnetic fields with minimum energy loss, mainly.

The interest in the construction of the present experimental set-up relies on the fact that there are many interesting systems, such as anisotropic superconductors or magnets, where the control over the direction of the magnetic field is important. Macroscopic measurements, such as resistivity, thermal conductivity or specific heat can be studied under tilted magnetic fields by using rotating sample holders [148,149]. Besides, the magnetic force microscopy (MFM) technique that correlates local magnetic imaging with morphological imaging, can provide essential information for nanometric morphological and functional characterization. The MFM technique embedded in the cryogenic system with the vector magnet enhances the capabilities of scanning probe microscopies adding new parameters due to the possibility to acquire data in a temperature range that goes from 1.5 to 300K and under magnetic fields in any direction of space that vary from 0 to 1.2 Tesla. The problem arises when the implementation of this technique in a cryogenic system is attempted. In these cases, a rotating head of the microscope would be utopic, due to the extreme mechanical stability it demands. At this point is where a three-axis vector magnet makes sense, where not the sample but the magnetic field is tilted.

There are other experimental techniques apart from MFM that can provide macroscopic as well as local magnetic information. There are measurement systems that provide an average magnitude of the magnetic properties of the material [150,151], and there are systems that study the local magnetic properties of the material [152,153]. MFM, as these latter techniques, is a local probe technique. The MFM acquires images by passing two times over the same area for the simultaneous acquisition of topographic and magnetic information and be able to correlate them. While in KPFS (chapter 2) the used tip is coated with a conductive material, for MFM measurements the tip of the microscope is coated with a magnetic material, in order to have sensitivity of the magnetic interaction the sample can generate. As told, the method scans the same are twice. This scan is performed in dynamic mode. Topography is measured in a first pass (the possibility to correlate the magnetic information with the topography can provide very useful information), while the magnetic response is measured in a second pass, with the tip retraced from the surface of the sample to a certain distance (100-120 nm) for a better magnetic signal acquisition. This is because the magnetic interaction is a long-range force, and this way the signals coming from other interactions can be minimized. The magnetic interaction is detected by changes in the phase of the oscillating cantilever (in the MFM measurements presented here, there are other systems were the controlled parameter is the amplitude of the oscillation), and this shift in the frequency phase of the cantilever oscillation is what is registered as magnetic image.

5.1.1 Cryogenic set-up

The achievement of high magnetic fields is not trivial, since it implies the use of high electric currents to induce the desired fields. It would be an impossible task with ohmic materials, because the Joule effect would melt the coil. The use of superconducting materials is mandatory, and that is why cryogenic technology needs to be implemented.

The cryogenic set-up described here, was designed considering the dimensions and characteristics of a commercial microscope from Nanomagnetics Ltd. The helium cryostat is a necessary but not sufficient condition to perform experiments at low temperatures. The control of the temperature with precise feedback is essential: the cool-down and warm-up ramps need to be made gradually not to damage the microscope, and the image acquisition requires a high temperature stability to avoid drift effects during measurements.

The system presented here fulfills these requirements. For a better comprehension, the description of the set-up will be divided in four parts, each one with a specific task inside the set-up in order to accomplish these requirements:

- The helium cryostat, with a top flange with all the electric and cryogenic connections, that allows a cryogenic environment.
- The tree-axis vector magnet that supplies the external magnetic field.
- A variable temperature insert (VTI) that provides thermal stability and controlled warm-up and cool-down ramps.
- Low temperature MFM, to perform local morphological and functional characterization at different temperatures and under applied magnetic fields.

- Helium cryostat

In low temperature physics, a vessel is needed in order to have a helium bath where the whole experimental system will be placed. Liquid helium (^{4}He) temperature at ambient pressure (1 bar) is 4.22 K. Moreover, if the pressure is lowered (with a primary vacuum pump connected to the bath, for example), the temperature reached is about 1.5 K (see ***figure 5.1***).

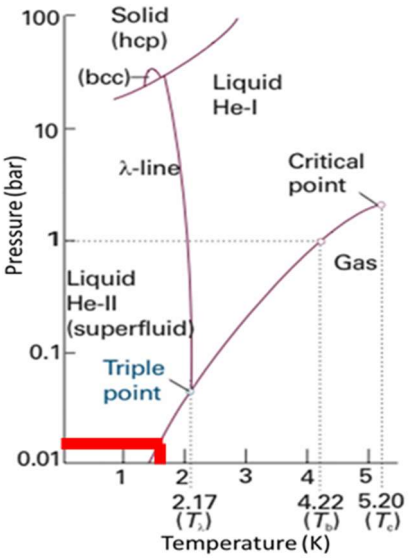

Figure 5.1. *Phase diagram of helium (4He) in a logarithmic scale of the pressure values. The condensation line shows that the lower the pressure, the cooler the liquid helium. Figure adapted from*[154].

Although cryostats are similar ones to others, here is described the system located at the *Magnetism and Magnetotransport Laboratory* at ICMM. The cryostat was home-designed to house a commercial variable temperature insert (VTI) and a home-made magnet inside. ***Figure 5.2*** shows a blueprint of the cryostat with the different parts highlighted with colors. The helium resides in the inner chamber, (green). This chamber is isolated with a vacuum (1 x10^{-6} mbar) jacket (blue). There is a nitrogen jacket (yellow) in the upper part, to decrease the temperature gradient of the system. The magnet, in red, lies at the bottom of the vessel.

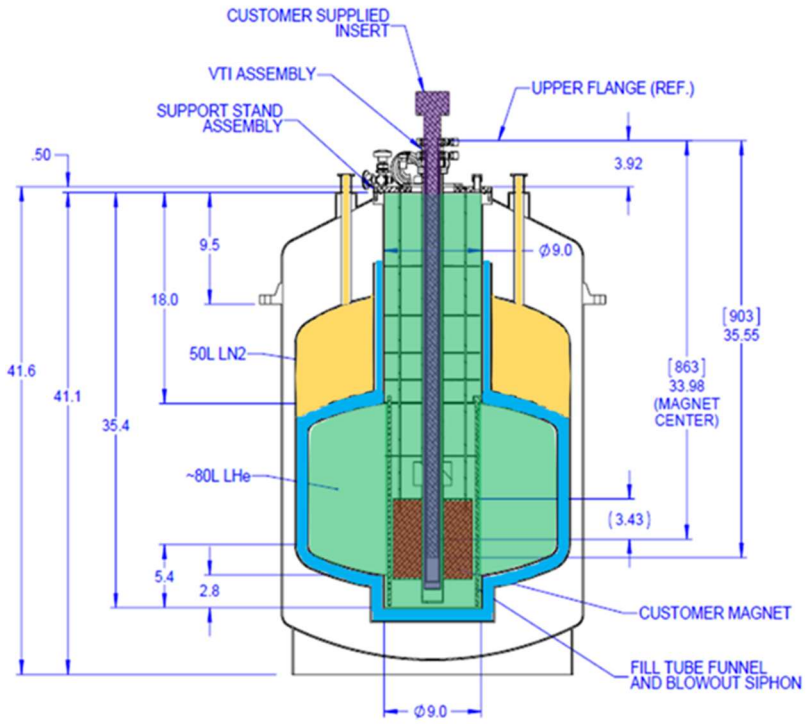

***Figure 5.2**. Blueprint of the experimental set-up: the inner chamber for helium (green), vacuum jacket (blue), nitrogen jacket (yellow), the magnet (red) and the microscope (magenta). SEGAINVEX.*

5.1.2 Three-axis vector magnet

The magnet consists of five coils, one solenoid for Z axis and two sets of split coils for the XY plane. The inside bore, of 56 mm in diameter, is fixed by the Z-axis coil, and the outside diameter of the magnet is 250 mm. The five coils are mounted in an Al cage designed to hold the forces that are generated by the interaction between coils. Al was chosen to reduce as much as possible the weight of the magnet. Stainless steel screws were used to fix the magnets and 1 cm thick Al plates for the magnet cage. The coils were built from Nb-Ti superconducting wires. These wires are formed by a composite of a titanium structure where a matrix of superconducting wires of Nb-Ti is embedded (***figure 5.3***). The number of turns and resistance at RT of each coil, measured in a two wires configuration, is presented in ***table 5.1.***

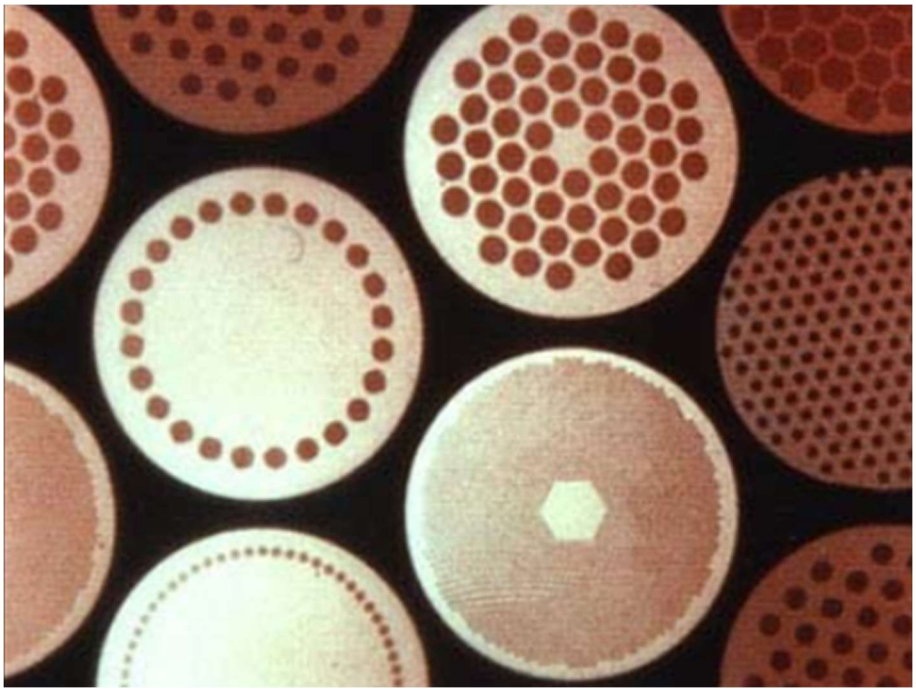

***Figure 5.3**. Image of the section of different configurations of superconducting wires. Adapted from* [155].

Coil	Turns	Resistance (Ω)
Z axis	5831	191.84
Y axis	2448(A) 2460(B)	130.50
X axis	2455(Y) 2460(Z)	128.20

***Table 5.1**. Number of turns of each coil that determines the magnetic field for a given current and the resistance of each coil at RT.*

The dimensions of the magnet are imposed by the microscope head that needs to be placed in the center to feel the fields of the three coils set in their maximum (***figure 5.4a and b***). The field has to be homogeneous at the microscope position, so that magnetic field gradients exert no force on sensitive parts of the microscope. The mechanical stability of the support system of the magnet is also important, because the magnet assembly is heavy and should not move to avoid vibrations and instabilities on the microscope head.

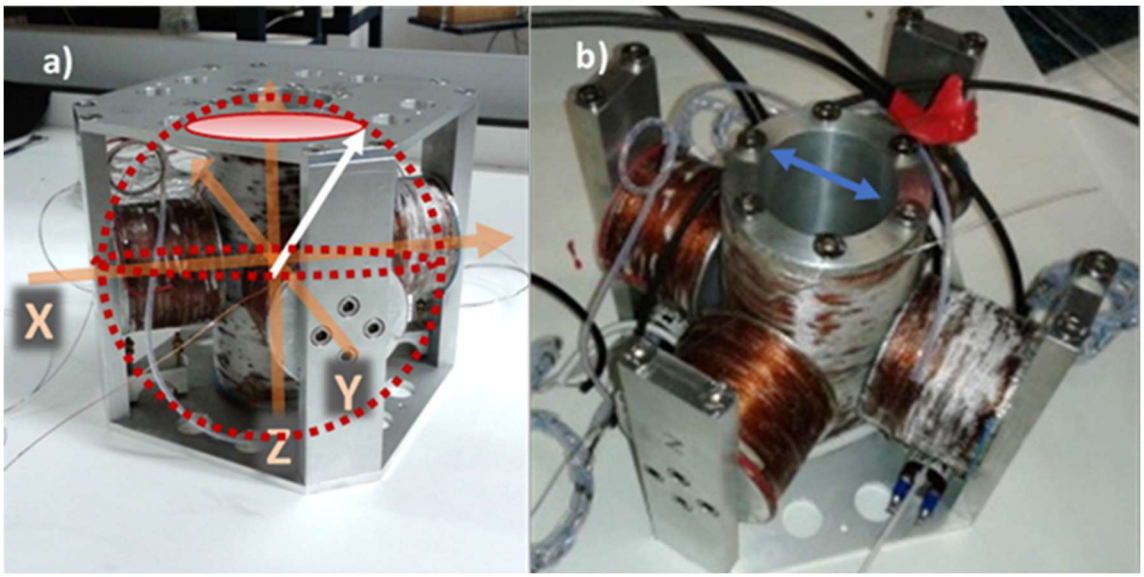

***Figure 5.4**. a) Image of the three-axis vector magnet assembled in the aluminum cage. The white arrow represents an arbitrary direction of the magnetic field achieved by the components of the X, Y and Z direction fields. b) Image of the coils where the blue arrow indicates the inside diameter of the Z coil where the head of the microscope is inserted.*

The maximum field reached is 5 T in the Z direction and 1.2 T in the X-Y plane using a current of 100 A. This gives a tilted magnetic field of 5 T at a cone opening angle of 13.5° around Z. The cone increases the opening angle towards lower fields on the Z-axis coil, and the three-dimensional vector capability is reached for fields below 1.2 T. The major concern is to obtain the maximum homogeneity of the field at the vicinity of the microscope head. At this position, measurements of the magnetic field as a function of the distance were done obtaining as a result that the variation of the field at the center of the coils, within a sphere of 0.5 cm radius, is lower than 0.2 % for the Z axis and lower than 1 % for the X-Y plane. This characterization will be widely shown in section 5.2 of this chapter.

The magnet is hanged from the cryostat top flange with four stainless steel bars of 4 mm diameter and a longitude of 77.5 cm, as shown in ***figure 5.5a*** (red arrows) and is immersed in the helium bath. It is important to minimize the mass holding the magnet, due to the extreme temperature gradient that can be reached between both ends of the bars, i. e. the top flange is at RT while the magnet is around 4 K. The magnet is powered with three pairs of copper strands that are thermalized attaching them to the radiation shields, as shown in ***figure 5.5b***. The final assembly of the magnet to the structure is shown in ***figure 5.5c***.

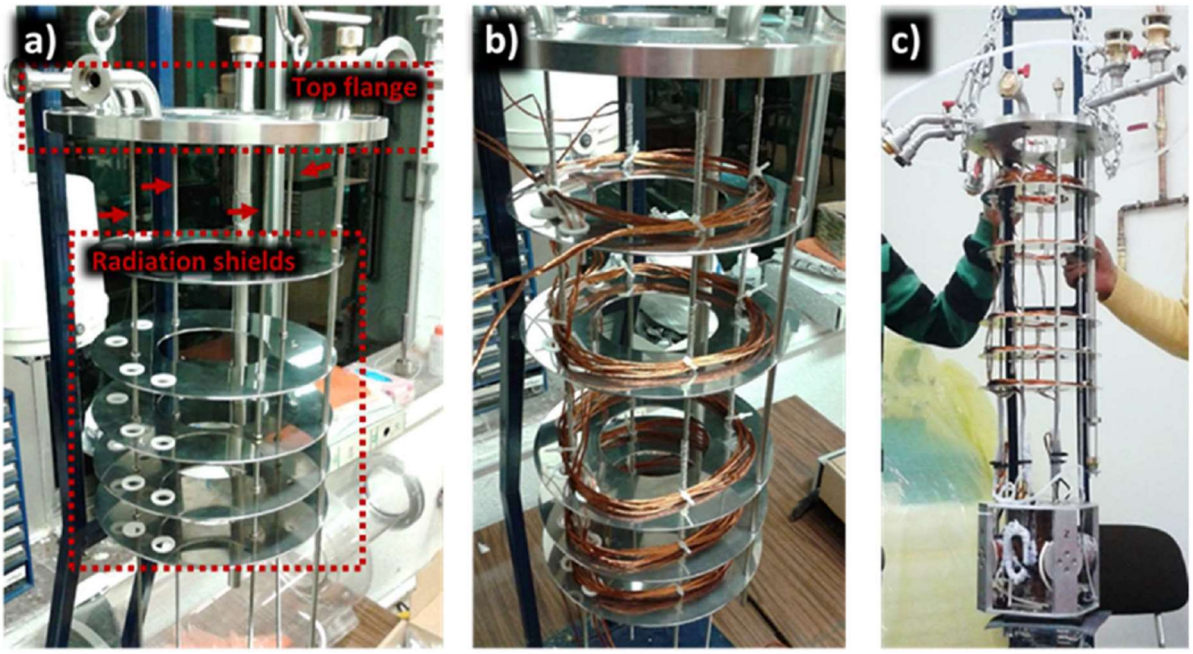

***Figure 5.5**. a) Image of the structure, prior to wiring. Top flange and radiation shields are highlighted. Arrows point to the bars that hang the magnet. b) Image of the copper strands attached to the radiation shields. c) Image of the magnet connected to the copper strands and hanged from the top flange.*

The copper strands are connected to the coils through three commercial switch heaters from Oxford Instruments (***figure 5.6a***), one per coil. The switch heaters allow driving the magnet in persistent mode i. e., the switches permit to isolate the superconducting circuit to maintain a given field with zero energy demand (almost zero, a minimum energy is dissipated from the vortices), and to connect it to the power supply in order to change the field. The technical specifications are shown in ***table 5.2***.

Switch	Switch value (Ω)	Heater value (Ω)
Z axis	10.5	99.6
Y axis	10.4	100.9
X axis	10.6	101.6

***Table 5.2**. Technical details of the switch heaters: resistance values of the switches and resistance values of the heaters.*

The copper wires, that connect the magnet with the power supply, and the superconducting wire, used for the coils, are intertwined for a long extension (30 cm) to have a large effective area of electrical contact. One of the critical points of this system resides at this connection (***figure 5.6b***, blue arrows). The copper is welded to the external titanium part of the superconducting wire. This means that between the copper wire and the superconducting wire

matrix exits a part of higher specific resistivity that needs a large contact to decrease the whole resistance and hence, the heat dissipation produced by Joule effect in ohmic materials.

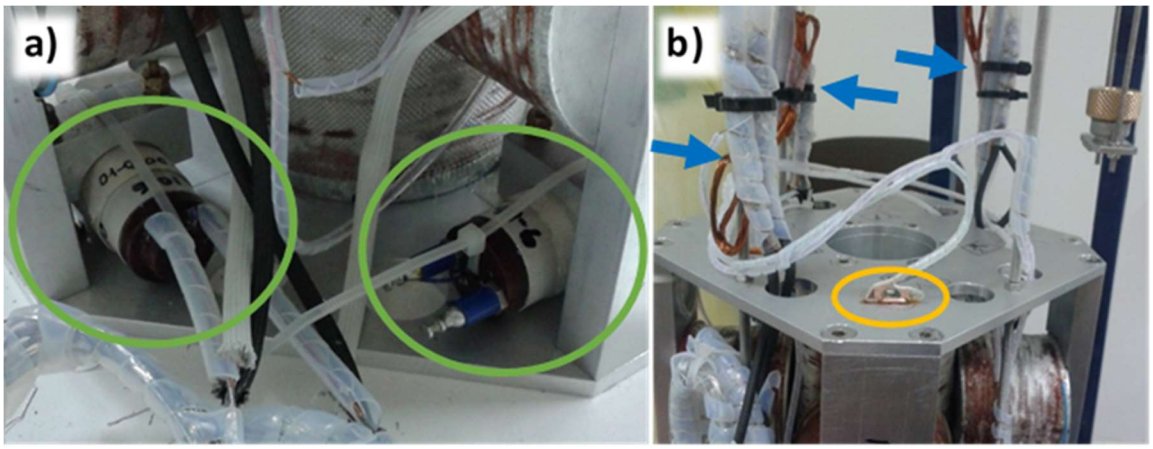

***Figure 5.6**. a) Image of two of the three switch heaters present in the system, highlighted with green circles. b) Image of the large connections between the copper strands and the switch heaters, pointed with blue arrows.*

The Nb-Ti wires (critical temperature ~10 K and critical field ~15 T) are polycrystalline, thus grain boundaries are present in the wires. The first time that currents are applied (tens of Amperes), local temperature increases can happen, normally due to the presence of those grain boundaries. If at some point the temperature exceeds the critical superconducting temperature the whole superconducting wiring will turn to its normal state, producing a sudden evaporation of liquid helium, due to heat dissipation. In addition to the security valves (flanges attached to a string, calibrated to 200 mbar of differential pressure in our case), the presence of a sensor (***figure 5.6b***, inside the yellow circle) is crucial to monitor the temperature of the magnet in order to take action in the case of an uncontrolled rise in temperature. This sensor is also used to control whether the helium level is covering the magnet or not. That is the reason why it was located at the top of the magnet cage, fixed with a screw and glued with epoxy for low temperature uses: this thermal anchorage assures that the sensor measures the temperature of the magnet cabinet. Additional wiring was used for measuring the induced voltage that the magnetic fields generate. Constantan wiring was used in this case, due to its high resistivity that provides a good resolution of the measured voltage by using a low current (mA).

The power supply (***figure 5.7***) was designed and built between LBTUAM (Laboratorio de Bajas Temperaturas de la Universidad Autónoma de Madrid) and SEGAINVEX (SErvicio General de

Ayuda a la INVestigación EXperimental), with the aim of having a compact measurement system with the lowest possible noise levels [paper iman]. The power supply consists of three independent and identic power supplies, one per each coil set. One of those three parts is highlighted in ***figure 5.7***. The upper part, (red square) is the display and the control of the magnetic field, where the set-point and the ramp can be configured. Buttons in the blue square allow to reset the magnet parameters. The voltage produced by the inductances of the magnets are shown in the display marked by the green square, where the scale can be adjusted. Finally, the connections of the power and of the switch heaters are also shown in ***figure 5.7*** (magenta square).

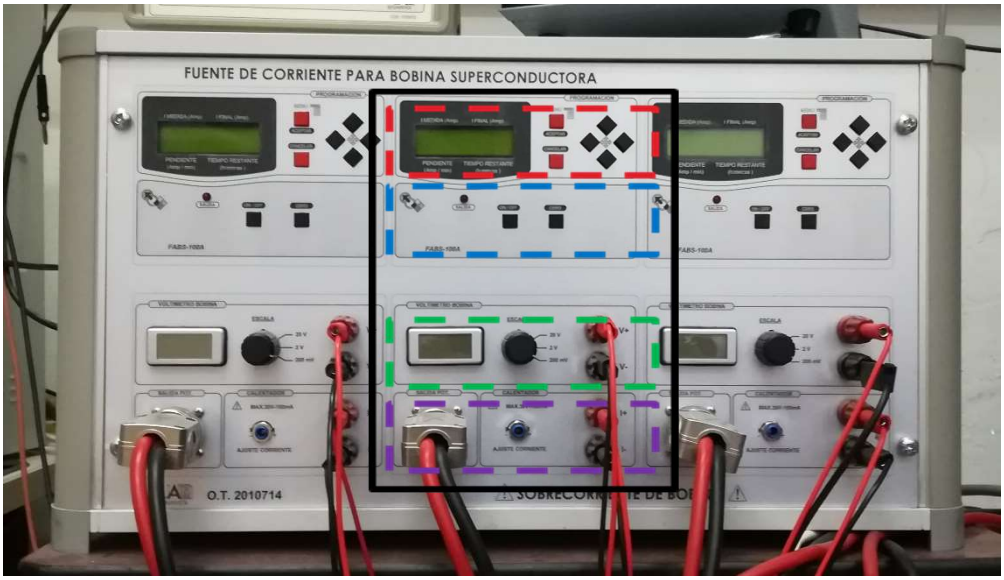

Figure 5.7*. Image of the power supply. The different parts are highlighted: in red, the display and control of the magnetic field; in blue the on/off buttons of the magnet; in green the display and the scale controller of the induced voltage; and in magenta, the power supply and the switch heaters connections.*

5.1.3 Variable temperature insert (VTI)

The cryostat provides a temperature environment of 4.22 K. If a microscope is placed directly in the bath, the exclusive temperature to acquire images would be that one. The interesting point is to be able to measure a wide range of temperatures (1.8 K – 300 K) and to be able to stabilize the system at any point within that range. For this purpose, a VTI is mandatory as the one shown in ***figure 5.8a***, acquired from Cryo Industries of American Magnetics, Inc., the VTI

is composed of three chambers: a vacuum jacket, an exchange gas jacket and the sample chamber. The vacuum jacket (1 x 10^{-6} mbar) isolates the rest from the helium bath. The exchange gas jacket takes helium from the bath by means of a gas flow entrance (***figure 5.8b***). Finally, the sample chamber is where the microscope is placed. This chamber is equipped with a threefold valve in order to purge the space with helium gas. Helium gas is also used to vent the chamber in a very low overpressure when opening, to avoid water condensation inside.

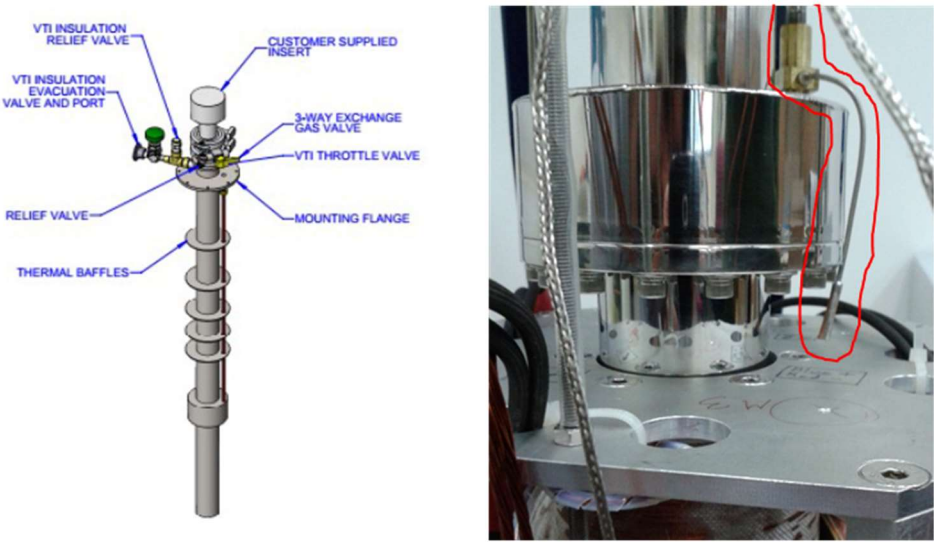

Figure 5.8*. a) Image of the schematic view of the VTI. b) Image of the gas flow entrance (highlighted in red) that access directly to the helium bath.*

The intermediate jacket, the one that takes helium from the bath by means of a gas flow entrance, allows the thermalization of the microscope. The gas that goes through the entrance, passes through a pipe where a heater (50 Ω) and a temperature sensor are located. This heater and the sensor are connected to the temperature controller (Cryo-Con Industries) that, with proper feedback parameters promotes the heating of the gas to the set temperature, with a selected temperature ramp.

5.1.4 Top flange-VTI

One of the most challenging tasks was the assembly of the magnet and the VTI, due to the large number of connections needed. ***Figure 5.9*** shows a top view of the final VTI-flange assembly, with the different connections numbered and described in the table below (table 5.3). Each feature is labeled with a number, distinguishing the ones corresponding to the VTI and the ones corresponding to the connections of the magnet.

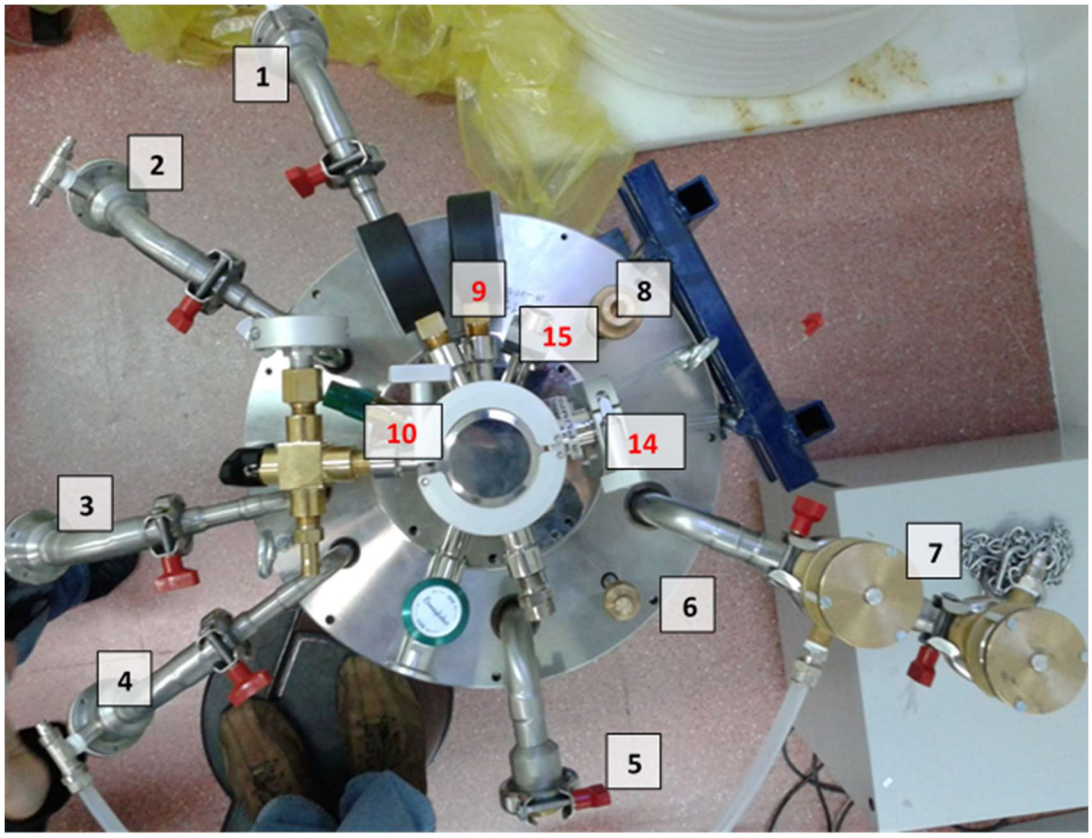

Figure 5.9*. Top view of the flange of the cryostat with the VTI assembled. The connections appear numbered for better identification. In black ones belonging to the magnet and in red those belonging to the VTI.*

Magnet	*VTI*
1,2,3) Power supply: *electrical feed to the three solenoids*	***9) Indicators:*** *pressure indicators*
4) Control connections: *voltmeter, temperature sensor and switch heaters*	***10) Security valve:*** *security valve of vacuum chamber*
5) Recovery: *helium recovery*	***11) Threefold valve:*** *sample chamber´s three position valve, which are: sealed, purge connected to a primary pump and a vent connected to the helium gas bottle*
6) Probe: *helium level probe*	***12) Vacuum valve:*** *connection for pumping the vacuum chamber*
7) Security valves: *helium recovery and two overpressure security systems*	***13) Security valves:*** *security valves of exchange gas chamber and sample space*
8) Refill: *helium refill*	***14) Exchange gas connection:*** *connection to exchange gas chamber to control the helium gas flow and go down to 2 K lowering the pressure of liquid helium*
	15) Control connections: *connections of the temperature sensor and the heater located near the needle valve to control the temperature of the incoming cold helium gas and make feedback loop for temperature stabilization and ramps*

Table 5.3*. Different parts of the top flange that is shown in figure 18. In black, the ones corresponding to the magnet and in red, to the VTI.*

5.1.5 Low temperature magnetic force microscope

The low temperature magnetic force microscope is a commercial system from Nanomagnetics Instruments Ltd. The whole cryogenic and magnetic system was designed considering the dimensions and necessities of the microscope. It has the shape of a stick (***figure 5.10***). The head of the microscope, in a red square in ***figure 5.10***, is the part that will be at the center of the magnet.

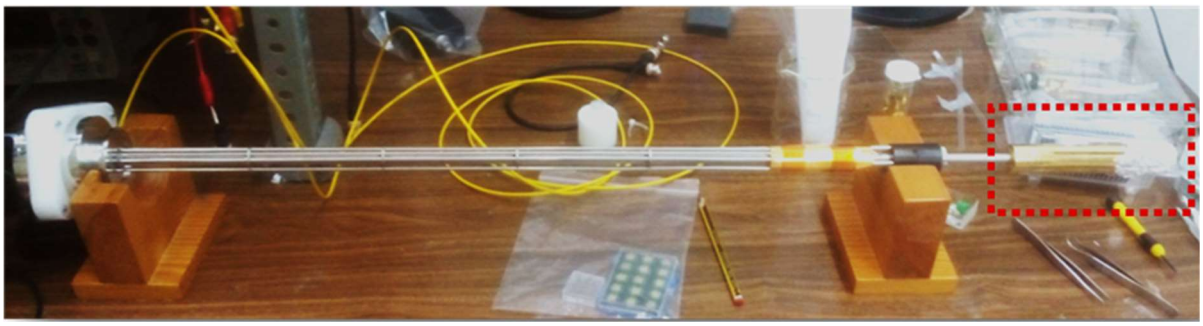

***Figure 5.10**. Image of the low temperature magnetic force microscope that will be placed inside the cryostat. The highlighted part (red square) is the head of the microscope, which will be located at the center of the magnet.*

5.2 Characterization of the magnetic field distribution

An appropriate MFM study requires the homogeneity of the field, at least at the tip-sample location, for the maximum scan area available (100 x 100 μm^2). For this purpose, a calibration of the magnetic field as a function of the distance in the out-of-plane (Z) and in the in-plane (X-Y) directions is essential. The calibration was performed by using two different Hall sensors, a longitudinal one and a transversal one.

As a first approach, and with the aim of obtaining data about the field distribution avoiding the influence of trapped fields in the coils, the initial measurements were done at RT, i. e. with the magnet in the normal state. Within these conditions, the applied current must be very low (100 mA), to avoid the melting of the coil due to Joule heating effect, present when the superconducting wire is in the normal state. The fields obtained with low currents can be linearly extrapolated to the superconducting regime if the conditions of the coil (number of turns and wire thickness) do not change. An additional advantage of making this characterization at RT was the possibility to measure the field of each coil individually, prior to the assembly of all the coils in the structure. For these reason, the fields measured, shown in ***figure 5.11***, are represented as a function of the distance to the coil. In the case of the in-plane field, considering that the coils are formed by two different coils (poles) connected, the field appears represented as a function of the distance to one of those poles.

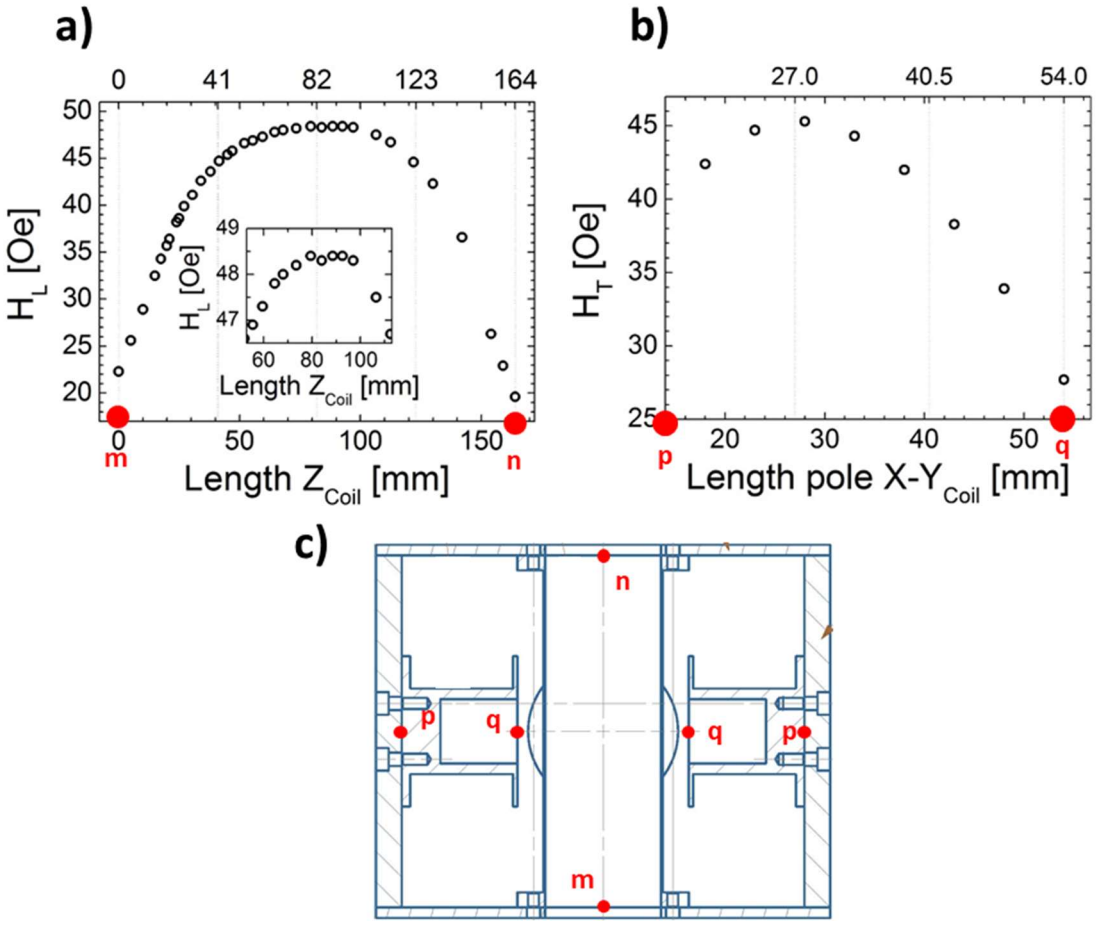

Figure 5.11*. a) Profile of the magnetic field at RT as a function of the position along the Z coil with an excitation current of 100 mA. Inset) A closer look to the field homogeneity in Z, where the variation of the field among to cm is of 1 Oe. b) Representative profile of the magnetic field of one of the in-plane poles. c) Blueprint of one of the sides of the magnet, as a guide for the magnetic profile across the coils. Adapted from SEGAINVEX.*

A second characterization was done at low temperatures (4.22 K), once the magnet was immersed in the helium bath. In this case, both longitudinal and transversal fields are represented as a function of the position along the Z coil (***figure 5.12***). The field variation within a sphere of 0.5 cm radius around the center of the coil system is 0.2 % for the magnetic field along the Z axis, and 1 % for the magnetic field in the plane (***figure 5.12***). There is no transversal magnetic field represented as a function of the position along the length of one of the transversal poles, because with the assembled magnet is not possible to insert a Hall sensor in that direction.

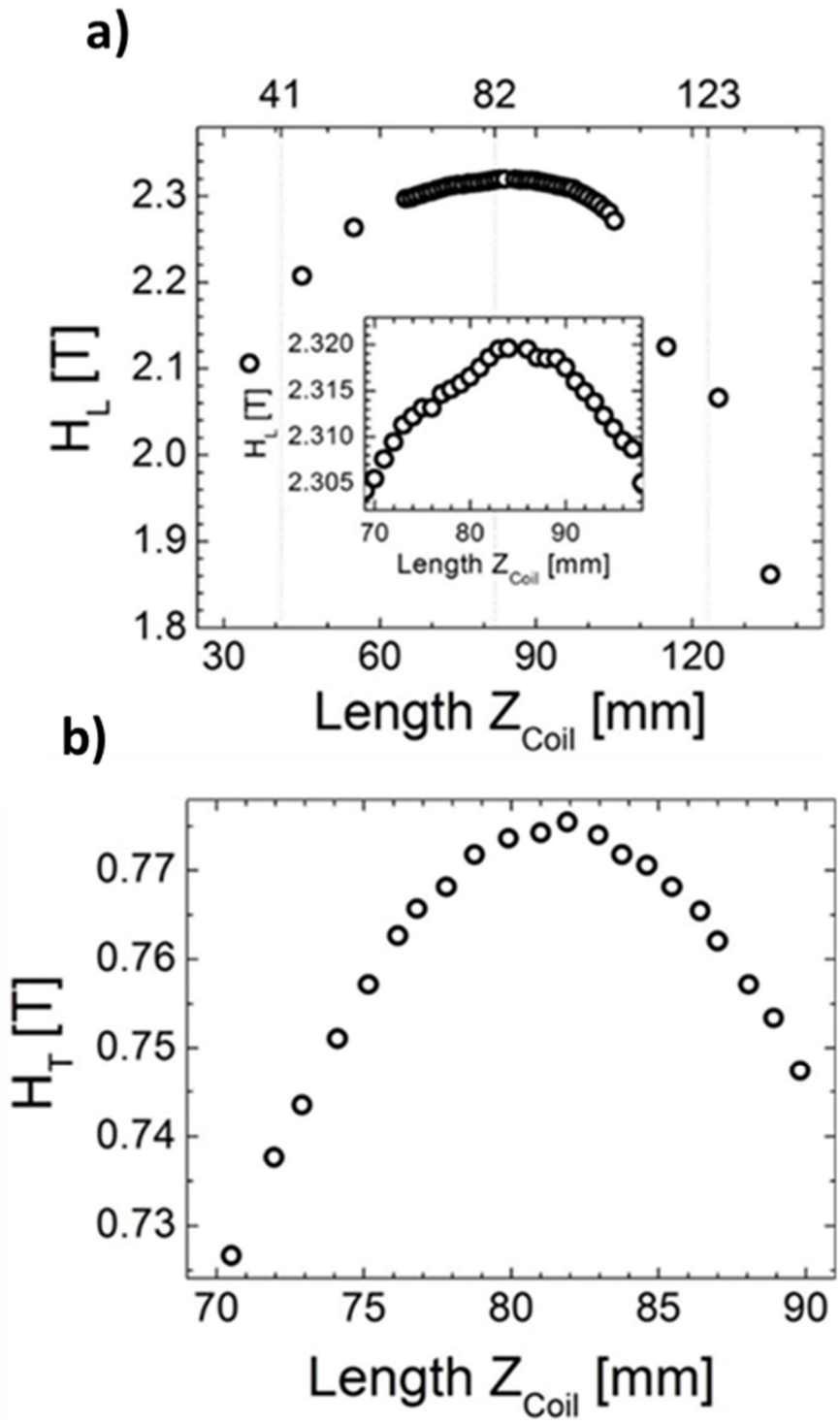

***Figure 5.12**. a) Longitudinal and b) transversal fields at low temperature (4.22 K) as a function of the position along the length of the Z coil.*

5.3 Low temperature magnetic imaging of a hard disk drive

Once described the different parts of this cryogenic system (the cryostat, the VTI and the magnet), and after the characterization of the fields at the position where the microscope is placed, local magnetic images were acquired at 100 K to test the system. For this purpose, a magnetic recording disk was employed, which is a standard test sample for MFM measurements. In ***figure 5.13a***, the topography and the magnetic image of the hard disk with parallel magnetic domains and axial tip magnetization are shown. MFM image reveals a linear pattern of black and white stripes perpendicular to the recording track of the disk (see ***figure 5.13b***).

MFM contrast in recording media is well understood and arises from the interaction of the local surface field component along the direction of the probes magnetization [156–158]. When the MFM probe is axially oriented, the contrast (black and white lines) provides the transition regions between bits [159].

By switching 180° the direction of the applied magnetic field perpendicular to the surfaced, the tip magnetization is reoriented, thus obtaining its axial hysteresis loop (***figure 5.13a***). Starting with a saturated state, + 0.1 T, the magnetic field was decreased in steps of 0.02 T, down to -0.1 T, and then back to positive values. Typically, the tip magnetization switches at ± 0.04 T [160].

The only way to obtain a transversal magnetization of the tip is by means of an applied transversal field. This is because along the transversal direction, the magnetic coating of the tip is so thin that it is below the superparamagnetic limit at that temperature. As the tip is not ferromagnetic in that direction and since there is no residual magnetization, the magnetic field has to be continuously applied in order to maintain the tip magnetic (paramagnetic-like behavior). With an in-plane magnetic field the probe magnetization can be switched between axial and transversal magnetization (***figure 5.13b***). We observe that increasing the magnetic field along one in-plane direction, the MFM contrast changes from bright and dark strips, located at the transition regions between bits, to fully bright and dark regions within each bit, depending on the writing state [20]. For the axial magnetization, the magnetic switching field was found to be 0.1 T.

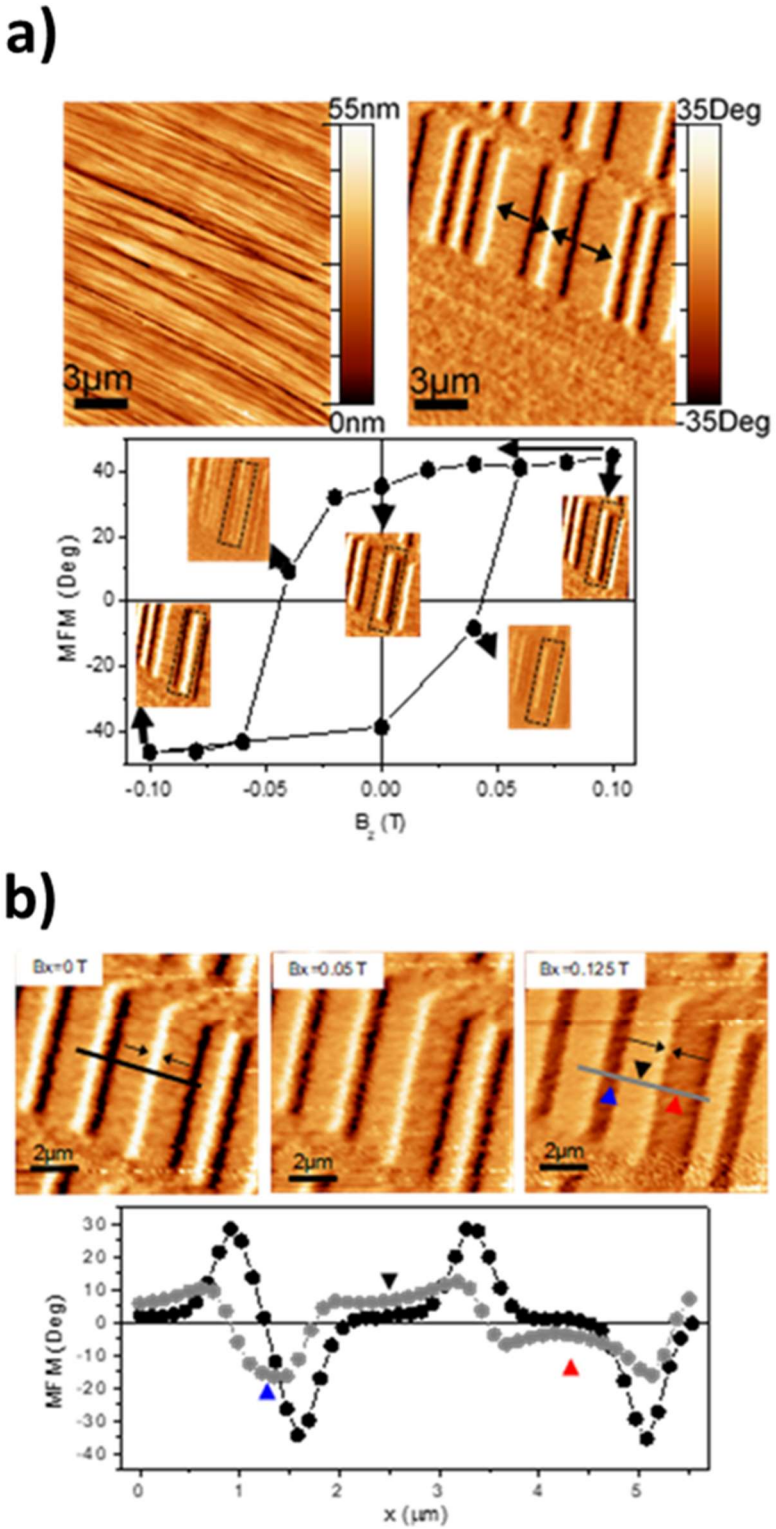

Figure 5.13. *a) Simultaneous topographic (left) and magnetic (right) images of a magnetic recording disk. Black arrows indicate the magnetization direction within the sample. Bottom panel shows axial hysteresis loops of the MFM probe deduced from images acquired at different applied fields at the same position. Insets show the images of the evolution of the domain walls of the bits. b) MFM images for different in-plane fields, always at the same location. Black arrows indicate the magnetization direction within the sample. Bottom panel shows line profiles (marked in the MFM images) showing the differences in contrast, measured when the probe magnetization direction switches from axial to transversal* [161].

The measurements shown in ***figure 5.13*** characterize the magnetic bits of a magnetic recording disk, proving the functioning of the experimental set-up developed. Nonetheless, an interesting and actual system will be studied in the next section to prove the usefulness of the equipment in real systems with real scientific interest, to show the competitiveness it could provide.

5.4 Magnetic imaging of the Graphene/β-Bi_2Pd heterostructure

This final section is dedicated to the first magnetic image acquisition of a more scientific physical system, to prove the versatility and power of the equipment described in the first part of this chapter. The studied system is the graphene/β-Bi_2Pd heterostructure, where the graphene layer was grown following the procedure explained in chapter 3, and it was transferred on the substrate as it was detailed in chapter 4. The substrate was grown by A. Correa at the *Low Temperature Laboratory* at the UAM (LBTUAM) as part of a collaboration between that group and the Magnetotransport and Heterostructures laboratory of ICMM.

5.4.1 The substrate: β-Bi_2Pd

It is a tetragonal symmetry crystal belonging to the space group *I4/mmm* with the c lattice constant almost four times greater than the in-plane one (a= 3.362(1) Å c= 12.983(1) Å) [E. Herrera PRB2015]. In addition, Bi-Bi bounds are much weaker than the Bi-Pd and Pd-Pd ones, making the compound a layered material, very easy to exfoliate [162,163]. As can be seen in ***figure 5.14***, it has an extremely flat surface. For a more detailed description, please go to references [164,165].

The critical temperature of β-Bi_2Pd is 5.4 K and the two critical fields at 0 K are at 200 Oe and 6000 Oe [163]. The growth method of the single crystal is described in [163], and is based in the so-called solution growth method.

5.4.2 Graphene transfer to the superconductor substrate

The graphene layer was grown on a polycrystalline copper foil, as it is described in chapter 2, and was transferred employing the electromechanical delamination method described in chapter 3. The β-Bi_2Pd is very easily cleaved, being very easy to obtain a clean and flat surface where graphene was placed.

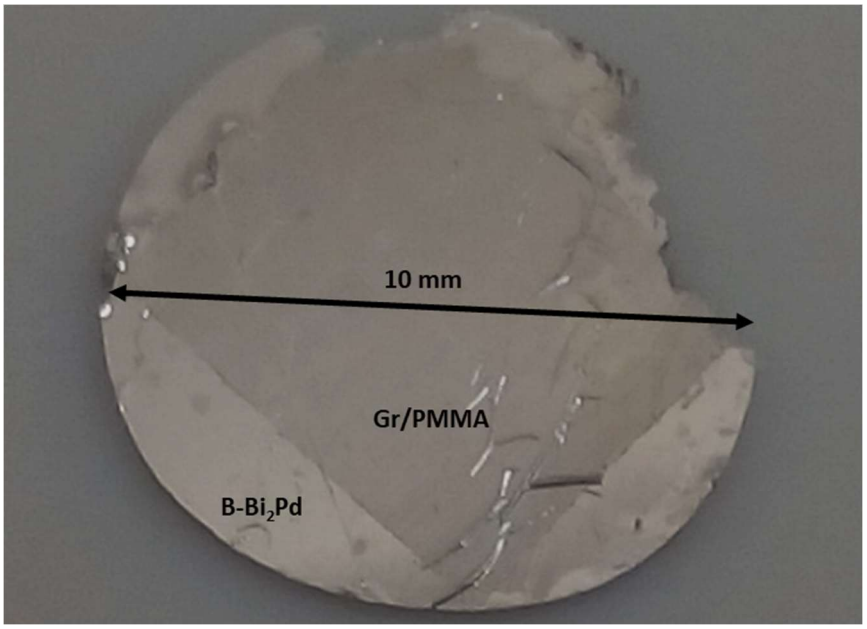

***Figure 5.14**. Picture of the superconductor β-Bi2Pd 10 mm diameter crystal with graphene transferred on top. What actually is visible in the picture is the PMMA support layer on top of graphene.*

Figure 5.14 shows the graphene already transferred to the target substrate. The transfer process was performed just an instant after cleaving it with the aim of avoiding some contamination on the surface. The transferred graphene, observed in ***figure 5.14***, appears still with the supporting layer (PMMA) not totally removed. The growth method of these crystals does not allow any annealing treatment of the transferred samples due to the metastable character of the β-phase. Any annealing treatment over 100ºC must be avoided because could generate an undesired transition out of this β phase. This was an added difficulty and then after the transfer, the remaining water was evaporated with temperatures not higher than 70ºC for several hours.

5.4.3 Characterization at RT

5.4.3.1 AFM

Prior to cool down the system for exploring the sample with the substrate in the superconducting state, it was important to check that the graphene layer was properly transferred. Then, the first characterization of the graphene/β-Bi_2Pd sample was made by acquiring topographic AFM images at room temperature, i. e. with the substrate in its normal state (***figure 5.15***).

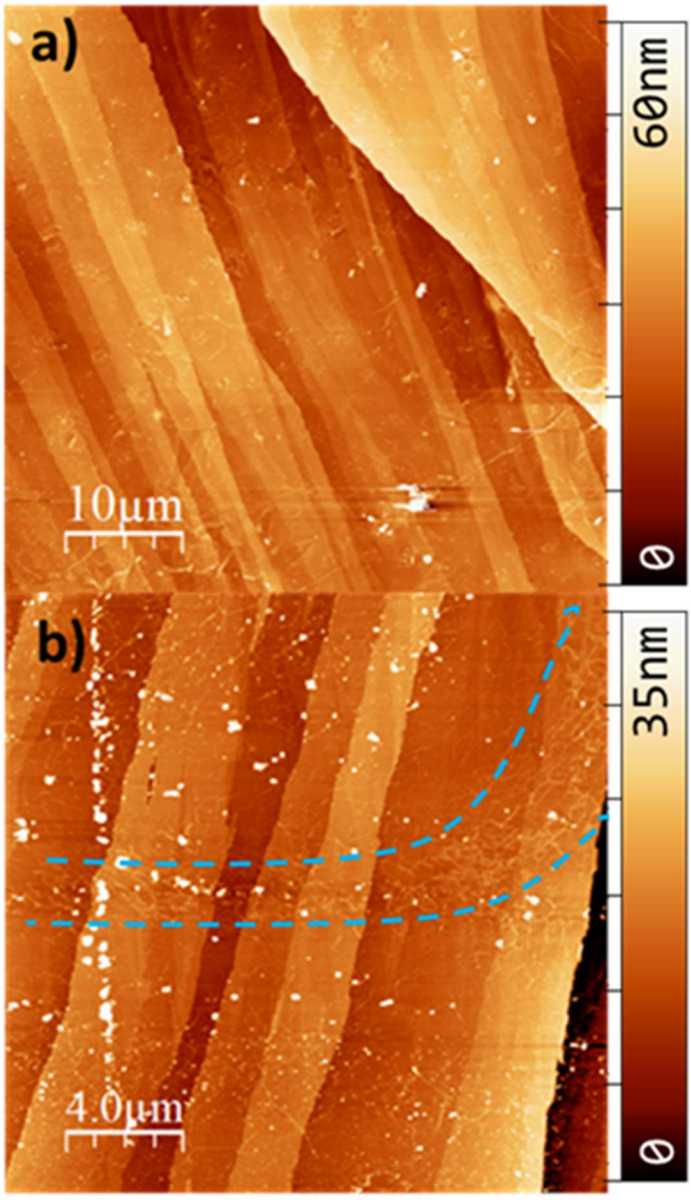

Figure 5.15 *AFM topographic images of the* graphene/β-Bi_2Pd *sample, where in addition to the flat terraces of the substrate, some of the characteristic wrinkles of graphene are visible. The dashed blue lines bounder a zone with higher density of wrinkles, formed due to manipulations when transferring.*

AFM images show that the graphene layer is extended widely over the substrate. Residuals of the polymer layer were not completely removed, but as can be seen, mainly in ***figure 5.15a***, there are clean zones were a local study can be performed. Moreover, local regions were cleaned in-situ with the probe. As a result, some contamination can be seen concentrated in a row (left side in ***figure 5.15b***) that was swept with the tip. Graphene wrinkles are visible across the terraces of the substrate. However, as can be observed in ***figure 5.15b*** there is a larger amount of wrinkles along some directions, as it has been highlighted with the blue dashed lines. This effect can be related to the manipulations that the graphene layer has suffered in the transfer process.

5.4.3.2 Raman spectroscopy

After the AFM topographic evaluation, Raman spectroscopy was performed at different points of the sample. ***Figure 5.16a*** shows the image of a confocal optical microscope with a 20x objective lens for the graphene/β-Bi_2Pd surface. In this optical micrography, the terraces of the superconducting crystal are visible. The Raman spectra (***figure 5.16b***) show the characteristic peaks of graphene, evidencing at some points a non-negligible defect peak. In the figure, it is also visible the fluorescence of the substrate as well as a peak at low energies (~60 cm^{-1}).

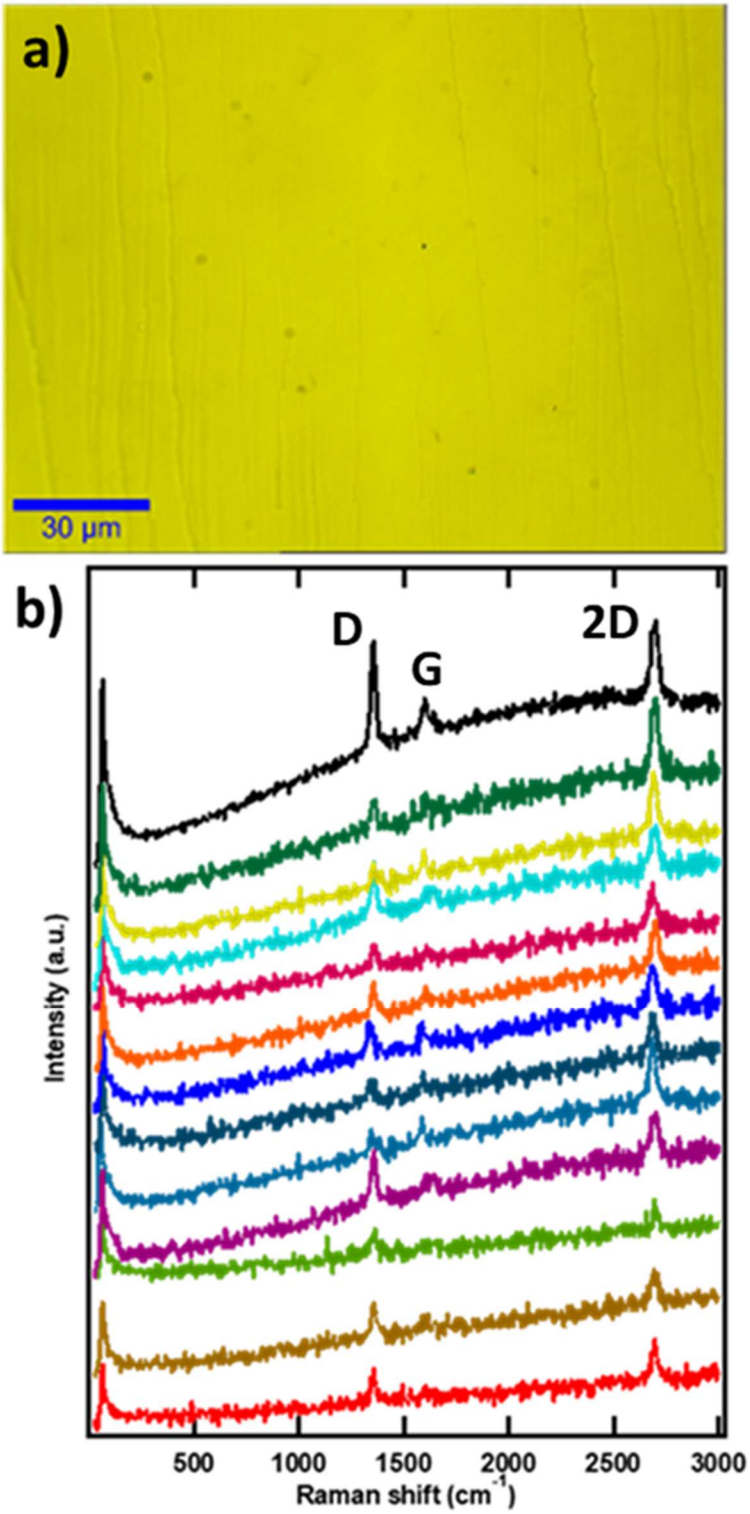

Figure 5.16. *. a) Optical image of the sample, where the terraces of the substrate are visible. b) Raman spectra acquired at different points where the graphene characteristic peaks are visible, as well as the fluorescence of the substrate and a peak at low energies (60 cm-1).*

The signal of the spectra is weak due to the high integration time needed to obtain counts, with the risk of degrading the graphene layer or have contributions from organic residuals, degraded by the incident laser. It must be considered that there are some evident differences between this sample and the graphene grown on Cu ones. From one side, the high thermal conductivity of copper and from the other, the fact that in the case of Cu no transfer was performed and, therefore, in that case there are no traces of contamination that could degrade and contribute to the Raman spectra. Due to these reasons, different integration times were applied in the Raman spectra for the graphene/β-Bi_2Pd sample. Nonetheless, although the acquisition time was enough for the case of the D and the 2D peak, it was not so in all cases for the G peak. The average values of the most interesting parameters are represented in ***table 5.4***.

G/β-Bi_2Pd	Peak position (cm^{-1})	Integrated intensity	FWHM (cm^{-1})
D	1356	300	26.3
G	1604	127	18.6
2D	2697	646	39.4

Table 5.4*. Average values of the positions, integrated intensities and FWHM of most relevant graphene peaks.*

Attending to the values of ***table 5.4***, it can be concluded that there is one monolayer graphene on top of the substrate ($\frac{I_{2D}}{I_G} \approx 5$). The 2D peak shows a symmetric shape, meaning that the contribution is made by one single component. The intensity of the D peak is three times higher than the G peak, and 0.5 times the integrated intensity of the 2D peak. In addition, there is a shift towards higher energy of the G and 2D peak, implying strain due to the transfer process in addition to an effective doping. The latter could be consequence of the previous growth of the graphene on copper with possible contribution of the supporting layer used for the transfer that could be not completely removed. This small presence could also contribute to the defect peak observed in the Raman spectra. The strains derived from the transfer process have been partially released at some points manifesting then a higher wrinkle density, which could also contribute to the defect peak. The graphene layer has been successfully transferred to this substrate, where there is a continuous layer, although the defect peak is high.

5.4.4 Characterization at LT

5.4.4.1 MFM

The main goal of the three axis vector magnet was to allow the measurements of the magnetic properties in the nanometer scale. Systems like the one presented in this chapter are susceptible to be measured in this kind of experimental set-up.

Figure 5.17 shows the simultaneously acquired images of the topography (figure a) and the magnetic signal (figure b) of a specific area of the graphene/β-Bi_2Pd sample. The image was done with the sample at 3 K and without tilting the magnetic field. The terraces of the substrate are visible in ***figure 5.17a***, and the graphene on top appears with a large wrinkle perpendicular to the step edge of the substrate. Due to this wrinkle of the layer, the zone is not homogeneous, having two different zones. The contamination produced by the transfer process has been not possible to be completely removed, although it has no further effect on the magnetic response. ***Figure 5.17b*** shows the magnetic signal of the same zone, where the hexagonal lattice of the superconducting vortices, through the graphene layer, is visible (also known as the Abrikosov lattice) . Unfortunately, the image has a bit of thermal drift. These images were acquired at 3 K temperature and at 50 Oe magnetic field.

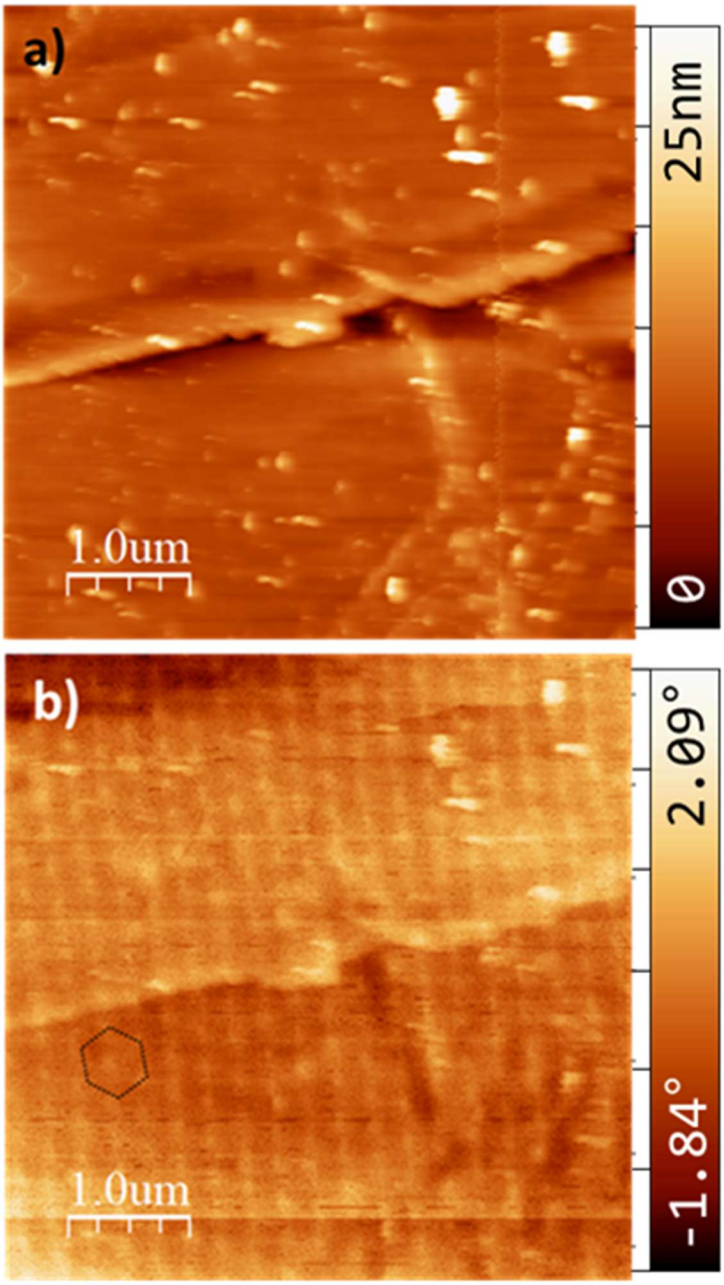

***Figure 5.17**. a) topographic image of graphene on β-Bi2Pd. b) simultaneous MFM image where the magnetic vortices are visible, with an applied magnetic field perpendicular to the surface of 50 Oe with the tip previously magnetized, at a temperature of 3 K. A hexagon is drawn to highlight the hexagonal lattice.*

5.5 Conclusions

In this chapter, as an experimental development, the description of an experimental set-up for low temperature MFM has been shown. The characterization of the magnetic field profiles has been also performed, to ensure the homogeneity of the field in the sample area. Then, to observe the capabilities of the constructed system, measurements on a recording magnetic disk have been shown, where the tilted magnetic fields have been employed, with satisfactory results.

In the last section of the manuscript, graphene (grown by using the method described in chapter 3) has been transferred to β-Bi_2Pd substrates, a superconducting material with a relatively high critical temperature (5.4 K). This heterostructure has been characterized by means of AFM and Raman spectroscopy, showing a continuous monolayer of graphene. Once the RT characterization was performed, MFM images were acquired at 3 K, showing the hexagonal (Abrikosov) lattice of vortices.

The construction of the presented experimental set-up, together with the primary results shown, the HDD magnetic measurement with differently oriented magnetic fields, as well as the vortex lattice with the perpendicularly applied field, open the possibilities of studying surface magnetic properties of different type of physical systems. Moreover, a MFM means that magnetic imaging is also possible to perform, in addition to different type of physical properties. Correlated systems where the topography, electrical transport and surface potential among others with a direct or indirect dependence with magnetic fields and/or temperature variations can be studied.

Chapter 6. Conclusions

The main goal of the present doctoral work is the growth of large area monolayer graphene on Cu foils in UHV conditions using C_{60} as precursor molecules. The growth mechanism is based on the decomposition of the C_{60} molecules, a thermally activated process promoted by the Cu surface and the posterior diffusion process given on the surface of the copper. This process presents several advantages with respect to the use of hydrocarbons as carbon sources. It requires lower substrate temperature than conventional CVD graphene growth methods, where typical temperatures of 1000°C are employed, while in the method presented here the temperature is of 800°C. The decrease of the temperature results in two main advantages: on one hand, fewer impurities are segregated to the surface, promoting an ultra-pure graphene-copper interface, and on the other hand the solubility of carbon into the Cu bulk is reduced, avoiding the formation of bilayer or few layer domains in the graphene layer. Moreover, in our experimental protocol UHV conditions were used. Therefore, the surface was atomically clean before experiments, so no oxygen was involved or intercalated during the process.

Different characterization techniques were applied on the as-grown samples in order to evaluate the quality and the properties of the graphene layer. The in-situ LEED pattern of the Cu foils after the surface cleaning process showed characteristic spots of different Cu facets, corresponding to a typical polycrystalline specimen. After graphene growth, a clear ring feature appears in the in-situ LEED pattern, that evidence the presence of a multigrain graphene film on the surface, although some graphene orientations prevail. The morphology of the graphene layer was studied by ex-situ AFM. The AFM images showed completely covered areas with a uniform graphene film on the Cu foil. Graphene wrinkles, crossing the substrate terraces, were also observed. Raman spectra, similar along the sample surface, showed a narrow 2D band as well as G and D peaks. By investigating the surface chemical composition by XPS, sp^2 hybridized carbon emission is the main contribution and only low contents in functional groups were observed after exposing the sample to atmospheric conditions. ARPES measurements showed that the band structure of graphene grown on the Cu foil is based on multiple linearly dispersing graphene bands, corresponding to different graphene grains as well as an n-type doping character. All results prove that the envisaged protocol to synthesize graphene from C_{60} molecules is a successful strategy to obtain large area uniform single layer graphene on technologically relevant substrates at lower temperature than the wide-spread CVD method.

The next step after the growth of graphene on transition metal substrates, in our case polycrystalline copper foils and copper single crystals consisted on the transfer of the graphene layer to insulating substrates. Firstly, the protocol employed for transferring the graphene layer

to a SiO_2 substrate as well as the difficulties found to achieve optimal results due to the interaction between graphene and the substrate were shown. Transport measurements at room and low temperature on the transferred graphene layer showed acceptable results, with expected manifestation of quantum interference phenomenon (Weak localization) and a coherence length of tens of nanometers. Nonetheless, the high-quality of the graphene layers obtained by the PVD method demanded an improvement of those results. The main problem relied on the interaction between the graphene layer and the underlying substrate generated by using the PVD method with C_{60} molecules for growing graphene and the UHV environment that provided a clean metal surface that the same interaction that provided the decomposition of the fullerenes, generated an interaction between the graphene layer and the metal.

For this purpose, two different approaches have been described to weaken this significant interaction: a chemical approach where a large molecule (TOA^+) is intercalated by using an electrolytic bath,and a physical approach where oxygen has been intercalated in UHV environment. Both approaches have shown to improve the transfer process and the results obtained on transferred samples. Moreover, we have demonstrated that the oxygen intercalation electronically decouples de graphene layer, as concluded by Raman spectroscopy, where the 2D graphene peak become detectable only after the intercalation. One could envisage that, with a proper optimization of the methodology, the intercalated oxygen could be tailored in order to have an insulating substrate without any transfer process. The main advantage would be that the whole process could be accomplished in UHV environment, avoiding contamination during the whole growth and intercalation process.

Finally, as experimental development, the description of an experimental set-up for low temperature MFM has been shown. The characterization of the magnetic field profiles has been also performed, to ensure the homogeneity of the field in the sample area. Then, to observe the capabilities of the constructed system, measurements on a recording magnetic disk have been shown, where the tilted magnetic fields have been employed, with satisfactory results.

The prove of the set-up on an actual physical system is shown in the last section of the manuscript, a graphene/superconductor heterostructure has been measured, where graphene (grown by using the method described in chapter 3) has been transferred to β-Bi_2Pd substrates, a superconducting material with a relatively high critical temperature (5.4 K). This heterostructure has been characterized by means of AFM and Raman spectroscopy, showing a continuous monolayer of graphene. Once the RT characterization was performed, MFM images were acquired at 3 K, showing the hexagonal (Abrikosov) lattice of vortices. Those magnetic measurements were performed after the construction of a specific experimental set-

up was carried out. A description of the implemented equipment is also detailed together with the primary results on a HDD magnetic measurement with differently oriented magnetic fields. Thus, the preliminary results on the vortex lattice of the graphene/β-Bi_2Pd sample performed with the perpendicularly applied field, open the possibilities of studying surface magnetic properties of different type of physical systems. Therefore, correlated systems where the topography, electrical transport and surface potential among others, with a direct or indirect dependence with magnetic fields and/or temperature variations, could be hereinafter studied using the new equipment.

Conclusiones

El objeto principal de la presente tesis doctoral has sido el crecimiento de grafeno en láminas de cobre en condiciones de UHV utilizando moléculas C_{60} como precursores de carbono. El mecanismo de crecimiento se basa en la descomposición de dichas moléculas, un proceso térmicamente activado y catalizado a su vez a través de la superficie del cobre y su posterior difusión que se da en la superficie del cobre. Este procedimiento presenta varias ventajas en comparación con los empleados utilizando hidrocarburos como precursores. Requiere una temperatura más baja del sustrato que el requerido en métodos CVD convencionales, donde la temperatura típica es de unos 1000°C, mientras que en este método que se expone es de unos 800°C. Esta disminución en la temperatura proporciona dos ventajas: por un lado, las impurezas que puedan ser segregadas del volumen a la superficie disminuyen, proporcionando una interfaz grafeno/cobre extremadamente limpia, y por otro desciende la solubilidad del carbón en el volumen del cobre, evitando así la formación de dominios de bicapas o multicapas de grafeno. Además, debido a la aplicación de protocolos de UHV, la superficie disponía de una extremada limpieza, a nivel atómico, por lo que no había ningún tipo de involucración ni intercalación de oxígeno durante todo el proceso.

Para la evaluación de la calidad y propiedades de la lámina de grafeno, se emplearon diferentes técnicas de caracterización en las muestras recién crecidas. El patrón LEED de las láminas de cobre, obtenido in-situ después del proceso de limpieza mostraba los puntos característicos de diferentes facetas del cobre, correspondientes a un patrón típico de cobre policristalino. Después del crecimiento de grafeno, el patrón de LEED mostraba un anillo proveniente del grafeno mutidominio de la superficie, aunque ciertas orientaciones prevalecían, provocando una pequeña modulación de dicho anillo. La morfología de la lámina de grafeno se estudió por medio de AFM, fuera de la cámara de crecimiento. Las imágenes obtenidas por dicha técnica mostraban áreas completamente cubiertas con una capa uniforme de grafeno encima de la lámina de cobre. También se observaron los pliegues del grafeno atravesando las terrazas de cobre. A su vez, en los espectros Raman se podían ver estrechos picos 2D así como los picos G y D. Examinando la composición química de la superficie por medio de XPS, se pudo observar que la principal emisión correspondía al orbital molecular sp^2, con pequeñas contribuciones de grupos funcionales después de haber sido expuesto a condiciones atmosféricas. La estructura de bandas fue observada con medidas de ARPES donde se veía una relación lineal en la dispersión alrededor del punto de alta simetría, así como un dopaje tipo n. Se apreciaba más de una relación de dispersión que provenían de distintos dominios de grafeno. Todos los resultados indican que el protocolo de síntesis utilizando moléculas C_{60} es un método que proporciona grandes áreas de una sola capa de grafeno en sustratos tecnológicamente relevantes a una temperatura sensiblemente inferior al utilizado en el tan extendido método CVD.

El paso posterior al crecimiento de grafeno en metales de transición como la lámina policristalina y monocristales de cobre en nuestro caso, consiste en la transferencia de la lámina de grafeno a sustratos aislantes. Primero se ha mostrado tanto el protocolo empleado como las dificultades encontradas para la transferencia de la lámina a sustratos de SiO_2. Estas dificultades son debidas a la interacción entre el sustrato y el grafeno. Se han hecho medidas de magnetotransporte tanto a temperatura ambiente como a baja temperatura (2 K) donde se han obtenido resultados aceptables y donde se ha observado la esperada manifestación de interferencia cuántica (Weak localization) a campos magnéticos bajos, de donde se ha podido determinar que la longitud de coherencia es del orden de decenas de nanómetros. A pesar de estos resultados, la alta calidad de grafeno obtenida de este método de crecimiento requiere una mejora en estos resultados. El problema de la transferencia ha resultado ser debido al mismo hecho por el que se ha conseguido crecer el grafeno a partir de fullerenos: la interacción del sustrato con la lámina de grafeno.

Con el propósito de eliminar o al menos disminuir esta interacción, se ha procedido por dos rutas radicalmente diferentes a debilitar dicha interacción: se ha empleado un método electroquímico para intercalar una molécula grande (TOA^+) por un lado, y por otro se ha intercalado oxígeno en condiciones de UHV. Ambos métodos han mejorado la transferencia y los resultados obtenidos en las muestras transferidas. Más allá, se ha demostrado que el oxígeno intercalado desacopla electrónicamente la lámina de grafeno, como se ha concluido de la espectroscopía Raman, donde el pico 2D es detectable una vez se ha intercalado el oxígeno. Se puede esperar que, con una optimización de la metodología, el oxígeno intercalado podría intercalarse de tal manera que se podría obtener un sustrato aislante sin necesidad de transferir la lámina de grafeno. Además, esto conllevaría a que todo el proceso (crecimiento en metales y grafeno sobre un aislante) podría llevarse a cabo en un entorno UHV, evitando la contaminación durante todo el proceso tanto de crecimiento como de intercalación.

Finalmente, como desarrollo experimental, se enseña la descripción de un equipo experimental para un MFM de baja temperatura. Se muestra la caracterización de los perfíles magnéticos, para asegurar la homogeneidad del campo en el área correspondiente a la muestra. Para observar la capacidad del sistema construido, se han hecho medidas de un disco de grabación magnético donde se han empleado campos magnéticos inclinados, donde los resultados han sido satisfactorios.

Para probar el montaje experimental en un sistema físico de interés científico, la última parte del manuscrito se centra en las medidas de una heteroestructura grafeno/superconductor

donde el grafeno (crecido con el método descrito en el capítulo 3) ha sido transferido al sustrato β-Bi_2Pd , un material superconductor con una temperatura crítica relativamente alta (5.4 K). Esta heteroestructura ha sido caracterizada por medio de AFM y espectroscopía Raman, donde se aprecia una monocapa continua de grafeno. Una vez hecha la caracterización a temperatura ambiente, las imágenes de MFM fueron adquiridas a 3 K, donde se observa la red hexagonal de vórtices (Abrikosov). Estas medidas preliminares, junto con las hechas en el disco duro (HDD), abren la posibilidad de estudiar las propiedades magnéticas de superficie de diferentes sistemas físicos. Así, sistemas fuertemente correlacionados donde la topografía, transporte eléctrico y el potencial superficial entre otros con una dependencia directa o indirecta con campos magnéticos y/o variaciones en temperatura pueden ser estudiados por medio de este nuevo equipo experimental.

Appendix

In order to understand the structural and electronic decoupling process of graphene from the copper substrate as the intercalated oxygen content increases in between the Gr/Cu interface, DFT based calculations for different intercalated oxygen coverages were performed. Thus, two different configurations were explored to position the single layer graphene on Cu(111). ***Figure A.1*** shows both configurations: a) with the centers of the graphene rings lying "on-top" Cu sites named as "configuration I" and b) with the centers of the graphene rings lying "on-hollow" 3-Cu sites named as "configuration II". The calculations indicate as slightly more energetically stable the "configuration II".

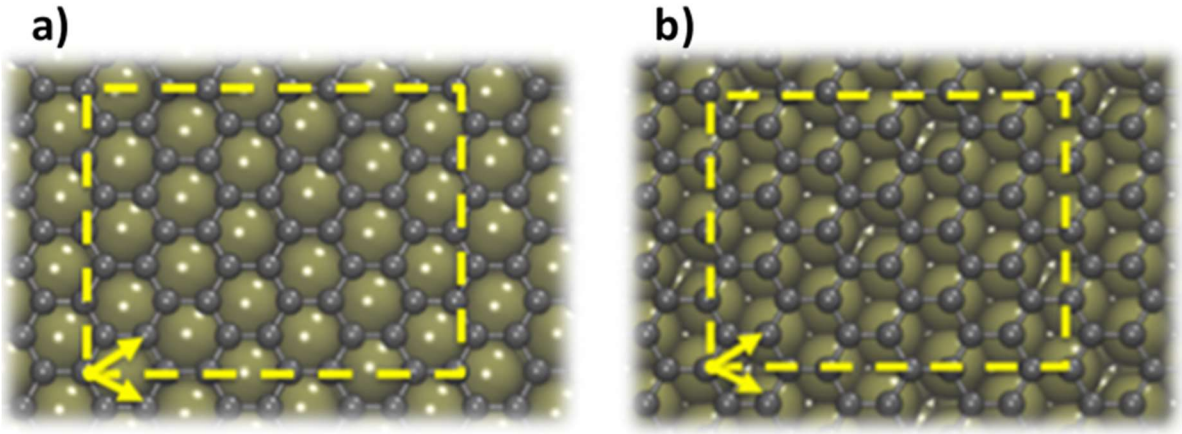

Figure A.1*. Two different configurations computationally explored to position the single layer graphene on the Cu (111) surface. a) centers of the graphene rings lying "on-top" Cu sites and b) centers of the graphene rings lying "on-hollow" 3-Cu sites. Yellow arrowed lines indicate the canonical lattice vectors and yellow dashed-line boxes indicate the unit cell used in the calculations.*

The top panel of ***figure A.2*** shows the graphene corrugation, C^{Gr} in Å (being the perpendicular distance between the topmost and bottommost C atoms in the graphene layer), as a function of the surface intercalated oxygen coverage (in monolayer units) in both "configurations I and II". For 0 ML the graphene shows corrugations of 0.17 and 0.15 Å, which decreases up to a value < 0.01 Å for 1 ML. It is important to notice that for 0.5 ML the graphene flattens almost completely by effect of the reduction in the interaction with the surface.

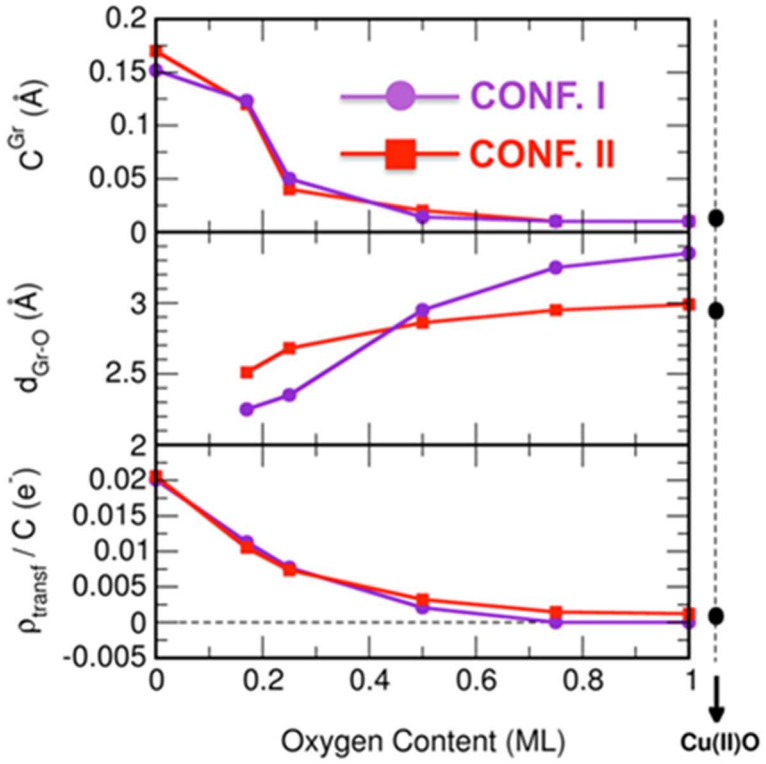

***Figure A.2**. Top panel: graphene corrugation, CGr (being the perpendicular distance between the topmost and bottommost C atoms in the graphene layer). Middle panel: average Gr-O perpendicular distance, dGr-O. Bottom panel: electronic charge transferred from the Cu surface towards the graphene as a function of the coverage of the surface intercalated oxygen.*

The middle panel of ***figure A.2*** shows the average Gr-O perpendicular distance, d_{Gr-O} in Å, as a function of the surface intercalated oxygen coverage in (ML units) in both "configurations I and II". The distance starts to increase from 2.5 Å (0.17 ML) up to 3 Å (1 ML) for "configuration II", while it starts at a lower value of 2.25 Å (0.17 ML) up to a higher one of 3.85 Å (1ML) for "configuration I". According to these values, the structural graphene decoupling seems to be more pronounced with the increasing of the surface O-content for the "configuration I", which makes sense given the weaker interaction between the graphene and the substrate for this configuration. In both configurations we observe that for O-contents higher than around 0.5 ML the distance is higher than 3 Å, which justifies the structural graphene decoupling. Finally, bottom panel of ***figure A.2*** shows the electronic charge transferred from the Cu surface towards the graphene [166] as a function of the surface intercalated oxygen coverage (in ML units) in both "configurations I and II". Curves for both configurations are very similar, and the electronic charge transferred from the substrate decreases from values around 0.02 (0ML) up to 0.002 (1 ML) e^-/C. Interestingly, the charge transferred almost vanishes from O-contents above 0.5 ML, which would also justify in both configurations a high degree of electronic decoupling. As observed in the variation of the different quantities shown in ***figure A.2*** with the

increasing O-content, the physical graphene decoupling produces independently on the configurations analyzed, not only from the structural point of view but also from the electronic considerations. It is interesting to notice that the quantities shown in ***figure A.2*** have been also computed for an optimized model of Gr/Cu(II)O (tenorite) interface, with an equivalent intercalated O-content of 1 ML. The results obtained for those quantities in that model are shown also in ***figure A.2*** (lateral points at the right side) and are practically equal than those obtained for the case of Gr/CuO@Cu(111) in its most stable "configuration II".

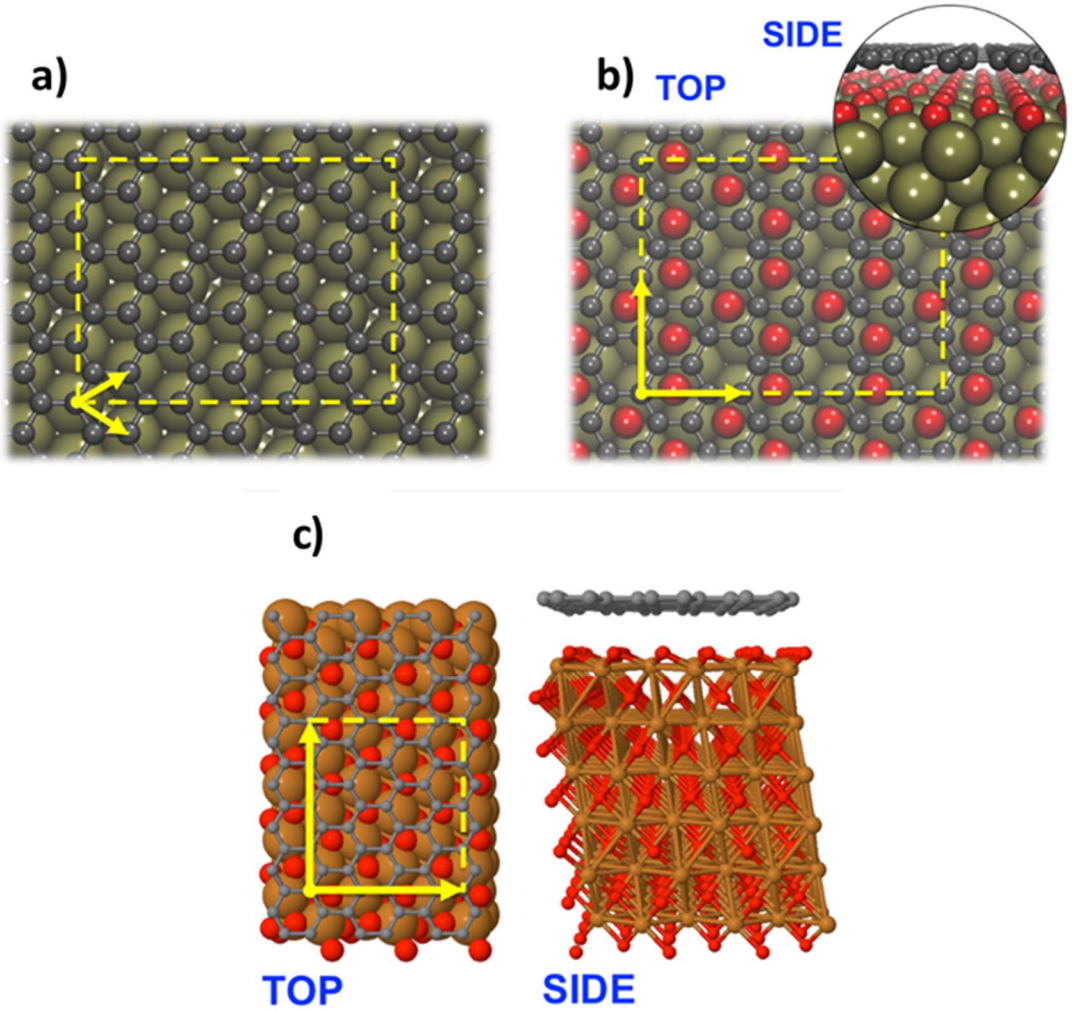

Figure A.3*. Top and side view pictorial schemes of the different geometries considered in the calculations. a) the Gr/Cu (111) without oxygen intercalation, b) the Gr/Cu4O3@Cu(111) interface (0.75 ML), and c) the Gr/Cu(II)O (tenorite) interface. C, O and Cu atoms correspond to grey, red and tan spheres.*

Figure A.3a shows the "configuration II" (graphene rings "on-hollow"), with no oxygen intercalation. In the next image (***figure A.3b***), the oxygen intercalation is simulated, with a 0.75

of coverage. The oxygen atoms are situated “on-hollow”, right below the graphene rings, with some oxygen vacancies, corresponding to the relation of 3 atoms of oxygen per 4 of copper. These observed vacancies, are filled when the monolayer is complete. The employed unit cell and canonical basis is changed due to the symmetry change with the oxygen layer intercalated. In ***figure A.3c*** Gr/Cu(II)O (tenorite) is represented, where the configuration of the graphene over the tenorite is different to the adsorbed oxygen layer on Cu (111) but, as has been shown in ***figure A.2***, the parameters taken into account (graphene corrugation, graphene-oxygen equilibrium distance and the charge transfer) are equivalent for the “configuration II” and the tenorite, suggesting that the topmost layer of the Cu substrate is the responsible of the graphene-copper coupling.

The projected density of states (PDOS) onto the graphene layer for the cases of free-standing single layer graphene, Gr/Cu(111) in its most stable configuration and for 0.75 ML (Gr/Cu_4O_3: solid orange line) as a function of the energy referred to the Fermi energy is represented in the figure 4.22 of the chapter 4.

References

[1] C.H. Online, the Cambridge Ancient History Volume Iii, III (2008).

[2] N. KS, G. AK, M. SV, D. Jiang, Y. Zhang, D. SV, G. IV, F. AA, Electric Field Effect in Atomically Thin Carbon Films, Science (80-.). 306 (2004) 666–669.

[3] P.R. Wallace, The band theory of graphite, Phys. Rev. 71 (1947) 622–634. doi:10.1103/PhysRev.71.622.

[4] A.H.C. Neto, F. Guinea, N.M.R. Peres, K.S. Novoselov, A.K. Geim, The electronic properties of graphene, 81 (2007). doi:10.1103/RevModPhys.81.109.

[5] S. Das Sarma, S. Adam, E.H. Hwang, E. Rossi, Electronic transport in two-dimensional graphene, Rev. Mod. Phys. 83 (2011) 407–470. doi:10.1103/RevModPhys.83.407.

[6] ando1998.pdf, (n.d.).

[7] N. Stander, B. Huard, D. Goldhaber-Gordon, Evidence for Klein tunneling in graphene p-n junctions, Phys. Rev. Lett. 102 (2009) 1–4. doi:10.1103/PhysRevLett.102.026807.

[8] A.F. Young, P. Kim, Quantum interference and Klein tunnelling in graphene heterojunctions, Nat. Phys. 5 (2009) 222–226. doi:10.1038/nphys1198.

[9] K.S. Novoselov, A.K. Geim, Sv. Morozov, D. Jiang, Mi. Katsnelson, Iv. Grigorieva, Sv. Dubonos, and A.A. Firsov, Two-dimensional gas of massless Dirac fermions in graphene, Nature. 438 (2005) 197.

[10] Y.-W. Tan, Y. Zhang, K. Bolotin, Y. Zhao, S. Adam, E.H. Hwang, S. Das Sarma, H.L. Stormer, P. Kim, Measurement of scattering rate and minimum conductivity in graphene, Phys. Rev. Lett. 99 (2007) 246803.

[11] N. Mounet, N. Marzari, First-principles determination of the structural, vibrational and thermodynamic properties of diamond, graphite, and derivatives, Phys. Rev. B - Condens. Matter Mater. Phys. 71 (2005) 1–14. doi:10.1103/PhysRevB.71.205214.

[12] S. Graphene, A.A. Balandin, S. Ghosh, W. Bao, I. Calizo, Superior Thermal Conductivity of, Nano. (2008).

[13] S. Ghosh, I. Calizo, D. Teweldebrhan, E.P. Pokatilov, D.L. Nika, A.A. Balandin, W. Bao, F. Miao, C.N. Lau, Extremely high thermal conductivity of graphene: Prospects for thermal management applications in nanoelectronic circuits, Appl. Phys. Lett. 92 (2008) 1–4. doi:10.1063/1.2907977.

[14] R. Boyd, M.W. Feldman, C. Transmission, K.N. Laland, P.J. Richerson, K. Aoki, J. Kumm, D. Nakanishi, T.J. Valone, J.J. Templeton, K. Eriksson, S. Ghirlanda, K. Laland, R.H. Wagner, S. Huck, J. Oechssler, L. Rendell, R.W. Osborne, C.L. Nehaniv, R. Mcelreath, T.W. Pike, W.D. Hamilton, A. Xanthopoulos, J. Valimaki, P. Fischer, J.N. Tsitsiklis, Two-Dimensional Phonon Transport, 328 (2010) 213–216.

[15] P. Blake, E.W. Hill, A.H. Castro Neto, K.S. Novoselov, D. Jiang, R. Yang, T.J. Booth, A.K. Geim, Making graphene visible, Appl. Phys. Lett. 91 (2007). doi:10.1063/1.2768624.

[16] K.I. Bolotin, K.J. Sikes, Z. Jiang, M. Klima, G. Fudenberg, J. Hone, P. Kim, H.L. Stormer, Ultrahigh electron mobility in suspended graphene, Solid State Commun. 146 (2008) 351–355.

[17] A. Castellanos-Gomez, M. Buscema, R. Molenaar, V. Singh, L. Janssen, H.S.J. Van Der Zant, G.A. Steele, Deterministic transfer of two-dimensional materials by all-dry viscoelastic stamping,

2D Mater. 1 (2014). doi:10.1088/2053-1583/1/1/011002.

[18] C. Berger, Z. Song, T. Li, X. Li, A.Y. Ogbazghi, R. Feng, Z. Dai, N. Alexei, M.E.H. Conrad, P.N. First, W.A. De Heer, Ultrathin epitaxial graphite: 2D electron gas properties and a route toward graphene-based nanoelectronics, J. Phys. Chem. B. 108 (2004) 19912–19916. doi:10.1021/jp040650f.

[19] Y. Hernandez, V. Nicolosi, M. Lotya, F.M. Blighe, Z. Sun, S. De, I.T. McGovern, B. Holland, M. Byrne, Y.K. Gun'ko, J.J. Boland, P. Niraj, G. Duesberg, S. Krishnamurthy, R. Goodhue, J. Hutchison, V. Scardaci, A.C. Ferrari, J.N. Coleman, High-yield production of graphene by liquid-phase exfoliation of graphite, Nat. Nanotechnol. 3 (2008) 563–568. doi:10.1038/nnano.2008.215.

[20] J.N. Coleman, M. Lotya, A.O.' Neill, S.D. Bergin, P.J. King, U. Khan, K. Young, A. Gaucher, S. De, R.J. Smith, I. V Shvets, S.K. Arora, G. Stanton, H.-Y. Kim, K. Lee, G.T. Kim, G.S. Duesberg, T. Hallam, J.J. Boland, J.J. Wang, J.F. Donegan, J.C. Grunlan, G. Moriarty, A. Shmeliov, R.J. Nicholls, J.M. Perkins, E.M. Grieveson, K. Theuwissen, D.W. Mccomb, P.D. Nellist, V. Nicolosi, Supporting Online Material for Two-Dimensional Nanosheets Produced by Liquid Exfoliation of Layered Materials Two-dimensional nano-sheets produced by liquid exfoliation of layered materials, Science (80-.). 331 (2011) 568–571. doi:10.1126/science.1194975.

[21] A. Reina, X. Jia, J. Ho, D. Nezich, H. Son, V. Bulovic, M.S. Dresselhaus, J. Kong, Large Area , Few-Layer Graphene Films on Arbitrary Substrates by Chemical Vapor Deposition 2009, (2009) 1–6.

[22] C. Mattevi, M. Chhowalla, A review of chemical vapour deposition of graphene on copper †, (2011) 3324–3334. doi:10.1039/c0jm02126a.

[23] P.W. Sutter, J.I. Flege, E.A. Sutter, Epitaxial graphene on ruthenium, Nat. Mater. 7 (2008) 406–411. doi:10.1038/nmat2166.

[24] S. Roth, J. Osterwalder, T. Greber, Synthesis of epitaxial graphene on rhodium from 3-pentanone, Surf. Sci. 605 (2011) L17–L19. doi:10.1016/j.susc.2011.02.007.

[25] A.T. N'Diaye, J. Coraux, T.N. Plasa, C. Busse, T. Michely, Structure of epitaxial graphene on Ir(111), New J. Phys. 10 (2008). doi:10.1088/1367-2630/10/4/043033.

[26] A.L. Pinardi, P. Merino, S. Gardonio, S. Lizzit, K. Van De Ruit, G. Otero, C. Gonza, P.L. De Andre, J.A. Martı, Ordered Vacancy Network Induced by the Growth of Epitaxial Graphene on Pt (111), 216102 (2010) 1–4. doi:10.1103/PhysRevLett.105.216102.

[27] L. Gao, W. Ren, H. Xu, L. Jin, Z. Wang, T. Ma, L.P. Ma, Z. Zhang, Q. Fu, L.M. Peng, X. Bao, H.M. Cheng, Repeated growth and bubbling transfer of graphene with millimetre-size single-crystal grains using platinum, Nat. Commun. 3 (2012) 697–699. doi:10.1038/ncomms1702.

[28] R. Muñoz, C. Gómez-Aleixandre, Review of CVD synthesis of graphene, Chem. Vap. Depos. 19 (2013) 297–322. doi:10.1002/cvde.201300051.

[29] G.A. López, E.J. Mittemeijer, The solubility of C in solid Cu, Scr. Mater. 51 (2004) 1–5. doi:10.1016/j.scriptamat.2004.03.028.

[30] S. Hussain, M. Iqbal, J. Park, M. Ahmad, J. Singh, J. Eom, J. Jung, Physical and electrical properties of graphene grown under different hydrogen flow in low pressure chemical vapor deposition, Nanoscale Res. Lett. 9 (2014) 546. doi:10.1186/1556-276X-9-546.

[31] S. Chen, H. Ji, H. Chou, Q. Li, H. Li, J.W. Suk, R. Piner, L. Liao, W. Cai, R.S. Ruoff, Millimeter-size single-crystal graphene by suppressing evaporative loss of Cu during low pressure chemical vapor deposition, Adv. Mater. 25 (2013) 2062–2065. doi:10.1002/adma.201204000.

[32] D. Geng, B. Wu, Y. Guo, L. Huang, Y. Xue, J. Chen, G. Yu, L. Jiang, W. Hu, Y. Liu, Uniform hexagonal graphene flakes and films grown on liquid copper surface, Proc. Natl. Acad. Sci. 109 (2012) 7992–7996. doi:10.1073/pnas.1200339109.

[33] A.B. Preobrajenski, M.L. Ng, A.S. Vinogradov, N. Mårtensson, Controlling graphene corrugation on lattice-mismatched substrates, Phys. Rev. B - Condens. Matter Mater. Phys. 78 (2008) 2–5. doi:10.1103/PhysRevB.78.073401.

[34] Q. Zhou, S. Coh, M.L. Cohen, S.G. Louie, A. Zettl, Imprint of transition metal d orbitals on a graphene Dirac cone, 235431 (2013) 1–5. doi:10.1103/PhysRevB.88.235431.

[35] J. Wintterlin, M.L. Bocquet, Graphene on metal surfaces, Surf. Sci. 603 (2009) 1841–1852. doi:10.1016/j.susc.2008.08.037.

[36] M. Andersen, L. Hornekær, B. Hammer, Understanding intercalation structures formed under graphene on Ir(111), Phys. Rev. B - Condens. Matter Mater. Phys. 90 (2014) 1–9. doi:10.1103/PhysRevB.90.155428.

[37] E. Grånäs, J. Knudsen, U.A. Schröder, T. Gerber, C. Busse, M.A. Arman, K. Schulte, J.N. Andersen, T. Michely, Oxygen intercalation under graphene on Ir(111): Energetics, kinetics, and the role of graphene edges, ACS Nano. 6 (2012) 9951–9963. doi:10.1021/nn303548z.

[38] R. Larciprete, S. Ulstrup, P. Lacovig, M. Dalmiglio, M. Bianchi, F. Mazzola, L. Hornekær, F. Orlando, A. Baraldi, P. Hofmann, S. Lizzit, Oxygen switching of the epitaxial graphene-metal interaction, ACS Nano. 6 (2012) 9551–9558. doi:10.1021/nn302729j.

[39] E. Starodub, N.C. Bartelt, K.F. McCarty, Oxidation of graphene on metals, J. Phys. Chem. C. 114 (2010) 5134–5140. doi:10.1021/jp912139e.

[40] P. Sutter, J.T. Sadowski, E.A. Sutter, Chemistry under Cover: Tuning Metal−Graphene Interaction by Reactive Intercalation, J. Am. Chem. Soc. 132 (2010) 8175–8179. doi:10.1021/ja102398n.

[41] C. Riedl, C. Coletti, T. Iwasaki, A.A. Zakharov, U. Starke, Quasi-free-standing epitaxial graphene on SiC obtained by hydrogen intercalation, Phys. Rev. Lett. 103 (2009) 1–4. doi:10.1103/PhysRevLett.103.246804.

[42] I. Gierz, T. Suzuki, R.T. Weitz, D.S. Lee, B. Krauss, C. Riedl, U. Starke, H. Höchst, J.H. Smet, C.R. Ast, K. Kern, Electronic decoupling of an epitaxial graphene monolayer by gold intercalation, Phys. Rev. B - Condens. Matter Mater. Phys. 81 (2010) 1–6. doi:10.1103/PhysRevB.81.235408.

[43] M. Petrović, I. Šrut Rakić, S. Runte, C. Busse, J.T. Sadowski, P. Lazić, I. Pletikosić, Z.H. Pan, M. Milun, P. Pervan, N. Atodiresei, R. Brako, D. Šokčević, T. Valla, T. Michely, M. Kralj, The mechanism of caesium intercalation of graphene, Nat. Commun. 4 (2013) 1–8. doi:10.1038/ncomms3772.

[44] T. Pichler, X. Liu, Core level shifts of intercalated graphene, (2017). doi:10.1088/2053-1583/4/1/015013.

[45] A.M.-R. (Universidad A. de Madrid), Estudio del crecimiento, difusión, intercalación y dopaje en grafeno/Rh(111) mediante STM en condiciones de UHV, 2016.

[46] N.H. Jo, Q. Lin, M.C. Nguyen, U.S. Kaluarachchi, W.R. Meier, S. Manni, S.S. Downing, A.E. Böhmer, T. Kong, Y. Sun, V. Taufour, C.Z. Wang, K.M. Ho, S.L. Bud'ko, P.C. Canfield, Growth and characterization of BaZnGa, Philos. Mag. 97 (2017) 3317–3324. doi:10.1080/14786435.2017.1380861.

[47] D. Shin, S.-K. Bae, C. Yan, J.-M. Kang, J.-C. Ryu, J.-H. Ahn, B.-H. Hong, Synthesis and

applications of graphene electrodes, Carbon Lett. 13 (2012) 1–16. doi:10.5714/CL.2012.13.1.001.

[48] J.C. Vickerman, Surface Analysis: Techniques and Applications, Wiley, 1997.

[49] G. Ertl, J. Küppers, R.L. Park, Low-Energy Electrons and Surface Chemistry, Phys. Today. 29 (1976) 57. doi:10.1063/1.3023372.

[50] L. DE BROGLIE, Waves and Quanta, Nature. 112 (1923) 540. http://dx.doi.org/10.1038/112540a0.

[51] C.J. Davisson, The Diffraction of Electrons by a Crystal of Nickel, Bell Syst. Tech. J. 7 (1928) 90–105. doi:10.1002/j.1538-7305.1928.tb00342.x.

[52] N.W. Ashcroft, N.D. Mermin, Solid State Physics, Holt, Rinehart and Winston, 1976. https://books.google.es/books?id=1C9HAQAAIAAJ.

[53] G. Binnig, H. Rohrer, C. Gerber, E. Weibel, Surface studies by scanning tunneling microscopy, Phys. Rev. Lett. 49 (1982) 57–61. doi:10.1103/PhysRevLett.49.57.

[54] G. Binnig, C.F. Quate, Atomic Force Microscope, Phys. Rev. Lett. 56 (1986) 930–933. doi:10.1103/PhysRevLett.56.930.

[55] G. Binnig, C.H. Gerber, E. Stoll, T.R. Albrecht, C.F. Quate, Atomic resolution with atomic force microscope, Europhys.Lett. 3 (1987) 1281–1286.

[56] N. Jalili, K. Laxminarayana, A review of atomic force microscopy imaging systems: Application to molecular metrology and biological sciences, Mechatronics. 14 (2004) 907–945. doi:10.1016/j.mechatronics.2004.04.005.

[57] R. García, Dynamic atomic force microscopy methods, 2002. doi:10.1016/S0167-5729(02)00077-8.

[58] I. Horcas, R. Fernández, J.M. Gómez-Rodríguez, J. Colchero, J. Gómez-Herrero, A.M. Baro, WSXM: A software for scanning probe microscopy and a tool for nanotechnology, Rev. Sci. Instrum. 78 (2007). doi:10.1063/1.2432410.

[59] www.next-tip.com, No Title, (n.d.).

[60] Lord Kelvin, V. *Contact electricity of metals*, Philos. Mag. Ser. 5. 46 (1898) 82–120. doi:10.1080/14786449808621172.

[61] M. Nonnenmacher, M.P. O'Boyle, H.K. Wickramasinghe, Kelvin probe force microscopy, Appl. Phys. Lett. 58 (1991) 2921–2923. doi:10.1063/1.105227.

[62] S.P. Microscopy, Scanning Probe Microscopy Electrical and Electromechanical Phenomena at the Nanoscale, 2007. doi:10.1007/978-0-387-28668-6.

[63] E. Palacios-Lidón, J. Abellán, J. Colchero, C. Munuera, C. Ocal, Quantitative electrostatic force microscopy on heterogeneous nanoscale samples, Appl. Phys. Lett. 87 (2005) 1–3. doi:10.1063/1.2099527.

[64] A. Krajewska, K. Oberda, J. Azpeitia, A. Gutierrez, I. Pasternak, M.F. López, Z. Mierczyk, C. Munuera, W. Strupinski, Influence of Au doping on electrical properties of CVD graphene, Carbon N. Y. 100 (2016) 625–631. doi:10.1016/j.carbon.2016.01.066.

[65] C. V. RAMAN, A Change of Wave-length in Light Scattering, Nature. 121 (1928) 619–619. doi:10.1038/121619b0.

[66] M.S. Dresselhaus, G. Dresselhaus, R. Saito, A. Jorio, Raman spectroscopy of carbon nanotubes, Phys. Rep. 409 (2005) 47–99. doi:10.1016/j.physrep.2004.10.006.

[67] A.C. Ferrari, J.C. Meyer, V. Scardaci, C. Casiraghi, M. Lazzeri, F. Mauri, S. Piscanec, D. Jiang, K.S. Novoselov, S. Roth, A.K. Geim, Raman spectrum of graphene and graphene layers, Phys. Rev. Lett. 97 (2006) 1–4. doi:10.1103/PhysRevLett.97.187401.

[68] K. Kneipp, H. Kneipp, I. Itzkan, R.R. Dasari, M.S. Feld, Ultrasensitive Chemical Analysis by Raman Spectroscopy, Chem. Rev. 99 (1999) 2957–2976. doi:10.1021/cr980133r.

[69] A.C. Ferrari, D.M. Basko, Raman spectroscopy as a versatile tool for studying the properties of graphene, Nat. Nanotechnol. 8 (2013) 235–246. doi:10.1038/nnano.2013.46.

[70] C. Casiraghi, Probing disorder and charged impurities in graphene by Raman spectroscopy pss, 177 (2009) 175–177. doi:10.1002/pssr.200903135.

[71] A. Einstein, Über einen die Erzeugung und Verwandlung des Lichtes betreffenden heuristischen Gesichtspunkt, Ann. Phys. 322 (1905) 132–148.

[72] D. Briggs, M.P. Seah, Practical surface analysis: by auger and x-ray photoelectron spectroscopy, Wiley, 2003.

[73] E.J. Gil, F.R. Morral, Metalurgia general: extractiva, física, mecánica y química, Universidad de Madrid, 1955.

[74] H.W. Kroto, J.R. Heath, S.C. O'Brien, R.F. Curl, R.E. Smalley, C60: buckminsterfullerene. Nature, v. 318, p. 162-163, (1985).

[75] G. Otero-Irurueta, Ciclodeshidrogenación catalizada por superficies: fullerenos a partir de precursores aromáticos, 2010.

[76] C.S. Sundar, A. Bharathi, Y. Hariharan, J. Janaki, V.S. Sastry, T.S. Radhakrishnan, Thermal decomposition of C60, Solid State Commun. 84 (1992) 823–826.

[77] T. Sakurai, X.D. Wang, T. Hashizume, V. Yurov, H. Shinohara, H.W. Pickering, Adsorption of fullerenes on Cu (111) and Ag (111) surfaces, Appl. Surf. Sci. 87 (1995) 405–413.

[78] T. Hashizume, K. Motai, X.D. Wang, H. Shinohara, Y. Saito, Y. Maruyama, K. Ohno, Y. Kawazoe, Y. Nishina, H.W. Pickering, Intramolecular structures of C 60 molecules adsorbed on the Cu (111)-(1× 1) surface, Phys. Rev. Lett. 71 (1993) 2959.

[79] E.I. Altman, R.J. Colton, Nucleation, growth, and structure of fullerene films on Au (111), Surf. Sci. 279 (1992) 49–67.

[80] C. Rogero, J.I. Pascual, J. Gomez-Herrero, A.M. Baro, Resolution of site-specific bonding properties of C 60 adsorbed on Au (111), J. Chem. Phys. 116 (2002) 832–836.

[81] E.I. Altman, R.J. Colton, The interaction of C60 with noble metal surfaces, Surf. Sci. 295 (1993) 13–33.

[82] G. Otero, J. Méndez, STM study of C 60 overlayers on Pt (111) surfaces, Vaccum. 85 (2011) 1059–1062. doi:10.1016/j.vacuum.2010.12.022.

[83] X. Wu, Y. Hu, M. Ruan, N.K. Madiomanana, J. Hankinson, M. Sprinkle, C. Berger, W.A. De Heer, Half integer quantum Hall effect in high mobility single layer epitaxial graphene, Appl. Phys. Lett. 95 (2009) 1–4. doi:10.1063/1.3266524.

[84] A.C. Ferrari, F. Bonaccorso, V. Fal'ko, K.S. Novoselov, S. Roche, P. Bøggild, S. Borini, F.H.L. Koppens, V. Palermo, N. Pugno, J.A. Garrido, R. Sordan, A. Bianco, L. Ballerini, M. Prato, E.

Lidorikis, J. Kivioja, C. Marinelli, T. Ryhänen, A. Morpurgo, J.N. Coleman, V. Nicolosi, L. Colombo, A. Fert, M. Garcia-Hernandez, A. Bachtold, G.F. Schneider, F. Guinea, C. Dekker, M. Barbone, Z. Sun, C. Galiotis, A.N. Grigorenko, G. Konstantatos, A. Kis, M. Katsnelson, L. Vandersypen, A. Loiseau, V. Morandi, D. Neumaier, E. Treossi, V. Pellegrini, M. Polini, A. Tredicucci, G.M. Williams, B. Hee Hong, J.-H. Ahn, J. Min Kim, H. Zirath, B.J. van Wees, H. van der Zant, L. Occhipinti, A. Di Matteo, I.A. Kinloch, T. Seyller, E. Quesnel, X. Feng, K. Teo, N. Rupesinghe, P. Hakonen, S.R.T. Neil, Q. Tannock, T. Löfwander, J. Kinaret, Science and technology roadmap for graphene, related two-dimensional crystals, and hybrid systems, Nanoscale. 7 (2015) 4598–4810. doi:10.1039/C4NR01600A.

[85] C. Lee, X. Wei, J.W. Kysar, J. Hone, Measurement of the elastic properties and intrinsic strength of monolayer graphene, Science (80-.). 321 (2008) 385–388.

[86] X. Li, W. Cai, J. An, S. Kim, J. Nah, D. Yang, L. Colombo, R.S. Ruoff, Large-Area Synthesis of High-Quality and Uniform Graphene Films on Copper Foils, 3893 (2009) 1312–1314.

[87] Q. Yu, J. Lian, S. Siriponglert, H. Li, Y.P. Chen, S.S. Pei, Graphene segregated on Ni surfaces and transferred to insulators, Appl. Phys. Lett. 93 (2008) 91–94. doi:10.1063/1.2982585.

[88] W. Norimatsu, M. Kusunoki, Epitaxial graphene on SiC{0001}: advances and perspectives, Phys. Chem. Chem. Phys. 16 (2014) 3501. doi:10.1039/c3cp54523g.

[89] L.M.A. Perdigão, S.N. Sabki, J.M. Garfitt, P. Capiod, P.H. Beton, Graphene formation by decomposition of C60, J. Phys. Chem. C. 115 (2011) 7472–7476. doi:10.1021/jp111462t.

[90] Y. Yamada, S. Yamada, T. Nakayama, M. Sasaki, T. Tsuru, Electronic modification of C60 monolayers via metal substrates, Jpn. J. Appl. Phys. 50 (2011) 6–9. doi:10.1143/JJAP.50.08LB06.

[91] J. Lu, P.S.E. Yeo, C.K. Gan, P. Wu, K.P. Loh, Transforming C 60 molecules into graphene quantum dots, Nat. Nanotechnol. 6 (2011) 247.

[92] X. Fei, X. Zhang, V. Lopez, G. Lu, H.-J. Gao, L. Gao, Strongly Interacting C60/Ir (111) Interface: Transformation of C60 into Graphene and Influence of Graphene Interlayer, J. Phys. Chem. C. 119 (2015) 27550–27555.

[93] R. Felici, M. Pedio, F. Borgatti, S. Iannotta, M. Capozi, G. Ciullo, A. Stierle, X-ray-diffraction characterization of Pt(111) surface nanopatterning induced by C60adsorption, Nat. Mater. 4 (2005) 688–692. doi:10.1038/nmat1456.

[94] R. Tatti, L. Aversa, R. Verucchi, E. Cavaliere, G. Garberoglio, N.M. Pugno, G. Speranza, S. Taioli, Synthesis of single layer graphene on Cu (111) by C 60 supersonic molecular beam epitaxy, RSC Adv. 6 (2016) 37982–37993.

[95] D. Wei, Y. Lu, C. Han, T. Niu, W. Chen, A.T.S. Wee, Critical crystal growth of graphene on dielectric substrates at low temperature for electronic devices, Angew. Chemie Int. Ed. 52 (2013) 14121–14126.

[96] A.L. Pinardi, G. Biddau, K. Van De Ruit, Vacancy formation on C60 / Pt (111): unraveling the complex atomistic mechanism, 385602 (n.d.). doi:10.1088/0957-4484/25/38/385602.

[97] J. Avila, I. Razado, S.S. Lorcy, R. Fleurier, D. Vignaud, X. Wallart, M.C. Asensio, E. Pichonat, Exploring electronic structure of one-atom thick polycrystalline graphene films: A nano angle resolved photoemission study., Sci. Rep. 3 (2013) 2439. doi:10.1038/srep02439.

[98] O. Frank, J. Vejpravova, V. Holy, L. Kavan, M. Kalbac, Interaction between graphene and copper substrate : The role of lattice orientation, Carbon N. Y. 68 (2013) 440–451.

doi:10.1016/j.carbon.2013.11.020.

[99] A.-Y. Lu, S.-Y. Wei, C.-Y. Wu, Y. Hernandez, T.-Y. Chen, T.-H. Liu, C.-W. Pao, F.-R. Chen, L.-J. Li, Z.-Y. Juang, Decoupling of CVD graphene by controlled oxidation of recrystallized Cu, RSC Adv. 2 (2012) 3008. doi:10.1039/c2ra01281b.

[100] G. V Bianco, M. Losurdo, M.M. Giangregorio, P. Capezzuto, G. Bruno, Exploring and rationalising effective n-doping of large area CVD-graphene by NH 3, Phys. Chem. Chem. Phys. 16 (2014) 3632–3639.

[101] K.C. Prince, I. Ulrych, M. Peloi, B. Ressel, V. Cháb, C. Crotti, C. Comicioli, Core-level photoemission from graphite, Phys. Rev. B - Condens. Matter Mater. Phys. 62 (2000) 6866–6868. doi:10.1103/PhysRevB.62.6866.

[102] X. Yin, Y. Li, F. Ke, C. Lin, H. Zhao, L. Gan, Z. Luo, R. Zhao, T.F. Heinz, Z. Hu, Evolution of the Raman spectrum of graphene grown on copper upon oxidation of the substrate, 7 (2014) 1613–1622. doi:10.1007/s12274-014-0521-0.

[103] R. Ramírez-Jiménez, L. Álvarez-Fraga, F. Jimenez-Villacorta, E. Climent-Pascual, C. Prieto, A. de Andrés, Interference enhanced Raman effect in graphene bubbles, Carbon N. Y. 105 (2016) 556–565.

[104] R. Wu, L. Gan, X. Ou, Q. Zhang, Z. Luo, Detaching graphene from copper substrate by oxidation-assisted water intercalation, Carbon N. Y. 98 (2016) 138–143.

[105] H.J. Monkhorst, J.D. Pack, Special points for Brillouin-zone integrations, Phys. Rev. B. 13 (1976) 5188.

[106] J.I. Martínez, P. Merino, A.L. Pinardi, O.-I. Gonzalo, M.F. López, J. Méndez, J.A. Martín-Gago, Role of the pinning points in epitaxial graphene Moiré superstructures on the Pt (111) surface, Sci. Rep. 6 (2016) 20354.

[107] H. Vita, S. Böttcher, K. Horn, E.N. Voloshina, R.E. Ovcharenko, T. Kampen, A. Thissen, Y.S. Dedkov, Understanding the origin of band gap formation in graphene on metals: graphene on Cu/Ir (111), Sci. Rep. 4 (2014) 5704.

[108] H. González-Herrero, P. Pou, J. Lobo-Checa, D. Fernández-Torre, F. Craes, A.J. Martínez-Galera, M.M. Ugeda, M. Corso, J.E. Ortega, J.M. Gómez-Rodríguez, Graphene tunable transparency to tunneling electrons: a direct tool to measure the local coupling, ACS Nano. 10 (2016) 5131–5144.

[109] A.J. Marsden, M.C. Asensio, J. Avila, P. Dudin, A. Barinov, P. Moras, P.M. Sheverdyaeva, T.W. White, I. Maskery, G. Costantini, N.R. Wilson, G.R. Bell, Is graphene on copper doped?, Phys. Status Solidi - Rapid Res. Lett. 7 (2013) 643–646. doi:10.1002/pssr.201307224.

[110] A.C. Ferrari, Raman spectroscopy of graphene and graphite: disorder, electron–phonon coupling, doping and nonadiabatic effects, Solid State Commun. 143 (2007) 47–57.

[111] J. Azpeitia, G. Otero-Irurueta, I. Palacio, J.I. Martinez, N. Ruiz del Árbol, G. Santoro, A. Gutiérrez, L. Aballe, M. Foerster, M. Kalbac, V. Vales, F.J. Mompeán, M. García-Hernández, J.A. Martín-Gago, C. Munuera, M.F. López, High-quality PVD graphene growth by fullerene decomposition on Cu foils, Carbon N. Y. 119 (2017) 535–543. doi:10.1016/j.carbon.2017.04.067.

[112] Y. Wang, Y. Zheng, X. Xu, E. Dubuisson, Q. Bao, J. Lu, K.P. Loh, Electrochemical delamination of CVD-grown graphene film: Toward the recyclable use of copper catalyst, ACS Nano. 5 (2011) 9927–9933. doi:10.1021/nn203700w.

[113] T. Ciuk, I. Pasternak, A. Krajewska, J. Sobieski, P. Caban, J. Szmidt, W. Strupinski, Properties of chemical vapor deposition graphene transferred by high-speed electrochemical delamination, J. Phys. Chem. C. 117 (2013) 20833–20837. doi:10.1021/jp4032139.

[114] https://www.youtube.com/watch?v=gExiX8oHhs0, (n.d.).

[115] VDP_PRR_13_1.pdf, (n.d.).

[116] Y. Zhang, Y.-W. Tan, H.L. Stormer, P. Kim, Experimental observation of the quantum Hall effect and Berry's phase in graphene, Nature. 438 (2005) 201. http://dx.doi.org/10.1038/nature04235.

[117] T.H.E.E. Method, Mobility in Silicon, 101 (1955) 1699–1701.

[118] D.R. Cooper, B. D'Anjou, N. Ghattamaneni, B. Harack, M. Hilke, A. Horth, N. Majlis, M. Massicotte, L. Vandsburger, E. Whiteway, V. Yu, Experimental review of graphene, 2012 (2011). doi:10.5402/2012/501686.

[119] H. Zhang, Q. Fu, Y. Cui, D. Tan, X. Bao, Growth Mechanism of Graphene on Ru (0001) and O 2 Adsorption on the Graphene / Ru (0001) Surface, 4 (2009) 8296–8301. doi:10.1021/jp810514u.

[120] I. Palacio, G. Otero-Irurueta, C. Alonso, J.I. Martínez, E. López-Elvira, I. Muñoz-Ochando, H.J. Salavagione, M.F. López, M. García-Hernández, J. Méndez, G.J. Ellis, J.A. Martín-Gago, Chemistry below graphene: Decoupling epitaxial graphene from metals by potential-controlled electrochemical oxidation, Carbon N. Y. 129 (2018) 837–846. doi:10.1016/j.carbon.2017.12.104.

[121] L. Koefoed, M. Kongsfelt, S. Ulstrup, A.G. Čabo, A. Cassidy, P.R. Whelan, M. Bianchi, M. Dendzik, F. Pizzocchero, B. Jørgensen, P. Bøggild, L. Hornekær, P. Hofmann, S.U. Pedersen, K. Daasbjerg, Facile electrochemical transfer of large-area single crystal epitaxial graphene from Ir(1 1 1), J. Phys. D. Appl. Phys. 48 (2015). doi:10.1088/0022-3727/48/11/115306.

[122] L. Álvarez-Fraga, J. Rubio-Zuazo, F. Jiménez-Villacorta, E. Climent-Pascual, R. Ramírez-Jiménez, C. Prieto, A. De Andrés, Oxidation Mechanisms of Copper under Graphene: The Role of Oxygen Encapsulation, Chem. Mater. 29 (2017) 3257–3264. doi:10.1021/acs.chemmater.7b00554.

[123] M. Schriver, W. Regan, W.J. Gannett, A.M. Zaniewski, M.F. Crommie, A. Zettl, Graphene as a long-term metal oxidation barrier: Worse than nothing, ACS Nano. 7 (2013) 5763–5768. doi:10.1021/nn4014356.

[124] R. Blume, P.R. Kidambi, B.C. Bayer, R.S. Weatherup, Z.-J. Wang, G. Weinberg, M.-G. Willinger, M. Greiner, S. Hofmann, A. Knop-Gericke, R. Schlögl, The influence of intercalated oxygen on the properties of graphene on polycrystalline Cu under various environmental conditions, Phys. Chem. Chem. Phys. 16 (2014) 25989–26003. doi:10.1039/C4CP04025B.

[125] Y. Hao, M.S. Bharathi, L. Wang, Y. Liu, H. Chen, S. Nie, X. Wang, H. Chou, C. Tan, B. Fallahazad, H. Ramanarayan, C.W. Magnuson, E. Tutuc, B.I. Yakobson, K.F. Mccarty, Y. Zhang, P. Kim, J. Hone, L. Colombo, R.S. Ruoff, The Role of Surface Oxygen in the, 342 (2013) 720–724. doi:10.1126/science.1243879.

[126] Q. Liao, H.J. Zhang, K. Wu, H.Y. Li, S.N. Bao, P. He, Oxidation of graphene on Ru(0 0 0 1) studied by scanning tunneling microscopy, Appl. Surf. Sci. 257 (2010) 82–86. doi:10.1016/j.apsusc.2010.06.037.

[127] L. Jin, Q. Fu, H. Zhang, R. Mu, Y. Zhang, D. Tan, X. Bao, Tailoring the growth of graphene on

Ru(0001) via engineering of the substrate surface, J. Phys. Chem. C. 116 (2012) 2988–2993. doi:10.1021/jp210206y.

[128] A. Dong, Q. Fu, M. Wei, Y. Liu, Y. Ning, F. Yang, H. Bluhm, X. Bao, Facile oxygen intercalation between full layer graphene and Ru(0001) under ambient conditions, Surf. Sci. 634 (2015) 37–43. doi:10.1016/j.susc.2014.10.008.

[129] W.-J. Jang, H. Kim, J.H. Jeon, J.K. Yoon, S.-J. Kahng, Recovery and local-variation of Dirac cones in oxygen-intercalated graphene on Ru(0001) studied using scanning tunneling microscopy and spectroscopy, Phys. Chem. Chem. Phys. 15 (2013) 16019. doi:10.1039/c3cp52431k.

[130] E. Voloshina, N. Berdunov, Y. Dedkov, Restoring a nearly free-standing character of graphene on Ru(0001) by oxygen intercalation, Sci. Rep. 6 (2016) 1–10. doi:10.1038/srep20285.

[131] P. Sutter, P. Albrecht, X. Tong, E. Sutter, Mechanical decoupling of graphene from Ru(0001) by interfacial reaction with oxygen, J. Phys. Chem. C. 117 (2013) 6320–6324. doi:10.1021/jp400838j.

[132] Y. Yao, Q. Fu, Y.Y. Zhang, X. Weng, H. Li, M. Chen, L. Jin, A. Dong, R. Mu, P. Jiang, L. Liu, H. Bluhm, Z. Liu, S.B. Zhang, X. Bao, Graphene cover-promoted metal-catalyzed reactions, Proc. Natl. Acad. Sci. 111 (2014) 17023–17028. doi:10.1073/pnas.1416368111.

[133] R.S. Weatherup, L. D'Arsié, A. Cabrero-Vilatela, S. Caneva, R. Blume, J. Robertson, R. Schloegl, S. Hofmann, Long-Term Passivation of Strongly Interacting Metals with Single-Layer Graphene, J. Am. Chem. Soc. 137 (2015) 14358–14366. doi:10.1021/jacs.5b08729.

[134] C. Romero-Muñiz, A. Martín-Recio, P. Pou, J.M. Gómez-Rodríguez, R. Pérez, Strong dependence of flattening and decoupling of graphene on metals on the local distribution of intercalated oxygen atoms, Carbon N. Y. 101 (2016) 129–134. doi:10.1016/j.carbon.2016.01.079.

[135] A.L. Walter, S. Nie, A. Bostwick, K.S. Kim, L. Moreschini, Y.J. Chang, D. Innocenti, K. Horn, K.F. McCarty, E. Rotenberg, Electronic structure of graphene on single-crystal copper substrates, Phys. Rev. B - Condens. Matter Mater. Phys. 84 (2011).

[136] S.D. Costa, J. Ek Weis, O. Frank, M. Kalbac, Temperature and face dependent copper-graphene interactions, Carbon N. Y. 93 (2015) 793–799. doi:10.1016/j.carbon.2015.06.002.

[137] P.R. Kidambi, B.C. Bayer, R. Blume, Z.J. Wang, C. Baehtz, R.S. Weatherup, M.G. Willinger, R. Schloegl, S. Hofmann, Observing graphene grow: Catalyst-graphene interactions during scalable graphene growth on polycrystalline copper, Nano Lett. 13 (2013) 4769–4778. doi:10.1021/nl4023572.

[138] Z.R. Robinson, E.W. Ong, T.R. Mowll, P. Tyagi, D.K. Gaskill, H. Geisler, C.A. Ventrice, In fl uence of Chemisorbed Oxygen on the Growth of Graphene on Cu(100) by Chemical Vapor Deposition, (2013).

[139] Z.R. Robinson, E.W. Ong, T.R. Mowll, P. Tyagi, D.K. Gaskill, H. Geisler, C.A. Ventrice, Influence of chemisorbed oxygen on the growth of graphene on Cu(100) by chemical vapor deposition, J. Phys. Chem. C. 117 (2013) 23919–23927. doi:10.1021/jp410142r.

[140] F.A. Akgul, G. Akgul, N. Yildirim, H.E. Unalan, R. Turan, Influence of thermal annealing on microstructural, morphological, optical properties and surface electronic structure of copper oxide thin films, Mater. Chem. Phys. 147 (2014) 987–995. doi:10.1016/j.matchemphys.2014.06.047.

[141] U.A. Schröder, E. Grånäs, T. Gerber, M.A. Arman, A.J. Martínez-Galera, K. Schulte, J.N.

Andersen, J. Knudsen, T. Michely, Etching of graphene on Ir(111) with molecular oxygen, Carbon N. Y. 96 (2016) 320–331. doi:10.1016/j.carbon.2015.09.063.

[142] N.S. Mcintyre, M.G. Cook, X-Ray Photoelectron Studies on Some Oxides and Hydroxides of Cobalt, Nickel, and Copper, Anal. Chem. 47 (1975) 2208–2213. doi:10.1021/ac60363a034.

[143] C.R. Parkinson, M. Walker, C.F. McConville, Reaction of atomic oxygen with a Pt(1 1 1) surface: Chemical and structural determination using XPS, CAICISS and LEED, Surf. Sci. 545 (2003) 19–33. doi:10.1016/j.susc.2003.08.029.

[144] M. Lazzeri, F. Mauri, Nonadiabatic Kohn anomaly in a doped graphene monolayer, Phys. Rev. Lett. 97 (2006) 29–32. doi:10.1103/PhysRevLett.97.266407.

[145] C. Casiraghi, Probing disorder and charged impurities in graphene by Raman spectroscopy, Phys. Status Solidi (RRL)-Rapid Res. Lett. 3 (2009) 175–177.

[146] L. Ferrighi, D. Perilli, D. Selli, C. Di Valentin, Water at the Interface Between Defective Graphene and Cu or Pt (111) Surfaces, ACS Appl. Mater. Interfaces. 9 (2017) 29932–29941.

[147] A. Eckmann, A. Felten, A. Mishchenko, L. Britnell, R. Krupke, K.S. Novoselov, C. Casiraghi, Probing the nature of defects in graphene by Raman spectroscopy, Nano Lett. 12 (2012) 3925–3930. doi:10.1021/nl300901a.

[148] H. Suderow, J.P. Brison, A. Huxley, J. Flouquet, Thermal conductivity and gap structure of the superconducting phases of UPt3, J. Low Temp. Phys. 108 (1997) 11–30. doi:10.1007/BF02396814.

[149] K. Izawa, H. Takahashi, H. Yamaguchi, Y. Matsuda, M. Suzuki, T. Sasaki, T. Fukase, Y. Yoshida, R. Settai, Y. Onuki, Superconducting gap structure of spin-triplet superconductor Sr2RuO4 studied by thermal conductivity, Phys. Rev. Lett. 86 (2001) 2653–2656. doi:10.1103/PhysRevLett.86.2653.

[150] J.A. Gerber, W.L. Burmester, D.J. Sellmyer, Simple vibrating sample magnetometer, Rev. Sci. Instrum. 53 (1982) 691–693. doi:10.1063/1.1137043.

[151] D. Drung, R. Cantor, M. Peters, H.J. Scheer, H. Koch, Low-noise high-speed dc superconducting quantum interference device magnetometer with simplified feedback electronics, Appl. Phys. Lett. 57 (1990) 406–408. doi:10.1063/1.103650.

[152] P. Fischer, G. Schütz, G. Schmahl, P. Guttmann, D. Raasch, Imaging of magnetic domains with the X-ray microscope at BESSY using X-ray magnetic circular dichroism, Zeitschrift Fr Phys. B Condens. Matter. 101 (1996) 313–316. doi:10.1007/s002570050214.

[153] A. Bezryadin, B. Pannetier, Role of edge superconducting states in trapping of multi-quanta vortices by microholes. Application of the bitter decoration technique, J. Low Temp. Phys. 102 (1996) 73–94. doi:10.1007/BF00755110.

[154] http://faculty.chem.queensu.ca/people/faculty/mombourquette/Chem221/5_PhaseChanges/PhaseD1.gif, (n.d.).

[155] Q.P.S.& E.E.C.P.T. for L. at C. Martin Wilson superconducting wires and cables EMAG-2005, 11 April 2005. Lecture 2 slide 2 Technical Readings for AGH-QPG Members, http://qps.web.cern.ch/qps/download/pdf/Quench_Wilson_1.pdf, (n.d.).

[156] A. Hadjipanayis, George C.Kim, M. Klaui, C.A.F. Vaz, J. Rothman, J.A.C. Bland, W. Wernsdorfer, G. Faini, E. Cambril, G. Tatara, H. Kohno, R. Lavrijsen, J.-H. Lee, A. Fernández-Pacheco, D.C.M.C. Petit, R. Mansell, R.P. Cowburn, R. Scha, U. Ru, C.A.F. Vaz, J.A.C. Bland, C. David, X.

Zhu, P. Grütter, J.F. Pulecio, S. Bhanja, X. Zhu, P. Grutter, Y. Martin, H.K. Wickramasinghe, J. Chang, V.L. Mironov, B.A. Gribkov, A.A. Fraerman, S.A. Gusev, S.N. Vdovichev, X. Zhu, P. Grütter, V. Metlushko, B. Ilic, L. Gross, R.R. Schlittler, G. Meyer, R. Allenspach, A. Lyle, A. Klemm, J. Harms, Y. Zhang, H. Zhao, J. Wang, A. Lyle, A. Klemm, J. Harms, Y. Zhang, H. Zhao, G. Binnig, D. Technical, X. Zhu, P. Grütter, V. Metlushko, B. Ilic, S.A. Haque, M. Yamamoto, R. Nakatani, Y. Endo, M.A. Siddiq, M.T. Niemier, G. Csaba, X.S. Hu, W. Porod, G.H. Bernstein, Domain wall pinning versus nucleation of reversed domains in R-Fe-B magnets (invited)., Phys. Rev. Lett. 92 (2013) 647–650. doi:10.1103/PhysRevLett.92.086601.

[157] D. Rugar, H.J. Mamin, P. Guethner, S.E. Lambert, J.E. Stern, I. McFadyen, T. Yogi, Magnetic force microscopy: General principles and application to longitudinal recording media, J. Appl. Phys. 68 (1990) 1169–1183. doi:10.1063/1.346713.

[158] D. Romel, E.R. Burke, I.D. Mayergoyz, Magnetic imaging in the presence of external fields: Technique and applications, J. Appl. Phys. 79 (1996) 6441–6446. doi:10.1063/1.361966.

[159] H. Zhong, W. Peng, G. Tarrach, A. Drechsler, J. Jiang, D. Wei, J. Yuan, Non-contact magnetic force microscopy of recording media by ex situ tip magnetization reversal method, J. Phys. D. Appl. Phys. 41 (2008). doi:10.1088/0022-3727/41/8/085002.

[160] A. Hubert, W. Rave, S.L. Tomlinson, Imaging Magnetic Charges with Magnetic Force Microscopy, Phys. Status Solidi. 204 (1997) 817–828. doi:10.1002/1521-3951(199712)204:2<817::AID-PSSB817>3.0.CO;2-D.

[161] J.A. Galvis, E. Herrera, I. Guillamón, J. Azpeitia, R.F. Luccas, C. Munuera, M. Cuenca, J.A. Higuera, N. Díaz, M. Pazos, M. García-Hernandez, A. Buendía, S. Vieira, H. Suderow, Three axis vector magnet set-up for cryogenic scanning probe microscopy, Rev. Sci. Instrum. 86 (2015). doi:10.1063/1.4905531.

[162] I.R. Shein, A.L. Ivanovskii, Electronic band structure and Fermi surface of tetragonal low-temperature superconductor Bi 2 Pd as predicted from first principles, J. Supercond. Nov. Magn. 26 (2013) 1–4.

[163] E. Herrera, I. Guillamón, J.A. Galvis, A. Correa, A. Fente, R.F. Luccas, F.J. Mompean, M. García-Hernández, S. Vieira, J.-P. Brison, Magnetic field dependence of the density of states in the multiband superconductor β− Bi 2 Pd, Phys. Rev. B. 92 (2015) 54507.

[164] E. Herrera Vasco, Visualizing the influence of the Fermi surface on superconductivity, (2016).

[165] A.C. Orellana, H.J. Suderow, C.M. López, Magnetic Force Microscopy study of layered superconductors in vectorial magnetic fields, (n.d.).

[166] pericles_0470845015, (n.d.).

Publication list

- J. Azpeitia, J. I. Martinez, I. Muñoz-Otxando, K. Lawaet, I. Palacio, F. Mompean, G. Ellis, M. García-Hernández, J. A. Martín-Gago, M. F. López and C. Munuera. "Oxygen intercalation in graphene grown on Copper Substrates", to be submitted shortly.
- Backes, A. M. Abdelkader, C. Alonso, A. Andrieux, R. Arenal, J. Azpeitia et al., "Synthesis of 2D materials across the Flagship "Graphene"", 2D Materials (2018) submitted.
- J. Azpeitia, G. Otero-Irurueta, I. Palacio, J. I. Martinez, N. Ruiz del Árbol, G. Santoro, A. Gutiérrez, L. Aballe, M. Foerster, M. Kalbac, V. Vales, F. J. Mompeán, M. García-Hernández, J. A. Martín-Gago, C. Munuera and M. F. López. "High-quality PVD graphene growth by fullerene decomposition on Cu foils". Carbon 119, 535 (2017).
- R. Muñoz, C. Munuera, J. I. Martinez, J. Azpeitia, C. Gómez-Aleixandre and M. García-Hernández. "Low temperature metal free growth of graphene on insulating substrates by plasma assisted chemical vapor deposition". 2D Mater. 4, 015009 (2017).
- A. Krajewska, K. Oberda, J. Azpeitia, A. Gutierrez, I. Pasternak, M. F. López, Z. Mierczyk, C. Munuera and W. Strupinski. "Influence of Au doping on electrical properties of CVD graphene". Carbon 100, 625 (2016).
- A. Alberca, C. Munuera, J. Azpeitia, B. Kirby, N. M. Nemes, A. M. Pérez-Muñoz, J. Tornos, F. J. Mompeán, C. León, J. Santamaría and M. García-Hernández. "Phase separation enhanced magneto-electric coupling in La0.7Ca0.3MnO3/BaTiO3 ultra-thin films". Sci. Rep. 5, 17926 (2015).
- M. Rocci, J. Azpeitia, J. Trastoy, A. Perez-Muñoz, M. Cabero, R. F. Luccas, C. Munuera, F. J. Mompeán, M. García-Hernández, K. Bouzehouane, Z. Sefrioui, C. León, A. Rivera-Calzada, J. E. Villegas and J. Santamaría. "Proximity Driven Commensurate Pinning in YBa2Cu3O7 through All-Oxide Magnetic Nanostructures". Nano Lett. 15, 11, 7526 (2015).
- R. F. Luccas, A. Fente, J. Hanko, A. Correa-Orellana, E. Herrera, E. Climent-Pascual, J. Azpeitia, T. Pérez-Castañeda, M. R. Osorio, E. Salas-Colera, N. M. Nemes, F. J. Mompean, M. García-Hernández, J. G. Rodrigo, M. A. Ramos, I. Guillamón, S. Vieira and H. Suderow. "Charge density wave in layered La1−xCexSb2". Phys. Rev. B 92, 235153 (2015).
- J. A. Galvis, E. Herrera, I. Guillamón, J. Azpeitia, R. F. Luccas, C. Munuera, M. Cuenca, A. Higuera, N. Díaz, M. Pazos, M. García-Hernandez, A. Buendía, S. Vieira, and H. Suderow. "Three axis vector magnet set-up for cryogenic scanning probe microscopy". Rev. Sci. Inst. 86, 1 (2015).
- T. Perez-Castaneda, J. Azpeitia, J. Hanko, A. Fente, H. Suderow, M. A. Ramos "Low-Temperature Specific Heat of Graphite and CeSb2: Validation of a Quasiadiabatic Continuous Method". J. Low. Temp. Phys. 173, 4 (2013).

Acknowledgments

Antes que nada, me gustaría agradecer a mis dos directoras de tesis, tanto a Carmen como a Paqui, todo lo que me han ayudado a lo largo de esta tesis. Con todos los problemas que han surgido, siempre he podido contar con vosotras. Ha sido un auténtico placer llevar a cabo este trabajo bajo vuestra dirección. Espero haber estado a la altura. Muchas gracias!

También quisiera agradecer a Hermann la oportunidad que me dio de trabajar en un laboratorio, con el trabajo de fin de máster, así como a todo el laboratorio de bajas temperaturas (ese Antón. cuánto cuarzo a la basura, keep rotating!). En especial, a Tomás. Gracias Maestro.

Quisiera agradecer a Mar no solo la oportunidad de hacer la tesis, sino el haberse preocupado de que llegase a buen puerto, a pesar de los jaleos en los que se mete, siempre ha sacado un rato para preocuparse por mi situación (Jon, vives en el caos). Lo bien recibido que me sentí en ese laboratorio, gracias a Aurora, Ana, Paco, Luis (tengo que probar el calmante del 27), Norbert (gracias por ayudarme y explicarme todo lo del botijo con el imán) y más tarde Alex, un crack, y el gran Roberto F. Luccas. No eres consciente de cuánto me has ayudado, gracias. Pero, sobre todo, Federico (Mompeán, que huele!). No sé cuánto tiempo te he hecho perder. Mucho. Gracias de verdad por todas las discusiones, de XRD, de grafeno, de las historias de Madrid… he aprendido mucho, pero lo mejor es que veo todo lo que me queda (por lo menos veo mucho, espero que no haya más por favor).

También me gustaría agradecer a José Ángel; además de aclararme ideas que llevaba meses dándoles vueltas, en un par de minutos y como quien no quiere la cosa, su manera de motivarme en sacar buenos resultados (esa miel de flores) ha sido clave. Además, aunque oficialmente no fuera del grupo, siempre me ha hecho que me sintiera uno más en ESISNA. Esto también es gracias a toda la banda, empezando por Gonzalo Otero (ostia lo que pude aprender en dos meses, también es verdad que no sabía por dónde me daba el aire, eso siempre ayuda). Muchas gracias tio!. Gonzalo se piró, luego apareció Irene, que todavía no se olía la que le iba a caer. Sabes que si no es por ti este trabajo no sale. Te debo mucho más que unas palabras, unas piparras, queso idiazábal y txakoli por lo menos. (Azpeitia, déjate de ostias y tira a hacer muestras! txop txop!). Gracias por todo el tiempo y la dedicación. Y por enseñarme a currar. A toda la peña que ya estaba, Nacho, van un vasco y un vallisoletano y en vez de ostiarse, se llevan de puta madre (creo que lo tuyo es diagnosticable), Nerea, con esa alegría, siempre dispuesta a ayudar, y a echarse unas risas (el agua!), no cambies nunca, solo podría ser a peor, eres muy grande! El gran Javi, por cada cosa que se me jodia sabia como arreglarla (que te crees, que solo a ti se te han jodido cosas?). También quiero agradecer a Carlos que haya desmantelado el Nautilus (no te lo perdonaré jamás!). Luego vinieron los nanocosmers (de verdad, pensaba que ibais a poner un billar). Gracias a Jesús, eres una puta maquina, y contra lo que decía aquel, las máquinas claro que hacen máquinas a su vez. Gracias a Koen, esos XPS hasta en la fiesta del tituto, Lidia, un encanto de persona, gracias por todo, desde inventar esas puntas con NPs (son la ostia y lo sabes!) hasta las conversaciones sobre todas las dudas que tenía sobre NPs, UHV… asi como de lo bien que va la sociedad. Y por supuesto, Gonzalo Santoro. Aunque hemos tenido muchas conversaciones sobre física (mucho raman, mucho fonón…), las mejores han sido las de literatura, existencialismo y no diré más, porque *de lo que no se puede hablar hay que callar*, como dice ese amigo tuyo. Y ese Jose, por mucha envidia que me dé cuando tiene que ir a Donosti. También quisiera agradecer al resto de la gente del grupo: Rebeca, Irene, Pablo, Pedro y Mario. Gracias!

También quisiera agradecer a Adolfo, por todas las mañanas que me pasé llevándole muestras jodidas para medir. A veces se veía, a veces no. Buenos ratos, gracias! Y a Isabel, también por las medidas, pero sobre todo por la pedrada que tienes en la cabeza, qué risas me echaba, muchas gracias!

Me gustaría agradecer a la peña del IKKM con los que me he echado buenos ratos, Pedro (the sentinel), Jorge y Juanma y esos pitis en la tercera (venga Jon, que ya lo tienes!...no lo tenía) y Valen (arratsalde on!) así como a Cayetana (Que pasa vasco!). A Cristina, a Carlos y a LuzK, de ese despacho donde nunca faltaban polvorones, pastas ni risas. Gracias!

También quiero agradecer a José Luis la oportunidad de trabajar en el proyecto de ESSBilbao, y a la peña de allí que aguantó mi agonía con la tesis, Rosalba (giputxi!), Javi Corres, el giputxi de verdad (que

tal vas?), y Carlos, *the engineer* (duermes algo ya?). Había mucha más gente que merecía mucho la pena (Gorka, JonBi, Aitor, Javi, Alex, Idoia, Miguel, Ander, Xabi…) espero que os vaya todo muy bien, allá donde andéis.

No puedo olvidarme de la peña raciones (de verdad, lo he intentado!), El puto Willy (jajajajaja lo siento lo siento jajajajaj) que se reía en tu cara, Ana, que está muy mal de la cabeza (tu tesis me ha ayudado muchísimo), Hector (salmorejo+ avispas=risas pa los demás) Javi, el Brian May del grupete, Marina, buenas discusiones; si ganase alguna… Alba (éramos los más alegres de la cafetería, lo sabes) y claro, el jodido Hugo (vasco de palo dice, qué de ostias te mereces) muy grande tio, esos pitillos en el IKKM y alguna que otra borrachera de domingo a la hora de comer (perdón, alargar el vermut), espero que andes bien por el yanqui.

I would also like to acknowledge to the people of the group of prof. Strupinski, with special mention to Ola. Thank you for standing me in your lab at Warsaw, and for all your help and *transfer* of knowledge. Dziękuję bardzo!

I Also would like to thank to the group of prof. Osterwalder in Zürich, specially to Elisa, that although you were moving to another job out of science, you spent a lot of time and effort in that week in your lab just for my own benefit. Mille grazie! (I remember the poster at your office: *Alles falsch!* Paradoxically, that is true).

También soy consciente de que las pelas no caen del cielo (en los bautizos cristianos si, no?).Gracias a todos los ciudadanos españoles (a los que pagan impuestos) por financiar mi jornal para realizar este trabajo a través de la beca BES-2012-058600 del programa FPI.

Nere betiko Leazpiko lagunei eskerrak eman nahi dizkizuet, kuadrilakoi, txikitatio zuen laguntasunagatik, eskerrik asko! (Xeura, Jozu, Kaiser, Poxi, Zata, Otsoa, Dennis…) Gora Legazpi!

Ta azkenik, garrantzitsunak zeatelako, zuek bukaerarako utzi zaituztet. Nere familiai, nere bi anaiei, Mikel ta Iñakiri, eskerrik asko beti hor eoteagatik ta beti zuekin kontau deiketelako.Nere aitai, eskerrik asko danagatik aita, asko lagundu diazu ez oain, baizik beti.

Ta nola ez, egunero zaittudalako nere gogon, eskerrik asko danagatik ama.

Hemen beharko zinake. Faltan botatzen zaittut.

Madrid, 2018-ko ekaina.